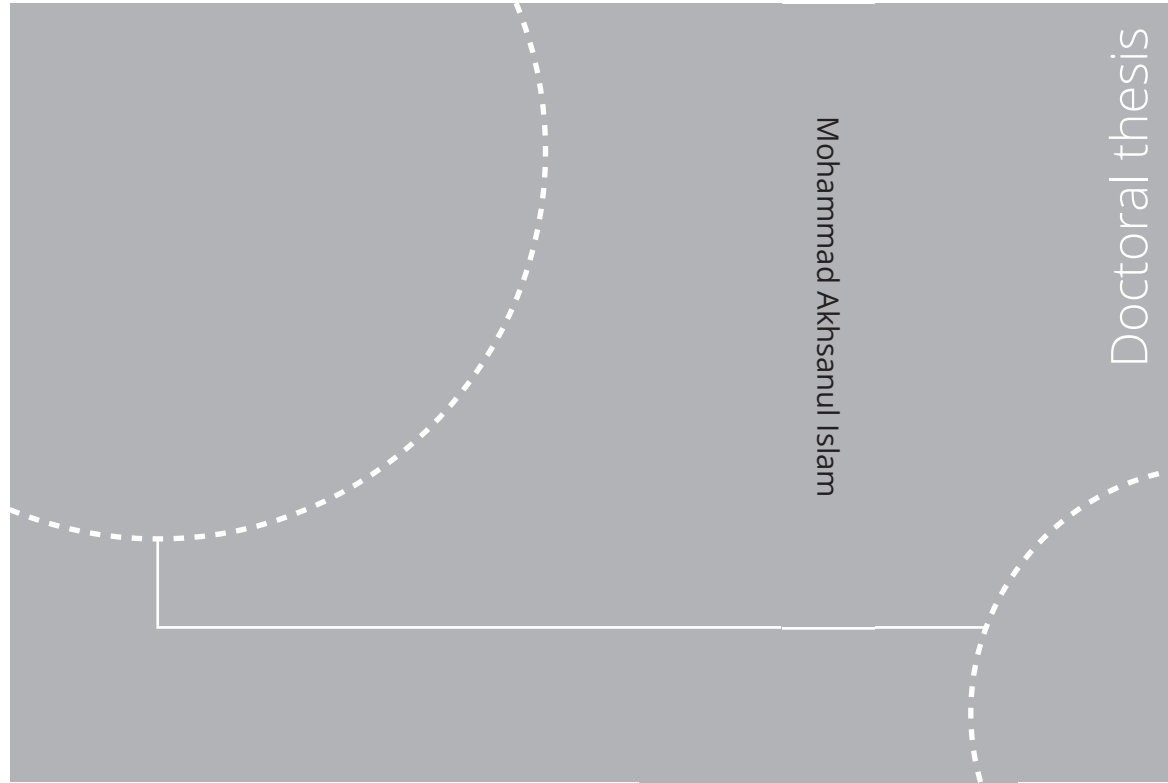


ISBN 978-82-326-7128-1 (printed ver.)
ISBN 978-82-326-7127-4 (electronic ver.)
ISSN 1503-8181 (printed ver.)
ISSN 2703-8084 (electronic ver.)



Doctoral theses at NTNU, 2023:213

Mohammad Akhsanul Islam

Numerical Modelling of Arctic Coastal Erosion

Doctoral theses at NTNU, 2023:213

NTNU
Norwegian University of
Science and Technology
Thesis for the degree of
Philosophiae Doctor
Faculty of Engineering
Department of Civil and Environmental
Engineering

Mohammad Akhsanul Islam

Numerical Modelling of Arctic Coastal Erosion

Thesis for the degree of Philosophiae Doctor

Trondheim, "JUNE" "2023"

Norwegian University of Science and Technology

Faculty of Engineering

Department of Civil and Environmental Engineering



Norwegian University of
Science and Technology

NTNU

Norwegian University of Science and Technology

Thesis for the degree of Philosophiae Doctor

Faculty of Engineering

Department of Civil and Environmental Engineering

© Mohammad Akhsanul Islam

ISBN 978-82-326-7128-1 (printed ver.)

ISBN 978-82-326-7127-4 (electronic ver.)

ISSN 1503-8181 (printed ver.)

ISSN 2703-8084 (electronic ver.)

Doctoral theses at NTNU, 2023:213



Printed by Skipnes Kommunikasjon AS

Mohammad Akhsanul Islam

Numerical Modelling of Arctic Coastal Erosion

Doctoral thesis
for the degree of Philosophiae Doctor

Trondheim, June 2023

Norwegian University of Science and Technology
Faculty of Engineering
Department of Civil and Environmental Engineering



NTNU

Norwegian University of Science and Technology

Doctoral thesis
for the degree of Philosophiae Doctor

Faculty of Engineering
Department of Civil and Environmental Engineering

© 2023 Mohammad Akhsanul Islam. All rights reserved

ISBN 978-82-326-7128-1 (printed version)
ISBN 978-82-326-7127-4 (electronic version)
ISSN N.A.

Doctoral theses at NTNU, 2023:213

Printed by NTNU

Abstract

Arctic coastal erosion is a growing concern as global climate change affects the planet. Unlike low-latitude and mid-latitude coastal areas, the sediments along Arctic coastlines are often frozen, even during summer. It is essential to consider both thermal and mechanical factors when analysing Arctic coastal erosion.

Two major erosion mechanisms in the Arctic have been identified: thermodenudation and thermoabrasion. Thermodenudation refers to the thawing and melting of the frozen soil, while thermoabrasion refers to the mechanical action of waves and ice against the coast. Various numerical models have been developed in recent years to describe these mechanisms, but one limitation of such models is the difficulty of including hydrodynamic forces. Moreover, the available coastal erosion models developed for warmer climates cannot be applied to Arctic coastal erosion, where permafrost is a significant environmental parameter.

To address these challenges, a new methodology has been proposed in this thesis that allows using models designed for warmer climates to simulate Arctic coastal erosion. A modular approach is adopted where the processes related to permafrost thawing and Arctic coastal erosion are represented as submodules. The open-source software XBeach is used to simulate the waves, sediment transport, and morphological changes in the nearshore. Different submodules are developed to simulate the processes unique to Arctic coasts, such as thawing-freezing, slumping, wave-cut niche, bluff failure, and more. These submodules are coupled with XBeach to enable concurrent simulation of the thermodenudation and thermoabrasion Arctic coastal erosion.

Since 2012, field investigations have been conducted at an Arctic coast named Baydaratskya Bay in the Kara Sea, Russia, as part of the Sustainable Arctic Marine and Coastal Technology (SAMCoT) project. These investigations are carried out annually in the summer by the Lomonosov Moscow State University (MSU) to collect data from the study area. The measurement of coastal profiles during these investigations are used in this study to calibrate and validate numerical models. The study area is unique since the two erosion mechanisms - thermoabrasion and thermodenudation - are both active. The backbone of this thesis is based on the reports, in situ tests, measurements, and observations

made during the field investigations carried out over the years. The investigations of the study area are critical to understanding the complex coastal dynamics in the region, and it provides an invaluable resource for working on issues related to climate change and coastal erosion.

Some of the model's input parameters are calibrated using field measurements and the model is then validated by another set of mutually exclusive field measurements under different morphological conditions from the study area. The sensitivity analysis of the model reveals that nearshore waves are a significant driver of erosion, and the inclusion of nearshore hydrodynamics and sediment transport is essential for accurately modeling the erosion mechanism. This finding highlights the importance of considering multiple physical processes and their interactive nature when modeling Arctic coastal erosion.

In data-poor environments such as the Arctic coastal regions, developing a deterministic model to describe the processes and predict the outcomes of coastal erosion can be challenging. Deterministic models rely on precise and accurate input data and may not capture the full range of uncertainties associated with the system being studied. A probabilistic model based on Monte Carlo simulation is developed by assuming a probabilistic distribution of the input parameters. The probabilistic approach is demonstrated using an earlier Arctic coastal erosion model version. Crest retreat due to thermoabrasion on the coastal profile is simulated, and the probability of the bluff collapsing during a storm is estimated.

One of the challenges in studying Arctic coastal erosion is the lack of temperature measurements of permafrost. The temporal and spatial resolutions of the temperature observations are relatively high, making it difficult to analyse the data. Therefore, in this study, a data-driven model is developed to interpolate, hindcast, and forecast temperature measurements within the active layer and shallow permafrost when the temperature measurements at the surface or near the surface are available. The temperature variations along the year are periodic, and hence attempts are made to express the seasonal variations with a combination of periodic functions (Fourier components), which are then used as boundary conditions to reach the analytical solutions.

Preface

This thesis is submitted to the Norwegian University of Science and Technology (NTNU) for partial fulfilment of the requirements for the degree of philosophy in civil engineering.

This doctoral work has been performed at the Department of Civil and Environmental Engineering (IBM) at NTNU with Professor Raed Lubbad as the main supervisor. The co-supervisors are Mohammad Saud Afzal, Assistant Professor, Department of Civil Engineering, Indian Institute of Technology, Kharagpur, West Bengal, India and Thomas Ingeman-Nielsen, Associate Professor, Department of Environmental and Resource Engineering Geotechnics & Geology, Technical University of Denmark, DTU.

This work has been supported by the EU H2020-funded Nunataryuk project (Grant: 773421), where it is filed as part of deliverable 6.4. Field measurements are provided by Research Council of Norway through NTNU's Research Centre for the Sustainable Arctic Marine and Coastal Technology (SAMCoT) and partners.

Acknowledgement

Writing a PhD thesis is not an easy task, and it takes a village of supporters to make it happen. As such, I would like to take this opportunity to express my sincere gratitude to all those who have played a role in supporting me during this journey.

First and foremost, I would like to extend my heartfelt appreciation to my PhD thesis supervisor, Professor Raed Lubbad, for his support and guidance throughout my research journey. His knowledge and expertise have been invaluable to me, and his dedication to my success has been unwavering. He has provided insightful feedback on my work, challenged my assumptions, and encouraged me to think critically. His willingness to invest time and effort in my work has been a constant inspiration, and I am deeply grateful for his patient mentoring and encouragement. I would not have been able to complete this thesis without his support, guidance, and encouragement.

I am also grateful to Dr. Saud Afzal for his contributions to my research. His feedback and insights have been invaluable in shaping the direction of my work, and their support and encouragement have helped me to stay motivated during the more challenging phases of my research.

Professor Vladislav Isaev and his team at Lomonosov Moscow State University have played a vital role in my field observations and data curation, and I am immensely grateful for the opportunities and resources they have provided me. These have been instrumental in shaping my research, and I owe much of my success to their support.

I would also like to extend my gratitude to Hossein Reza Abbasi, Hongtao Li, Adrianna Correia, Ahmet Soydan, Eva Schmitt, Sebastian Drexler, Vegard Hornnes and Weizi Wang. I am deeply grateful for the social interactions I had with them.

Finally, I would like to express my appreciation to my family and friends for their unwavering support and encouragement throughout my studies. Their love and encouragement have given me the strength and resilience to persevere through the many challenges of graduate school. I am grateful for their belief in me, and I feel truly blessed to have such wonderful people in my life.

I would like to apologise to my beloved children, Sayan and Einar, for the selfish pursuit of my degree. I regret not obtaining my Ph.D. before they were born. Looking back, I realise that my actions caused them immense suffering, and for that, I am truly remorseful. It was not fair to them, and for that, I am eternally ashamed.

In conclusion, I thank all those who have supported me in one way or another during my PhD journey. Your support, guidance, and encouragement have made all the difference, and I am deeply grateful for everything you have done for me.

Declaration of the authorship

Three international journal papers are appended as appendices to this thesis.

1. Islam, M. A., Lubbad, R., & Afzal, M. S. (2020). A probabilistic model of coastal bluff-top erosion in high latitudes due to thermoabrasion: a case study from Baydaratskaya Bay in the Kara Sea. *Journal of Marine Science and Engineering*, 8(3), 169.
<https://doi.org/10.3390/jmse8030169>
2. Islam, M. A., Lubbad, R., Amiri, S. A. G., Isaev, V., Shevchuk, Y., Uvarova, A. V., & Kumar, A. (2021). Modelling the seasonal variations of soil temperatures in the Arctic coasts. *Polar Science*, 30, 100732.
<https://doi.org/10.1016/j.polar.2021.100732>
3. Islam, M. A., & Lubbad, R. (2022). A Process-Based Model for Arctic Coastal Erosion Driven by Thermodenudation and Thermoabrasion Combined and including Nearshore Morphodynamics. *Journal of Marine Science and Engineering*, 10(11), 1602.
<https://doi.org/10.3390/jmse10111602>

Paper 1

The first, second and third co-authors were responsible for conceptualisation, review and editing. The second authors contributed to methodology, supervision and project administration. The first author was responsible for numerical codes, analysis, results, visualisation and manuscript writing.

Paper 2

The first and second authors were responsible for conceptualisation, review and editing of the manuscript. The third author contributed to part of the numerical implementation. The fourth, fifth and sixth co-author contributed to field investigations, in situ measurements and data curation. The fourth co-author contributed to review and editing of the manuscript. Field measurement was conducted under supervision of fourth co-author. The seventh and eighth co-authors contributed to the conceptualisation, reviewing and

project administration. The first author was responsible for software development, analysis, visualisation and manuscript writing.

Paper 3

The first and second authors were responsible for conceptualisation, methodology and draft writing. Additionally, the first author was responsible for the software, validation, visualisation and formal analysis. The second co-author contributed to write the manuscript, review, supervise, edit, and investigate.

Contents

Contents	XIV
List of Tables	XV
List of Figures	XXI
1 Introduction	1
1.1 Background	1
1.2 Motivation of the study	5
1.3 Research questions	7
1.4 Research plan	8
1.4.1 Phase 1: Defining the research problem and scope of the work	8
1.4.2 Phase 2: Conducting a literature review	8
1.4.3 Phase 3: Execution of the various research tasks	8
1.4.3.1 Field observation	8
1.4.3.2 Data curation	9
1.4.3.3 Model development	9
1.4.3.4 Dissemination of results	10
1.5 Limitation of the study	10
1.6 The organisation of the thesis	11
1.6.1 Readership	11
1.6.2 List of chapters	11

2	Mechanisms of Arctic coastal erosion	13
2.1	Background	13
2.1.1	Lithified and unlithified Arctic coasts	13
2.1.2	Definitions	13
2.1.3	Permafrost	15
2.1.4	A typical Arctic coast	15
2.2	Thermodenudation	16
2.2.1	Initial phase	16
2.2.2	Thawing phase	17
2.2.3	Slumping phase	17
2.3	Thermoabrasion	20
2.3.1	Initial phase	20
2.3.2	Niche growth phase	20
2.3.3	Bluff collapse phase	21
2.3.4	Collapsed-bluff degradation phase	21
2.4	Drivers of Arctic coastal dynamics	22
2.4.1	Air and seawater temperature	23
2.4.2	Waves	23
2.4.3	Open water period	24
3	Modelling of Arctic coastal erosion	25
3.1	Computational domain	25
3.2	Description of a process-based model for Arctic coastal erosion	26
3.2.1	Module: Thermodenudation	27
3.2.1.1	Submodule: Permafrost thaw	27
3.2.1.2	Submodule: Slumping of thawed layer	31
3.2.2	Module: Thermoabrasion	32

3.2.2.1	Submodule: Niche growth	33
3.2.2.2	Submodule: Bluff collapse	34
3.2.2.3	Submodule: Degradation of collapsed bluff	36
3.3	Numerical implementation	37
3.3.1	Assumptions	37
3.3.2	Threshold value control	38
3.3.3	Simulation of offshore hydrodynamics	38
3.3.4	Simulation of nearshore hydrodynamics	39
3.3.4.1	XBeach model set up	40
3.3.4.2	Variable grid spacing	40
3.3.5	Simulation of permafrost within XBeach	40
3.3.6	Numerical implementation of slumping	42
3.3.6.1	Assumptions	42
3.3.7	Coupling submodules to establish a combined model of thermode- nudation and thermoabrasion	44
3.4	Probabilistic approach for data-poor environments	48
3.4.1	Assumptions	49
3.4.2	Description of the approach	49
3.5	Data driven model of permafrost temperature	51
3.5.1	Thermal regime of permafrost	52
3.5.2	Problem formulation	53
3.5.2.1	Assumptions	54
3.5.2.2	Boundary condition	54
3.5.2.3	Analytical solution	54
3.5.3	Numerical implementation	55
3.5.3.1	Training, testing and prediction data set	55
4	Field Measurements	58

4.1	Location of the study area	58
4.2	Geomorphological description	59
4.2.1	Description of the beach	60
4.2.2	Vegetation condition	62
4.2.3	Hydrodynamic conditions	63
4.2.3.1	Water flow	63
4.2.3.2	Tide	63
4.2.3.3	Waves	64
4.2.3.4	Water temperature	64
4.2.3.5	Ice conditions	64
4.3	In-situ measurements	65
4.3.1	Ground temperature measurements	65
4.3.2	Sediment size distribution	66
4.3.3	Historical air temperature records	66
4.3.4	In-situ test of the thermal properties	66
4.3.5	Coastal profiles	67
4.4	Observation of erosion in the study area	68
4.4.1	Thawing and slumping	68
4.4.2	Niche openings	68
4.4.3	Permafrost	69
4.4.3.1	Temperature profiles of the coastal bluffs	70
4.5	Environmental forcing	72
4.5.1	Solar radiation (short wave)	73
4.5.2	Historical wind storms	74
4.5.3	Thawing index	74
4.5.4	Wind speed	75
4.5.5	Historical Air temperature	76

5	Result and Discussion	78
5.1	Process-based model for Arctic coastal erosion	78
5.1.1	Methodology of calibration and validation	79
5.1.1.1	Standard Error of Estimates (SEE)	79
5.1.1.2	Coefficient of determination	79
5.1.1.3	Root Mean Square Error (RMSE)	79
5.1.1.4	Upper and lower limit determined by field observations	80
5.1.2	Calibration and validation of thawing submodule using in situ temperature measurements	80
5.1.2.1	Discussion	83
5.1.3	Calibration of the input parameters by iterations	83
5.1.3.1	Calibration of water level	83
5.1.3.2	Calibration of convective heat transfer coefficients	84
5.1.3.3	Calibration of the critical slope (m_{cr})	84
5.1.3.4	A summary of the calibrated parameters	85
5.1.4	Results of the simulation	86
5.1.4.1	Defining a case	86
5.1.4.2	Environmental forcing	87
5.1.4.3	Simulation of thawing depth	89
5.1.4.4	Prediction of the shape of coastal profile	89
5.1.4.5	Simulation of erosion	90
5.1.4.6	Simulation of crest retreat	91
5.1.5	Simulation of long term erosion	91
5.1.5.1	Defining a case	91
5.1.5.2	Result of long term simulation	92
5.1.6	Effect of environmental forcing on long term erosion	93
5.1.6.1	Air temperature	93

5.1.6.2	Thawing index	94
5.1.6.3	Wind speed	94
5.1.7	Sensitivity of the process-based model	95
5.1.7.1	Methodology of the sensitivity analysis	95
5.1.7.2	Defining a base case	96
5.1.7.3	Sensitivity of erosion to waves	96
5.1.7.4	Sensitivity of erosion to niche growth	98
5.1.7.5	Sensitivity of erosion to slumping	98
5.1.7.6	Sensitivity of erosion to other input parameters	99
5.1.8	Discussion on process-based model	99
5.2	Probabilistic approach using Monte Carlo simulation	101
5.2.1	Probability of the bluff failure during a storm	101
5.2.1.1	Probability of crest retreat	102
5.3	Data-driven temperature model of permafrost	104
5.3.1	Pre-processing of the raw data	105
5.3.1.1	Removal of outliers	105
5.3.1.2	Removal of trend	105
5.3.2	Training and testing dataset	105
5.3.3	Fast Fourier Transformation of training dataset	106
5.3.4	Regression to estimate the parameters and reverse FFT	106
5.3.5	Simulation Vs measurements	107
5.3.6	Discussion	108
6	Conclusions and recommendation for the future works	109
6.1	Conclusion	109
6.2	Future development	110
6.2.1	Process-based model of thermodenudation and thermoabrasion	110

6.2.2	Probabilistic approach for data-poor environment	111
6.2.3	Data driven temperature model of permafrost	111
A	Coastal profiles	123
A.1	Four zones of a coastal profile	123
A.2	Coastal profiles	124
B	Numerical implementations	129
B.1	Storm surge submodule	129
B.2	Sensitivity analysis of the process-based model	132
B.2.1	The Effect of Tide	132
B.2.2	The Effect of Water Level	132
B.2.3	The effect of water temperature	133
B.2.4	The effect of air temperature	133
B.2.5	The effect of convective heat transfer coefficient of water	134
B.2.6	The effect of XBeach parameter 'dry slope'	134
C	Journal papers	136
C.1	Journal Paper#1	136
C.2	Journal Paper#2	157
C.3	Journal Paper#3	170

List of Tables

3.1	The list of main parameters used to describe the models.	27
3.2	A simplified representation of the four routes.	47
3.3	Description of the input parameters for the numerical model	50
4.1	List of boreholes at the study area	66
4.2	The sediment size distribution of the study area.	66
4.3	Thermal properties of the sediments on the bluffs.	67
4.4	Distribution of wind speed during summer and winter.	76
5.1	Summary of the calibrated parameters.	86
5.2	A case to demonstrate the combined model of erosion.	86
5.3	Summary of calibration	91
5.4	A summary of the case#L for long term simulation.	92
5.5	The training and testing dataset of bh2.	105
5.6	Amplitude reduction of the top three harmonic functions.	107
5.7	Phase lag over the depth.	107

List of Figures

1.1	The time and scale of the numerical modelling.	6
1.2	The study area, an Arctic coasts in Kara Sea.	9
2.1	Definitions used in this thesis.	14
2.2	A typical Arctic coast during summer.	16
2.3	The initial phase of thermodenudation.	17
2.4	The thawing phase of thermodenudation.	17
2.5	Slumping phase of thermodenudation.	18
2.6	Various mass movement modes of the thawed layer.	19
2.7	The initial phase of thermoabrasion.	20
2.8	The niche growth phase.	21
2.9	Bluff collapse phase	22
2.10	Degradation of the collapsed bluff.	22
3.1	The domain of the Arctic coastal erosion	26
3.2	Thawing and freezing of permafrost and thermal energy flux.	28
3.3	The changes in thawing depth.	30
3.4	Slumping of permafrost	31
3.5	The sequences of thermoabrasion.	33
3.6	The geometry of niche opening.	34
3.7	Two modes of bluff collapse.	35
3.8	Overturning failure leads to a bluff collapse.	36

3.9	Domain of offshore zone.	38
3.10	Domain of nearshore zone.	39
3.11	The domain of XBeach.	40
3.12	Variable grid spacing in XBeach.	41
3.13	Simulation of permafrost using XBeach.	41
3.14	Numerical implementation of slumping submodule	42
3.15	Workflow of the slumping module.	44
3.16	Coupling of XBeach.	45
3.17	Numerical implementation workflow of the submodules.	46
3.18	A simplified representation of the four routes.	48
3.19	Algorithm of the model with three numerical modules and Monte Carlo simulation.	50
3.20	The thermal regime of permafrost.	52
3.21	Thermal energy transfer between two points	53
3.22	Dividing dataset into testing and training.	55
3.23	The workflow of the data-driven temperature model of permafrost.	57
4.1	The map of the study area.	59
4.2	The geomorphic condition of the study area	62
4.3	The vegetation cover in the study area.	63
4.4	A coastal profile showing the position of boreholes.	65
4.5	Two coastal profiles of the study area.	68
4.6	Some photographs of the field investigation.	69
4.7	The temperature profile of the coastal bluff S#1	71
4.8	The temperature profile of the coastal bluff S#2	72
4.9	SW radiation reaching the bluff surface of the study area.	73
4.10	Historical storms during summer and winter	74
4.11	Historical thawing index of the study area.	75

4.12	Historical air temperature of the study area.	76
5.1	Calculation of thawing depth from temperature measurements.	80
5.2	Field measurement of thawing depth.	81
5.3	The thawing and freezing rate.	81
5.4	Iteration seeking the optimum value of h_c	82
5.5	Result of calibration of thawing depth module.	82
5.6	The validation of thawing submodule.	83
5.7	Relation between the bluff height and bluff slope in the study area.	85
5.8	Coastal profile of case#1	87
5.9	The environmental forcing during the calibration cases is shown.	88
5.10	The thawing depth at the bluff for case#1.	89
5.11	Case#1: Prediction of the coastal profile shape after normalising the simulation around the middle of the bluff slope. The RMSE of the prediction is 0.56 m.(Islam and Lubbad 2022)	89
5.12	Simulation results of case#1	90
5.13	The crest retreat as a time series is shown.	91
5.14	Coastal profile changes of case#L.	92
5.15	Simulation results for case#L.	93
5.16	Air temperature and cumulative erosion (simulation).	93
5.17	Cumulative thawing index and erosion (simulation).	94
5.18	Wind speed and cumulative erosion (simulation). (Islam and Lubbad 2022)	95
5.19	Coastal profile of the base case.	95
5.20	The environmental forcing applied to the base case. [a] cumulative erosion over time, [b] air temperature and wave heights (H_s) and [c] wind speed and storm surge.	96
5.21	The effect of waves on erosion. sub-figure[a]: cumulative erosion as a time series. Cumulative erosion is almost zero when the wave module inside XBeach is turned off. sub-figure[b]: comparison of total erosion.	97

5.22	The effect of wave inputs on erosion.	97
5.23	Effect of the niche-growing process on erosion. Without niche growth, the bluff collapse can not occur but the sediment transport from the base of the bluff remains active. This leads to higher thermodenudation.	98
5.24	Effect of the slumping process on erosion.	99
5.25	case#P, coastal profile and crest retreat is shown.	101
5.26	The probability of the bluff collapse during a storm for the case#P.	102
5.27	Results of the probabilistic model	103
5.28	Temperature measurement of a coastal bluff.	104
5.29	FFT analysis on time series of temperature measurement.	106
5.30	Comparing observation and prediction values.	108
A.1	The four zones of the coastal profile based on the heat transfer mechanism.	123
A.2	Profile#1	124
A.3	Profile#2	125
A.4	Profile#3	125
A.5	Profile#4	125
A.6	Profile#5	126
A.7	Profile#6	126
A.8	Profile#7	126
A.9	Profile#8	127
A.10	Profile#9	127
A.11	Profile#10	127
A.12	Profile#11	128
B.1	water level difference due to pressure drop.	129
B.2	surge created by the wind stress on the surface.	130
B.3	The effect of tide on erosion.	132
B.4	The effect of water level inputs on erosion.	133

B.5 The effect of water temperature on erosion. 133

B.6 The effect of air temperature on erosion. 134

B.7 The effect of convective heat transfer coefficient of water on erosion. 134

B.8 The effect of convective heat transfer coefficient of water on erosion. 135

List of Abbreviations

ACD Arctic coastal database

BC boundary condition

BH bore hole

CC creative common license

CoV coefficient of variation

COSMOS coastal storm modelling system

DGPS differential global positioning system

ESM earth system model

FEM finite element method

FFT fast Fourier transformation

GIS geographic information system

IC initial condition

LiDAR light detection and ranging

MSU Lomonosov Moscow State University, Russia

MSL mean sea level

MSL mean sea level

NDTI normalised difference thermo-erosion index

NTNU Norwegian University of Science and Technology

PL phase lag

RR reduction rate

LIST OF FIGURES

RMSE root mean square error

SAMCoT Sustainable Arctic Marine and Coastal Technology

SWAN simulation of waves nearshore

std standard deviation

SEE standard error of estimates

TOC total organic carbon

Tg tera grams

TA thermoabrasion

THM thermo-hydro-mechanical

TD thermodenudation

List of Symbols

- h_a convective heat transfer coefficient of air
- h_w convective heat transfer coefficient of water
- L_t latent heat of permafrost(volumetric)
- T_a temperature of the air
- T_s temperature of the soil/permafrost/thawed layer
- T_w temperature of the sea water
- h_{id} water depth at the base of bluff
- x_t thawing depth
- h_m mean water depth
- h_t tide compared with MSL
- β niche opening parameter
- η storm surge level compared with MSL
- m_{cr} critical slope of slumping
- T_{HF} horizontal failure line of bluff collapse
- T_{VF} vertical failure line of bluff collapse
- U_w wind speed at 10m height
- wl water level
- dt_x timestep within XBeach
- dt global timestep of the combined model
- dt_m timestep between two field measurement

LIST OF FIGURES

- q heat flux at the bluff surface
- q_L heat flux requirement for phase change
- q' net heat flux within permafrost during summer
- q_r net heat flux within permafrost during winter
- T_m mean temperature of the soil
- T_{a_n} amplitude of n number of the harmonic functions
- f_n frequency of the n number of harmonic function
- ϕ phase of the harmonic function
- e_w internal energy of water
- e_v internal energy of vapour
- e_s internal energy of soil
- Q_T source/sink of heat equation
- J_w advective internal energy flux in water
- J_v advective internal energy flux in vapour
- J_s advective internal energy flux in soil
- n_p porosity of the soil
- ρ_w density of sea water
- ρ_v density of vapour
- ρ_s density of soil
- k thermal diffusivity
- λ correct it
- C_g volumetric heat capacity of soil
- W liquid water flux density
- C_w heat capacity of water

x_m niche depth

Nu Nusselt number

Q_r net solar radiation on bluff surface

S_{sw} short-wave solar radiation corrected for cloud cover

S_r reflected short-wave solar radiation

T_m salinity adjusted melting point of ice

c tensile strength of soil

x_n vertical thawing depth

i_{con} ice concentration

Th_i thawing index

x_p niche depth at which the stability is lost/ critical niche depth

x_{edge} position of the ice-wedge polygon from the base of the bluff

y_{base} y coordinate of the top of the niche growth melting point

y_{top} y coordinate of the top of the bluff

ρ_b density of the bluff

\mathbf{g} gravitational acceleration

τ_b the tensile strength of the frozen bluff

τ_i tensile strength of ice

CHAPTER 1

Introduction

1.1 Background

One-third of the world's coastline is located in the Arctic ([Lantuit et al. 2012](#)) and affected by the abundance of sea ice, frozen soil (permafrost), and ground ice ([Lim et al. 2020](#) ; [Nielsen et al. 2022](#)). A considerable portion of the coastline in the Arctic undergoes erosion (most observable as a retreat of the shoreline position) and the situation is worsening due to the effects of climate change ([Jones et al. 2020](#) ; [Lantuit et al. 2012](#)). The mean coastal retreat rate in the Arctic is approximately 0.5 m per year ([Lantuit et al. 2012](#)). The mean erosion measured in the last decade at the Arctic coast at the Kara Sea is between 1 to 1.7 m per year ([Isaev et al. 2019b](#)). The coast of the Beaufort Sea in Alaska demonstrates a mean erosion of 1.7 m per year ([Gibbs et al. 2018](#)). Even though the measured mean erosion rates are relatively low, the variability in measurements is significant and a trend of increasing erosion rates is noticeable ([Bull et al. 2020](#)). The highest erosion rate in recent years is measured in the Alaskan Beaufort Sea, where the coast retreated more than 22 m in one year ([Gibbs et al. 2018](#) ; [Jones et al. 2008](#)). A similar trend is observed for the coasts along the Kara Sea, Russia, where 19.6 m of the coastal retreat was recorded in 2010-2011 ([Ogorodov et al. 2020](#)). Based on measurements from 2007 to 2016, [Jones et al. \(2018\)](#) estimated an average retreat rate of 17.2 m per year along the Kara Sea, a rate that is 2.5 times higher than the historical mean. Erosion at the western part of the Alaskan Beaufort Sea measured by [Tweedie et al. \(2016\)](#) is 2 to 4 times greater than the earlier measurements of [Brown et al. \(2003\)](#). The erosion in the permafrost-rich coasts of the Laptev sea near Siberia increased by 1.5 to 3 times compared with the erosion rate in the 1950s ([Günther et al. 2013, 2015a](#)).

The environmental changes due to the warming of the climate are triggering significant coastal erosion in the Arctic (Rowland et al. 2010). The effect of climate change is particularly enhanced in the Arctic coastal zones as the erosion dynamics are moulded by the shrinking of sea ice and the extension of open-water days (Irrgang et al. 2022). Permafrost coasts are particularly affected by the increase of the ambient air temperature as the warmer air thaws the exposed permafrost during the summer (Irrgang et al. 2022). Increased thawing of permafrost augments the top-down slumping by gravitational force (Kupilik et al. 2020 ; Lim et al. 2020). Permafrost thaw will also weaken the mechanical properties of the soil, which may destabilise coastal bluffs leading to slope failures (Frederick et al. 2021). Here, it is worth mentioning that the anomalies in surface air temperature in the Arctic are increasing and the difference between the mean air temperature in the Arctic and the global mean is amplified by a factor of 2.4 during the period from 1971 and 2017 (Box et al. 2019). In addition to air temperature, seawater temperature is a prominent driver of erosion at the base of the ice-rich bluffs (Barnhart et al. 2014a ; Kobayashi et al. 1999). The sea water temperature anomalies reached 5°C in the Arctic Ocean (Steele et al. 2008).

Further, the frequency and intensity of storms during summer are also expected to increase (Holland-Bartels and Pierce 2011). Amplified thawing of the permafrost inside the coastal bluffs leads to a higher slumping rate and, consequently, loss of mass along the Arctic coast. On the other hand, the sea ice extent is shrinking, enabling longer fetches to generate larger waves (Wobus et al. 2011). A longer open sea season also increases erosion along the coast. As a result, Arctic coastal retreat has increased more than two times in the last few decades (Günther et al. 2015a ; Irrgang et al. 2022 ; Jones et al. 2008, 2018, 2020). Observations along the various Arctic coasts have led to the establishment of a link between increased coastal erosion and a smaller extent of sea cover (Barnhart et al. 2014b ; Stroeve and Notz 2018), warmer air temperature (Cohen et al. 2014 ; Serreze et al. 2009) and increased permafrost temperature (Nielsen et al. 2022).

As roads in the Arctic are not accessible throughout the year, indigenous settlements and related infrastructures are generally concentrated near rivers and coasts (Bull et al. 2020). Arctic coastal erosion has a negative influence on economic activities in such areas. The eroding coasts pose a risk to infrastructures, wipe out cultural sites and hamper the traditional practices of the indigenous people (Jones et al. 2008). The erosion in the permafrost-rich coasts also releases organic matter, fine sediments and excess nutrients into the ocean (Ping et al. 2011). The organic carbon released from the Arctic coasts is almost equal to organic carbon carried by all the Arctic rivers (Vonk et al. 2012 ; Wegner et al. 2015). Bluffs along the shores of Alaskan Beaufort contain 40 to 150 total organic carbon (TOC) in the top layer (up to 3m) (Fuchs et al. 2019 ; Hugelius et al. 2014 ; Schuur

et al. 2015). Coastal erosion may release a large amount of frozen organic matter on the beach and nearshore (Fritz et al. 2017 ; Stein and Macdonald 2004 ; Vonk et al. 2012). As an effect of coastal erosion, approximately 5-41 Tg (tera grams) of TOC is released each year from bluffs and rivers, which eventually reach the Arctic oceans (Wegner et al. 2015).

The impact of the Arctic coastal erosion on infrastructure, ocean ecology and global carbon budget is substantial. However, most of our current understanding of the coastal processes is limited to warmer-climate processes of the tropics and subtropics, which are fundamentally different from the cold-climate processes in the Arctic (Bull et al. 2020). The presence of sea ice and permafrost changes the processes related to erosion. In contrast to coastal erosion in warm climates, which is mainly mechanical, coastal erosion in cold climates is both thermally and mechanically driven. Therefore, predictive models developed for the lower latitude coasts have minimal application in the Arctic (Rolph et al. 2021).

Arctic coastal erosion is grouped under two primary mechanisms: thermodenudation (TD) and thermoabrasion (TA) (Are F 1988 ; Günther et al. 2013). In the thermodenudation mechanism, thermal energy melts the permafrost during the summer, leading to the slumping of the thawed bluffs by gravitational forces and possibly loss of bluff stability. The slumped materials are removed from the beach by waves, tides and storm surges. Thermodenudation is a continuous process during summer and contributes to the slow retreat of the coast. In contrast, thermoabrasion is rapid and episodic. Thermoabrasion is triggered during summer storms when surges cause inundation of the beach. This leads to forming of the wave-cut niche at the bluff's base. The growing niche becomes deep enough to trigger bluff collapse at one point. The collapsed bluff degrades on the beach and eventually washes away under hydrodynamic forcing.

Earth System Models (ESMs) are developed to simulate Arctic coastal erosion by coupling atmosphere-ocean-land-surface models (Frederick et al. 2016). ESMs described by Vincent et al. (2017) ; Chylek et al. (2011) ; Notz et al. (2013) ; Koven et al. (2013) and numerous others establish links between permafrost thaw dynamics and climate changes. However, the recent trend of increased permafrost thaw rates is not well presented in the current generation ESMs and has not been considered for the climate projections; thus, a mismatch exists between the outcome of modern ESMs and the observations of the Arctic coastal erosion (Nielsen et al. 2022). Rolph et al. (2021) proposed a simplified pan-Arctic coastal erosion model based on Kobayashi et al. (1999) to parameterise the Arctic shoreline retreat in ESMs using a computationally inexpensive physics-based model. The Arctic Coastal Database (ACD) by Lantuit et al. (2012) shows that coasts

consisting of low bluffs and high ice content erode most rapidly. [Nielsen et al. \(2022\)](#) developed a semi-empirical data-driven large-scale model to simulate erosion using the ACD database to connect the local variability with ESMs. [Nielsen et al. \(2022\)](#) considered both thermal and mechanical drivers of erosion. They used yearly accumulated temperature (thawing and freezing index) as the main thermal driver and yearly averaged accumulated significant wave height as a representation of the mechanical driver.

Besides the aforesaid large-scale models, several process-based models have also been developed during the past decades to simulate Arctic coastal erosion on local scales. Such models are useful to improve our understanding of the underlying mechanisms of Arctic coastal erosion, to help identify the root cause of erosion, and to quantify its main drivers. The local-scale process-based models are also helpful as engineering and decision-support tools for planning, designing, and assessing risk and vulnerability.

[Leont'yev \(2003\)](#) proposed a numerical model of Arctic coastal erosion, assuming the thermodenudation to be the only active erosion mechanism. This was achieved by coupling the morphodynamics model of [Nairn et al. \(1998\)](#) with his own thermal energy balance module. Later, he updated the model by incorporating the thermoabrasion mechanism ([Leont'yev 2003](#)). The collapse of the bluffs undergoing thermodenudation can be attributed to the melting of permafrost that reduces the soil shear strength ([Gruber and Haeberli 2007](#)). [Isaev et al. \(2019b\)](#) showed that the retreat rate is highly correlated with the wind-wave energy influx to the coasts during the open sea period. Thermo-hydro-mechanical (THM) models are developed to simulate bluff failures under the thermodenudation mechanism. THM models incorporate three coupled modules for thermal and mechanical drivers with hydraulic aspects. [Ghoreishian Amiri et al. \(2015\)](#) developed a THM model for saturated frozen soil, assuming the mechanical loading is carried by the solid grains. Based on the works of [Ghoreishian Amiri et al. \(2016\)](#), [Schneider \(2017\)](#) analysed the slope stability of Arctic bluffs by coupling water flow and shear strength stability, assuming failure only occurs in the thawing portion of the bluff. A simplified general slope stability model for the frozen and saturated Arctic coast is proposed by [Guégan \(2015\)](#). [Frederick et al. \(2021\)](#) developed a thermo-mechanical model based on the coupling of a thermal module of three-dimensional heat transfer and phase change with a mechanical module of mechanical strength of the soil.

Most of the available local-scale models for Arctic coastal erosion assume thermoabrasion to be the only active mechanism and thus focus on crest retreat due to bluff failure, where the growth of the niche leads to a bluff collapse. Such process-based models simulate wave-cut niche growth at the bluff base and destabilisation of the overhanging portion. The earlier work of [Kobayashi \(1985\)](#) is the basis for most of these models. [Kobayashi](#)

(1985) developed an analytical solution of the inward growth rate of the niche as a function of the temperature of the incoming seawater, the depth of the water at the base of the bluff and the duration of the inundation. Additionally, niche models developed for melting icebergs via waves and currents (Russell-Head 1980 ; White et al. 1980) have also been used with modifications (Bull et al. 2020). The root cause of the erosion or the bluff instability is controlled by the mechanical strength of frozen soil, which is governed by the thermal state of the permafrost (Frederick et al. 2021). Hoque and Pollard (2009) developed analytical solutions for bluff failure as a loss of balance (moment failure) and shear failure (mechanical strength).

A process-based model to connect niche growth and bluff collapse with hydrodynamic forcing was introduced by Ravens et al. (2012). They included oceanographic boundary conditions using 12-hour time steps. Ravens et al. (2012) coupled four physical processes as modules: storm surge, niche growth, the collapse of the overhanging bluff over the niche and degradation of the collapsed bluff. Barnhart et al. (2014a) expanded the model of Ravens et al. (2012) and incorporated the stability concept of Hoque and Pollard (2009). Barnhart et al. (2014a) also used smaller time steps (3 h) to capture erosion at higher temporal resolutions. To include the effect of morphological changes such as changes in the coastal profiles of the Arctic coasts, Ravens et al. (2017) used the open-source software package XBeach (Roelvink et al. 2010) to simulate wave propagation, sediment transport and slumping. The latter was achieved by modifying the avalanching module in XBeach, originally developed for sandy dunes. Bull et al. (2020) introduced finite element analysis to understand niche-induced bluff collapse in detail. Frederick et al. (2021) developed the finite element model to obtain a detailed analysis of the formation of the niche and subsequent bluff collapse without assuming any predetermined failure planes.

1.2 Motivation of the study

The large-scale models mentioned in the earlier sections (i.e., ESMs) are either based on oversimplified physics or include only a few physical processes; thus, the causal effect cannot be established reliably. On the other hand, existing local-scale process-based models of thermoabrasion usually simplify the interactions between the processes or make the feedback mechanism one-way (the processes are consequential, following a strict order of precedence). The existing thermodenudation models consider the hydraulics of the bluffs (pore pressure, water flow etc.) but are typically not coupled with the hydrodynamics boundaries (nearshore wave conditions, sediment transports etc.). The localised process-based models cannot accurately capture the response of the Arctic coasts to the variability of the environmental forcing predicted by the ESMs (Irrgang et al. 2022). Combined

effects from thermodenudation and thermoabrasion mechanisms are usually overlooked since most existing models simulate only the dominant mechanism in the site of interest. Further, the existing models either neglect or oversimplify nearshore morphodynamics (e.g., nearshore hydrodynamics including modelling of waves and water level, sediment transport, update of coastal profile) (Irrgang et al. 2022). Thus local-scale models are usually limited in their application to the particular stretch of coastline for which they are developed and tailored.

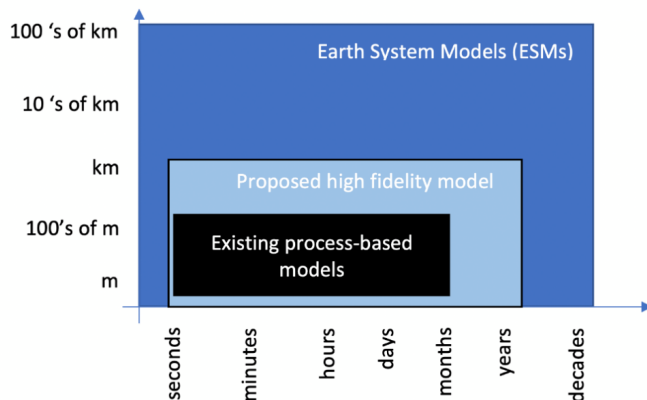


Figure 1.1: The time and spatial scale of the numerical models. The existing process-based models have a typical time domain of few months and spatial domain within 100's of m. The ESMs have a time domains of decades and spatial domain of 100's of kms. The model proposed in this study can be placed in between, a time domain from months to few years and a spatial domain of few kms.

The current understanding and modelling efforts to simulate Arctic coastal erosion have a knowledge gap, as shown in Figure 1.1. Most of the existing process-based models are local scale and short term with a domain of a hundred meters and a duration of one summer. On the other hand, the ESMs have poor spatial and temporal resolutions and cannot capture the variabilities of the Arctic coastal dynamics at local scales. This thesis presents a comprehensive and unified model to capture the local variability with high fidelity on a scale of a few km and the time duration of one storm to a few years.

While detailed models of some of the processes exist, for example, the formation of a wave-cut niche during a storm (Frederick et al. 2021 ; Kobayashi 1985), a long-term generic (not site-specific) model that accounts for the combined effects from thermodenudation and thermoabrasion has yet to be achieved (Irrgang et al. 2022 ; Ravens et al. 2018). The existing models are not generic to all Arctic coasts, specifically for beaches where erosion is a mix of thermodenudation and thermoabrasion. Field observations and numerical

modelling in various geomorphic conditions suggest that the nearshore hydrodynamics, morphological changes, sediment transport and offshore conditions such as the length of the open-water days during the summer and water level play a vital role in the erosion mechanism (Barnhart et al. 2014b ; Casas-Prat et al. 2018). The strong dependency of erosion mechanisms on the environmental forcing spanning from offshore to nearshore emphasises the need for a unified erosion model.

1.3 Research questions

Based on the above observations and discussion on the status of the numerical models of Arctic coastal erosion, the research questions of this thesis can be summarised as follows:

Q1: How can we fill the knowledge gap shown in Figure 1.1? What physical processes affect the two mechanisms, thermoabrasion and thermodenudation, in the Arctic coasts? This implies answering a series of questions such as: what processes should be considered? How to model each individual process? How to couple these processes to simulate a particular erosion mechanism? And what input parameters should we consider to calibrate and validate the numerical model?

Q2: Is it possible to adopt probabilistic approach to develop numerical model for data-poor Arctic environment?

Q3: In addition to the development of a process-based model which is based on the real world physics, can we develop any data-driven model(s) applying statistical correlation (regression, machine learning) based on the valuable field data acquired during the project?

To resolve the research questions, the following objectives were envisioned:

1. Developing a comprehensive generic model of Arctic coastal erosion, including the nearshore hydrodynamics, sediment transport, and morphological changes. The two major erosion mechanisms of the Arctic, thermodenudation and thermoabrasion, should be coupled within the model.

2. Developing a probabilistic numerical model of Arctic coastal erosion for data-poor conditions.
3. Examine the available field data and suggest one or more data-driven models.

1.4 Research plan

The research work performed under this thesis had three distinct phases. The outcome of each step paved the way for the next one.

1.4.1. Phase 1: Defining the research problem and scope of the work

The research question briefly presented in the earlier section were identified during the inception of the study and formulated after reviewing data reports from previous fieldwork in the Arctic.

1.4.2. Phase 2: Conducting a literature review

The literature review helped author to dismantle the various observations reported in the previous field reports and refine the research questions. Author greatly benefited from the previously established models for the Arctic coasts of the Alaskan Beaufort Sea. A thorough literature review and observations from field campaigns have resulted in the identification of the four challenges of the Arctic coastal erosion modelling: (a) inclusion of hydrodynamic forcing and sediment transport, (b) modelling temperature of permafrost, thawing and slumping, (c) coupling of the physical processes with a proper feedback mechanism to reach a unified model and (d) validation of the numerical model.

1.4.3. Phase 3: Execution of the various research tasks

1.4.3.1. Field observation

Field investigations have been conducted at Baydaratskya Bay, Kara Sea, Russia, since 2012 as part of the project Sustainable Arctic Marine and Coastal Technology (SAMCoT). The Lomonosov Moscow State University (MSU), Russia, conducts yearly field surveys in the summer. The two erosion mechanisms, thermoabrasion and thermodenudation, are active in the study area. The coast is straight and consists of ice-rich permafrost in the bluffs (Figure 1.2). The reports, in situ tests, measurements and observations are the backbones of this thesis. The author participated in the field investigation in the year

2019. The measurements obtained from the study area are used to calibrate and validate the numerical models.



Figure 1.2: The study area is an Arctic coast at the Baydaratskya, Kara Sea, Russia. A bluff consisting of permafrost stands at the end of the narrow beach. The bluff is made of fine sediments.

1.4.3.2. Data curation

The initial step of developing the model was the data curation of the available measurements. The anomalies were identified, and outliers were removed. The interpolation of the missing measurements was completed after consulting with the various stakeholders. Some unforeseen issues like errors with sensors, damage to the equipment by local people, etc., halted the continuous measurement of temperature in the study area.

1.4.3.3. Model development

A modular approach is adopted for the development of the numerical model. The spatial domain is divided into three zones offshore, nearshore and bluffs. SWAN (SWAN 2021) and a simplified 1D storm surge module are used to simulate wave generation and storm surge in the offshore zone. Wave transformation, sea level changes, sediment transport and morphological changes in the nearshore zone are simulated using XBeach (Roelvink et al. 2010). The coupling of XBeach with SWAN and the 1D storm surge model is established at the boundary dividing the offshore and nearshore zones. XBeach has the feature of a non-erodible surface which is used to simulate the non-erodible nature of permafrost (details of the numerical modelling are described in Chapter 4). Separate numerical modules are developed for thawing, slumping, wave-cut niche, bluff collapse and degradation.

These modules are coupled with XBeach. The calibration of the model is achieved using field measurements from 2015 to 2016 of two cases with different morphological conditions. The model is then validated using three other sets of measurements from the same site. Unifying thermodenudation and thermoabrasion mechanisms into one generic Arctic coastal erosion model is achieved. The model can simulate short-term (one storm or one summer) to long-term (several years) with the same level of fidelity.

The temporal and spatial resolution of the measurements taken at the Arctic coasts are generally high and discontinuous. A probabilistic model based on Monte Carlo simulation is developed by assuming a probabilistic distribution of the input parameters. Thermoabrasion, the dominating mechanism of erosion is simulated and the probability of the bluff collapsing during a storm is estimated.

The models discussed earlier are process-based which simulate several physical processes and solve system of equations numerically. The project extensively measured permafrost temperature at the coastal bluffs of the study area. Several boreholes were constructed in the study area inside which a thermistor was placed to measure temperature at different depths. A data-driven model is developed based on simplified analytical solution of heat transfer. The parameters of the model is estimated using the temperature measurement of the coastal bluffs in the study area. The data-driven model is developed using Fourier analysis of the temperature measurements coupled with a machine learning algorithm (supervised learning and regression).

1.4.3.4. Dissemination of results

Three open-access journal papers contain the results of the numerical models. The codes of the numerical models are uploaded to Github ([click here](#)) with a creative common (CC) license.

1.5 Limitation of the study

A few salient limitations of the numerical models are presented in this section. One of the challenges of numerical modelling is the simulation of the effect of sea ice on the waves and, eventually, on coastal erosion. The wave attenuation due to sea ice is controlled within the model as a binary condition, sea ice concentration of less than 20% is assumed to have no effect on the waves.

The two mechanisms, thermodenudation and thermoabrasion are not directly coupled. Field measurements for a single mechanism are not available; hence they are not validated individually. Instead, the physical processes are represented as numerical submodules and

coupled in a certain order of precedence.

Under the thermodenudation mechanism, only failure of the thawed layer under gravitational force is considered. The geotechnical aspect of the bluff collapse and failure of thawed layers are simplified and treated with a few predetermined failure modes.

The probabilistic distribution of the input parameters could not be estimated due to lack of measurements. The probabilistic model assumes a normal distribution for most input parameters and log-normal distribution for strength-related parameters.

The data-driven temperature model of permafrost is based on regression analysis of the analytical solution of thermal heat transfer. The model does not include the heat sink and source due to the phase change of the water-ice.

1.6 The organisation of the thesis

1.6.1. Readership

The thesis is written as a 'mini-monograph'; the research methodologies, understanding of the current status of the models, conceptual designs, and numerical implementation of the erosion mechanism are presented in Chapters 1 to 3. The chapters are written as a whole and can stand alone. The reader can systematically understand the numerical modelling of Arctic coastal erosion by following the order of the chapters. The journal papers are compiled as appendices and considered supplementary detailed information to earnest readers. The implementation of the numerical models, the discretisation of the equation, and the workflow of the modules are included in Chapter 3. The codes of the numerical model are made open source and available online at <https://github.com/akhsanul/codes>.

1.6.2. List of chapters

The structure of the thesis is as follows:

Chapter 1: Introduction

Chapter 2: Formulation of the problem

Chapter 3: Description of the numerical model

Chapter 4: Study area and summary of field observations

Chapter 5: Calibration, validation and sensitivity analysis of the numerical models

Chapter 6: Conclusions and recommendations for future work.

Appendix [A](#): The definitions used in this thesis, coastal profiles and some numerical implementations.

Appendix [B](#): Journal papers published as part of the PhD work.

CHAPTER 2

Mechanisms of Arctic coastal erosion

2.1 Background

2.1.1. Lithified and unlithified Arctic coasts

Approximately 65% of the Arctic coasts are unlithified (Martini and Wanless 2014) nearly 66,386 km long (Brown and Solomon 1999). Lithified coasts consist of rocky bluffs with small bluff heights along the fjords and rocky coastlines (Martini and Wanless 2014). Unlithified coasts are mostly ice-bonded permafrost-rich in the Beaufort, Kara and Laptev Seas (Baranskaya et al. 2021 ; Irrgang et al. 2018 ; Novikova et al. 2018). Most of the unlithified coasts in the Arctic demonstrate ice volume that exceeds the total sediment pore volume (Lantuit et al. 2011). This thesis focuses on the numerical modelling of the unlithified Arctic coasts.

2.1.2. Definitions

The following definitions are used to describe various features of the Arctic coasts (shown in Figure 2.1). The origin of the coordinates is placed inside the bluff. The x-axis is along the shore-normal direction, the y-axis is along the shoreline and the z-axis is along the vertical.

Coastal profile

The cross-shore section of the coast along the x-axis (along shore-normal direction).

Cliff point

The end of the bluff surface where the slope of the coastal profile faces a sudden change.

Base point

The point at the end of the bluff face where we assume the beach begins.

Bluff surface

The bluff surface is the top of the bluffs beyond the cliff point in the onshore direction. The slope of the bluff surface is mild. Vegetation grows on the bluff surface where an active organic layer is present.

Bluff face

The portion of the coastal profile from the cliff point until the base point. This portion of the coastal profile is most active in terms of erosion. Thermodenudation occurs at the bluff face.

Bluff slope

The slope of the coastal profile from base point to cliff point.

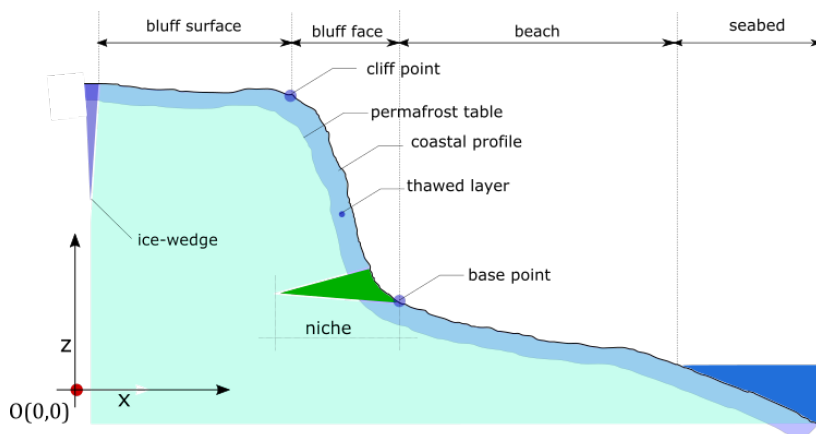


Figure 2.1: Definitions used in this thesis.

Permafrost table

The permafrost table in this thesis is used to refer to the bottom surface of the thawed layer. Below the table line or surface, the soil is assumed to be frozen with high mechanical strength. The thawed layer is a function of time and hence the position of the table is assumed to change during summer. In the winter, the permafrost table increases to the surface as thawed layer ceases to exist.

Thawing depth

The thickness of the upper layer of the bluff that is not frozen in summer is termed

thawing depth. The depth increases during summer and is considered zero during the winter.

2.1.3. Permafrost

The presence of permafrost inside the bluffs and seabed renders the Arctic coast unique. Permafrost is perennially frozen soil that remains frozen for two consecutive years or, in other words, frozen soil that does not melt in the summer. Generally, continuous permafrost is found at the bluffs of the Arctic coasts. The density and composition of the sediments influence erosion; dense clay demonstrates lower erodibility than loose sands (Irrgang et al. 2022). Bluffs subject to colder conditions demonstrate increased mechanical strength and decreased erodibility. When bluffs are subject to warmer air and water, thawing of the permafrost begins and the erodibility of the thawed portion increases considerably (Baranskaya et al. 2021). The sediment from the thawed ice-rich bluffs is removed rapidly by wave action and tides (Schirrmeister et al. 2011).

Lantuit and Pollard (2008) demonstrated a link between the ice content of the coastal bluffs and mean annual retreat rates of the crest, the correlation being stronger for the coasts with higher ice content. Ice wedge inside the bluffs is another feature of the Arctic coasts. The ice wedge forms by a crack opening due to the contraction during winter and water infiltration during the summer. Ice wedge formation may take several seasons and most likely be visible on the surface.

2.1.4. A typical Arctic coast

A typical unlithified Arctic coast consists of frozen bluffs at the end of the beach, as shown in Figure 2.2. The bluff height varies depending on the geomorphic conditions. The elevation of the beach is such that wave run-ups rarely touch the base of the bluff. The beach is narrow and composed of the sediments exerted from the bluffs. Typically, the bluffs consist of fine sediments.

Vegetation covers the bluff surface during the summer. The top organic active layer is thin and lacks nutrients for the vegetation. The root systems of the vegetation are shallow but still demonstrate a considerable resistance to erosion by surface runoff. Ice wedge polygons are quite common on the bluff surface; most of the time, the polygons are visible on the surface. During the winter, the bluff surface and bluff face are covered by snow and the beach goes under the sea ice. No erosion occurs during the winter. During summer, the hydrodynamic forcing on the beach, i.e., sediment transport, currents, wave action, etc., acts similarly to non-Arctic coasts (Are et al. 2008).

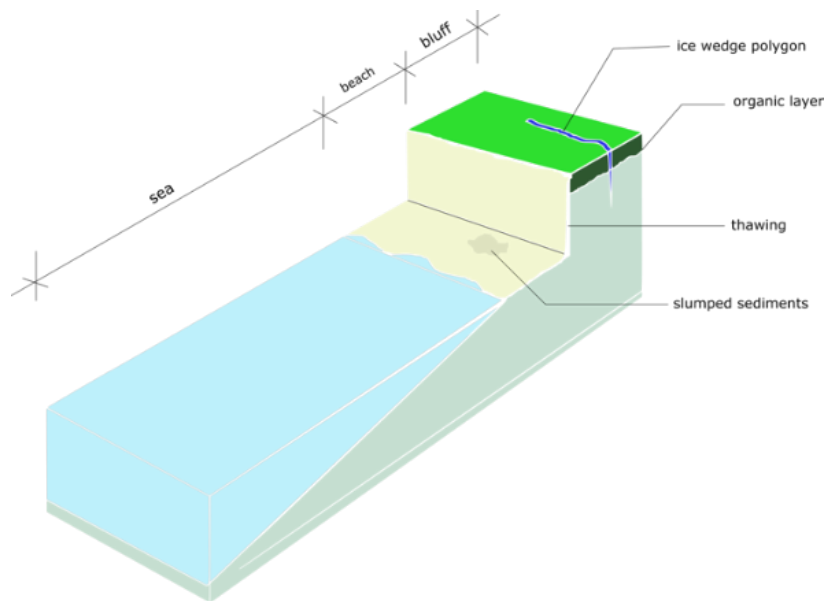


Figure 2.2: A typical Arctic coast during summer. The beach is narrow and a bluff stands at the end of the beach. The ice wedge splits the bluff.

2.2 Thermodenudation

When subject to warm air and solar radiation, the frozen bluffs gradually thaw (Guégan 2015). Thermodenudation occurs during calm conditions. It is the only erosion process during the early open sea season (Overeem et al. 2011). Thermodenudation is a thermally dominated process where the warm sea water has little to no direct contact with the bluffs (Are et al. 2008 ; Lantuit et al. 2012). The thawed sediments have significantly less strength than the permafrost. The thawed bluffs eventually fail under gravitational force. The unconsolidated sediments accumulate at the bluff's base. The sediments are typically washed away by waves and currents (Lantuit et al. 2011). The thermodenudation can be said to have three phases: initial, thawing and slumping.

2.2.1. Initial phase

The initial phase of thermodenudation is shown in Figure 2.3. Snow covers the bluff surface, bluff face and most of the beach. The snow acts as a thermal blanket and limits the exposure of the bluffs to solar radiation and ambient air. Land-fast sea ice prevents waves from reaching the beach. Warmer air and water cannot initiate the thawing of the permafrost at this phase.

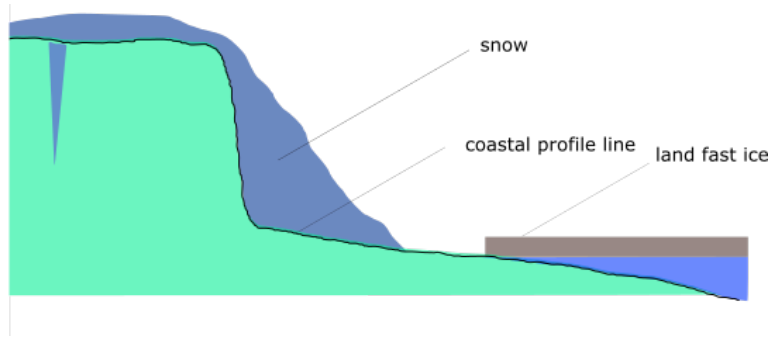


Figure 2.3: The initial phase of thermodenudation.

2.2.2. Thawing phase

The thawing phase initiates when snow begins to melt by the warm air (Figure 2.4). The bluff is now directly in contact with air and solar radiation. Thawing is weaker at the bluff surface as the vegetation cover acts against the thawing process. Typically, no vegetation grows on the bluff face. Warmer sea water thaws the submarine permafrost. Waves can now carry the energy to the beach. The depth of thawed layer starts to increase; however, the sediments are still considered consolidated (Pearson et al. 2016).

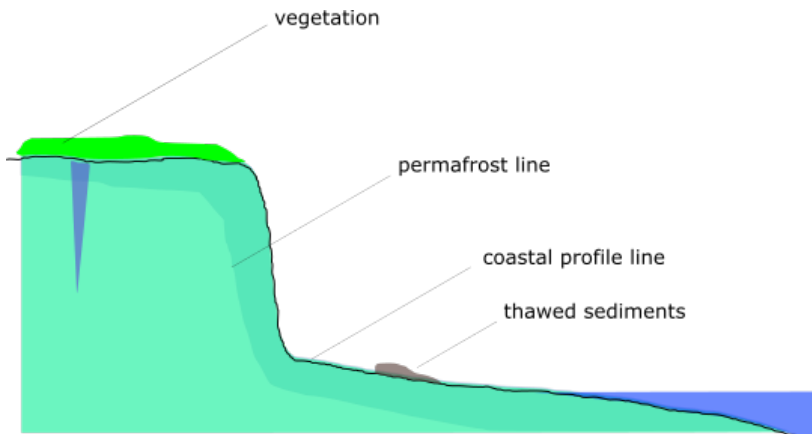


Figure 2.4: The thawing phase of thermodenudation.

2.2.3. Slumping phase

The strength of the soil at the thawed layer decreases with the increasing thawing depth by warm air (Figure 2.5). The thawed layer exhibits a lower mechanical strength. The thawed layer may become unstable, and various types of failure may occur depending on

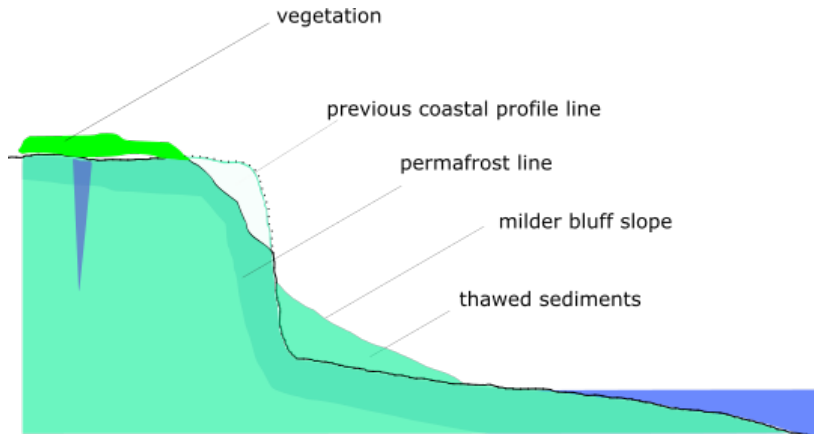


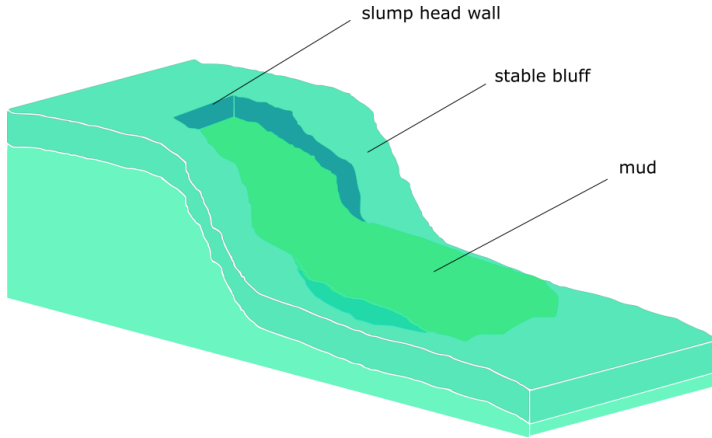
Figure 2.5: Slumping phase of thermodenudation.

the conditions. Soil mass movement on the bluff surface, such as retrogressive thaw slumps ¹ (Figure 2.6a), solifluction ² (Figure 2.6b) and active layer detachment ³ (Figures 2.6c) are observed (McRoberts and Morgenstern 1974). After the failure, the thawed portion falls at the bluff base. The sediments excreted from the thawed bluffs are unconsolidated and initially rest on the beach. Eventually, the sediments are removed from the beach by waves, tides and currents. However, the sediments may change the elevation of the beach and delay the direct wave attack on the bluff (Nairn et al. 1999).

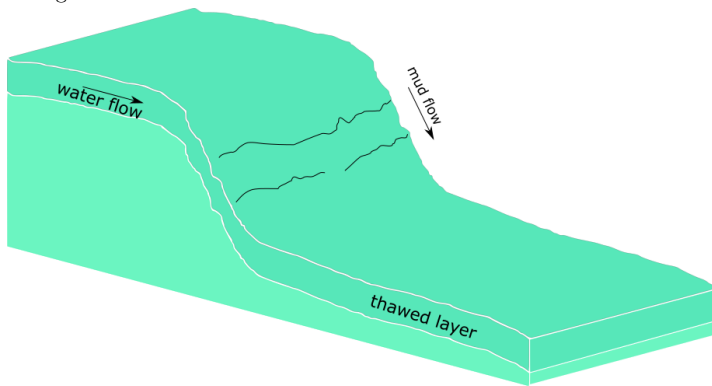
¹Retrogressive thaw slump is a circular shear failure along the bluffs due to the melting of permafrost that cannot hold a massive ice block.

²Solifluction is a slow movement of the fine-grained saturated thawed layer by gravitational force and water flow from the ice melting.

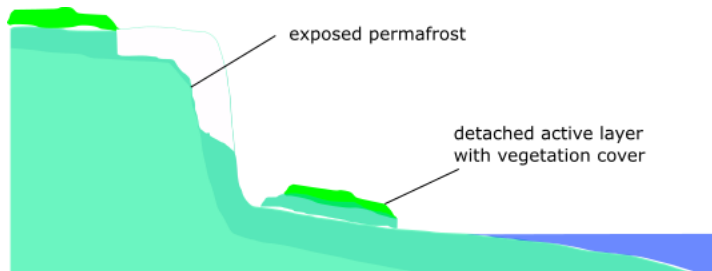
³Active layer detachment occurred at the low bluff slope where the effective shear stress between the active layer and permafrost are greatly reduced as a result of thawing.



a retrogressive thaw: circular shear, part of the bluff lost mechanical strength and fails.



b solifluction: a slow movement of the thawed layer by gravitation, similar to mud flow.



c active layer detachment: shear force between the thawed layer and permafrost is lost and part of the bluff is collapsed.

Figure 2.6: Various mass movement modes of the thawed layer.

2.3 Thermoabrasion

Thermoabrasion dominates during extreme events (storms) on the Arctic coasts. Along the ice-rich bluffs of the Arctic coasts, thermoabrasion is the dominant erosion mechanism. The prominent thermal driver is the warm sea water and the mechanical driver is the surge created by the storm (Are 1988 ; Barnhart et al. 2014a ; Günther et al. 2013 ; Manson and Solomon 2007 ; Ravens et al. 2012). The temperature of the water, the mechanical strength of bluffs and the intensity and frequency of the storm surge influence the effectiveness of thermoabrasion. Are (1988) estimates thermoabrasion is three to four times stronger than thermodenudation for most Arctic coasts. Similar to thermodenudation, thermoabrasion can be said to have four distinct phases.

2.3.1. Initial phase

Thawed sediments lying at the base of the bluffs and on the beach must be cleared before thermoabrasion occurs (Nairn et al. 1999). The storm surges during the early summer usually carry away this accumulated thawed sediments (Are et al. 2008). An Arctic beach at such phase is shown in Figure 2.7. The storm surge increases the water level to such an extent that warm seawater comes in contact with the bluff's base (Kobayashi and Aktan 1986).

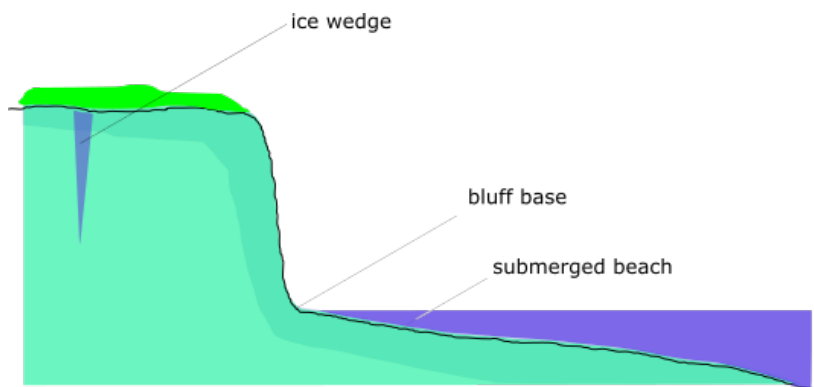


Figure 2.7: The initial phase of thermoabrasion.

2.3.2. Niche growth phase

During the storm, when seawater inundates the beach and reaches the base of the bluffs, convective heat transfer via warm seawater thaws the permafrost (Kobayashi 1985). The rapid thawing of the bluff's base results in the formation of a niche; see Figure 2.8

(Overeem et al. 2011). The temperature difference between the seawater and bluff is the thermal driver (Wobus et al. 2011) and influences the growth rate of the niche (Kobayashi 1985).

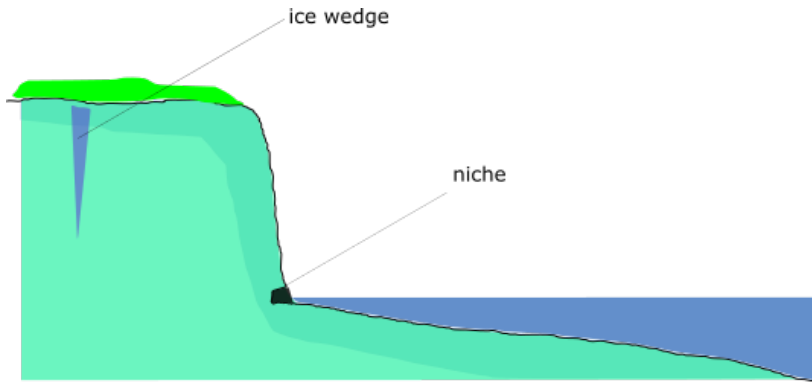


Figure 2.8: The niche growth phase.

Niche may grow with several storms. The fine sediments from the niche are moved offshore by the waves and return-current created during storms (Kobayashi 1985). The geometry of the niche depends on the storm surge level and the mechanical strength of the bluffs (Kobayashi and Aktan 1986).

2.3.3. Bluff collapse phase

Niche may continue to grow to such an extent that the overhanging bluff creates instability (Figure 2.9). Two types of failure, moment failure and shear failure, are identified (Hoque and Pollard 2009). In the moment failure mode, the overhanging portion at the melting face of the niche may lead to a failure when part of the bluff loses balance and topples over on the beach (Barnhart et al. 2014a ; Hoque and Pollard 2016 ; Ravens et al. 2012). In shear failure mode, the lower mechanical strength of the bluff cannot hold the weight of the overhanging portion of the bluff, leading to collapse.

2.3.4. Collapsed-bluff degradation phase

The collapsed bluff remains on the beach (see Figure 2.10). The fallen bluffs are then subject to thawing by warm sea water and may take a few days (Barnhart et al. 2014a ; Jones et al. 2018 ; Overeem et al. 2011 ; Ravens et al. 2012) to a few weeks (Lantuit et al. 2012), depending on the various conditions. The sediments exerted from the fallen bluffs rarely contribute to the beach (Barnhart et al. 2014a).

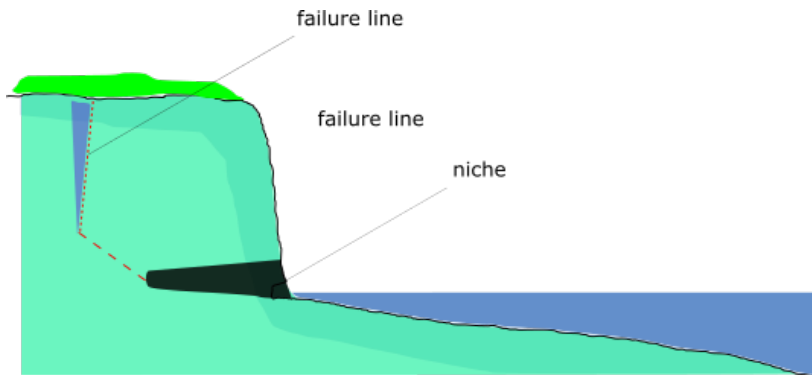


Figure 2.9: Bluff collapse phase (moment failure is shown, the failure line is along the ice wedge).

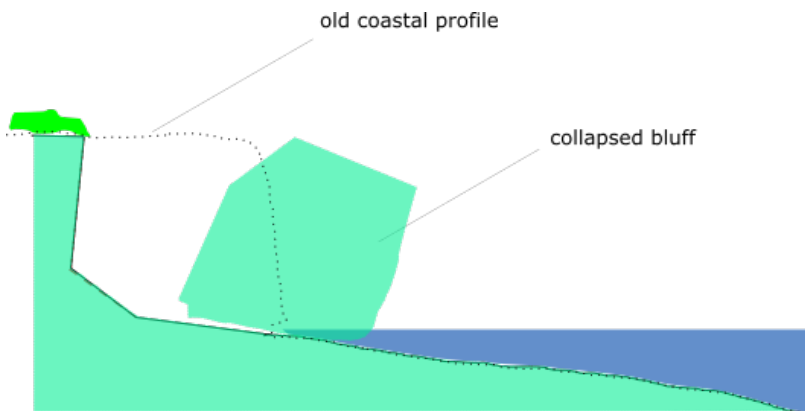


Figure 2.10: Degradation of the collapsed bluff.

2.4 Drivers of Arctic coastal dynamics

The coastal dynamics of the Arctic depend on several factors, including the wave action, exposure of the coasts to wave energy, availability of solar radiation, nearshore coastal morphology, geomorphology of the beach and bluffs, ice content of soil and the thermal regime (Irrgang et al. 2022). Among the environmental drivers of Arctic coastal erosion, air and water temperature, sea ice concentration nearshore and offshore, intensity and frequency of the summer storms and sea level changes are prominent. The variability of the local and regional environmental drivers shapes the Arctic coasts (Farquharson et al. 2018 ; Manson et al. 2005). A complex interaction between the processes occurs at the local and large scale with phase lags, threshold control and feedback mechanism; thus, very difficult to distinguish or correlate the influences of environmental drivers. In the

upcoming chapters, the interactions between the processes and feedback mechanisms are investigated, focusing on the regional and local scales.

2.4.1. Air and seawater temperature

Air and seawater temperatures are significant thermal drivers for thermodenudation. The warm air brings thermal energy to the bluffs and greatly influences the thawing depth. Warm air, water and solar radiation deliver the required energy of latent heat of melting ice, causing the previously bonded fine sediments of the bluff to lose mechanical strength and move down the bluff face under a gravitational force (Are 1988). Observations at the Laptev and Kara seas show that warm air triggers thermodenudation of the bluff surface and bluff face of the ice-rich coast where the wave action is either absent or weak (Günther et al. 2013 ; Sinitzyn et al. 2020).

Thawed sediments as the result of thermodenudation accumulate at the bluff's base. Removal of the accumulated sediment is the prior condition of the thermoabrasion Nairn et al. (1999), which is generally achieved by the storm and some cases, by high tides (Are 1988). Without any hydrodynamic actions of the waves, the unfrozen sediments accumulated at the base will act as a protective layer and limits the growth of the niche (Kobayashi 1985 ; Kobayashi and Aktan 1986 ; Kobayashi et al. 1999).

2.4.2. Waves

In the lower latitudes, waves depend on the wind speed, direction, fetch length and bathymetry (Young 1999). In contrast to lower latitudes, fetch lengths in the Arctic zones greatly depends on the sea-ice extent (Ogorodov et al. 2016 ; Shabanova et al. 2018). The sea-ice extent is generally minimum in September and maximum in March (Barnhart et al. 2014b). The wave characteristics are also influenced by the presence of sea ice (Shabanova et al. 2018). The perennial sea-ice limits the fetch length to a great extent which halts the wave generation (Frederick et al. 2016). Thomson and Rogers (2014) showed that the reduction of sea-ice extension enables the waves in the Arctic seas to transform to swell. This finding has multiple implications, such as a longer attenuation scale, longer time period for waves travelling within ice packs and greater wave energy reaching the shore (Frederick et al. 2016 ; Stopa et al. 2016).

In most locations around the Arctic, including the Laptev, Kara, Chukchi and Beaufort seas, the strongest storms occur during September and October (Manson et al. 2005). Coincidentally the thawing depth of the permafrost is typically the highest during these months (Brown et al. 2000 ; Nicolsky et al. 2017) which amplifies the erosion. The study

by [Hequette and Barnes \(1990\)](#) found a positive correlation between the wave height in the nearshore and retreat of the Canadian Beaufort Sea coasts.

2.4.3. Open water period

The sea-ice extent is reducing; consequently, the open-water season is getting longer, leading to a larger fetch for wave generation and longer exposure of the coasts to wave actions ([Irrgang et al. 2022](#)). [Barnhart et al. \(2014b\)](#) estimate the trend of ice melting is 1.5 days per year earlier than the previous year and delays in forming sea ice in the fall by two days per year. The vulnerability of the Arctic coasts to erosion increases as the frequency and intensity of the summer storms are projected to increase in the coming decade ([Casas-Prat and Wang 2020](#) ; [Günther et al. 2015b](#)). [Günther et al. \(2015b\)](#) showed two most important factors that strongly influence erosion at the coasts of the Laptev Sea were the open water days and thawing degrees. [Overeem et al. \(2011\)](#) suggest that the open water condition can be used as the first-order predictor for erosion at the Alaskan Beaufort Sea.

The next chapters present a process-based model combining thermodenudation and thermoabrasion and the application of the model to one study area.

CHAPTER 3

Modelling of Arctic coastal erosion

This chapter thoroughly describes a process-based model developed herein for Arctic coastal erosion driven by thermodenudation and thermoabrasion combined, including nearshore morphodynamics. First, conceptual models for the thermodenudation and thermoabrasion processes are explained. This is followed by establishing the theoretical understanding and deriving the governing equations for the various erosion processes. Further, the numerical implementation, workflow, and algorithms of the unified model are presented. A discussion on the use of such process-based models in data-poor environments like the Arctic is discussed. Finally, a data-driven model to estimate permafrost temperatures is presented towards the end of this chapter.

3.1 Computational domain

The model domain considered herein is shown in Figure 3.1. Four boundaries, BC1 to BC4, divide the domain into three zones, namely (1) offshore, (2) nearshore and (3) beach and bluffs.

The purpose of dividing the domain into several zones is to reduce computational demands. Division of the zones are based on two criteria: (a) requirement of updating bed profile at each timestep and (b) simulating the movement permafrost table. Simulation of morphological changes of the seabed is essential only in the nearshore zone because the waves are affected by the water depth. At the end of each timestep, bed profiles must be updated to reflect the changes in the seabed as a result of sediment transport. The boundary BC2 is placed where the water depth begins to affect the waves. The criteria $h_m/\lambda < 0.5$ (where h_m is water depth and λ is the wavelength) is used. The seabed profile

must be updated at every timestep beyond BC2 boundary towards the onshore direction (nearshore, beach and bluffs). Offshore of BC2, the waves do not *feel* the seabed and thus, the simulation of morphological changes is not a strict requirement. On the other hand, the movement of the permafrost table inside the bluff is one of the most important physical processes. The processes related to permafrost within the beach and bluff zone are simulated separately and coupled with the morphological module of the nearshore.

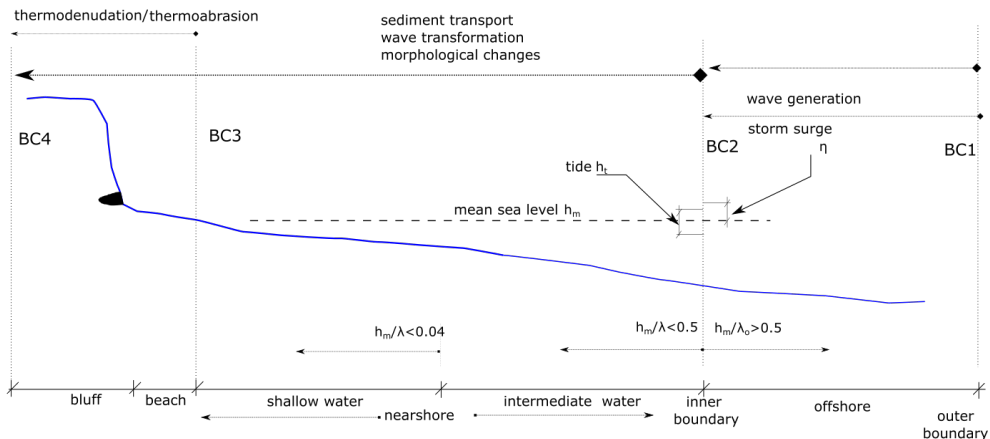


Figure 3.1: The spatial domain of the Arctic coastal erosion is from the polar ice until the bluff surface. The domain is divided into three zones, namely offshore, nearshore and bluff and beach by four boundaries, BC1 to BC4.

BC1 and BC2 bound the offshore zone. BC1 is a moving boundary that is at the end of the polar ice cap. The offshore zone has two processes: wave generation and storm surge. The nearshore zone is from BC2 until BC3. BC3 boundary is placed at the shoreline. Wave transformation, currents, tides, wave setup-setdown, sediment transport and hydrodynamic forcing are the processes considered in the nearshore zone. Thermodenudation and thermoabrasion occur at the beach and bluff zone, which is contained within BC3 to BC4.

3.2 Description of a process-based model for Arctic coastal erosion

A comprehensive model couples the thermodenudation and thermoabrasion processes with nearshore hydrodynamics and sediment transport is developed under this study. The waves and related hydrodynamic forcing in the nearshore zone, together with sediment transport and morphodynamics are simulated using XBeach (Roelvink et al. 2010). The

processes of thawing, slumping, niche growth, bluff collapse and collapsed-bluff degradation are modelled using in-house submodules and coupled with the coastal erosion model in XBeach. Two-way coupling is established between (1) hydrodynamic forcing and sediment transport in XBeach on the one hand and (2) mechanical and thermal erosion processes in the in-house model on the other hand. A modular approach is adopted for the numerical implementation where the submodules communicate at three-hour intervals. Table 3.1 lists the parameters used to define and describe the processes of thermodenudation and thermoabrasion in the model.

Table 3.1: The list of main parameters used to describe the models.

parameter	definition	typical value	units	references
thermal properties				
h_a	convective heat transfer coefficient of air	100	$W/m^2 - k$	Kobayashi et al. (1999)
h_w	convective heat transfer coefficient of water	700	$W/m^2 - k$	Kobayashi et al. (1999)
L_t	latent heat of permafrost	1.6×10^7	kg/m^3	Kobayashi et al. (1999)
T_a	Temperature of air	varied	$^{\circ}C$	NOAA
T_w	Temperature of water	varied	$^{\circ}C$	NOAA, sea surface temp
T_s	Temperature of soil	varied	$^{\circ}C$	field measurements
geometry				
x_t	thawing depth	varied	m	
h_{id}	water depth at the base	varied	m	
h_m	mean water depth	varied	m	
h_t	tide compared with MSL	varied	m	
β	niche opening parameter	2	-	Kobayashi (1985)
η	storm surge level compared with MSL	-	m	Eq. B.7
m_{cr}	critical slope of slumping	0.1-1	-	field observations
T_{HF}	distance from niche to the ice-wedge polygon	5-14 metre	m	field observations
U_w	wind speed	-	m/s	NOAA reanalysis
time steps				
dt_e	timestep within XBeach	varied	s	XBeach Manual
dt	timestep within modules/ global timestep	10800	s	based on 3 hour sea state
dt_m	timestep between two field measurements	365	days	Field report

3.2.1. Module: Thermodenudation

The thermodenudation mechanism, discussed in section 2.2 (page 16) can be divided into two processes: permafrost thawing and mass loss (slumping). Two submodules are developed to simulate the physical processes; submodule permafrost thaw to simulate the heat transfer to thaw the permafrost during summer and freezing of the thawed layer during the winter. Submodule slumping is to simulate the mass loss of the thawed layer and move the slumped material to the bluff's base.

3.2.1.1. Submodule: Permafrost thaw

Assumptions

The following assumptions are made to model the permafrost thaw:

1. Heat flux at the bluff surface delivers the thermal energy requirement of permafrost thawing during summer. The reverse heat flux at the bluff surface due to colder air during winter freezes the thawed layer.
2. The heat fluxes at the bluff surface during summer and winter are significantly higher than the heat flux within permafrost (for example, heat flux of 250 w/m^2 at bluff surface during summer compared to around 1 w/m^2 within permafrost (Lachenbruch and Marshall 1969)).

Heat flux

A schematisation of the permafrost and heat flow is shown in Figure 3.2. The permafrost typically lies beneath the active layer, which thaws and refreezes yearly.

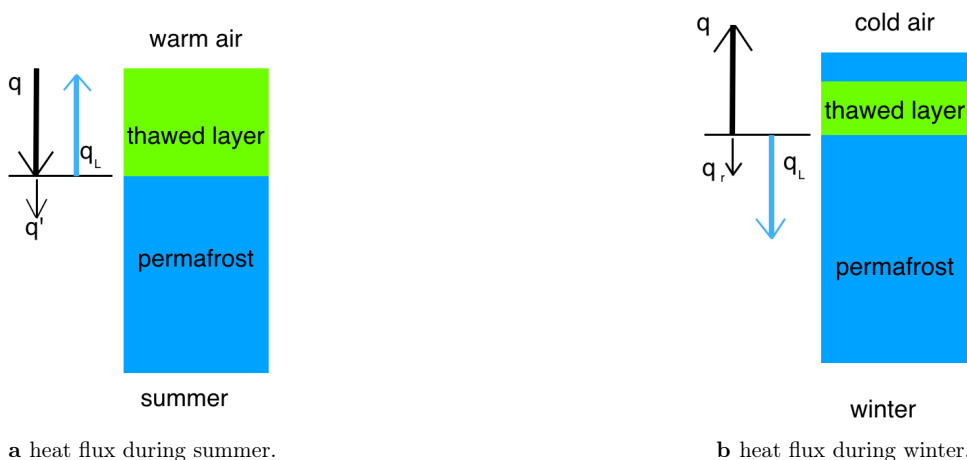


Figure 3.2: Thawing and freezing of permafrost and thermal energy flux.

During the summer (Figure 3.2a), the direction of the heat flow is from the warm air to the permafrost. The energy required for ice melting comes from the heat flow through solar radiation and convective heat transfer via air and water. The heat flux q at the surface is divided into two parts (simplified, during summer):

$$q' = q - q_L \quad (3.1)$$

where q_L is flux related to the latent heat of ice melting and q' is the net flux that enters the permafrost.

The direction of heat flux is reversed during the winter:

$$q = q_r - q_L \quad (3.2)$$

where q_r is the net heat flux within permafrost during winter and q_L is the latent heat of phase change.

Assuming [a] heat flux at the surface of the coastal bluff delivers the energy requirement of permafrost thawing and [b] $q_L \gg q$ in Eq. 3.1 and $q_L \gg q_r$ in Eq. 3.2, the following section describes the submodule: permafrost thaw.

Convective heat transfer via air and water

Convective heat transfer involves the combined processes of conduction and advection. This thesis uses the term convection to represent the heat transfer process from warmer fluid (air and water) to permafrost (solid). The heat transfer along the coast is considered forced convection. The governing equation of the convective heat transfer is based on Newton's law of cooling. Newton's law states that the rate of heat loss in a body is proportional to the difference in temperature between the body and its surroundings while under the effects of a breeze. The constant proportionality is the heat transfer coefficient (h_c). The coefficient is assumed to only depend on the temperature in classical physics, which closely approximates reality. The value of the coefficient h_c depends on the nature of the fluid.

The coastal profile is divided into four zones and different h_c values are used for each zone. The Appendix A.1 at page 123 defines four zones in detail. The purpose of using different zones for convective heat transfer is to enable the model to behave according to the wet and dry conditions.

The basic relationship of the heat transfer per unit time (Q_c) with convection is:

$$Q_c = h_{c_{w/a}} A (T_{a/w} - T_s)^b \quad (3.3)$$

where $h_{c_{w/a}}$ is the heat transfer coefficient, A is the surface area, $T_{a/w}$ is the temperature of the air/water, T_s is the temperature of the permafrost, b is the scaling exponent. The value of $h_{c_{w/a}}$ depends on the fluid's physical properties and flow orientation. The warmer airflow over a flat surface has a h_{c_a} value of $25 \text{ W m}^{-1} \text{ K}^{-1}$.

The $h_{c_{w/a}}$ for air can be estimated using the Prandtl number and Nusselt number correlation:

$$Nu = 0.339 Re^{1/2} Pr^{1/3} \quad (3.4)$$

The above relation is valid for incompressible flow over a flat plate. Nu is the Nusselt

number, Pr is the Prandtl number and Re is the Raleigh number. For air, the Pr number is 0.71.

Radiative heat transfer by solar radiation

The solar radiation of the sun also brings thermal energy to the bluffs. A simplified relation of heat flux at the surface due to solar radiation can be expressed as follows:

$$Q_r = S_{sw} - S_r \quad (3.5)$$

Where S_{sw} is the shortwave solar radiation corrected for cloud cover and measured at the earth's surface, S_r is the reflection of the radiation from the surface.

Movement of the melting front of permafrost

The heat flux from the air and water and solar radiation melts the ice inside the permafrost. The energy requirement of phase change limits the thawing process;

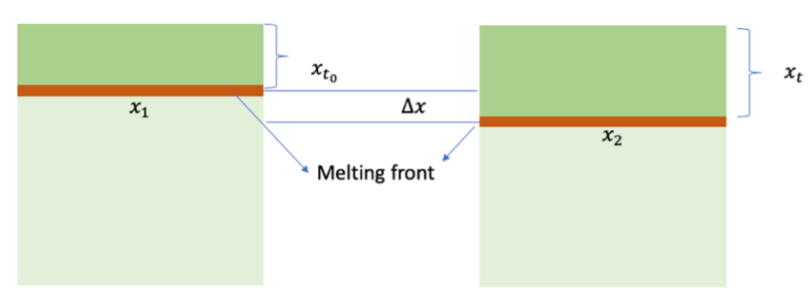


Figure 3.3: The movement of the melting front. A thawing rate of the permafrost (dx_t/dt) is established using Eq. 3.8.

Let's assume that within t seconds, the melting face of permafrost moved from x_1 to x_2 in Figure 3.3, resulting in a movement of the melting face by Δx . The thawing depth, x_t at the beginning was x_{t_0} . The thawing depth at the end of time t is x_t where $x_t = x_{t_0} + \Delta x$. The volume of the changed material is $V = \Delta x \times A$.

Assuming a unit surface area and ice content of the permafrost as n_{ice} , the melting volume of ice is $\Delta x n_{ice}$, which has a mass of $\rho_s \Delta x n_{ice}$.

The required energy for the melting of ice will be:

$$Q_L = L_s \rho_s \Delta x n_{ice} \quad (3.6)$$

The available energy Q_a is $(Q_c + Q_r) \times t$ to thaw the Δx thickness. We can express the

energy balance as: $Q_L = Q_a$

$$L_s \rho_s \Delta x n_{ice} = [h_{c_w/a} (T_a - T_s)^b + (S_{sw} - S_r)] \times t \quad (3.7)$$

Which is re-written as the thawing rate (dx_t/dt) by assuming $b = 1$:

$$\frac{dx_t}{dt} = \frac{h_{c_w/a} (T_a - T_s) + S_{sw} - S_r}{L_s \rho_s \Delta x n_{ice}} \quad (3.8)$$

3.2.1.2. Submodule: Slumping of thawed layer

The detachment of the thawed layer is possible in various mechanisms, such as solifluction, active layer detachment, slumping and retrogressive thaw-slumping. The model presented here only considers the slumping of the thawed layer due to gravity. The model does not consider the hydraulics (water table changes, pore water pressure, water flow); hence solifluction and active layer detachment are not included. Retrogressive slumping is also not included.

The term slumping is used in this thesis to describe the movement of the thawed layer by gravity. The thawed layer of the bluff has very low mechanical strength. The thawed layers may fall by the gravitational force and accumulate at the bluff base. Slumping occurs at the bluff face of the coastal profile since the slope of the other parts is mild.

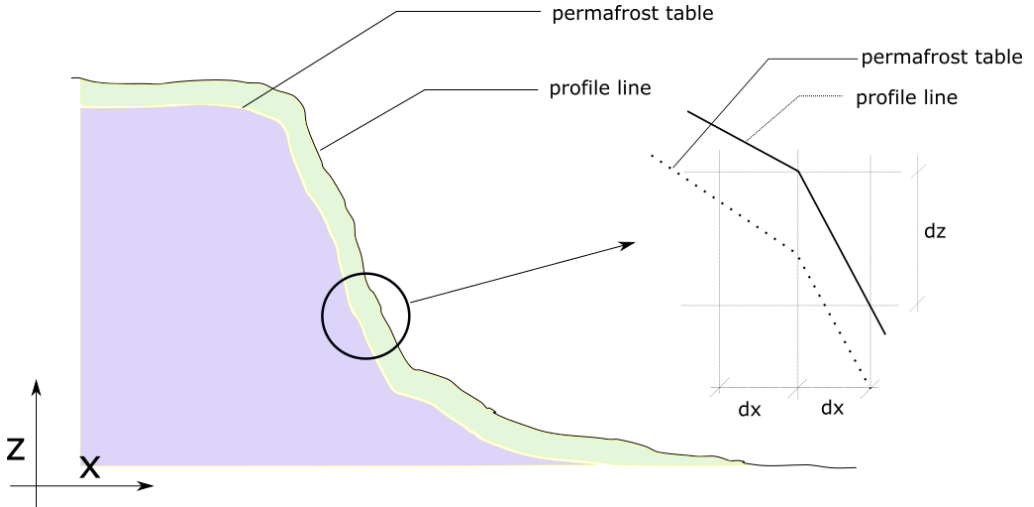


Figure 3.4: Slumping of the thawed permafrost at the bluff surface (Islam and Lubbad 2022).

Assumptions

The following assumption are made to simplify the slumping process:

1. A critical slope exists for the coastal profile above which the thawed layer will lose stability and climb down along the bluff face.
2. The mass flux or the movement does not depend on the slope (critical slope is a pre-requisite only and does not influence the flux rate) but rather depends on the thickness of the thawed layer.

A critical slope (m_{cr}) is defined for the coastal profiles above which the thawed layer will slump. Below the critical slope, the thawed layer will not move by gravitational force but is open to sediment transport by water. The critical slope differs for wet/submerged and dry/un-submerged conditions. We define the critical slope for the two phases: dry and wet.

We can write the condition of slumping as follows (Figure 3.4):

$$\frac{dz}{dx} \geq \begin{cases} m_{cr;w} & \text{if } x_t > 0, h > 0.05m \\ m_{cr;a} & \text{if } x_t > 0, h < 0.05m \end{cases} \quad (3.9)$$

where dz/dx is the slope of the coastal profile at a given point, $m_{cr;a}$ and $m_{cr;w}$ are the critical slopes for dry and wet conditions, respectively, and h is the time-averaged water depth. Some parts of the beach may temporarily go underwater by wave run-ups and the time-averaged water depth (in the numerical model) will have a small positive value at some of the grid points even though the heat is exchanged from the warm air. To overcome this problem, an arbitrarily small threshold value of 0.05 m is chosen for wet/dry conditions.

3.2.2. Module: Thermoabrasion

The thermoabrasion module simulates the niche growth, subsequent bluff collapse, and collapsed-bluff degradation as three submodules. These three submodules are coupled with a strict order of precedence (sequences 2 to 4 in Figure 3.5). The behaviour of the submodules is highly dependent on the boundary conditions at the base of the bluffs, especially the water level at the base of the bluffs (h_{id}) and water temperature (T_w). In the upcoming sections, three submodules are discussed.

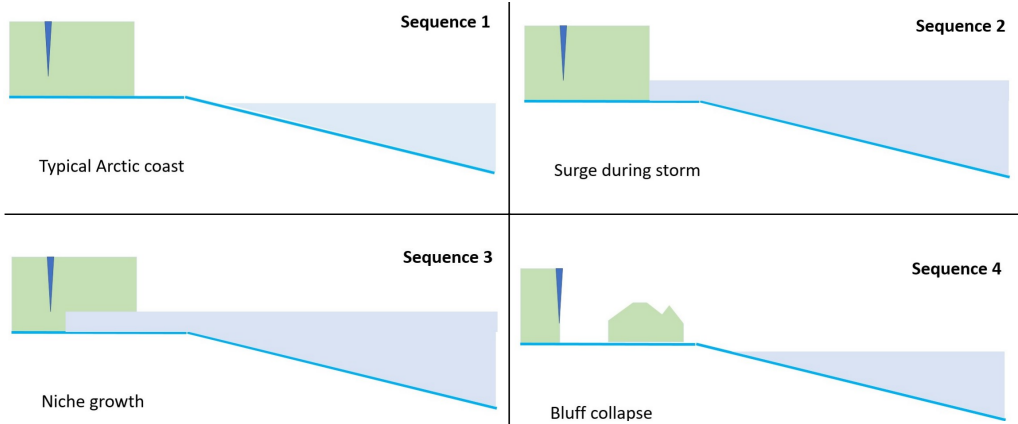


Figure 3.5: The sequences of thermoabrasion. The physical processes begin from sequences 2 to 4, and strict order of precedence is maintained.

3.2.2.1. Submodule: Niche growth

The niche grows at the base of the bluffs when the warm seawater melts the ice within the soil pores. The melted sediments are taken away offshore by the return currents. A conceptual model of niche growth by Kobayashi (1985) is depicted in Figure 3.6.

Assumptions

1. The permafrost is assumed to be composed of fine sediments and can be transported via water as a suspended load.
2. At the melting face, the salinity of the seawater decreases due to the influx of water from the ice.
3. A vertical uniformity is assumed for salinity, sediment concentration and temperature (Kobayashi 1985).

The water depth at the base of the bluff, point B in the Figure 3.6, is termed h_{id} - obtained from the results of the XBeach simulation. The thawing face, line EE', is vertical and assumed to be βh_{id} , where β is the empirical parameter. The value of β is taken as 2 (Ravens et al. 2012). The niche depth, line BE'= x_m , is estimated from the equation:

$$x_m = 2\zeta_m \sqrt{\epsilon t} \quad (3.10)$$

where h_{id} is the time-averaged depth of water at the base of the bluff (m), g is the gravitational acceleration (m/s^2), ϵ is the surf zone diffusivity $\epsilon = Ah_{id}\sqrt{gh_{id}}$, A is an

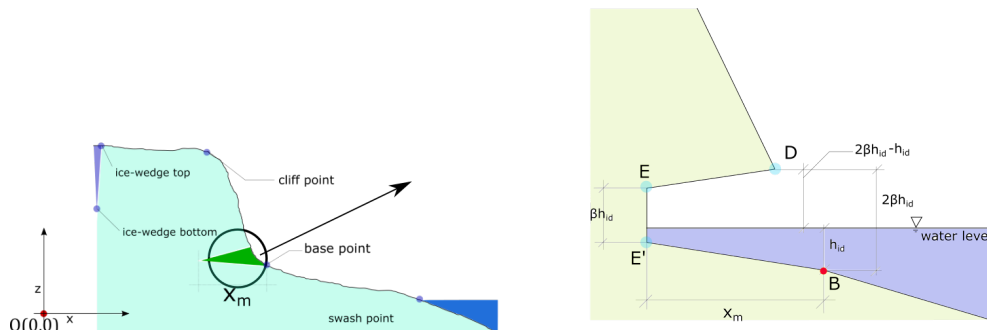


Figure 3.6: Niche geometry during the storm surge; simplified from Kobayashi (1985) (Islam and Lubbad 2022).

empirical constant, taken as 0.4 (Longuet-Higgins 1970), $\zeta_m = 0.0094(T_w - T_m)$, T_w is the temperature of the seawater and T_m is the salinity adjusted melting point of the ice.

The Eq. 3.10 describes the two most important driving forces of niche growth, T_d and h_{id} . The parameter h_{id} , the inundation depth of the bluff's base, represents the mechanical driving force. The h_{id} values during the storm are not very high (a typical value is around 0.5 to 2 m), which makes the waves on the beach depth limited. The shallow water equation can describe the movement of water inside the niche. T_d , on the other hand, represents the thermal driving force. From the empirical equation, we notice that for a constant water depth (h_{id}), the relation between the niche growth rate (x_m/dt) and temperature (T_d) is linear.

3.2.2.2. Submodule: Bluff collapse

The bluff collapse submodule considers two failure mechanisms (a) overturning failure and (b) shear failure described by (Hoque and Pollard 2009).

Assumptions

1. The mechanical strength is not dependent on the temperature of the permafrost. A depth-averaged mechanical strength is used for the model.
2. The friction between the permafrost and ice-wedge is considered as the tensile strength of the failure line at the overturning failure.

Shear Failure

In Figure 3.7, one of the three shear failure modes is depicted (the other modes are discussed in Appendix C.3). The shaded region over the niche is susceptible to collapse.

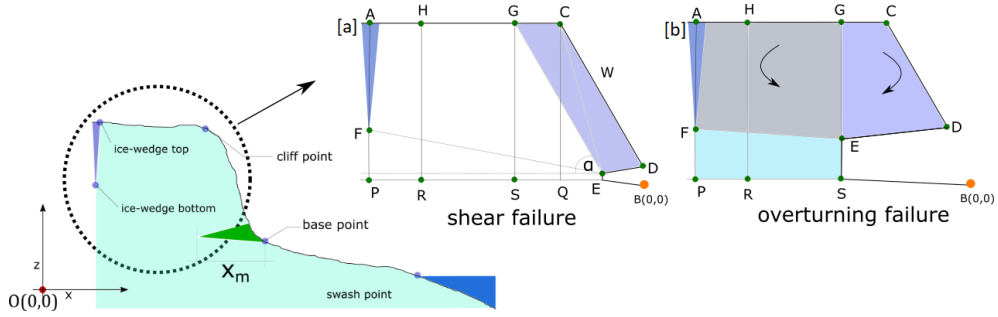


Figure 3.7: Two common failure modes of bluff collapse. [a] Shear failure of the bluffs, described by Eq. (3.11) and [b] Overturning failure of the bluff, described by Eq. (3.12) (Islam and Lubbad 2022).

The failure line, in this case, is GE, and the shaded region by the geometry GCDE is collapsed. A generalised and simplified condition of shear failure of the bluff is (Hoque and Pollard 2009):

$$c \cdot T_{ib} + W \cos \alpha \cdot \tan \phi < W \sin \alpha \quad (3.11)$$

where α is the angle of inclination of the failure plane, ϕ is the angle of internal friction of the bluffs, T_{ib} is the tensile failure line of the bluff (m), c is the tensile strength of the bluff (N/m), and W is the weight of the collapsed bluff (N) (weight of the GCDE portion in Figure 3.7a).

Overturning Failure

The governing equation for the stability is (Barnhart et al. 2014a):

$$\begin{aligned} \rho_s \int_{y_{base}}^{y_{top}} \int_0^{x_p} (x_p - x) dx dy &= \rho_s \int_0^{y_{top}} \int_{x_{edge}}^{x_p} (x_p - x) dx dy \\ &+ \int_{x_{edge}}^{x_p} \tau_b (x_p - x) dx + \int_0^{y_{base}} \tau_i (x_{edge} - x_p) dy \end{aligned} \quad (3.12)$$

The geometric parameters are shown in Figure 3.8, where x_p = niche depth at which the stability is lost, x_{edge} =position of the ice-wedge polygon from the base of the bluff, y_{base} =y coordinate of the top of the niche growth melting point, y_{top} = y coordinate of the top of the bluff, ρ_b = density of the bluff, g = gravitational acceleration, τ_b = the tensile strength of the frozen bluff and τ_i = tensile strength of ice.

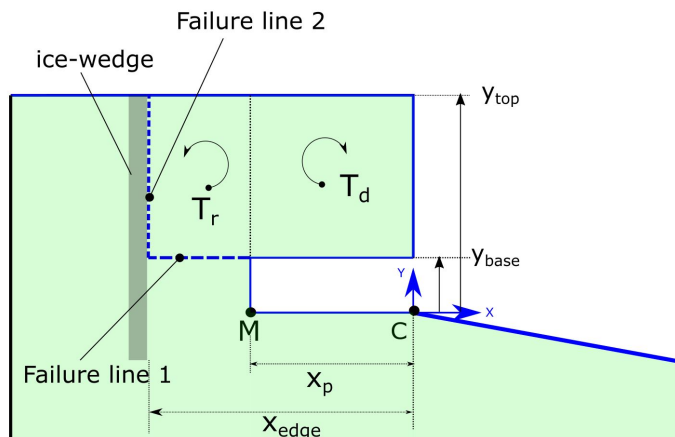


Figure 3.8: Stability of an overhanging bluff of a niche. Two failure lines are marked 1 (horizontal) and 2 (vertical). The balance is lost when $T_d > T_r + T_b + T_w$. image source: (Islam 2018).

3.2.2.3. Submodule: Degradation of collapsed bluff

The collapsed bluff remains on the beach and is subject to degradation by warm air and seawater. The geometry of the collapsed bluff depends on the niche depth and failure modes described in the earlier section.

Assumptions

The collapsed bluff is assumed to remain on the beach. The collapsed portion is subject to quicker degradation due to warm water. The degradation rate of the bluff can be estimated from the following equation (used by Ravens et al. (2012)):

$$M_i = M_{i-1} - aH^n[T_w - T_m] \quad (3.13)$$

where M_i is the mass of the collapsed bluff at the end of timestep i , M_{i-1} is the mass of the bluff at the end of the previous timestep $i - 1$, T_w is the seawater temperature, T_m is the salinity adjusted melting point of ice, H is the significant wave height at the 3m water depth, and a and n are the empirical parameters. Ravens et al. (2012) estimated that the values of a and n are $800 \text{ kg/m}^\circ \text{C}$ and 1.47, respectively.

In the numerical implementation of bluff degradation, we assume an immediate degradation of the collapsed bluff and the sediments are distributed evenly on the beach. The coupled hydrodynamic module simulates the removal of sediments from the beach.

3.3 Numerical implementation

From the conceptual models of thermodenudation and thermoabrasion described in the earlier sections, numerical implementation of the submodules is constructed. A feedback algorithm between the submodules is established based on the field observations, theoretical understanding and simplification of the physics. The feedback between the submodules is activated at the end of each timestep.

XBeach simulates nearshore hydrodynamics, including wave transformation, water level fluctuation due to tides, sediment transport and morphological changes. On the outer boundary of XBeach, BC2, in Figure 3.1, the wave conditions are required as input. A simplified storm surge module is used to estimate the water level changes at the BC2 boundary.

3.3.1. Assumptions

The following assumptions are made to establish the numerical model:

1. Thawing: Thawing is assumed to be controlled and dominated by convective heat transfer from the air. Thus, convective heat transfer by the pore-water is not included. Conductive heat transfer within the bluff is not included in the simulation, i.e., the depth-averaged temperature within the frozen bluff is used for the numerical calculations.
2. Slumping: A simplified 1D slumping module, as described in section 3.3.6 is used. No rotation (2D) of the bluffs and slip circle failures are considered. A depth-averaged mechanical strength of the bluff is used.
3. Snow and sea ice: Snow accumulation and melting are not simulated. The effect of sea ice on wave attenuation is simplified using a threshold value control (discussed in section 3.3.2).
4. Bluff collapse: Bluff collapses are simulated using two failure modes: (a) overturning failure and (b) shear failure with a pre-determined failure plane.
5. Degradation of collapsed bluff: The sediment exerted from the collapsed bluff is assumed to be evenly distributed on the beach immediately after the collapse, unlike the models by Ravens et al. (2012) and Barnhart et al. (2014a).

3.3.2. Threshold value control

Threshold values are used as binary conditions (on/off switch) for some processes. The following three threshold value controls are imposed:

1. **Ice concentration:** The effect of wave attenuation due to the presence of sea ice is not simulated. Instead, a 20% threshold value control is imposed. When ice concentration, $i_{con} < 20\%$, waves are assumed to be unaffected. Above 20%; the waves are assumed to be completely attenuated by the sea ice (adopted from [Rolph et al. \(2021\)](#) and [Overeem et al. \(2011\)](#); instead of 15%, 20% is used).
2. **Wet/Dry condition:** Due to wave run-up, the time-averaged water depth of the grid cells near the swash zones has a small positive value of water depth. The dominating heat transfer mechanism is still convection from the warmer air. To resolve this issue, a cut-off value of 5cm is used instead of 0cm. The grid cell is assumed to be dry when the average water depth is less than 5cm.
3. **Niche growth:** A threshold value of 10 cm to the time-averaged water depth at the base of the bluff (h_{id}) is used as a trigger condition for niche growth. When the time-averaged h_{id} value is less than 10cm, the niche process is assumed to be inactive. The choice of this value is also optimised to assure model stability.

3.3.3. Simulation of offshore hydrodynamics

Waves generated offshore travel to the shore and acted as a mechanical driver of erosion during the open season. Storm surges created during the summer act as the triggers for niche development. When measurements are available, one can choose not to simulate offshore processes. In this study, we used SWAN to simulate wave generations. The wave conditions are coupled to XBeach on the BC2 boundary.

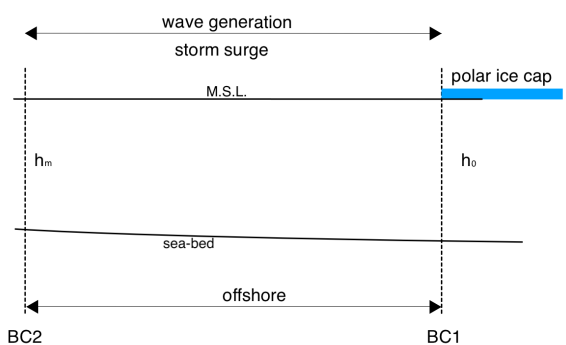


Figure 3.9: Offshore zone is contained within BC1 and BC2 boundary. Wave generation and storm surge are simulated in this zone.

Wave conditions and the water level are determined at the BC2 boundary, as shown in Figure 3.9. SWAN determines the wave generation in the domain contained by the boundaries BC1 to BC2. A one-dimensional (1D) storm surge model calculates the storm surge (η) at the BC2 boundary. The storm surge model is a function of wind speed, alongshore current, pressure drop, and the Coriolis effect. The storm surge module is based on simplified physics. The governing equation and numerical implementation of storm surge are described in Appendix B.1.

3.3.4. Simulation of nearshore hydrodynamics

A morphological model of nearshore is required to capture the hydrodynamics of the waves, water level, currents, tide and morphodynamics of the seabed changes (Figure 3.10). We used XBeach, an open-source software, to simulate nearshore processes. XBeach is coupled with other submodules at both offshore (BC2) and onshore (BC3) ends. XBeach has no in-built thermal modules, so processes related to permafrost are simulated using other modules.

XBeach simulates hydrodynamics, sediment transport and morphological changes from BC2 (in Figure 3.10) from nearshore until bluffs. The bed level changes due to sediment transport is an important phenomenon to simulate. In the offshore zone, the simulation of bed changes is ignored. The input parameters at the BC2 are time series of the JONSWAP spectrum for waves and the water level is the combination of tide, mean sea level and storm surge.

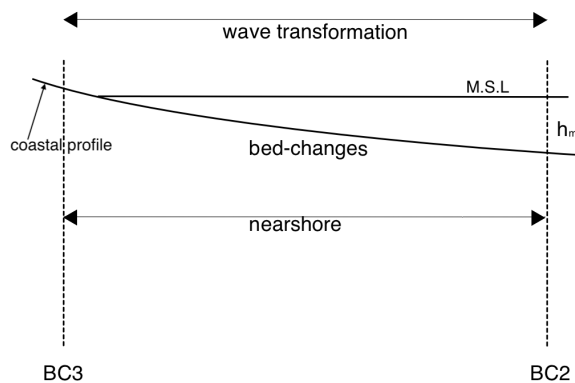


Figure 3.10: Nearshore zone is contained within BC2 and BC3 boundary. Wave transformation and other hydrodynamics are simulated in this zone.

3.3.4.1. XBeach model set up

A typical XBeach model setup is shown in Figure 3.11. Depending on the water depth of the nearshore, the boundary BC2 (line CD) should be placed. The criteria adopted for this study is the $h_m/\lambda < 0.5$ where h_m is the water depth and λ is the peak wavelength. The distance between the swash and cliff points depends on the beach conditions. The measurements showed that the crest retreat is in the range of 4 to 10m and the ice wedge polygon has a radius of about 10 to 12m. We chose 50m from the cliff to the onshore direction as the BC3 boundary.

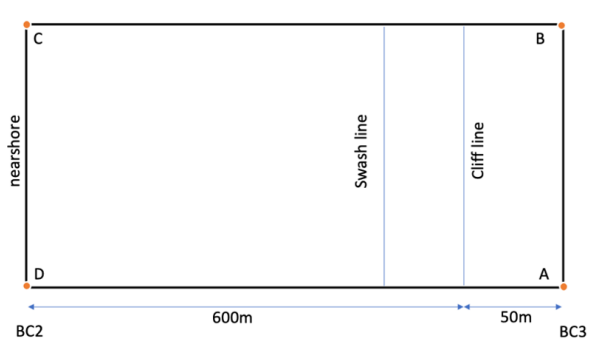


Figure 3.11: The onshore (BC2) and offshore (BC3) boundary of XBeach model set up.

3.3.4.2. Variable grid spacing

Variable grid spacing is allowed in XBeach. A typical variable grid spacing used in the study is shown in Figure 3.12. The bluff slope is the most active part of the Arctic coastal profile because of the occurrence of niche growth and slumping. The highest resolution of grids is used on the beach and bluff surface zones.

3.3.5. Simulation of permafrost within XBeach

The permafrost in the coastal profile is treated as a non-erodible surface in XBeach. No morphological changes are allowed in the permafrost table by XBeach during the model run in one particular time step. After the XBeach run is complete, the thawing permafrost module estimates the new position of the permafrost table. Figure 3.13 depicts the XBeach setup with a permafrost layer. Grid point A has a corresponding point B which is on the permafrost table. Using the parameter ne_layer , the value x_n determines the position of the non-erodible surface, i.e. permafrost table. However, thawing depth, x_t is calculated normal to the coastal profile and corresponds to point B. Using the geometric relation of line AB and AB, the position of point B on the permafrost table is calculated for each

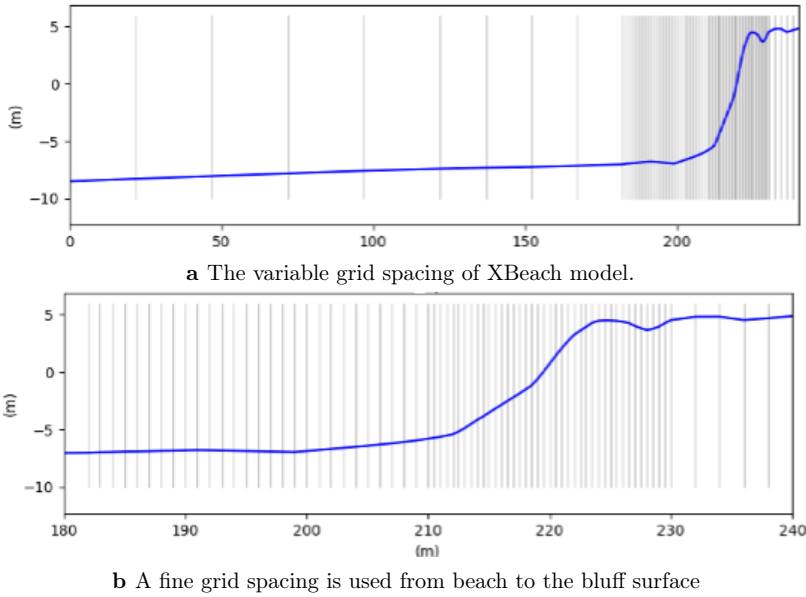


Figure 3.12: Variable grid spacing of XBeach is used in the model to accommodate finer spatial resolution from the bluff's base until a few metres of bluff surface. (Islam and Lubbad 2022)

grid point at the end of each timestep.

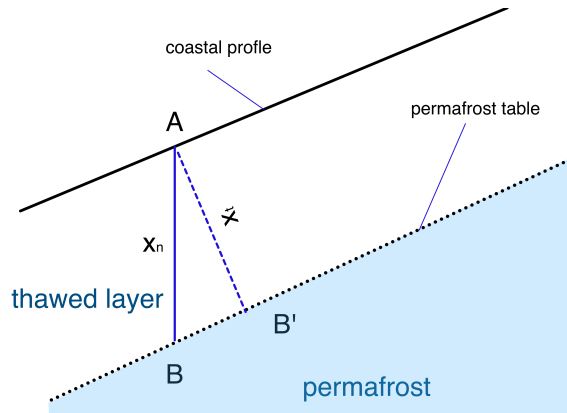


Figure 3.13: Simulation of permafrost within XBeach is shown. The thawing module calculates the thawing depth in the direction normal to the coastal profile at each grid point. XBeach only considers vertical distance from the coastal profile. Hence a correction must be done at the end of each timestep to convert the values of x_t from the thawing submodule to x_n to be used by XBeach.

3.3.6. Numerical implementation of slumping

The numerical schematisation of slumping used in this study is shown in Figure 3.14. In the figure, line ABCD is the original coastal profile before slumping. Point A has a slope less than the critical slope (m_{cr}). The next grid point B has a slope greater than m_{cr} . Slumping occurred at point B, which resulted in a shift in the coastal profile from line ABCD to the new line AB'C'D. The permafrost table WXYZ remained unchanged since slumping can only occur on the thawed layer; however, the thawed layer thickness at grid points B and C are changed due to slumping. The criterion to initiate slumping as described earlier:

$$S_i > m_{cr} \tag{3.14}$$

where S_i is the slope of the grid point i and m_{cr} is the critical slope of the grid point i .

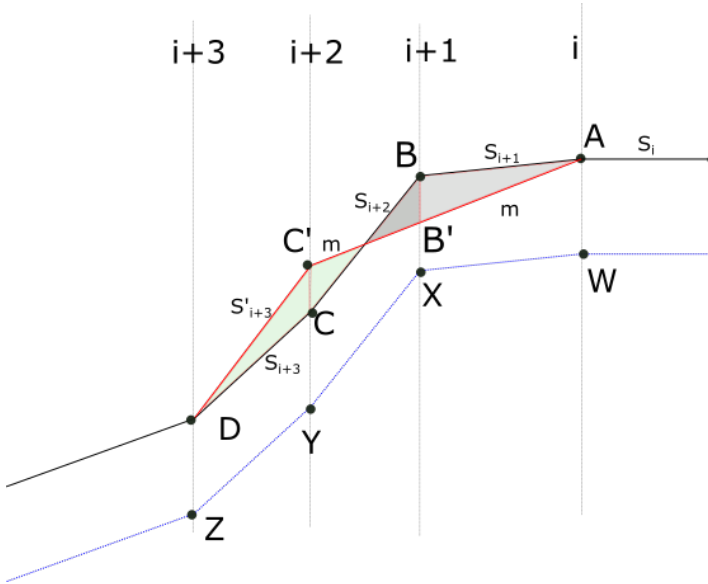


Figure 3.14: Numerical schematisation of slumping based on critical slope and fall by gravity only. The line ABCD is the profile line which had WXYZ permafrost table at various thawing depths of each grid point. The slope at point B is greater than m_a , which triggers the slumping and the new position for point B at the same grid line is B'. (Islam and Lubbad 2022)

3.3.6.1. Assumptions

The slumping module is based on the following assumptions:

1. The slumping process is initiated by gravitational force only. We ignore the movement of thawed material by the water flow created due to permafrost thawing.
2. The constraints of the initiation of the slumping at the $i+1$ th grid point (point B in the figure) are as follows:
 - C1. No slumping occurs at the permafrost table, the line WXYZ, irrespective of the slope. The failure within permafrost is considered in the bluff stability submodule. This submodule only simulates until the thawing depth.
 - C2. The slope at the grid point before the i th cell (point A) has a lower slope than critical $S_i > m_{cr}$.
 - C3. The n -th timestep has j number of iterations where j is any number iteration until Equation (3.14) is no more satisfied.
 - C4. For slumping at i -th grid point at j th iteration, the mass transfer is limited to two adjacent grid cells; points B and C are moved to B' and C'.
 - C5. As a result of slumping, the grid point in consideration, point B, will be subsided to B', increasing the elevation of point C to C'.
 - C6. The subsidence of point B is such that the area under the curve ABCD will be equal to the area AB'C'D so that the conservation of mass is maintained.
 - C7. Rule C6 is overridden when the subsidence of point B' is limited by the permafrost line. Point B is not allowed to be lowered than point X. If C6 is overridden, then point C will move and still maintain mass balance. In this case, the movement of the mass will be lower.
 - C8. The slumping process is always triggered in the downward direction. If for n th timestep, if two grid points have a slope more than the critical value m_{cr} , slumping will be initiated at the grid point in the higher vertical position.
3. There is no limit to the iterations for each time step, i.e., the module will run until all the grid points in the profile satisfy the governing equation.

At the n -th timestep, let us assume that the numerical submodule is checking whether slumping is triggered at each grid point. Using the critical slope criteria, the model finds point A, the i th grid point does not satisfy the criteria $S_i > m_{cr}$, then it checks the $i+1$ th grid, the point B.

If the slumping occurs, it overrides the thawing depth, x_t estimated by the thawing depth modules.

The workflow of the numerical model is shown in Figure 3.15. Each grid point is checked for the triggering condition, and then the profile is continuously updated until the last grid point. When all the grid points are examined, the numerical model allows for the next coupled module or next time step.

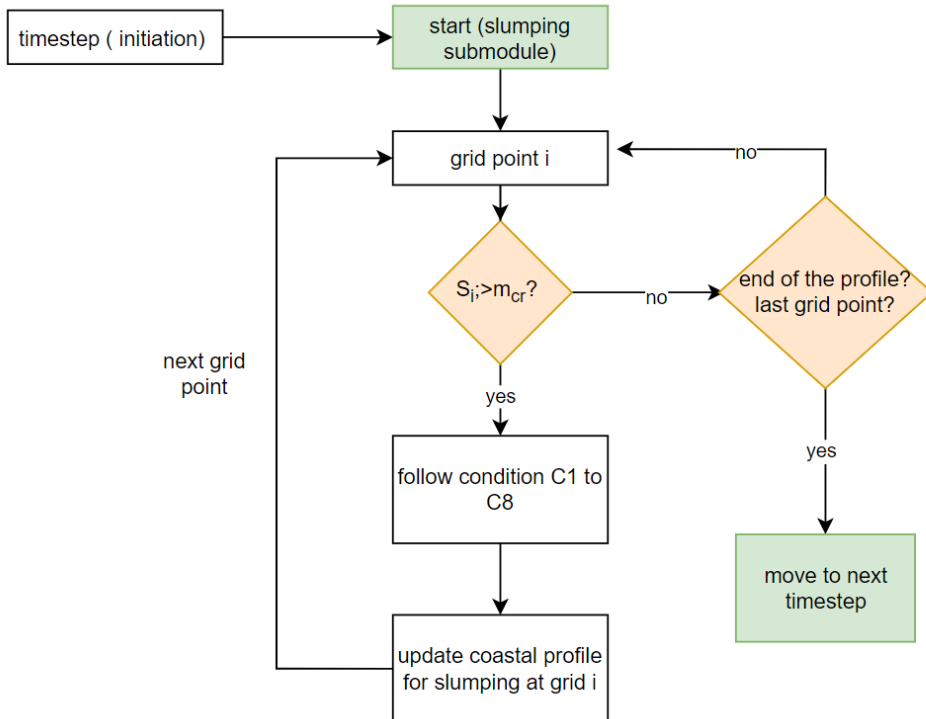


Figure 3.15: Workflow of the slumping module. (Islam and Lubbad 2022)

3.3.7. Coupling submodules to establish a combined model of thermodenudation and thermoabrasion

The two mechanisms of Arctic coastal erosion, thermodenudation and thermoabrasion can be independent, i.e. only one of the mechanisms can occur on a beach. When both mechanisms are active on the coast, the two mechanisms affect each other. For example, bluff collapse exposes the bluff face and reduces the thawing depth for thermodenudation whereas thawed material from slumping may increase the elevation of the beach near the bluff base; thus reducing the growth of the niche during a storm. This section presents the methodology of coupling submodules to mimic the two mechanisms.

The results of the XBeach simulation are used as inputs for the in-house submodules of thermodenudation and thermoabrasion. XBeach simulates uninterruptedly for three hours, so we can consider the timestep of the global model as the same (Figure 3.16). The three-hour timestep is used to be aligned with the standard practice of describing sea state at three-hour intervals. We simulate the hydrodynamic forcing and sediment transport of nearshore with XBeach for the i -th timestep and analyse the results. We determine the bed level changes, average water depth at the base of the bluffs (h_{id}), and the mean water depth at each grid (to determine the wet/dry condition for convective heat transfer). The output of XBeach is then fed into the submodules of slumping, thawing depth, niche growth, and bluff collapse.

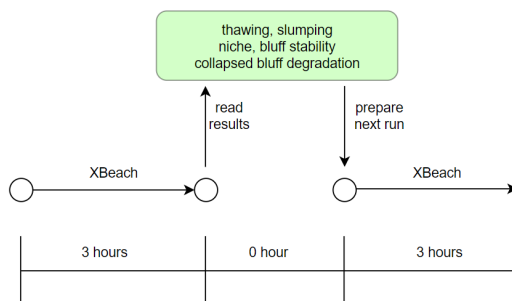


Figure 3.16: XBeach simulates the nearshore module. The XBeach output is analysed and used as inputs for other submodules. (Islam and Lubbad 2022)

The workflow of the coupling is shown in Figure 3.17. At the inception of the simulation, global parameters such as the volumetric latent heat of permafrost thawing (L_t), the tensile strength of bluffs (τ), geometric parameters such as β and m_{cr} for air and water, etc., are loaded. These parameters are time-independent, i.e., they remain the same for all timesteps. The input parameters, such as air temperature (T_a), water temperature (T_w), ice concentration (i_{con}), wind speed (U_w), bluff temperature (T_s), and tide (h_t) are dependent on time. The model requires the time series of these input parameters at the same time interval as the global timestep. We set the global timestep as 3 h to be consistent with the three-hour sea-state and wave spectrum.

At the beginning of the i -th timestep, we must check whether the current timestep is within the simulation duration. If the condition is satisfied, we load the input parameters from the respective time series for the i -th timestep. The numerical model checks the ice concentration (i_{con}) for the current time step. From here, it is possible to proceed following two different routes. The offshore wave generation and storm surge is calculated

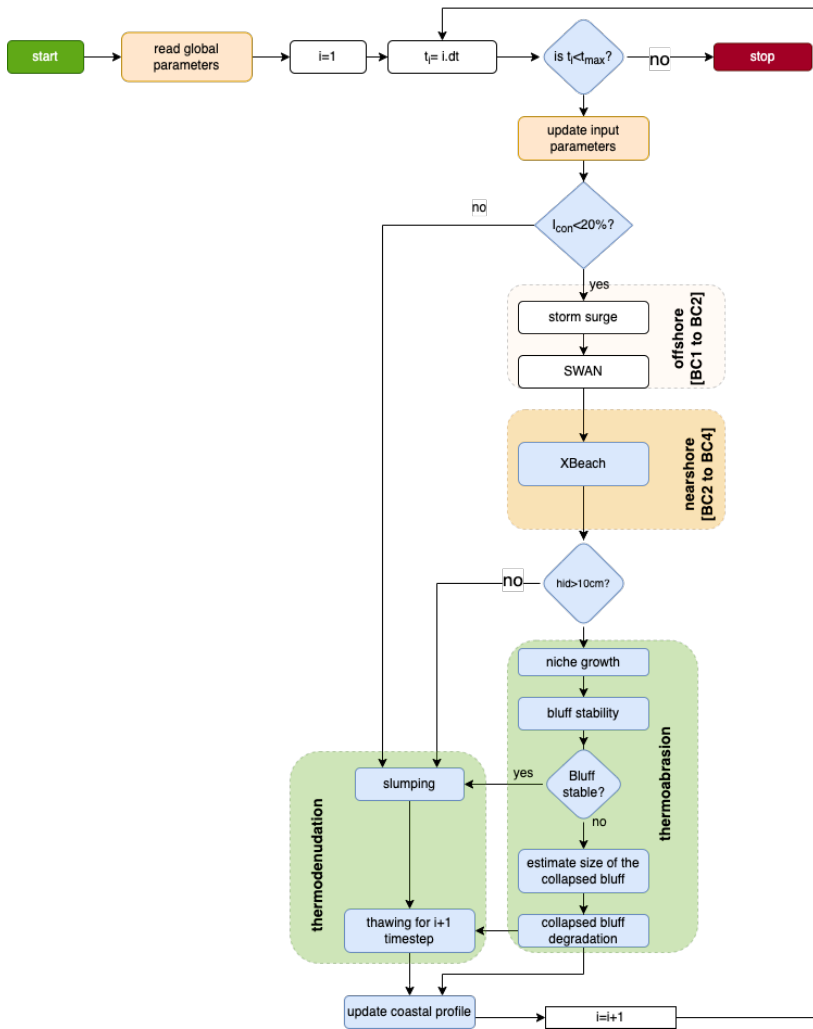


Figure 3.17: Numerical implementation workflow of the submodules. (Islam and Lubbad 2022)

only if the ice concentration is less than 20%. If the ice concentration is more than 20%, then the numerical model does not run SWAN, storm surge model and XBeach. We skip to the slumping submodule. An ice concentration of more than 20% indicates no wave activity.

Another route in the workflow is triggered when the ice concentration is less than 20%. If this condition is satisfied, then SWAN and storm surge submodule is turned on. The storm surge water level (η) and wave spectrum are calculated at boundary BC2. The water level is updated at BC2 for the tide and storm surge.

The XBeach simulates sediment transport, currents, water level setup, and morphological changes. The niche submodule becomes activated when the water level at the bluff (h_{id}) reaches more than 10 cm. We also calculate the time-averaged water depth at every grid point to determine whether the coastal profile is wet or dry at the i -th time step. The dry and wet grid points of the coastal profile are treated differently with respect to convective heat transfer and slumping.

The model enters the thermodenudation module if the h_{id} is less than 10 cm (which means the sea is calm, it is a 'no storm' condition), the slumping submodule is turned on. If h_{id} is greater than 10 cm the model enters to thermoabrasion module and the niche submodule is activated. It calculates the growth of the niche (x_m). The niche geometry is fed into the bluff stability submodule to check whether a collapse is triggered. The model returns on the thawing depth submodule when no bluff failure is recorded. When the model registers a bluff failure, it estimates the collapsed bluff's size and volume, and the collapsed bluff degradation module is activated. After that, we calculate the thawing depth at each grid point for the $i+1$ th time step. The last step of the model run at the i -th time step is registering the changes and updating the coastal profile to simulate the $i+1$ th iteration.

Four major routes or combinations of processes representing four different phases of erosion are observed within the workflow. A summary of the four routes is given in Table 3.2.

Table 3.2: A summary of the routes combinations of submodules based on the environmental forcing. (TA=thermoabrasion, TD=thermodenudation)

route	i_{con}	wave	air temp	thawing	h_{id}	niche	mechanism
R#1	>20%	no	<0	yes	-	no	TD
R#2	>20%	no	>0	yes	-	no	TD
R#3	<20%	yes	>0	yes	<10cm	no	TD
R#4	<20%	yes	>0	yes	>10cm	yes	TA

Before the beginning of summer, only the thawing module is active and calculates the

freezing of the thawed layer. Sea ice covers the nearshore and waves can not reach the shore. Only the thawing module is active during this time which calculates the freezing of the active layer. This phase is termed R#1 (Figure 3.18). The air temperature rises over zero before the ice concentration (i_{con}) goes below 20%. This phase is termed R#2. The thawing module now calculates the movement of the permafrost table since the average air temperature is positive, initiating the thawing of the permafrost. Since sea ice is still present, XBeach is not activated. Slumping may occur; in this case, the sediments stay on the base of the bluffs and accumulate over time.

In the summer, waves can reach the shore, so XBeach is activated in route R#3. The numerical model uses this route during calm summer days. Morphological changes nearshore may occur; sediment transport is possible. If any sediment accumulates during the R#2 phase, it will be removed. R#4 route is activated during storm surge to simulate thermoabrasion.

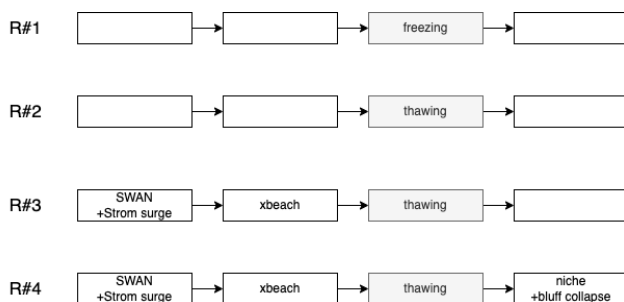


Figure 3.18: A simplified representation of the four routes.

The model described in this chapter simulates nearshore hydrodynamics with high fidelity and simultaneously estimates both thermoabrasion and thermodenudation. Consecutive years of simulation can be achieved as the model simulates the freezing as a negative movement of thawing depth during winter. The model can estimate the fate of an Arctic coast due to the mass influx to the nearshore zone by thermodenudation and thermoabrasion in both the short and long term.

The calibration, validation and application of the numerical model are discussed in Chapter 5 (section 5.1 on page 78).

3.4 Probabilistic approach for data-poor environments

The model described in the earlier sections requires detailed field measurements and environmental forcing as input parameters. Many Arctic coasts are only accessible during

summer when the coast is ice-free. Poor communication infrastructure and harsh environment limit access to the coasts. In situ measurements are very few and generally have a coarse temporal and spatial resolution.

A probabilistic approach to a process-based model in a data-poor environment is a practical solution because it considers the uncertainty. The probabilistic approach incorporates the inherent uncertainty due to a lack of measurements. This allows for more robust and flexible solutions that adapt to changing conditions or new information. The probabilistic approach can also generate a range of potential outcomes, providing a deeper understanding.

The application of a probabilistic approach for data-poor environments like Arctic coasts was examined in this study. The approach was applied to an earlier version of the process-based model of thermoabrasion. The probabilistic approach could not be applied to the combined model of thermodenudation and thermoabrasion due to the time constraints of the study. The methodology was examined using a simpler process-based thermoabrasion model of coastal erosion. Only crest retreat due to thermoabrasion was simulated and nearshore hydrodynamics along with morphodynamical changes were ignored.

3.4.1. Assumptions

Two specific assumptions in terms of probability are made: (a) the input parameters follow a normal or lognormal distribution with a 10% coefficient of variance (CV) while some input parameters are kept deterministic, and (b) the probability distributions of the input parameters are independent, i.e., no correlation between parameters.

3.4.2. Description of the approach

A Monte-Carlo simulation was adopted to account for the uncertainties in the input parameters. The sequence of submodules of thermoabrasion described in the earlier section was used. The coupling of the submodules of thermoabrasion using Monte Carlo simulation is shown in Figure 3.19). A random number generator spawns random numbers following a particular distribution. For the Monte Carlo simulation, 1000 sets of input parameters were generated.

The density of the sediments, water and porosity of the soil parameters are kept deterministic. The numerical model initially loads the coastal profiles as shown in Figure 3.19. The numerical model consists of three submodules connected as a series, one after another, in a strict order of precedence. The first submodule, storm surge, was kept outside of the probabilistic approach and the surge (η) was used as one of the input parameters for

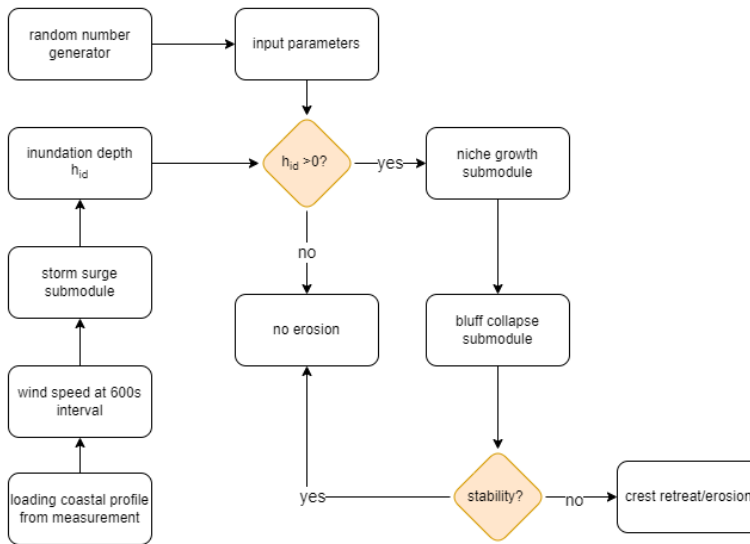


Figure 3.19: Algorithm of the model with three numerical modules and Monte Carlo simulation.

the niche submodule. A short list of parameters with typical values and the probability distribution is shown in Table 3.3.

Table 3.3: Distributions of the input parameters for the numerical model. Here, $N[p,q]$ presents a normal distribution with a mean of p and a standard deviation of q , $D[r] =$ deterministic value of r and $\text{Log } N[x,y]$ represents a log-normal distribution with a mean of x and a variance of y .

Parameter	Symbol	Distribution
Inundation depth	h_{id}	deterministic [calculated]
Ice-wedge size	x_{edge}	$N[14,1.4]$
Bluff height	$y_{top} - y_0$	$N[5.2,0.52]$
Salinity of seawater	S_a	$N[30,3]$
Porosity of frozen sediments	n	$D[0.4]$
Density of ice	ρ_i	916 kg/m^3
Density of sediments	ρ_s	$D[2650 \text{ kg/m}^3]$
Seawater temperature	T_a	$N[\text{monthly mean, 10\% cov}]$
Friction factor	c_f	$D[1 \times 10^{-6}]$
Longshore current	v	$N[1,01]$
Beta (Kobayashi formula)	β	$N[2,0.2]$
Tensile strength (ice)	T_i	$\text{Log } N[1 \times 10^4 \text{ Pa, } V = 100]$
Tensile strength (bluff)	T_b	$\text{Log } N[2 \times 10^4 \text{ Pa, } V = 200]$

Using the water level changes due to storm surge and tide, the value of inundation depth, h_{id} is calculated. The next submodule of the sequence is niche growth. Probabilistic distributions were used for some of the input parameters like salinity of seawater, sea water temperature, niche opening parameter (β) etc. The outcome of the niche submodule, the growth of the niche (x_m), followed a probabilistic distribution. The subsequent submodule: bluff stability also uses probability for the input parameters. The bluff failure probability can be calculated from the N=1000 cases. The numerical model estimates crest-retreat after analysing all the cases. The probability distribution of the crest retreat was found to follow a normal distribution. The standard deviation of the distribution, however, increases over time. The application of the numerical model is demonstrated with one profile in section 5.2 on page 101. The model details are attached as Appendix C.1.

For the numerical parameterisation of the governing equations, an explicit Euler scheme is used. The numerical model has a time step of 10 min (600 s) for all the three submodules. The grid size is 1 m for the storm surge submodule. A higher spatial resolution (10 cm) is used for the niche growth submodule. The algorithm for the interaction between the three submodules is explained in Figure 3.19.

3.5 Data driven model of permafrost temperature

In addition to the process-based model for coastal erosion, a data-driven model to estimate the permafrost temperature using measurements near the surface is developed in this study. Once calibrated for a site, the permafrost temperature model can be used for interpolation of missing measurements and as a prediction tool to forecast. The model can be used to estimate the thawing depth when the measurements of the temperature of permafrost are not available. It is also possible to calibrate the model on the pan-Arctic scale to predict the thawing depths.

The model is based on the analytical solution of conductive and convective heat transfer within coastal bluff. A summary of the model is presented here (details can be found in journal paper C.2).

3.5.1. Thermal regime of permafrost

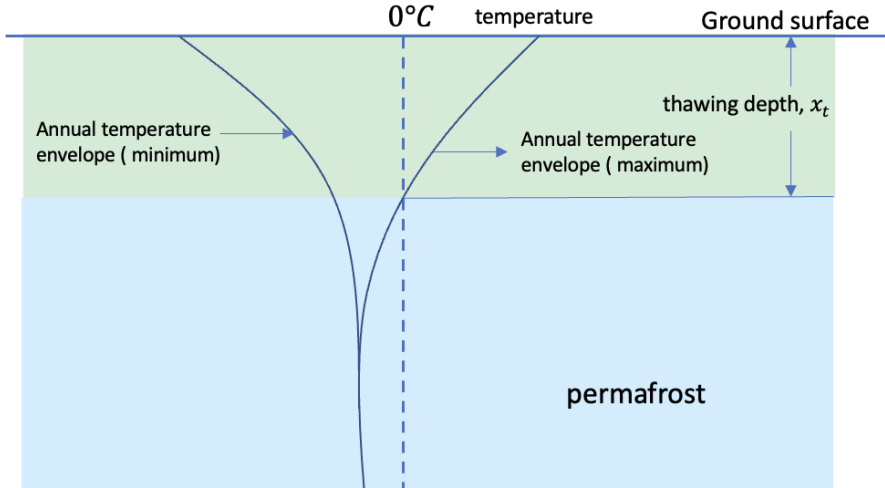


Figure 3.20: Permafrost thermal regime is shown. The annual maximum and minimum temperatures are drawn along the depth. The annual maximum crosses the zero-degree temperature line at the end of the active layer. The distance from the surface to the end of the thawed layer is termed thawing depth (x_t).

A typical temperature curve (trumpet curve) describing the thermal regimes is shown in Figure 3.20. The active layer is the top layer of soil which freezes and thaws every summer. Thawing depth (x_t) is the thickness of the thawed layer. The maximum thawing depth can be assumed at the point where the annual maximum temperature curve crosses the zero-degree line. A thin organic layer consisting of nutrients for vegetation is typically found near the surface.

The seasonal variation of the temperature is greater near the surface; the difference between the annual minimum and maximum is highest at the surface ($z = 0$). The temperature variations follow an annual cycle; based on this concept, [Van Wijk and De Vries \(1963\)](#) and [Andersland et al. \(2003\)](#) proposed the following equation to express the temperature variation at any depth in the soil as a summation of a mean and a harmonically fluctuating component :

$$T_g(z, t) = T_m(z) + T_a(z) \cdot \sin(2\pi t f + \phi(z)) \quad (3.15)$$

where T_m is the mean temperature, T_a is the amplitude of the harmonic wave, f is the frequency of the harmonic function, f is interchangeable with $\omega (= 2\pi f)$ -the angular

frequency, ϕ is the phase of the wave. The amplitude, T_a and the phase, ϕ is function of depth (z), but the frequency, f remains the same.

3.5.2. Problem formulation

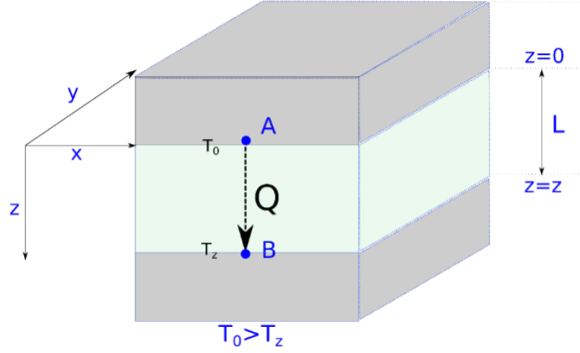


Figure 3.21: Thermal energy transfer between two points in the permafrost. image source: Islam et al. (2021).

Two points, A and B, inside the coastal bluff are shown in Figure 3.21. The temperature of point A is known. To determine the temperature of point B, one can, in principle, solve the heat balance equation of the porous medium as shown in Eq. 3.16 (Plaxis 2021).

$$\frac{\partial}{\partial t} (n_p S \rho_w e_w + n_p (1 - S) \rho_v e_v + (1 - n_p) \rho_s e_s) = -\nabla \cdot (\underline{J}_w + \underline{J}_v) + Q_T \quad (3.16)$$

where e_w, e_v and e_s are the internal energy in the water, vapour and solid phases, Q_T is the heat source term, \underline{J}_w and \underline{J}_v are the advective internal energy flux in water, vapour and soil (porous medium), n_p is porosity of the soil, ρ_w , ρ_v and ρ_s are the density of the water, vapour and soil.

An alternate approach to determine the temperature of point B adopted for the model is to indirectly estimate the parameters of the analytical solution (Eq. 3.19) using field measurements. The indirect estimate of the parameters is achieved by Fast Fourier Transformation (FFT) and regression analysis.

Based on the conservation of the energy, the Fourier thermal conduction and convection equation for the 1D case is expressed as (Stallman 1965 ; Gao et al. 2003, 2008):

$$\frac{\partial T(z, t)}{\partial t} = \frac{\partial^2 k(z) T(z, t)}{\partial z^2} + \frac{\partial W(z) T(z, t)}{\partial z} \quad (3.17)$$

where k is the thermal diffusivity (unit= m^2s^{-1}) and $k = \lambda/Cg$ where λ is the thermal conductivity (unit= $Wm^{-1}C^{-1}$) and C_g is the volumetric heat capacity of the soil (unit= $Jm^{-3}C^{-1}$), W is the liquid water flux density. $W = \partial k/\partial C_w/C_g w \eta z$, $\partial k/\partial z$ is the gradient of the soil thermal diffusivity in the z-direction, C_w is the heat capacity of the water ($J^\circ C^{-1}m^{-3}$), w is the liquid water velocity (m/s), η is the volumetric water content of the soil (unit-less).

3.5.2.1. Assumptions

The following assumptions are made to establish the data-driven model:

1. Eq. 3.17 describes the heat transfer via conduction and convection between two points within coastal bluffs. Eq. 3.17 does not consider the sink and source term of the phase change.
2. If combinations of harmonics describe the boundary condition, the final solution can be achieved by superimposing the solutions of Eq. 3.17 for each harmonic.

3.5.2.2. Boundary condition

Instead of applying Eq. 3.15 as a boundary condition, the temperature measurement at the surface can be expressed as a combination of harmonics using Fast Fourier Transformation (FFT). The boundary condition is decomposed to N number of the harmonic component with different frequencies and amplitudes.

$$T(z = 0, t) = T_m(z) + \sum_{n=1}^N T_{a0_n} \sin(2\pi f_n t - \phi_{0_n}), n = 0, 1, 2, \dots, N \quad (3.18)$$

3.5.2.3. Analytical solution

Applying Eq. 3.18 as a surface boundary condition (as temperature profile at point A at a depth z), the temperature at point B can be determined using Eq. 3.17. A solution to soil temperature T_z at point B can be expressed as shown in Eq. 3.19 (Verhoef et al. 1996 ; Hu et al. 2016):

$$T_z(z, t) = T_m(z) + \sum_{n=1}^N T_{a0_n} e^{\left[\frac{-W-\alpha_n}{2k}\right]z} \sin \left[2\pi f_n t - \phi_{0_n} - z \frac{\beta_n}{2k} \right] \quad (3.19)$$

where T_m is the mean temperature at depth z , independent of the frequency, T_{a0_n} is the amplitude of each harmonic function, ϕ_{0_n} is the phase of each harmonic function at the

surface. W and k are independent of the harmonic functions but dependent on depth (for simplicity, W and k are made depth-averaged), and α and β are different for each harmonic function.

We re-write part of the Eq. 3.19 to be used for regression as follows:

$$T_a(z, t) = T_{a_0} \cdot e^{-z \cdot \sum_{n=1}^N RR_{FS_n}} \quad (3.20)$$

$$\phi_n(z) = \phi_{0_n} - z \cdot PL_{FS_n} \quad (3.21)$$

where $RR_{FS_n} = \frac{-W_n - \alpha_n}{2k}$ and $PL_{FS_n} = \frac{\beta_n}{2k}$ for $n = 0, 1, 2, 3, \dots$

The solutions are independent of the frequencies of the harmonic functions and do not change over depth (Van Wijk and De Vries 1963). A data-driven model is developed by calibrating the parameters RR_{FS_n} and PL_{FS_n} .

3.5.3. Numerical implementation

3.5.3.1. Training, testing and prediction data set

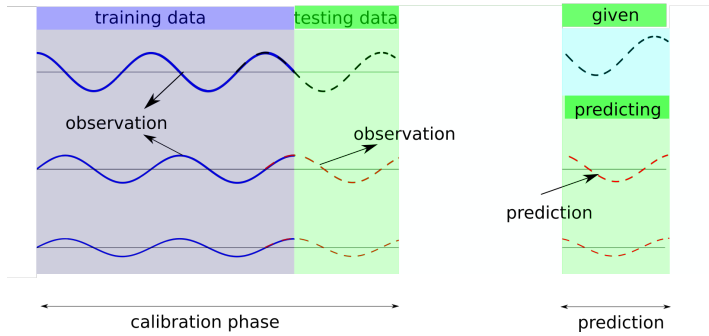


Figure 3.22: The temperature measurement is divided into testing and training datasets. Parameters of Eq. 3.19 to 3.21 are estimated using the training dataset. A prediction is made and the simulation is compared with the testing dataset.

The temperature measurement at various soil depths is divided into two datasets, as shown in Figure 3.22. Initial 80% of the data points for all the depths are kept as a training data set, and the rest is reserved as testing data set. The training dataset is used to calibrate the parameters of Eq. 3.19 to 3.21. The testing dataset is not used for the regression; the dataset is used to determine the model's accuracy. Using the parameters obtained from the training dataset, another set of data is prepared, named the prediction dataset.

The prediction dataset contained simulated or estimated temperature measurements of the same time period of the testing data set.

The workflow of the methodology is shown in Figure 3.23. The solution of Eq. 3.18 is fitted to the training data set to determine the parameters (RR and PL for each FFT harmonic component). After that, the calibrated solutions are used to numerically reproduce the remaining data, i.e. the testing data set. The calibration accuracy is determined by comparing the numerical prediction with the measurements, and the decision is made whether to accept the calibration or to re-calibrate the parameters. If the error is within the limit, the calibrated equation can be used as the governing equation to hindcast or forecast soil temperatures for the specific local area.

The calibration and validation of the model are demonstrated using one set of field measurements in Chapter 5 section 5.3 on page 104. Details of the numerical implementation can be found in Appendix C.2.

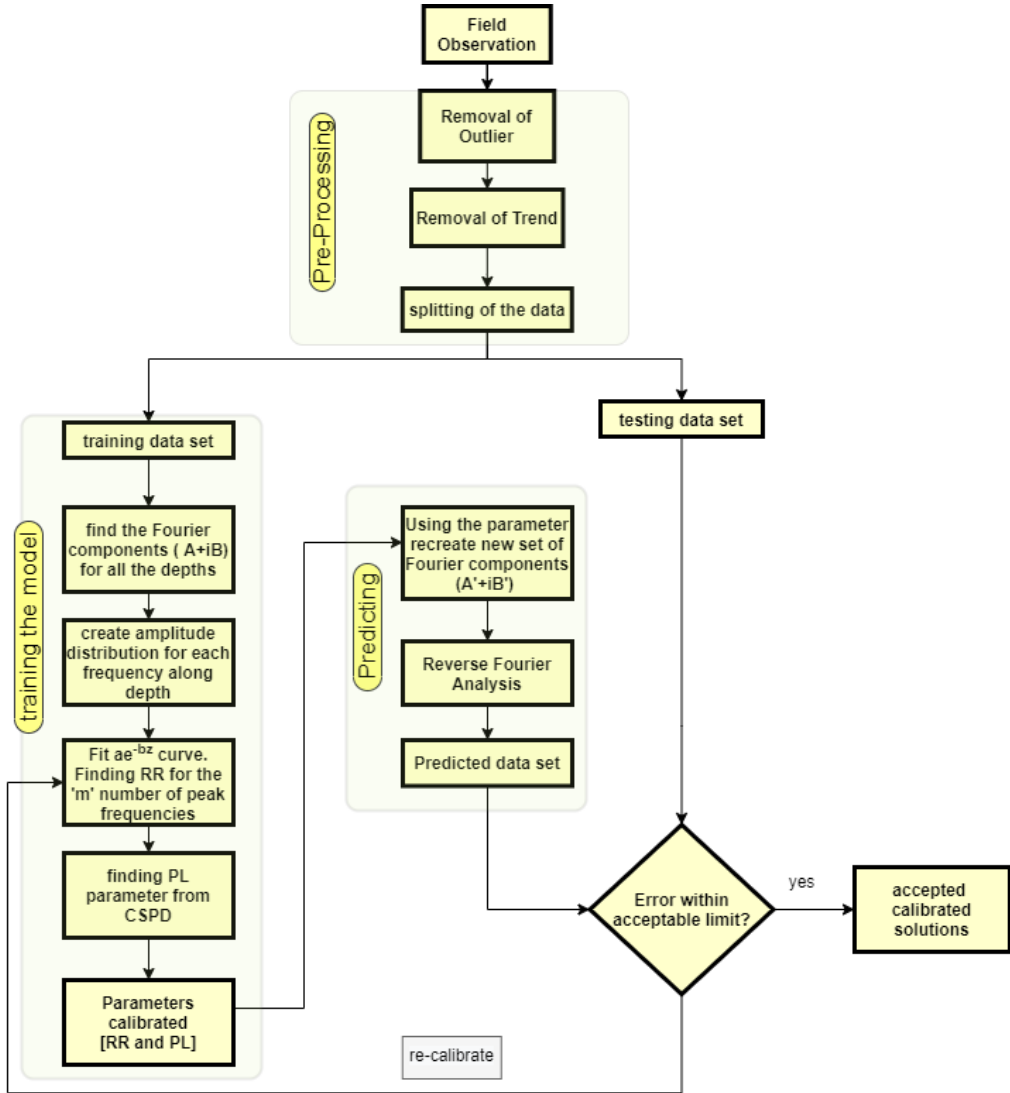


Figure 3.23: The workflow of the data-driven temperature model of permafrost. image source: [Islam et al. \(2021\)](#).

CHAPTER 4

Field Measurements

Field investigation of one of the Arctic coasts at Baydaratskya Bay, Kara Sea, Russia, is being conducted each year at the end of the summer. The project Centre for Research-based Innovation (CRI): Sustainable Arctic Marine and Coastal Technology ([SAMCoT](#)) surveyed the coast from the year 2012. Under this project, Lomonosov Moscow State University (MSU) investigates the coasts and conducts site visits in collaboration with the Norwegian University of Science and Technology (NTNU). The observations, lab tests, in-situ tests and reports form the basis for this study. The author participated in the field investigation from 26 October-12 September 2019.

4.1 Location of the study area

The location of the study area is shown in Figure [4.1](#). The study area is an Arctic coast in the Kara Sea, Russia. The coast is situated between two peninsulas, Yamal and Yugra. The coastline is straight and creates a 72° angle with the line of North (Figure [4.1c](#)).

The study area is not densely populated; only a few indigenous settlements are found. The infrastructures are very limited and minimal access is possible due to the harsh climate and lack of communication facilities. The Nord Stream gas line was constructed near the study area in 2011, after which the importance of studying the coasts increased ([Ogorodov et al. 2013](#)).



Figure 4.1: [a] The study location is situated in the Kara Sea. [image source: Google Earth]. [b] The sea is shallow and funnel-shaped, which makes it susceptible to storm surges [image source: navionics.com]. [c] The study area has a straight coasts (68.853096° N, 66.891730° E).

4.2 Geomorphological description

The study area is mostly made with Pleistocene marine and glacial sediments. However, some alluvial patches, lacustrine and deposits of boggy materials are found. The area is believed to be modified by the Pleistocene ice sheets, unlike the eastern Russian coasts (Ogorodov et al. 2020). Massive ice beds are present in the study area. Visible ice-wedge

polygons are formed along the cliffs of the beaches and contribute to the large collapses of blocks by thermoabrasion (Ogorodov et al. 2020). The depression formed by the ice glaciers during the Pleistocene era developed the shallow gulf and during the Holocene period, the area was submerged (Isaev et al. 2019a). The permafrost underneath the active layer is mostly continuous and reaches 30-70 meters in thickness (Isaev et al. 2017). The study area is around 6 km NW of the river system of Oyu-Yakha. The gasoline pipe of Bovanenkovo-Uhta that transports gas to Europe passes the study area 0.1 km in the southeast direction (Isaev et al. 2019a). The total length of the study area is 8 km. Ngouyaha river divides the study area into two almost equal parts (Isaev et al. 2017).

The Baydaratskaya bay is a depression along the coast of the Kara sea, among others found along the Kara sea. A zone of active faults on the west side bounds the bay. The clay and bottom mud found in the deeper part of the bay are well-sorted-fine sands along the Ural shoreface and silty sand along the Yamal coast.

The severe climatic condition created a thick layer of low-temperature permafrost during the Pleistocene and Holocene era. The recent warming of the atmosphere has started to affect the permafrost. Below the depth of 100m and more, the ground is supercooled without the phase changes of the water. Depending on the water depth, the annual ground temperature at the bottom varies from 0.1 to 1.2. Seabed permafrost exists to a depth of 25m (Romanovsky and Osterkamp 1997).

During the Holocene, the coastline faces a dramatic change. Almost 30m of vertical movement of the shoreline changes occurred and the sea level moved up to present conditions. It was a combined effect of the global progression of sea level at the end of the ice age (Isaev et al. 2019a) and the coast is built with fine-grained perennially frozen sediment.

4.2.1. Description of the beach

The beach consists of coarser sediments; some consolidated clays may also be present. The sediment distribution of the study area is provided in Table 4.2. D_{90} and D_{50} of the sediments on the beach are 0.82mm and 0.31mm. The width of the beach is narrow. The width varies from 10-25m during high tide to 50-50m m in low tide (Isaev et al. 2017). A frozen bluff stands at the end of the beach. The study area is divided into two distinct zones, marked S#1 and S#2. The low marine terrace with bluff heights around 4-6m is termed zone S#1. Zone S#2 has bluff heights of 12-17m. In total, 11 cross sections are measured (see Figure 4.2).

The presence of coarse sediments on the beach, while the bluffs consist of mostly clay, indicates the eroded and collapsed deposits from the bluff are more sorted, the coarser

particles form the stable beach zone and while clay particles are carried by seawater to the deeper sea. The main direction of the sediment/mass transport is along the bluff in the NW-SE direction (Belova et al. 2016). The elevation of the beach is not greater than 3m from the MSL. The beach is submerged during high tides. The same also happens with greater intensity during the storm due to the surge created by the wind blowing over the gulf. The return currents created during tides and storm surges are strong enough to carry the fine sediments away from the base of the bluffs.

The coarser sediments created a layer above the finer sediments on the beach. The coating is thinnest near the base of the cliffs (around 0.1-0.2m deep), and the thickness of the layer increases considerably (to around 1m) near the shoreline. Beneath the sand layer, the clay is similar to the sediments in the cliffs indicating the previous position of the beach was far ahead of the current location.

The S#1 and S#2 sites are located about 3.5 km in N-W direction from the cofferdam of the Bovanenkovo-Uhta gas pipeline. The study area is spread from North West (68.867459, 66.741529) to East South (68.842112, 66.984593). The zone S#1 is a low marine terrace with a length of about 4 km and a bluff height of 4-6 m high, starting directly from the gas pipeline (the most south-eastern point). The bluff surface is smoothly sloping. The S#1 zone has some shallow thermokarst lakes, ice-wedge polygons are visible on the ground surface and erosion trenches are found along the coastline.

The bluff heights of the S#1 gradually lowers and transforms into a laida of 1.5-2 m high with Ngouyaha river valley. The laida shoreline is almost 1.2 km long. The elevation of the laida is such that it never goes underwater during the high tides. But it is flooded by seawater during storm surges created during the summer. This laida consists of depressions with frost-thaw lakes; some of them are drained due to the retreat of the coastline. Lake occupancy on some of the high laida areas exceeds 50%. The lower sections of the laida are followed by the S#2 zone; a more elevated terrace of 10-17m. This S#2 zone is 4.65km along the coastline. The surface of the higher terrace is more frequently cut by deep trenches with dry thermokarst lake basins (hasyrey) and younger thermokarst lakes, polygonal-shaped frost clefts and weathering spots on the sandy soil.

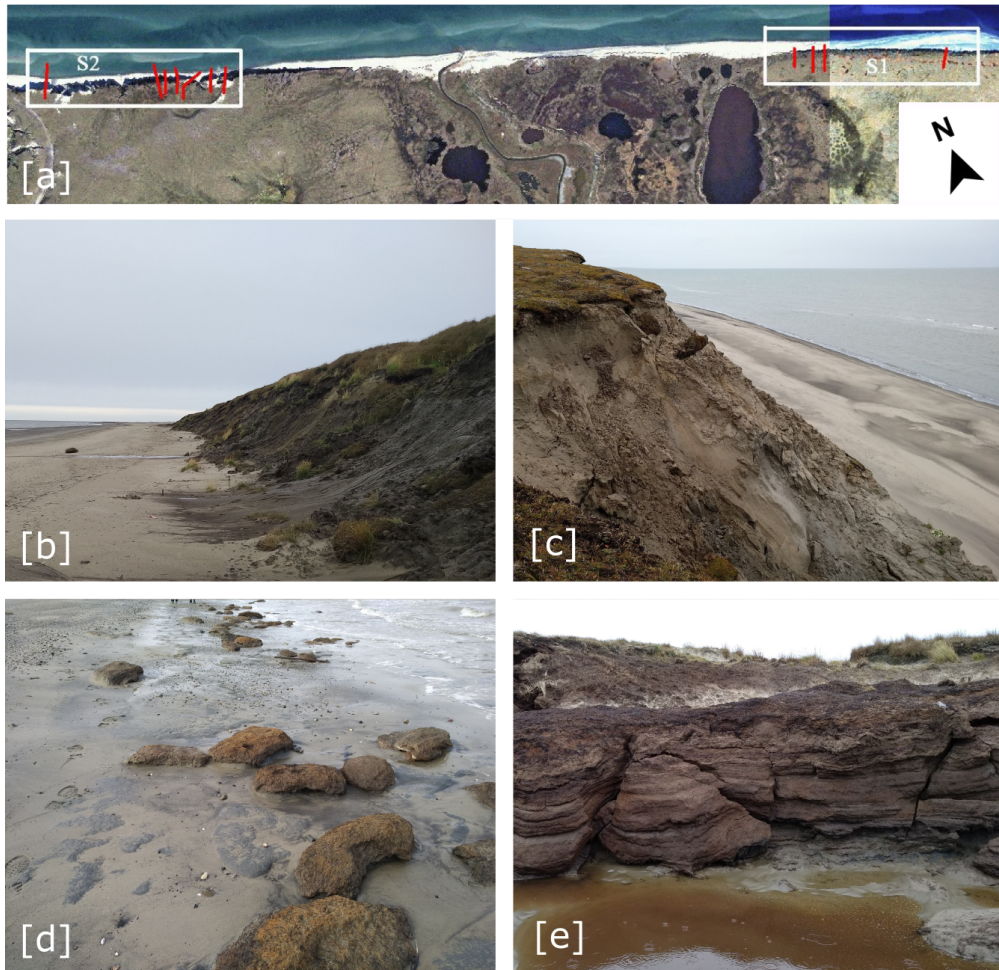


Figure 4.2: [a] Beach profile lines in zone S#1 and zone S#2 (shown in thick red lines) [b] Bluff in zone S#1 and [c] bluff in zone S#2. [d] Remnant of an earlier collapsed bluff. [e] Niches in the bluff face. (image source: (panel (a): [Isaev et al. \(2017\)](#) and panels (b)–(e): author, 2019)

4.2.2. Vegetation condition

The bluff surface is covered with vegetation, while the bluff slope and the beach lack any vegetation in most of the profiles. The height of the plants is around 0.2m (Figure 4.3). Lack of nutrition limits the growth of vegetation. The short duration of ice-free summer, along with the shallow organic active layer, also prohibits relatively larger plants from growing ([Isaev et al. 2016](#)). The study area is located in the subzone of typical moss-shrub and lichen tundras. The general features of the vegetative cover of the study

area are (a) poverty of the species composition; (b) low activity of species, their narrow confinement to redistributed types of habitats and low abundance; (c) stuntedness due to the insignificant thickness of the snow cover; complexity associated with permafrost and microclimatic conditions. The vegetation cover is represented by the following formations: lichen, mohoy, sedge, dwarf shrub and shrub.



Figure 4.3: The study area is covered with low-lying berries and moss during summer.[image source: [Isaev et al. \(2017\)](#)]

4.2.3. Hydrodynamic conditions

The bay cuts deeply into the land and creates a funnel-like shape. Both the west and east part of the bay interact with the waves coming from the Kara sea. During the winter, the sea is covered with sea ice. Open seasons are around 100 days in length ([Isaev et al. 2017](#)).

4.2.3.1. Water flow

The water circulates in the bay under the influence of the tide and wind drift. The water density or gradient currents are also observed. The resulting movements of water from all the forces in the northwest and southwest direction. The maximum speed of the current in the open water season was observed to be 0.85 m/s. During the winter, the current speed drops to 0.11 m/s ([Isaev et al. 2016](#)).

4.2.3.2. Tide

The tidal range of the bay increases in a southward direction. At the west part of the pipeline (study area), the tidal range is 1.1m which decreases to 0.8m at the eastern side of the pipelines. The characteristic of the tide is semi-diurnal. The ebb duration is approximately 20 minutes longer than flood tide ([Pearson et al. 2016](#)).

4.2.3.3. Waves

The 100-year mean return period wave height is 2.9 m at the central deepest part of the bay (Isaev et al. 2016). When the coasts are considered, the height is reduced to 1.1 to 1.2m near a water depth of around 3m. The highest water levels due to joint action of the tides and storm surges are up to 1.5m above the mean sea level.

4.2.3.4. Water temperature

During the ice-free period, the water temperature near the surface remains over zero degree celsius. The maximum temperature observed is 34.46°C during the month of July (20 July 2016). When the ice starts to melt, the freshwater exerted from the ice reduces the salinity of the water near the coast. The salinity drops to 20 to 23ppt at the surface of the water while the water at the deeper part remains at the 30ppt salinity. During the long cold winter, the water temperature under the ice sheet remains close to the freezing point (-1.8°C) and salinity slowly increases, which may reach 34 ppt during the maximum ice thickness.

4.2.3.5. Ice conditions

The Baydaratskaya bay is covered with ice most of the time of the year (around 300 days of the year, there is some snow). During the winter, the land-fast ice reaches around 5km wide on the Ural coast and 15 to 20km at the Yamal side of the bay. In the middle of the bay, we find some drift ice. The thickness of the land-fast ice is around 1.1 to 1.7m. The thickness of sea ice near the Yamal coast is 0.3 to 0.5m more than the Uralian coast. A portion of the ice drifted out of the bay by tidal currents and winds. The drift of the ice is around 5-10 cm/s.

The duration of melting of the ice is around 45 days during the start of the summer. It typically starts to melt at the end of May and the freezing starts again at the beginning of August. The bay becomes totally ice-free, mostly at the end of July. The average period of the ice-free season in the bay is about 65 days, the longest being recorded for 126 days in 1944. During the recorded history, it was not ice-free during the summer only three times; eight times it happened the ice-free duration was more than 85 days, and 4 times it was observed that an ice-free season is less than 45 days (Isaev et al. 2017).

4.3 In-situ measurements

4.3.1. Ground temperature measurements

Various boreholes are constructed in the study area to measure the temperatures (list of the boreholes provided in Table 4.1). Initially, two boreholes were drilled, and temperature sensors were placed during field measurements in June 2013 (bh#4, 6m deep) and June 2014 (bh#6, 3.5m deep). BH#4 borehole was dug in the low terrace (S#1) and bh#6 was on the high terrace (S#2). Boreholes were made using handheld Augers and M_log5W (GeoPrecision GmbH) thermistors were placed inside them. The boreholes are protected by a plastic pipe to avoid internal collapse. The sensors of the thermistors are typically kept 0.3m to 0.5m apart. But near the surface, sensors are placed at 0m and 0.1m to capture the temperature of the surface and just below the vegetation cover (lichen and moss). The position of bh#4 and bh#5 is shown in Figure 4.4.

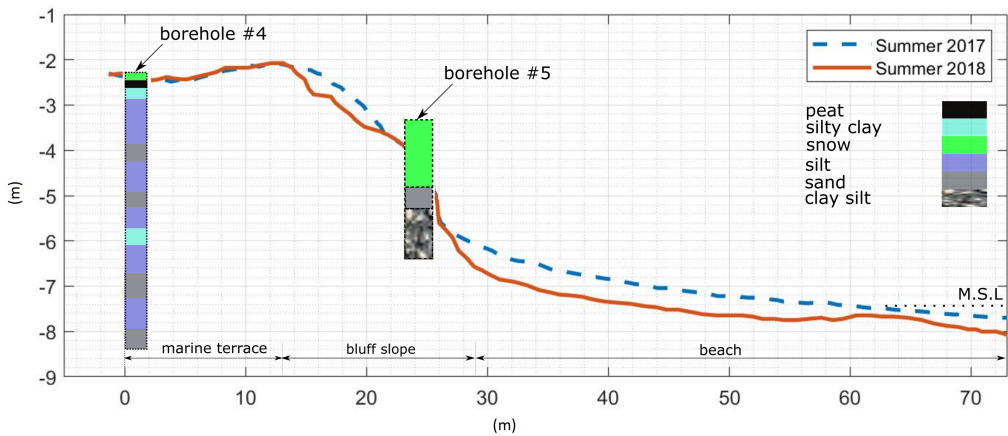


Figure 4.4: Typical cross section at zone S#1 depicting the positions of the boreholes. The boreholes are equipped with thermistor strings to measure the temperature at various levels (Isaev et al. 2017).

The boreholes are 3.3m to 9.9m deep. Due to some technical issues, continuous measurements of temperature were not achieved. The temperature measurements of the bluffs are shown in Figure 4.7 and 4.8 (trumpet curves; monthly). The measurements are collected from the equipment once a year during field investigations.

4.3.2. Sediment size distribution

Samples were collected from the beach to perform a sieve analysis. The results are shown in Table 4.2. The D_{50} of the study area is estimated to be 0.31mm.

4.3.3. Historical air temperature records

Historical temperature data is available from two meteorological stations, Ust Kara station (N 69.25 E 64.93) and Marresale station (N 69.71 E 66.80). Ust Kara station is 88.65 km North-West of the study area and situated on the same coastline. Marresale station is farther up North, 95.82 Km in the north direction from the study area, and situated on the opposite coastline. Historical temperature data is available from the year 1914 at Marresale stations, whereas data from the year 1934 is available for Ust Kara station.

4.3.4. In-situ test of the thermal properties

Thermal properties of the coastal bluff of the study area are shown in Table 4.3 from the in-situ test. The thermal conductivity of the upper layer, which consists of peat, and vegetation decomposition, exhibits a lower conductivity than the non-organic active layer and permafrost. The permafrost in the study area demonstrates a thermal conductivity of 1 to 1.5 $W/m - K$.

Table 4.1: List of boreholes at the study area are shown. The boreholes are placed in the cliffs, both at the high and low marine terraces (Isaev et al. 2017).

zone	Borehole ID	Depth	Coordinates	Drilled on	Remarks
S#1	bh2	9.9 m	N 68.853004 E 66.899996	Sep 2016	On the slope
S#1	bh3	9.9 m	N 68.852599 E 66.899767	Sep 2016	30 m inside the crest
S#1	bh4	6.2 m	N 68.853797 E 66.889794	Jun 2013	Inside the cliffs, discarded
S#1	bh5	9.9 m	N 68.858327 E 66.838207	Sep 2014	5 m above the water level
S#2	bh6	5 m [3.31 m]	N 68.857162 E 66.843057	Jun 2014	15 m above the water level

Table 4.2: The sediment size distribution of the study area (Isaev et al. 2016).

sample ID	sediment size (mm)								remarks
	<0.0002	0.0002-0.001	0.001-0.05	0.05-0.1	0.1-0.25	0.25-0.50	0.50-1.00	1.00-2.00	
sample#1	2.5	10.39	19.46	29.33	38.03	0.28	0.00	0.00	S#1, bluff
sample#2	3.2	12.56	27.93	31.8	24.51	0.0008	0.00	0.00	S#1, bluff
sample#3	11.29	42.65	34.07	8.59	3.33	0.07	0.00	0.00	S#2, bluff
sample#4	0.00	0.22	0.15	0.0003	40.87	58.19	0.57	0.00	S#1, beach
sample#5	0.0002	0.48	0.36	0.0002	33.69	62.09	3.38	0.00	S#1, beach

Table 4.3: Thermal properties of the sediments on the bluffs. The top organic active layer has very low thermal conductivity and thus acts as a blanket hindering the thawing process. Other than the top organic layer, thermal properties vary a little along the depth. data source: (Isaev et al. 2017)

Location	Depth	Soil type	Temp	Thermal conductivity
	m		°C	W/(mK)
Excavation-1 N68.85305 E66.88763	0-0.15	Peat, middle stage of decomposition, dark brown	1.3	0.386
	0-0.20	Layering of sand light-grey, frozen and dark gray light loam, cryoturbation	1.94	0.732
	0.42-0.75	Sand, grey, fine-grained, with layers of ferruginous matter	1.0	1.42
Excavation-2 N68.85361 E66.89361	0.40-0.60	Loam, dark grey, soft plasticity with deep decomposed organics	1.5	1.48
	0.60-0.9	Sand fine grain, light-grey with a vertical band of ferruginous matter	1.15	1.16
	0.9-1.3	Sand fine grain, light-grey with a vertical band of ferruginous matter	0.47	1.39
Excavation-3 N68.85277 E68.87778	0-0.30	Loam dark-grey, soft plasticity with ferruginous matter	3	1.64
	0.30-0.53	Sand light brownish grey, middle grain size, with ferruginous matter layers and inclusions of fine gravel matter	1.4	1.58
	0.61-1.64	sand, light-grey, middle grain size, with horizontal layers of dark sand and vertical bands of ferruginous matter	1.13	1.04

4.3.5. Coastal profiles

The coastal profiles of the study area are surveyed using the Differential Global Positioning System (DGPS). Geo-referencing is completed using handheld DGPS receivers and employing datum to identify the profile in the field. After that, the observations are transferred to the Russian State Geodetic Coordinate System (GSK-2011). Coastal features such as bluffs and shorelines are recorded. Surveying via light detection and ranging (LiDAR) began in 2018. Figure 4.5 shows one profile from each site of S#1 and S#2. The rest of the profiles are shown in Appendix A.2.

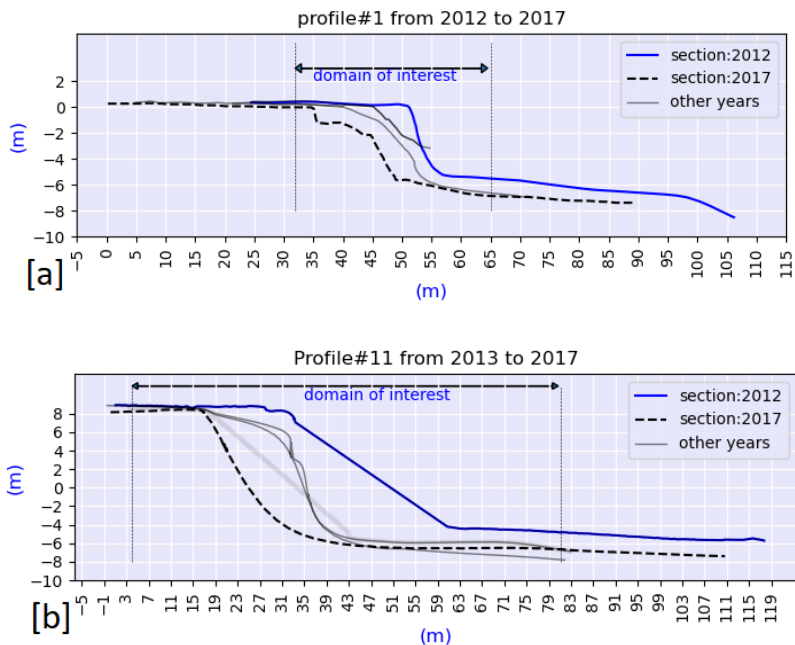


Figure 4.5: Measurements of two coastal profiles in S#1 and S#2 are shown. [a] Measurements of profile P#1 in the zone S#1. [b] Measurement of profile P#11 in zone S#2. The bluff height in this profile is approximately 14m.

4.4 Observation of erosion in the study area

4.4.1. Thawing and slumping

Both thermoabrasion and thermodenudation are active in the study area. During the summer, the thawing is continuous, and slumped materials accumulate on the beach. Two photos of 12 hours apart are shown in Figure 4.6-d. The thawed sediments are accumulated at the base of the bluff and are clearly unconsolidated. During high tides or storms, the sediments will be carried away offshore.

4.4.2. Niche openings

Figure 4.6 depicts the wave-cut niche at the base of the bluff at profile#11. The niche has not reached a critical length; the overhanging bluff is still stable. The vertical position of the niche is higher than that at high tide. It was formed by a storm surge before the observation was made. During observation, no loose sediment was noticed at the base

or inside the niche opening. The return currents must have carried away the sediments when the storm flooded the beach.



Figure 4.6: [a] Status of Profile#11 during the 2015 measurement. The coastal profile#11 is shown as a black line. A wave-cut niche is visible at the base of the bluffs. Image source: (Isaev et al. 2016) [b] Permafrost inside the bluff was excavated during the field investigation in 2015. Image source: (Isaev et al. 2016), [c,d] six-hour time-lapse of thermodenudation in S#1. Niche is visible at the base of the bluffs, but the bluffs are stable. Accumulation of slumped sediments at the base. Image source: Vladislav Isaev. SAMCoT Report, 2015.

4.4.3. Permafrost

The permafrost layer inside the bluffs during summer is shown in Figure 4.6b. The thawed layer above the permafrost is approximately 0.5 to 1 m at the bluff surface. It is clear from the figure that the thawed layer has a considerable thickness at the bluff slope. Since all the thawed layer is not slumped, we can infer that the intensity of the slumping (mass flux) is limited by the slope or stability of the thawed layer rather than thickness. In other words, the observations indicate the thawing rate (dx_t/dt) is clearly higher than the reduction rate (slumping) of the thawed layer (dz/dt).

The following summarises the observations from several years in the study area:

- Thermodenudation at the bluff face may be active, even when sea ice is present and land-fast ice remains at the base of the bluffs. Unlike thermoabrasion, the open water season is not a prerequisite for thermodenudation. Thermoabrasion, however, has some pre-conditioned that must be fulfilled, such as open water, warm seawater and storm surge.
- Thawed sediments from the bluffs fall under gravity and expose the permafrost underneath. The slumped materials are loose and accumulate on the beach. So the thawing depth and slumping influence each other; the two modules can not have an order of precedence, as the two processes are parallel.
- Wave-cut niches are developed at the base of the bluffs, while the bluffs may still be stable. Several storms may elongate the niche depth to a critical depth. Unless the niche depth reaches the critical length, the bluff remains stable.
- Thawed sediments accumulated at the base of the bluffs remain there until an extreme event creates a higher water level and return current.

4.4.3.1. Temperature profiles of the coastal bluffs

The temperature profile of the coastal bluff is shown in Figure 4.7. The monthly average, monthly maximum, and monthly minimum are shown with three lines. After the depth of 0.5m, the temperature variations are quite small.

Figure 4.8 depicts the temperature profiles at zone S#2. The temperature profiles are similar to S#1. But the thawing depth is higher for zone S#2. S#2 consists of bluff heights of 12-17m, and the water table during the summer is found to be quite low. This may result in higher thawing depths.

4.4. OBSERVATION OF EROSION IN THE STUDY AREA

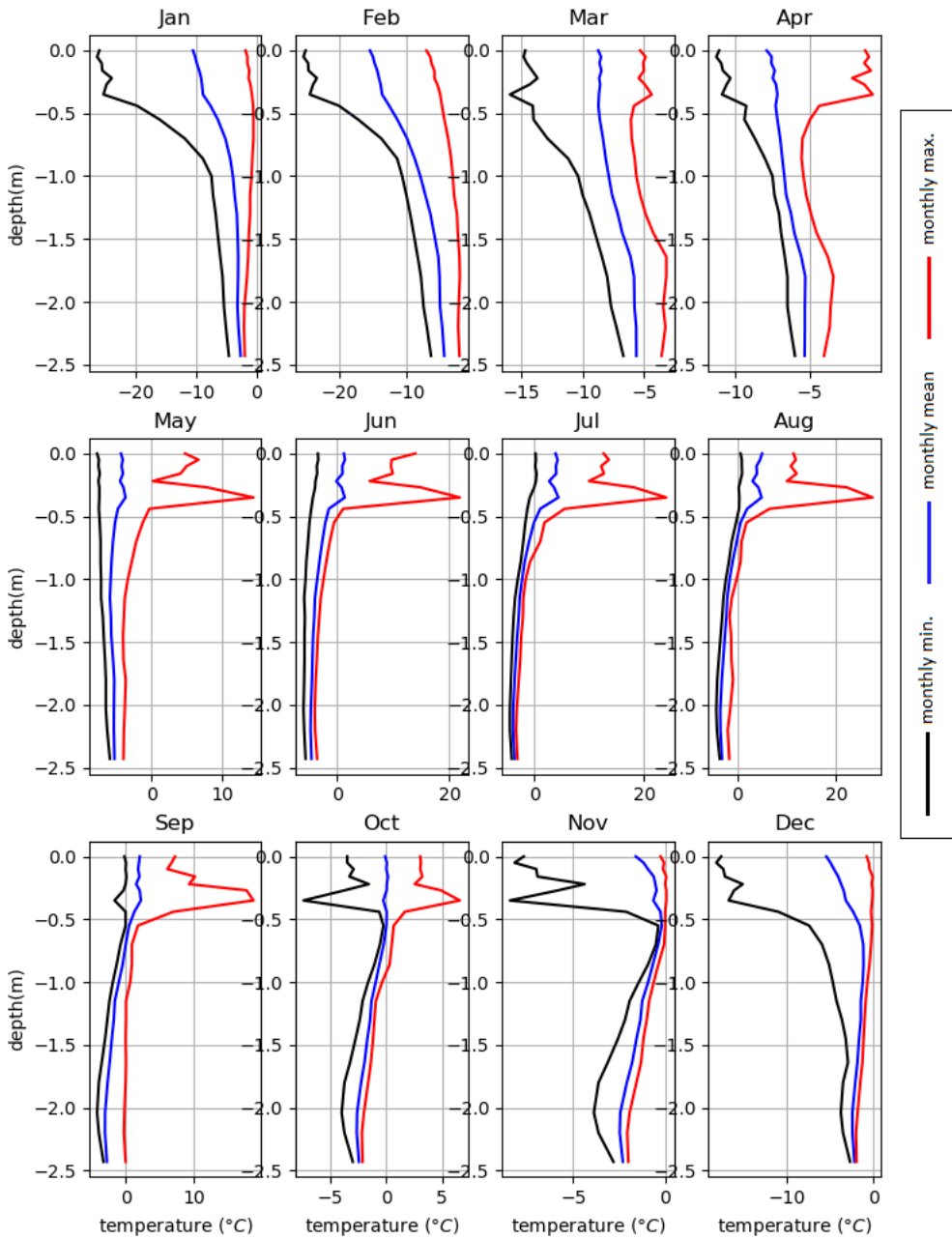


Figure 4.7: The temperature profile of the coastal bluff S#1 until the depth of 2.43m. The monthly mean(blue line), monthly maximum (red line), and monthly minimum (black line) are shown.

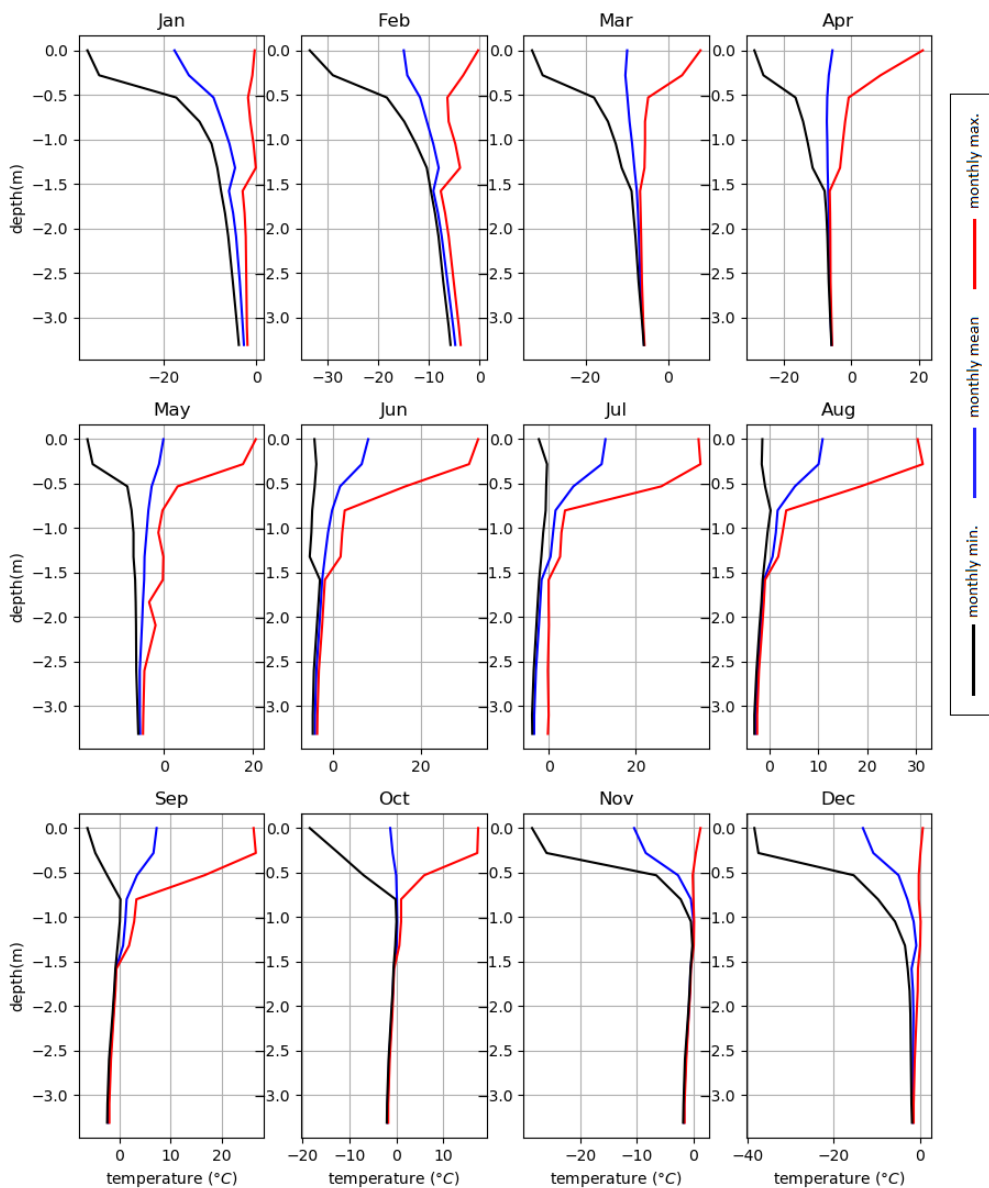


Figure 4.8: The temperature profile of the coastal bluff S#2. The monthly mean (blue line), monthly maximum (red line), and monthly minimum (black line) are shown.

4.5 Environmental forcing

The environmental forcing as input parameters are available from the re-analysis model of the NCEP climate forecast system (Saha et al. 2014). The re-analysis was

obtained from metocean data-portal of Danish Hydraulic Institute (available using the web portal at: v1.metocean-on-demand.com). The input parameters are taken at the point $66.89^{\circ}E, 68.9^{\circ}N$. The time interval between two measurements is three hours.

4.5.1. Solar radiation (short wave)

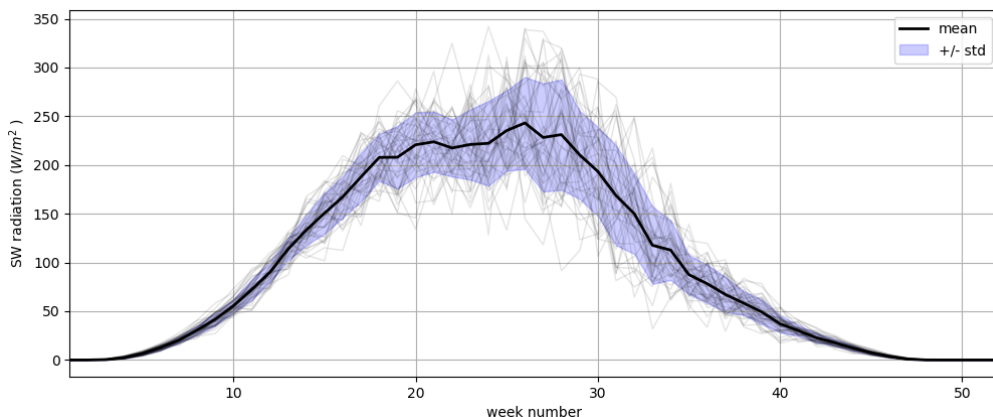


Figure 4.9: SW radiation reaching the bluff surface of the study area. data source: NOAA, (Saha et al. 2014)

The solar radiation reaching the bluff surface as a short wave from 1978 to 2020 is shown in Figure 4.9. The maximum level is close to $350 W/m^2$, whereas the average SW radiation in the warmer climate is close to $4000 W/m^2$. The radiation energy is almost zero to negligible during the months of December to January. Redistribution and absorption of solar radiation and large-scale circulation of the air masses determine the rate of degradation of the permafrost. The annual arrival of total solar radiation in the study area is estimated to be $3,000 MJ/m^2$. Out of the total energy, $800 MJ/m^2$ is coming from direct solar radiation as solar heat. Due to the closure of the sky by clouds, the radiation comes in the form of scatter radiation. Half of the total amount reaches the study area during the months of May-June. Estimated absorbed solar radiation is close to $1,500 MJ/m^2$, and the rest of the energy is reflected in the atmosphere. The average heat fluxes reach close to $250 W/m^2$ in between week#25 to week#30. The cloud cover of the study area is quite high throughout the year. On average, more than 50% of the time, the sky is covered by clouds. During the winter seasons, the clearance is close to 20% only, whereas, during the summer, the clearance increases slightly and reaches close to 40%. The higher standard deviation during the summer than that of winter indicates the variability is higher during the summer.

4.5.2. Historical wind storms

The frequencies and direction of the storms in the study area are shown in Figure 4.10. Storms are defined as at least 12 m/s wind speed sustained for 36 hours. The number of storms is greater in winter (marked with a green dot). Summer storms are smaller in amplitude and lower in frequency.

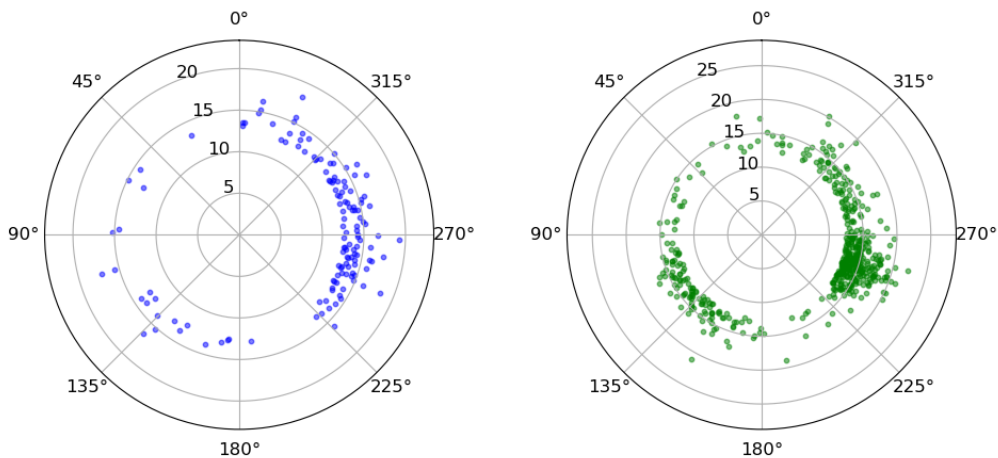


Figure 4.10: Historical storms during summer and winter. The directions are shown as an angle with North. The wind speed is marked on the radius. data source: NOAA, (Saha et al. 2014).

4.5.3. Thawing index

Thawing index (Th_i) is defined as the sum of all the positive average daily temperature days, expressed with the following equation:

$$Th_i = \sum_{i=1}^n \theta \quad (4.1)$$

Where n is the number of summer days where the average daily temperature is more than zero-degree Celsius, θ is the average daily temperature of the n th day. Figure 4.11 depicts the thawing index of the study area. The recent increase in the thawing index is immediately visible. The latest hottest summer is found to be 2016. During the 80s and 90s, the thawing index was around 600-degree days, whereas during 2016 thawing index is estimated to be more than 1500.

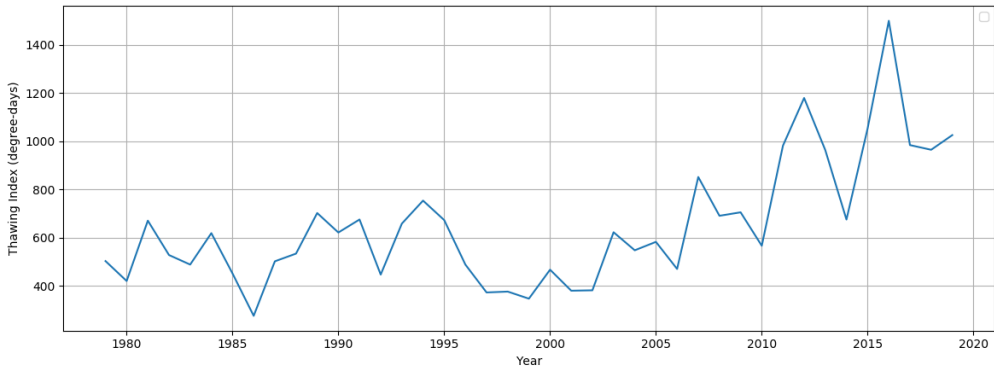


Figure 4.11: Historical thawing index of the study area. The trend shows an increase in the thawing index; compared to the 90s, it increased by almost two folds. data source: NOAA, (Saha et al. 2014)

4.5.4. Wind speed

Winter and summer have different wind conditions. During the winter, the wind speed is observed to be up to 20 to 25 m/s which is far higher than that of summer. Also, the direction of the winter wind is different. In every season, we identified ten to twelve cold storms passing the bay. During the open season, the frequency of cyclones and storm winds is lowered by around 50% (see Figure 4.10). Maximum wind speed during the summer was recorded to be 19.24 m/s (see Table 4.4). The top 75% value for the wind speed during the storm during summer is 14.62 m/s. The mean direction of the wind is 255° with the North which translates to a 3° angle with the shore normal.

During the summer, the wind blows almost vertically to the shoreline. The storms are stronger during the winter season and higher in magnitude. The average number of storms during summer is estimated to be 3.52 (a wind speed of at least 12.5 m/s and duration of 48 hours is considered a storm). In contrast, during the winter, the average number of annual storms reaches 12.83 in number (see Table 3 for details). The maximum number of storms occurred during 1988, 1995 and 1997 in winter ($n=20$). The maximum number of storms during the summer was in 2009 ($n=9$). The average direction is 270° with N, which is 33° with normal shore direction) whereas the winter average direction is 227° which is -25° with the shore-normal direction). The total number of storms during the observation from 1979 to 2019 is 141 in summer and 539 in winter.

4.5. ENVIRONMENTAL FORCING

Table 4.4: Distribution of wind speed during summer and winter. data source: NOAA, (Saha et al. 2014)

		Wind (speed)	Wind (dir)	Air pressure	Air temp	Sea temp
		m/s	degree	KPa	°C	°C
Summer	mean	14.04	255.16	999.26	3.59	3.01
	std	1.35	68.36	9.11	3.30	3.22
	min	12.50	25.64	972.00	0.03	-1.01
	25%	12.93	243.93	993.70	1.23	0.29
	50%	13.76	265.07	999.00	2.95	2.51
	75%	14.62	297.07	1005.80	4.93	4.38
	max	19.24	358.30	1023.80	20.78	21.14
Winter	mean	14.50	226.81	1000.91	-8.58	-8.24
	std	1.75	70.88	13.14	5.68	5.53
	min	12.50	0.90	966.59	-30.62	-28.82
	25%	13.20	175.52	991.93	-12.18	-11.89
	50%	14.10	249.76	1001.30	-7.46	-7.22
	75%	15.21	264.26	1009.44	-4.34	-3.96
	max	22.24	357.28	1040.55	-0.03	3.61

4.5.5. Historical Air temperature

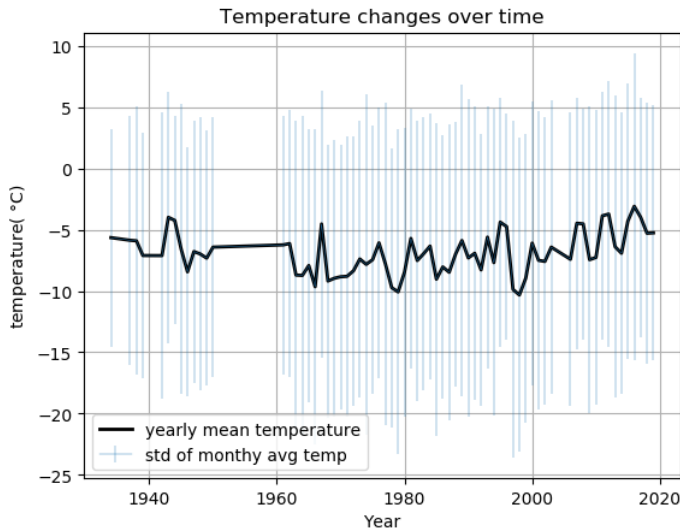


Figure 4.12: Yearly mean temperature values are drawn with the standard deviation of each year (derived from monthly averaged values) (observations missing from 1953 to 1962). data source: field measurements (Kokin et al. 2019) and NOAA, (Saha et al. 2014).

The annual mean temperature was observed in 1934 to be around -8°C , which is increased to now -6.5°C . When we consider the trend-line of the annual temperature, we observe the

annual average calculated from the monthly average temperature is increasing over time, albeit the rate is slow. However, if we consider the coldest month of the year (February) and the warmest month (July), we notice the trend is different. The coldest month demonstrates almost no increase over time; though fluctuation exists, the long-term trend is very stable. We cannot say the same for July. The trend shows the temperature in the month of July is sharply increasing.

The yearly average temperature of the study area is drawn along with the standard deviation of the temperature (Figure 4.12). The standard deviation is increasing over time, indicating the anomalies are increasing steadily.

CHAPTER 5

Result and Discussion

Chapter 3 presented a process-based model for Arctic coastal erosion driven by thermodenudation and thermoabrasion combined and including nearshore morphodynamics. In addition, for the data-poor environment, a probabilistic approach to handle the uncertainties related to the input parameters was demonstrated. Further, a data-driven model of permafrost temperature was introduced. The models were calibrated and validated using the field measurements described in Chapter 4. This chapter presents the calibration and validation, together with results and findings from various model sensitivity analyses.

5.1 Process-based model for Arctic coastal erosion

As discussed earlier, each process of Arctic coastal erosion is represented within the numerical model as a submodule. The mechanism of thermodenudation and thermoabrasion is simulated using a combination of the submodules. These submodules can not be validated as stand-alone models except for the thawing submodule (see section 5.1.2). However, the process-based model, after coupling the submodules, can be calibrated and validated using the yearly measurements of coastal profiles. The model must simulate at least one year of erosion to use the measurement properly. With several iterations during the calibration, a combination of input parameters of the submodules can be obtained. The parameters are chosen in a way so that the outcome of the model matches as closely as possible to three indicators: (a) crest retreat, (b) erosion volume per width (volume per metre along the crest line) and (c) changes in the bluff slope.

5.1.1. Methodology of calibration and validation

The deviation of the simulation results of the numerical models from the observations is measured using the following error formulas:

5.1.1.1. Standard Error of Estimates (SEE)

The standard error of estimate (SEE) (Eq. 5.1) measured the mean deviation between the simulated and measured values.

$$SEE = \sqrt{\frac{\sum_{t=1}^N [o(t) - \hat{o}(t)]^2}{N - 2}} \quad (5.1)$$

where, N is the number of the samples, $\hat{o}(t)$ is the observed N values, $o(t)$ is the value by simulation.

5.1.1.2. Coefficient of determination

The coefficient of determination (R^2) indicates the part of the variance in the dependent variable, which we can estimate from the independent variables. However, the value of R^2 does not indicate whether an appropriate regression is used.

$$R^2 = 1 - \frac{\sum (o_i(t) - P_i(t))^2}{\sum (o_i(t) - \bar{o})^2} \quad (5.2)$$

where o_i is the i th observation, P is the prediction of the statistical model and \bar{o} is the average of the observation.

5.1.1.3. Root Mean Square Error (RMSE)

The root mean square error (RMSE) is used to estimate the deviation from the measurement. The following formula is used to determine RMSE:

$$RMSE = \sqrt{\frac{\sum_{i=1}^N (o_i - \hat{s}_i)^2}{N}} \quad (5.3)$$

where RMSE is the root mean squared error, i is the variable, N is the number of grid points of simulation and observation, o is the observed value at the grid point and \hat{s} is the simulated value at the grid point.

5.1.1.4. Upper and lower limit determined by field observations

For some parameters where field measurement is not available, an upper and lower limit is established from either field observations or a theoretical understanding of a similar case. For example, the upper and lower limit of the parameter water level (wl) is estimated from the observations (a) the water in the calm weather does not reach the base of the bluffs (upper limit) and (b) the width of the beach is 40 to 60m (lower limit). The coefficient of convective heat transfer is estimated to be at least $25W/m^2 - k$ using the idealised case of airflow over a flat plate.

5.1.2. Calibration and validation of thawing submodule using in situ temperature measurements

Temperature measurement inside the bluffs is obtained by digging boreholes and placing thermistors inside the borehole. A short description of the boreholes and temperature measurements is provided in section 4.3.1 on page 65. In this section, calibration and validation of the thawing submodule using temperature measurement from borehole bh#4 are presented. Assuming the temperature curve crosses the zero-degree line at the melting face and a linear temperature profile between the two measuring points, a time series of thawing depth is calculated.

Two measurements of nodes at points A and B at a particular time are such that $T_A > 0$ and $T_B < 0$ (see Figure 5.1). A linear temperature profile is assumed between the two points which crossed the zero-degree line at a depth x from point A. Using the proportional properties, x is calculated by following:

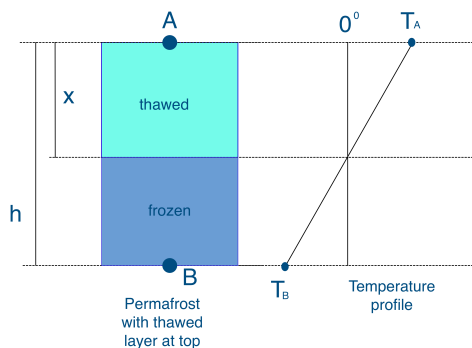


Figure 5.1: Assuming a linear temperature profile between the two nodes, the thawing depth is calculated.

$$x = \frac{h}{T_A - T_B} T_A \quad (5.4)$$

where T_A and T_B are two consecutive measurement such that $T_A > 0$ and $T_B < 0$, h is distance between the two points and x is the thawing depth from point A. The thawing depth, x_t measured from the surface and thus adjusted accordingly.

Temperature measurement from bh#4 is used to estimate the thawing depth of zone S#1. The thawing depth of summer, 2017 is shown in Figure 5.2.

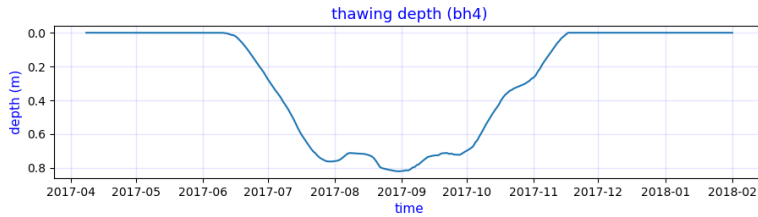


Figure 5.2: The thawing depth calculated from the permafrost temperature measurement of bh#4.

From the figure, we notice thawing depth sharply increases at the beginning of summer. The maximum depth reaches around 0.8m and after September, freezing started.

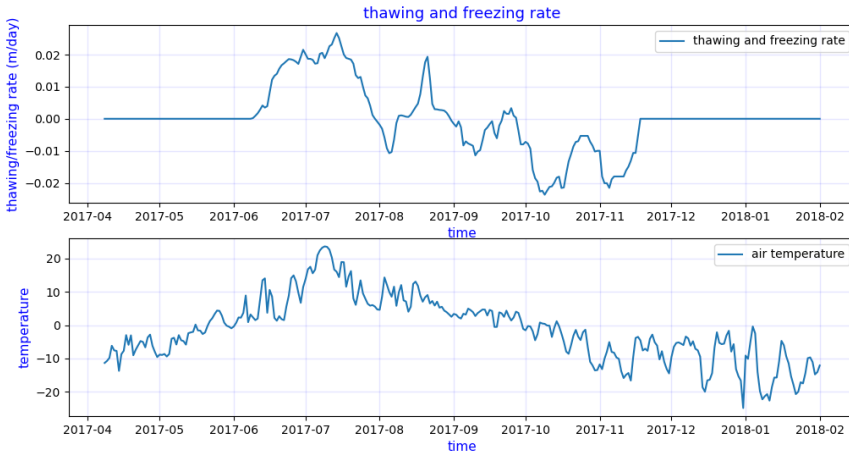


Figure 5.3: The thawing and freezing rate.

The air temperature and thawing rate are shown in Figure 5.3. The air temperature has almost no phase-lag with the thawing rate. The maximum air temperature and highest

thawing rate almost coincide. The freezing rate is almost the same as the thawing rate (2cm per day).

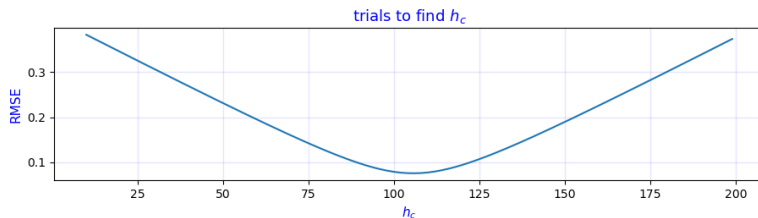


Figure 5.4: Iteration seeking the optimum value of h_c (Islam and Lubbad 2022).

Using the thawing module, the thawing depth (x_t) can be calculated from the environmental forcing. The field measurement is then compared with the simulated value and RMSE error is determined. Many iterations are performed to seek the optimum h_c value that results in the lowest RMSE. The result of the iterations is shown in Figure 5.4. It is clear from the figure that an optimum value of h_c can be found, which leads to the lowest error. For the zone S#1 it is $106W/m^2 - K$. The simulation by thawing the submodule using $h_c = 106$ is shown in Figure 5.5.

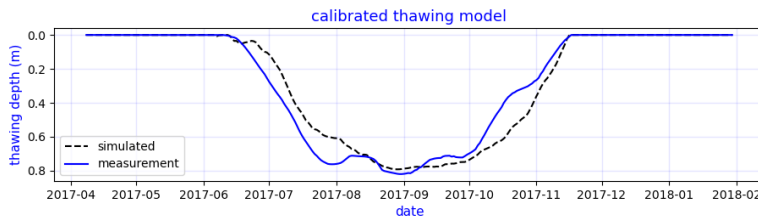


Figure 5.5: The thawing depth obtained using Eq.5.4 from the measurements of permafrost temperature; compared with the simulation. The module estimated the maximum thawing depth close to the measurements. However, the thawing and freezing rates are not matching perfectly with the measured values.

Keeping the parameters unchanged, the model is applied to the measurements of summer, 2014 as shown in Figure 5.6. The maximum thawing depth is quite accurately simulated. However, the numerical model simulates a shorter duration of thawing. The thawing process is being simulated with a time lag and the numerical model also simulated faster freezing.

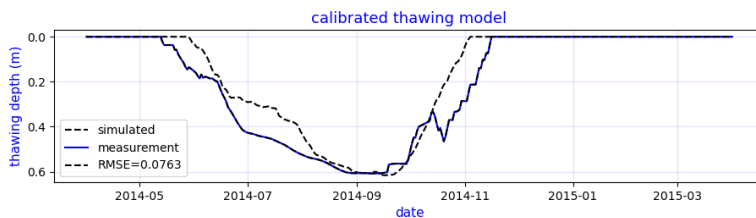


Figure 5.6: Application of the thawing module to another set of measurements for a different year is shown here. The model predicts the maximum thawing depth with good precision.

5.1.2.1. Discussion

The following comments are made on the thawing submodule:

- The numerical model simulates slower thawing but faster freezing. This indicates the simplification imposed by the assumptions has consequences.
- The numerical model is optimised to capture the lowest RMSE which almost accurately captures the highest thawing depth. However, the small undulation in the middle of summer is loosely captured by the numerical model.
- The minimum RMSE attained after optimisation and calibration was 0.1m which is almost 12% of the maximum thawing depth.

5.1.3. Calibration of the input parameters by iterations

5.1.3.1. Calibration of water level

The water level (wl) at the offshore and nearshore boundary (outermost boundary of XBeach) is updated at every timestep. Mean sea level (wl) is estimated by superimposing water level changes due to tide (h_t) and storm surge (η) on the mean sea level (h_m), expressed by the following equation:

$$wl(t) = h_t(t) + \eta(t) + h_m \quad (5.5)$$

where h_m is the mean sea level, which is constant during the simulation (not a function of time), h_t denotes tidal water-level changes at three-hour intervals (interpolated from the measurement), and η is the storm surge level estimated at three-hour intervals by the

storm surge submodule. The model is calibrated by altering the value of wl of Eq. 5.5; the values of h_t and η are not subject to calibration. We use the initial value for wl from the field measurements during the calm summer days.

The parameter wl has upper and lower limits; the constraints are imposed from field observations: (1) the water level does not touch the base of the bluffs during high tide on a calm day (upper limit of wl), and (2) the length of the beach from the base of bluffs to the swash zone varies from 40 to 70 metres (lower limit of wl).

5.1.3.2. Calibration of convective heat transfer coefficients

In section 5.1.2, we calibrated the h_{c_a} for the bluff surface. The remaining three other values are calibrated using trials and errors to match the total erosion volume.

For the wet portion of the coastal profile, the initial value of h_{c_w} is determined from the following formula Kobayashi et al. (1999):

$$h_{c_w} = \frac{a f_w C_w U_w}{1 + F \sqrt{0.5 f_w}} \quad (5.6)$$

where a is the empirical parameter equal to 0.5, f_w is the wave friction factor, C_w is the volumetric heat capacity of seawater, U_w is the fluid velocity and F is the parameter depending on the turbulence and Prandtl number. Kobayashi et al. (1999) estimated the value of h_c within the range of 500 to 800 W/m^2-k . After several iterations, we reach $h_{c_w} = 700W/m^2 - k$ for our cases.

For the h_{c_a} of air of bluff slope and dry portion of the beach, the initial value of iteration is determined by using the equation for the forced convection of a turbulent flow over a flat plate:

$$N_u = \frac{h_c \cdot L}{k_f} = 0.037 Re^{0.8} Pr^{1/3} \quad (5.7)$$

where N_u is the Nusselt number, k_f is the thermal conductivity of the fluid, L is the characteristic length, Re is the Reynolds number, and Pr is the Prandtl number. Using $Pr=0.71$ for air, we estimate the initial value of h_{c_a} to be approximately 25 $W/m^2 - k$.

5.1.3.3. Calibration of the critical slope (m_{cr})

The slumping process simulated within the numerical model is controlled and triggered using one single parameter, the critical slope (m_{cr}) of Eq. 3.9. The calibration is achieved by running the model with various values of m_{cr} within an acceptable range and then selecting the m_{cr} value that yields the closest estimate of total erosion volume and the profile shape.

We estimated initial values for the trials from field measurements of the coastal profiles. The bluff height and bluff slope of 30 measurements are shown in Figure 5.7. These measurements were taken between 2012 and 2017 on several profiles of S#1 and S#2. The slope of the profiles varies from 0.1 to 1.1. A distinct difference is visible between the bluff slopes of zones S#1 and S#2. The coastal profiles are measured at the end of the summer when the thermodenudation is almost complete. We infer that the slopes of the bluff faces are near-stable slopes, and thus, the critical slope should be more than these measured slopes. We also note that the profiles at S#2 have a greater bluff height and steeper slope. We used a lower limit of Figure 5.7 for 0.2 and 0.4 for the S#1 and S#2, respectively. The upper limit was set at 0.45 and 0.8 for S#1 and S#2.

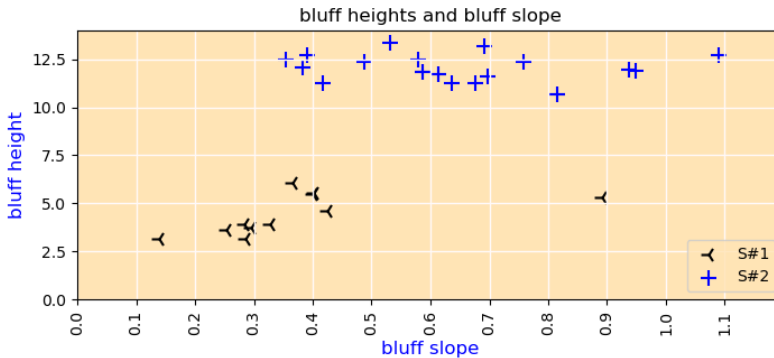


Figure 5.7: Relation between the bluff height and bluff slope in the study area (Islam and Lubbad 2022).

5.1.3.4. A summary of the calibrated parameters

The model is applied to field measurements of coastal profiles with environmental forcing. The input parameters are calibrated to match the simulation outcome to the three targets: net erosion volume, crest retreat and bluff slope as closely as possible. The combination of the input parameters for which the simulation demonstrated lowest deviation is taken as calibrated parameters. A summary of the calibrated values of the parameters is shown in Table 5.1. In the upcoming sections, we discuss the results of the calibration and application of the model.

Table 5.1: Summary of the calibrated parameters.

parameter	zone	symbol	calibrated value	unit	remarks
convective heat transfer coefficient (air)	S#1 & S#2	$h_{c_a;surface}$	90	$W/m^2 - k$	for bluff surface
	S#1 & S#2	$h_{c_a;face}$	98	$W/m^2 - k$	for bluff slope
	S#1 & S#2	$h_{c_a;beach}$	120	$W/m^2 - k$	for beach
convective heat transfer coefficient (water)	S#1 & S#2	$h_{c,w}$	700	$W/m^2 - k$	for seabed
Tensile strength of ice	S#1 & S#2	c_{ice}	1×10^4	N/m	
Tensile strength of permafrost	S#1 & S#2	c_p	1.2×10^5	N/m	
critical slope (dry)	S#1	$m_{cr;a}$	0.35	-	
	S#2	$m_{cr;a}$	0.5	-	
critical slope (wet)	S#1 & S#2	$m_{cr;w}$	0.2	-	
mean water level	S#1 & S#2	h_m	-7.7	m	Ref:GSK-2011

5.1.4. Results of the simulation

The application of the model is demonstrated in this section using one case, the calibration and validation cases are described in the journal paper attached as Appendix C.3.

5.1.4.1. Defining a case

The erosion measurement using coastal profiles of two consecutive years, named case#1, is shown in Figure 5.8. The coastal profile is in zone S#1 with a bluff height of around 6m. The profile has undergone a net erosion volume of $7.03 \text{ m}^3/\text{m} - \text{width}$. The lower part of the coastal profile gained $3.28 \text{ m}^3/\text{m} - \text{width}$, but overall, the erosion is almost three times higher than accretion. The crest retreat as a result of the erosion is 4.1m. A summary of the case is shown in Table 5.2.

Table 5.2: The summary of the case#1. The net erosion from 2015 to 2016 on profile#1 is $7.03 \text{ m}^3/\text{m} - \text{width}$.

Cases	Zone	Profile	Time		Crest Retreat (m)	Erosion ($\text{m}^3/\text{m} - \text{width}$)	Accretion ($\text{m}^3/\text{m} - \text{width}$)	Net Erosion ($\text{m}^3/\text{m} - \text{width}$)
			From	To				
case#1	S#1	P#1	15-09-2015	14-09-2016	4.1	10.31	3.28	7.03

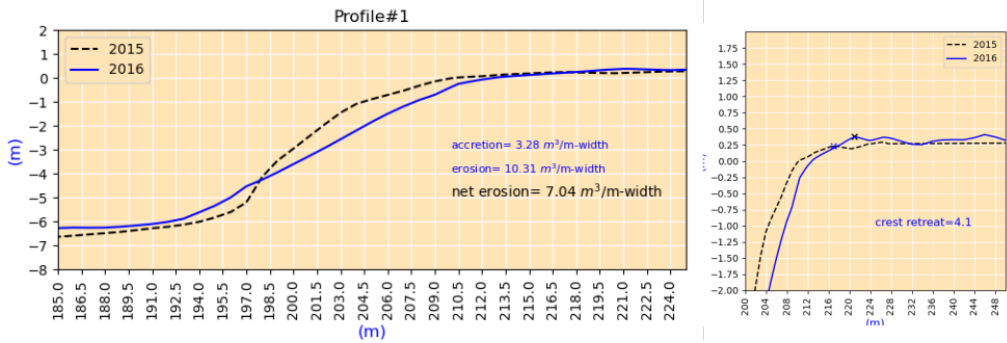


Figure 5.8: Coastal profiles of case#1, two measurements are from 2015 and 2016. Part of the coastal profile is accreted; however, the erosion is greater than accretion. Net erosion is $7.03 \text{ m}^3/\text{m} - \text{width}$.

5.1.4.2. Environmental forcing

In order to run the one-year simulation, environmental parameters to force the model are required. The air temperature, water temperature, significant wave heights (H_{m0} calculated at BC2 by SWAN), and wind speeds from September 2015 to September 2016 are shown in Figure 5.9. The air and sea-surface temperatures show almost no phase lag. The wind speeds are higher during the winter. Storms are defined as wind speeds greater than 10 m/s within a 36-hour window. The air temperature during the summer of 2016 reached 28°C , which presents a significant anomaly. The source of these input parameters is the NOAA reanalysis model (Saha et al. 2014).

The winter and summer conditions are shown with a blue and red line respectively (except for H_{m0} since no wave is considered during winter). Winter started on 28 September and ended on 16 May the following year.

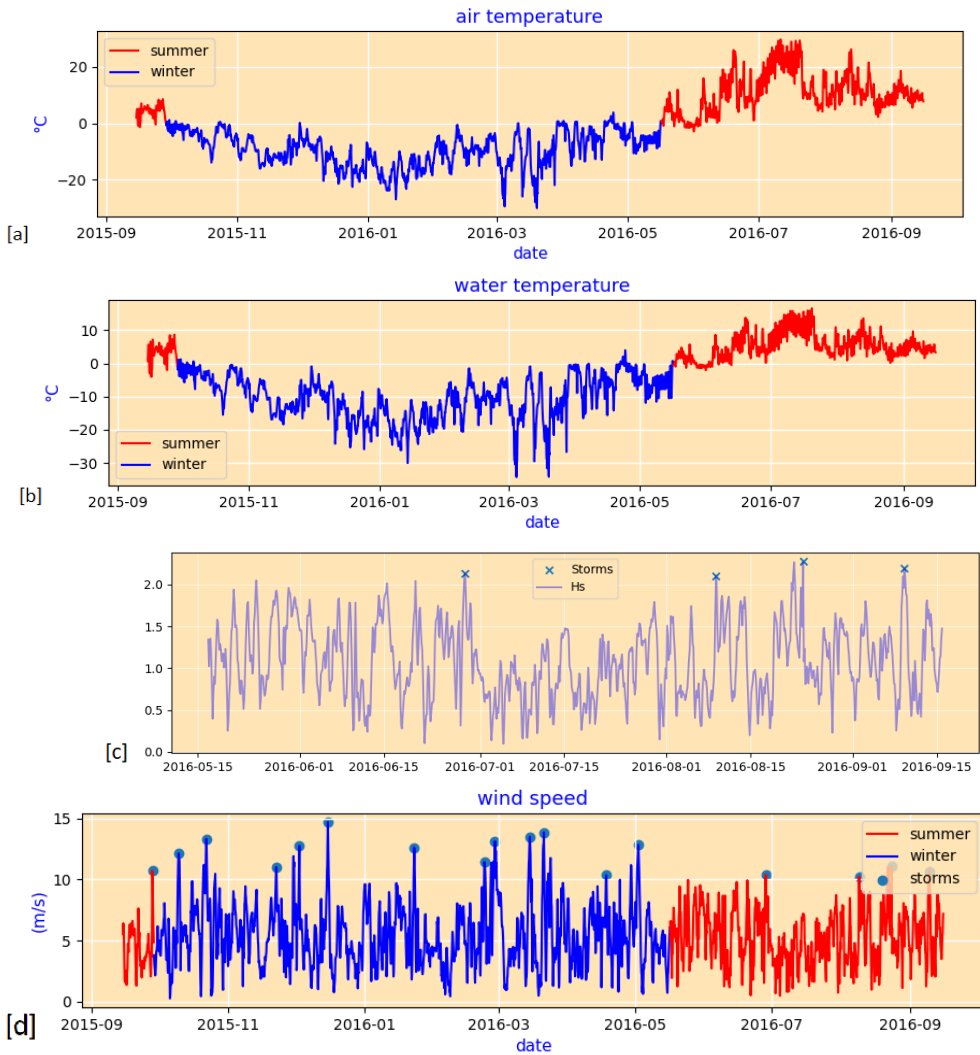


Figure 5.9: The environmental forcing during the calibration cases is shown. [a] The air temperature of the study area is shown; summer with a red line and winter with a blue line. During the summer of 2016, the temperature reached 28°C. The year 2016 was the hottest in recent decades. [b] Sea-surface temperature is shown, summertime with a red line and winter with a blue line. The phase lag between air and sea-surface temperature is minimal. [c] The wave conditions at the BC2 boundary during summer, the input for the XBeach, are shown. The storms are marked with 'x'. [d] Wind speed and storms are shown. Wind speed is higher during the winter.

5.1.4.3. Simulation of thawing depth

The model requires thawing depth as an initial condition. We calibrate the model with 0.4 metres of initial thawing depth. The thawing depth at the bluff surface by the simulation is shown in Figure 5.10. Thawing depth had a small initial increase followed by a sharp decrease due to winter. The numerical model estimates no thawing depth from January until almost the end of May. No erosion is recorded for this period.

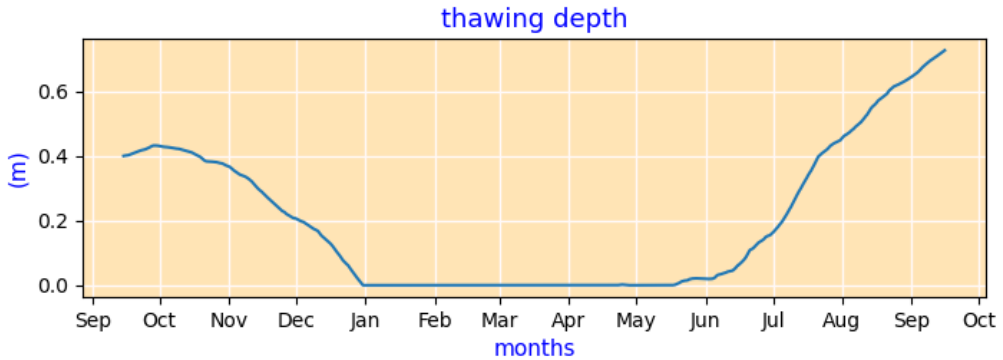


Figure 5.10: The thawing depth at the bluff for case#1.

5.1.4.4. Prediction of the shape of coastal profile

The secondary aim of the calibration is to forecast the shape of the profile at the bluff face and the elevation of the beach. The elevation of the beach is crucial since it affects the inundation depth (h_{id}), which in turn controls the thermoabrasion. The performance of the model for case#1 is shown in Figure 5.11. Before estimating the RMSE value, we 'normalise' the profile around the middle of the bluff slope. Hence, the RMSE values are only related to the shape of the profile, and not associated with the position of the bluff.

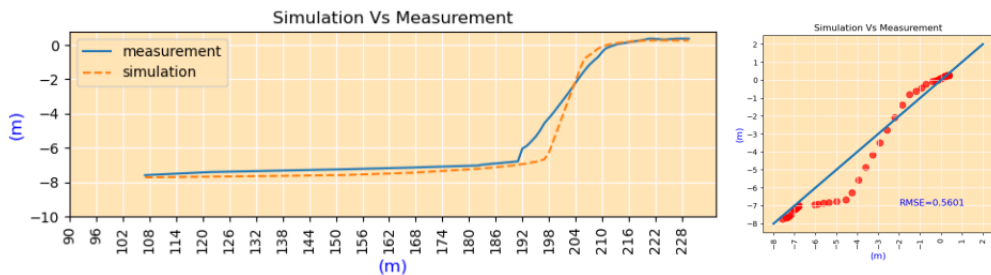


Figure 5.11: Case#1: Prediction of the coastal profile shape after normalising the simulation around the middle of the bluff slope. The RMSE of the prediction is 0.56 m. (Islam and Lubbad 2022)

For case#1, we observe that the simulation predicted a slope slightly steeper than the measurement. The predicted elevation of the beach was close to the measurements, although it overestimated the erosion by sediment transportation. The deviation is highest near the base of the bluff; errors near the beach are negligible. The model overestimates the erosion at the base of the bluffs.

5.1.4.5. Simulation of erosion

The two mechanisms, thermodenudation and thermoabrasion, are active within the numerical model simultaneously. The model attributed almost 76% of the erosion volume to thermoabrasion, which is aligned with the observation by [Are F \(1988\)](#) that thermoabrasion along the Kara Sea coasts is three to four times stronger than thermodenudation. One big collapse, followed by two small collapses, occurred during the middle of the summer of 2016. At the end of the summer, there were some storms, but the water temperature was not high enough to accelerate niche growth. The model over-estimate the erosion volume; the crest retreat was underestimated by almost 5%. Table 5.3 provides a summary of the simulation result.

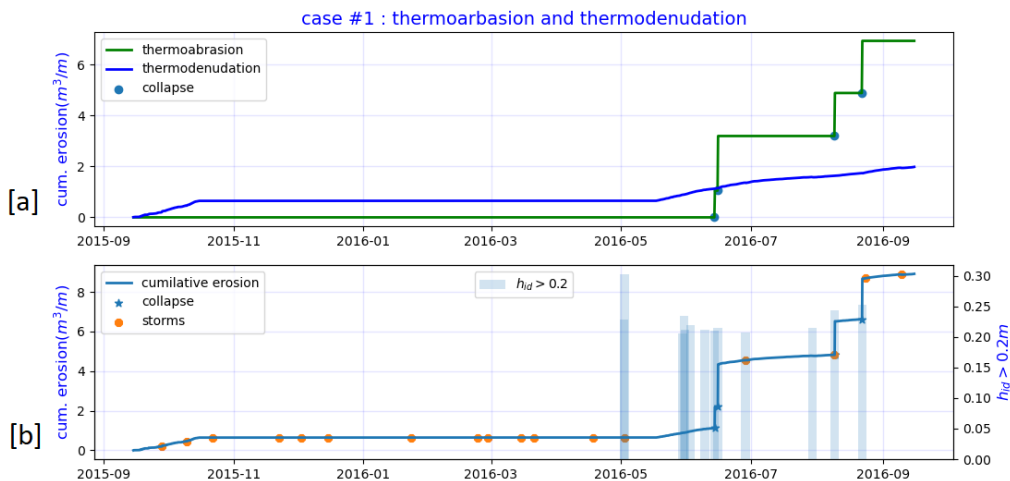


Figure 5.12: Simulation of case#1 is shown. subfigure [a] cumulative thermodenudation and thermoabrasion as time series are shown with collapses. The model attributed 24.22% of erosion volume to thermodenudation and the rest to thermoabrasion. subfigure [b] Net cumulative erosion along with the parameter h_{id} is drawn. The collapses are not aligned with the frequencies of the h_{id} indicating several storms result in a bluff collapse. The collapses did not occur at the beginning of summer or at the end. ([Islam and Lubbad 2022](#))

5.1.4.6. Simulation of crest retreat

The secondary aim of the simulation is to predict the crest retreat of the bluffs. The crest retreat of the Arctic coast is retrogressive, i.e., always retreating as there is no restoration mechanism similar to the dune systems of the sandy beaches in warmer climates. The crest of the bluff is always moving towards the land. The annual crest retreat rate is important for predicting vulnerability and associated risks. For case #1, the crest retreat rates were 4.1m. The model predicts crest retreats of 3.9 m (Figure 5.13).

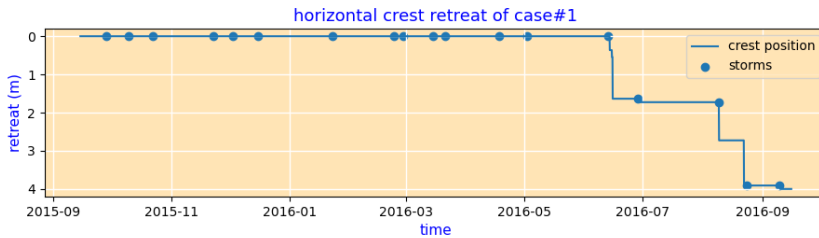


Figure 5.13: The crest retreat as a time series is shown. The crest retreats coincide with the bluff collapses. The sudden drops are due to thermoabrasion, which contributed the most to the retreat. (Islam and Lubbad 2022)

Table 5.3: Summary of the calibration of case#1. (td = thermodenudation and ta = thermoabrasion).

Case	Criteria	Measured	Simulation			Error (%)	
			Volume	(%)	net		
case#1	erosion volume (m^3/m –width)	7.03	td	2.01	24.22%	8.3	17.9%
			ta	6.29	75.78%		
	crest retreat (m)	4.1	-	-	-	3.9	4.8%

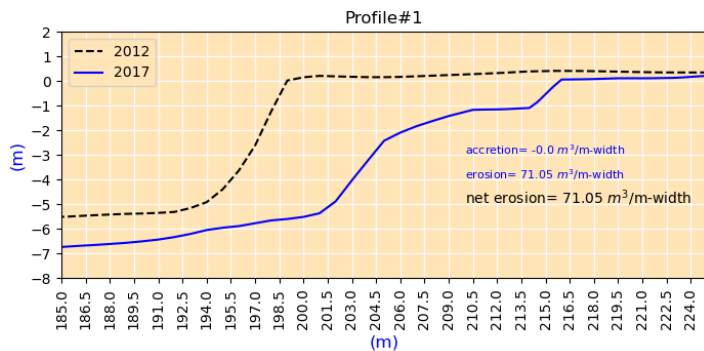
5.1.5. Simulation of long term erosion

5.1.5.1. Defining a case

The application of the model for the long-term erosion simulation is demonstrated by case#L (adopted from case#5 of Appendix C.3). The simulation duration of the case is five years and four months. A summary of the case is shown in Table 5.4. The crest retreat is 16m for the five years and the erosion volume is $71.05 m^3/m$ – width. The changes in the coastal profile are shown in Figure 5.14.

Table 5.4: A summary of the case#L for long term simulation.

Cases	Zone	Profile	Time		Crest Retreat (m)	Erosion (m^3/m -width)	Accretion (m^3/m -width)	Net Erosion (m^3/m -width)
			From	To				
case#L	S#1	P#1	13-06-2012	15-09-2017	16	71.05	0.00	71.05

**Figure 5.14:** Coastal profile changes of case#L. The case is based on profile#1, from 2012 to 2017. The measured erosion volume is $71.05 m^3/m - width$.

5.1.5.2. Result of long term simulation

The erosion pattern of case#L is similar to the other cases. The erosion is dominated by thermoabrasion (70.68%). The thermodenudation rate differs each year. The h_{id} values during the simulation are shown in the secondary y-axis. We observe higher h_{id} values for the earlier years; the highest h_{id} is observed during the summer of 2014. The effect of the higher h_{id} values of 2014 did not translate to many bluff collapses. The bluff collapse by niche growth requires a positive h_{id} value, but the intensity of the erosion does not depend on the frequency and magnitude of the h_{id} values.

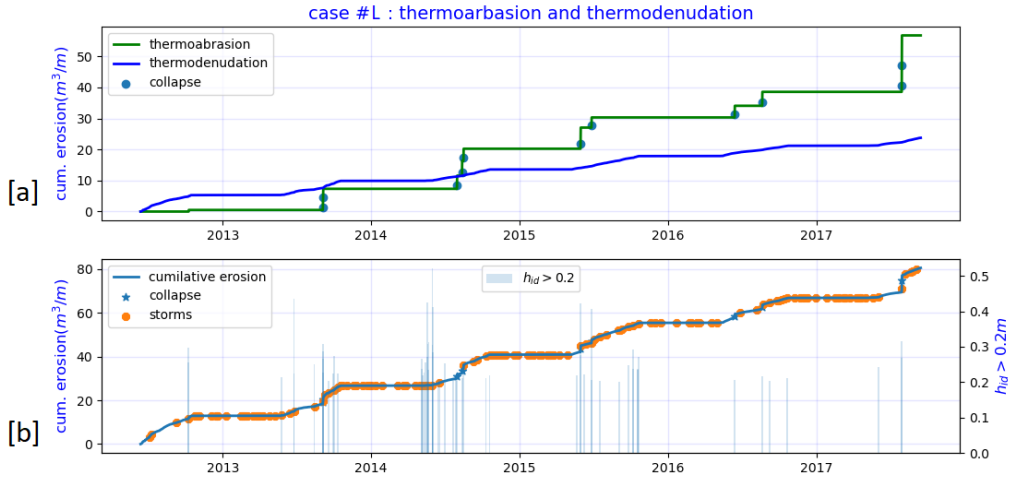


Figure 5.15: Simulation results for case#L. sub-figure [a]: The cumulative thermoabrasion and thermodenudation are shown separately. Thermoabrasion is the dominating mechanism; similar to earlier cases. sub-figure [b]: The combined erosion volume is $80.5 \text{ m}^3/\text{m} - \text{width}$ which is over estimation of measurement. (Islam and Lubbad 2022)

5.1.6. Effect of environmental forcing on long term erosion

5.1.6.1. Air temperature

In Figure 5.16, the air temperature and simulated cumulative erosion are drawn. The upwards zero crossing of the air temperature and the inception of the erosion in the summer have a small phase lag. The erosion rate correlates with air temperature; higher air temperature leads to increased erosion. At the end of the summer, the erosion stops as soon as the air temperature exhibits a downward zero crossing.

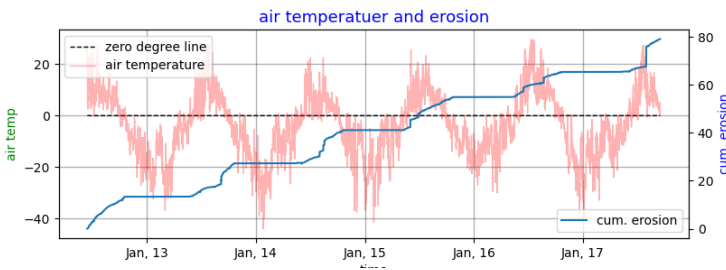


Figure 5.16: Air temperature and cumulative erosion (simulation) (Islam and Lubbad 2022).

5.1.6.2. Thawing index

The thawing index of air is used in many empirical equations concerning the thawing of permafrost and erosion. Figure 5.17 draws the measured cumulative thawing index of case#L juxtaposed with the simulated cumulative erosion. The correlation between the two parameters is very strong even though the thawing index is only one of the environmental forcing parameters of erosion. The cause of the erosion can be partly attributed to the thawing index. We cannot establish a direct causation-relation of the thawing index of air with thermoabrasion; warm air has almost no immediate effect on erosion by thermoabrasion. From the simulation result, we notice that even though erosion is dominated by thermoabrasion, a strong correlation exists between the cumulative thawing index and cumulative erosion.

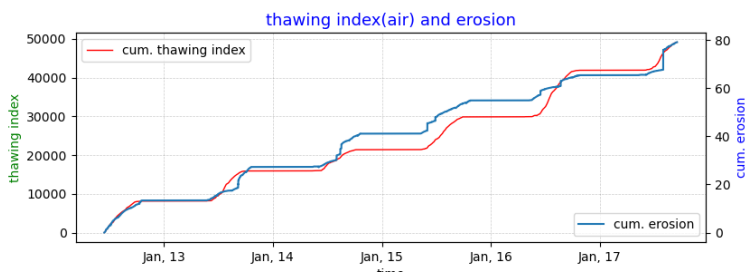


Figure 5.17: Cumulative thawing index and erosion (simulation)(Islam and Lubbad 2022).

5.1.6.3. Wind speed

However, the wind speed and the simulated cumulative erosion of case#L are not correlated (Figure 5.18). The wind speeds are higher during the winter when there is no erosion. The bluff collapses (creating a jump on the cumulative erosion) rarely coincide with the storms of the summer. We can infer that the bluff collapse by thermoabrasion is not dominated by storms in the summer; instead, a combination of various environmental forcing results in bluff failure, justifying the inclusion of hydrodynamic and morphological submodules into the numerical model of Arctic coastal erosion.

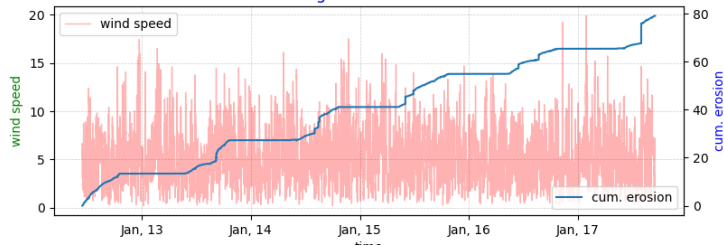


Figure 5.18: Wind speed and cumulative erosion (simulation). (Islam and Lubbad 2022)

5.1.7. Sensitivity of the process-based model

Considering the scarcity of measurements to identify and discern the individual effect of the coastal processes, a sensitivity analysis is undertaken to demonstrate the behaviour of the numerical model and its potential applicability. For this purpose, a base case is defined where the erosion is a combination of thermodenudation and thermoabrasion.

5.1.7.1. Methodology of the sensitivity analysis

Sensitivity analysis is performed on the base case shown in Figure 5.19, and some conclusions are inferred. Two approaches are adopted: (a) turning off a process and comparing it with the base case and (b) amplifying or damping one environmental forcing to observe the deviation from the base case.

The calibrated model is used to simulate the erosion of a hypothetical coastal profile over a period of 31.25 days, from 7 June 2016 to 8 July 2016. Environmental forcing are taken from NOAA reanalysis (Saha et al. 2014). The base case coastal profile has a bluff slope of 0.35 and a height of around 7 m. The base case is developed in such a way that one single mechanism does not dominate; erosion volume due to thermoabrasion and thermodenudation is almost equal.

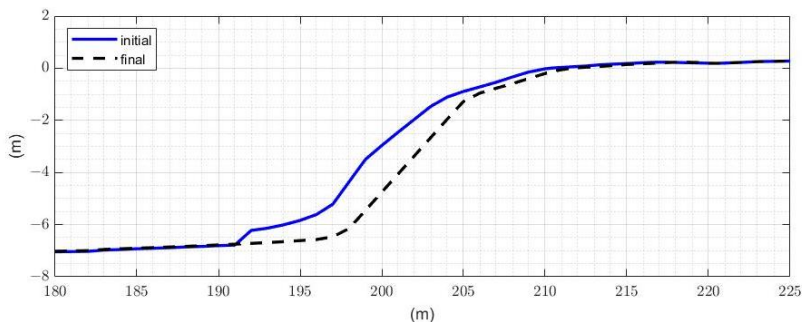


Figure 5.19: Coastal profile of the base case.

5.1.7.2. Defining a base case

The environmental forcing applied to the base case is shown in Figure 5.20. The erosion volume reveals one collapse due to thermoabrasion occurs near the end. Almost no erosion is recorded during the calm period.

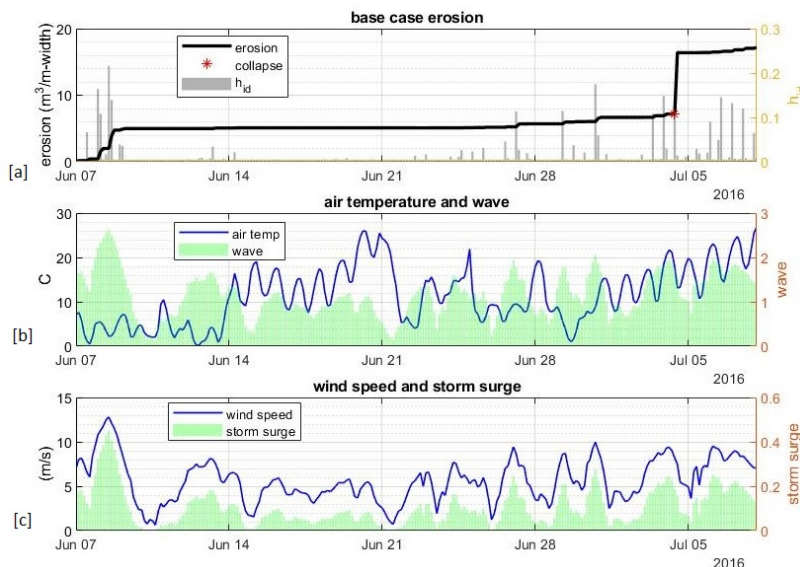


Figure 5.20: The environmental forcing applied to the base case. [a] cumulative erosion over time, [b] air temperature and wave heights (H_s) and [c] wind speed and storm surge.

5.1.7.3. Sensitivity of erosion to waves

The wave is the prominent mechanical driver of both erosion mechanisms. When we turn off the wave inside the XBeach, the h_{id} values become very small to non-existent (Figure 5.21). No sediment transport along the cross-shore is simulated, eventually stopping thermodenudation by stabilising the slope. The model detects almost no erosion as a result. We can infer the following:

- Thermoabrasion is controlled by both mechanical and thermal driving forces; the absence of one of the driving forces can withhold thermoabrasion.
- Mechanically driven forces do not control thermodenudation, i.e., they are not the limiting factor, but nearshore hydrodynamics can influence the rate of thermodenudation.

- Without the presence of waves, no bluff collapse occurs even when the model simulates positive values of h_{id} ; indicating the importance of the combination of thermal and mechanical drivers.

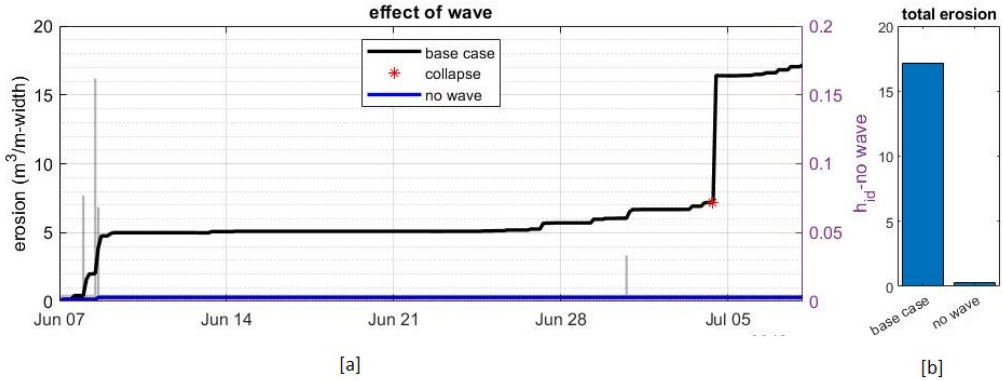


Figure 5.21: The effect of waves on erosion. sub-figure[a]: cumulative erosion as a time series. Cumulative erosion is almost zero when the wave module inside XBeach is turned off. sub-figure[b]: comparison of total erosion.

Figure 5.22 shows the effect of the amplitude of the wave heights (h_{m_0}) at BC2 as an environmental forcing. A 20% increase in the significant wave height increases the cumulative erosion by more than 30% (qualitative assessment) as simulated by the model. The bluff collapses are more frequent and occur earlier in the summer when amplitudes are increased. Thermodenudation also increases as stronger waves enable a faster removal of the thawed materials from the bluff base.

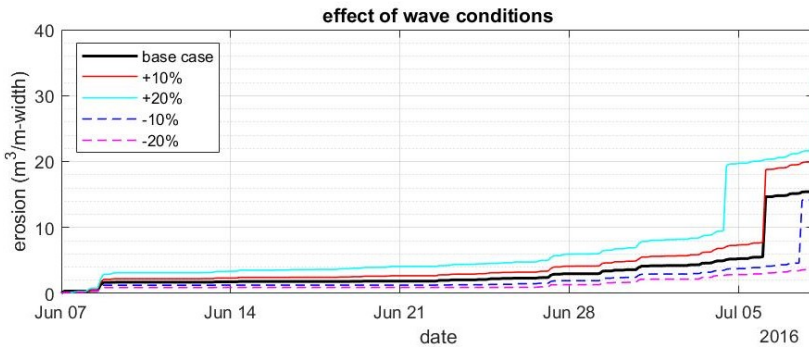


Figure 5.22: The effect of wave inputs on erosion.

5.1.7.4. Sensitivity of erosion to niche growth

When we turn off the niche growth submodule, the model essentially converts to a thermodenudation model ignoring thermoabrasion even when the other submodules of thermoabrasion are active. Figure 5.23 describes the result where erosion is only allowed by removing the sediments from the bluff-base via waves and currents, dominated by thermodenudation. We notice an initial high erosion. The frequent h_{id} values indicate that the erosion is due to waves and currents removing the thawed material from the base of the bluffs and beaches.

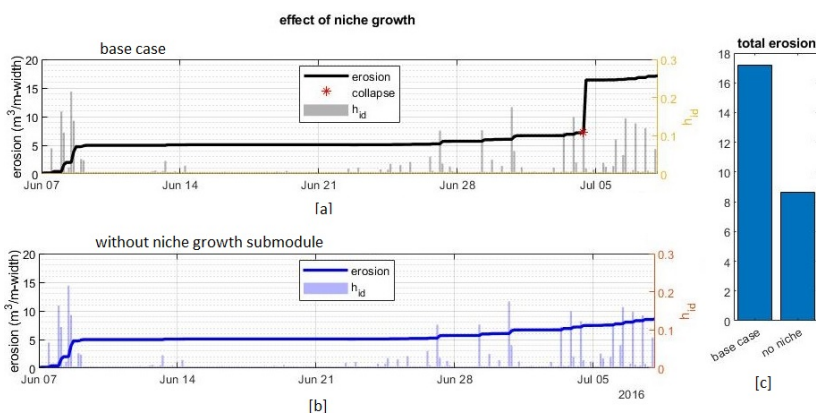


Figure 5.23: Effect of the niche-growing process on erosion. Without niche growth, the bluff collapse can not occur but the sediment transport from the base of the bluff remains active. This leads to higher thermodenudation.

5.1.7.5. Sensitivity of erosion to slumping

The results of turning off the slumping module are shown in Figure 5.24. The model allows the removal of sediments from the beach, but the influx from the slumping module is turned off. The result shows that the erosion initially has a smaller value than the base case. However, the erosion volume increased significantly later in summer with frequent collapses. A comparison of the h_{id} values reveals that higher and more frequent h_{id} are observed for this case, indicating the importance of the influx of sediments by thermodenudation as an erosion-resisting mechanism in the model. The sediment influx from the slumping elevates the base and reduces the probability of thermoabrasion. Thus, two erosion mechanisms are intertwined.

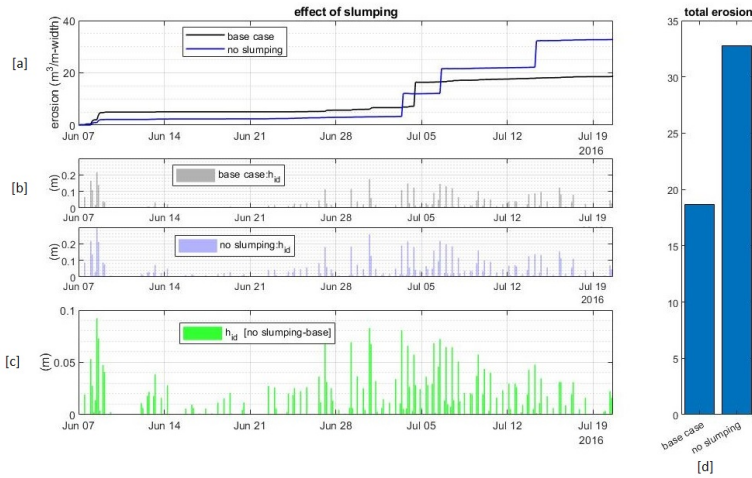


Figure 5.24: Effect of the slumping process on erosion.

5.1.7.6. Sensitivity of erosion to other input parameters

The model's sensitivity to water level, tide, air temperature, water temperature, convective heat transfer coefficients are added as Appendix B.2.

5.1.8. Discussion on process-based model

The salient outcomes of the calibration, validation and sensitivity analysis are summarised as follows:

1. Erosion during the winter is negligible or absent. Barnhart et al. (2014a) concluded in their model that low erosion occurs at the end of summer and beginning of fall for the coast of the Alaskan Beaufort Sea, whereas our numerical model for Baydaratskya Bay in the Kara Sea simulates higher erosion at the middle and end of summer.
2. There is a slight phase lag between the commencement of summer (measured by air temperature) and the beginning of slumping. The air temperature had an upwards zero crossing at the end of May, but thawing began after June.
3. Smaller sudden spikes in air and water temperature at the beginning of summer do not contribute to thermodenudation. The model also does not show any immediate response to the spikes of temperature anomalies. One of the possible explanations for this behaviour is the low thermal conductivity of the permafrost and active layer.

4. Thermodenudation is continuous and of lower intensity, whereas thermoabrasion causes spikes in erosion volume. The limiting factors for thermodenudation and thermoabrasion are, respectively, the latent heat requirement for phase change and water depth at the base of the bluffs (h_{id}).
5. The results of the numerical model suggest that thermoabrasion is a complex process and does not demonstrate a linear relation with the intensity of storms. In other words, the strongest storm does not necessarily lead to a collapse. A bluff collapse by wave-cut niche results from a combination of the nearshore beach profile, storm surge duration, water temperature, and bluff geometry. A similar observation was made by [Barnhart et al. \(2014a\)](#) for the thermoabrasion numerical model of the Alaskan Beaufort coast.
6. The two consecutive bluff collapses routinely have an interval between them, and the time lapse between the two collapses is four to six weeks. The sediments released from the collapsed bluff alter the elevation near the swash zones, reducing the probability of inundating the beach with warm water and resulting in slow niche growth. The model by [Ravens et al. \(2012\)](#) considered a numerical elevation of the beach by about 0.28 m to calibrate the model and achieve optimised calculation. In contrast, the model proposed herein assumes the sediment from the bluffs increases the elevation of the beach and the elevation is controlled by the morphodynamic module (XBeach).
7. The parameter inundation depth, h_{id} , acts as an on-off switch for thermoabrasion; however, the numerical model does not show a clear relationship between the magnitude of h_{id} and erosion. Our model agrees with the previous observation of [Ravens et al. \(2012\)](#) that overall crest retreat is controlled by the niche erosion process.
8. The erosion rate of thermodenudation was found to be approximately $0.4 \text{ m}^3/\text{month}$ for low bluff-height profiles in zone S#1. The erosion rate by thermodenudation for the zones with a high bluff is estimated to be close to $1 \text{ m}^3/\text{month}$. The erosion rate of thermodenudation does not show a strong relationship with the thawing depth (x_t).
9. The hydrodynamic forcing, especially wave condition, plays a vital role in the erosion mechanism; hence the inclusion of the nearshore hydrodynamics and morphological changes is important.
10. Thermodenudation and thermoabrasion are intertwined; one mechanism can affect the other. For beaches where the two mechanisms are active, this feedback should be taken into consideration.

5.2 Probabilistic approach using Monte Carlo simulation

The application of a process-based erosion model using Monte Carlo simulation is discussed in section 3.4 of Chapter 3 for data-poor environment. The approach is demonstrated here using one coastal profile from the study area. The coastal profiles of the year 2012 and 2013, named case#P are shown in Figure 5.25.

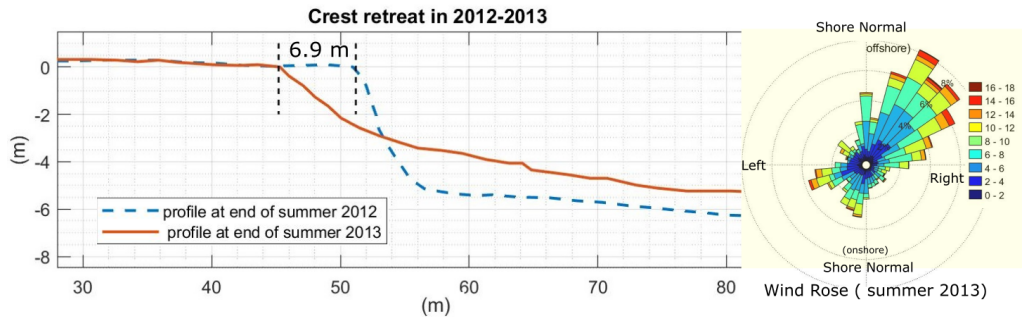


Figure 5.25: case#P, coastal profile and crest retreat is shown along with the wind rose. The crest retreat of 6.9m was measured between the two measurements of 2012 and 2013.

5.2.1. Probability of the bluff failure during a storm

The numerical model simulates crest retreat for each of the $N=1000$ cases generated using normal and log-normal distributions. The probability of the bluff collapse during a storm is calculated for the bluffs shown in case#P. Provided that the inundation depth (h_{id}) is kept constant at 0.25m, the probability of the bluff collapse is shown in Figure 5.26. At the beginning of the storm, the probability is very low for a bluff collapse. As time progresses, the probability increases almost linearly. The probability after 10 hours of the storm is more than 50%.

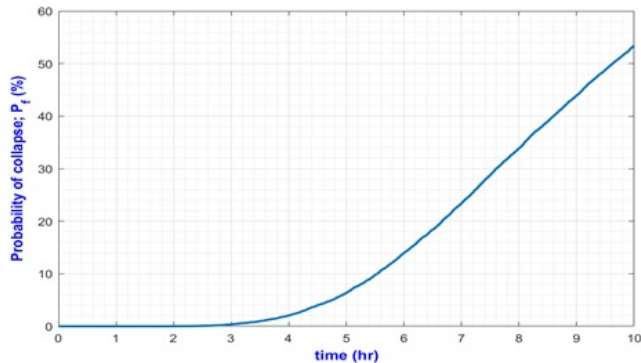


Figure 5.26: The probability of the bluff collapse during a storm for the case#P. The probability is calculated by Monte Carlo simulation after applying the environmental forcing of 2012-2013.

5.2.1.1. Probability of crest retreat

The probability of the crest retreat after $N=1000$ simulation is shown in Figure 5.27. A deterministic storm surge module is used. The surge level η is calculated from the wind speed and direction. From the water level simulation, the parameter h_{id} is calculated. The niche and bluff collapse submodules are probabilistic. The distribution of crest retreat is estimated from all the cases. The crest retreat follows a normal distribution. Figure 5.27-d shows the mean and 1.96σ (σ =standard deviation) as a time series. The mean crest erosion at the end of the simulation is found 6.6m with a standard deviation of 0.39m. The numerical model predicts that 95% probability that the crest retreat is within 5.83m to 7.36m when the field measurement was 6.9m.

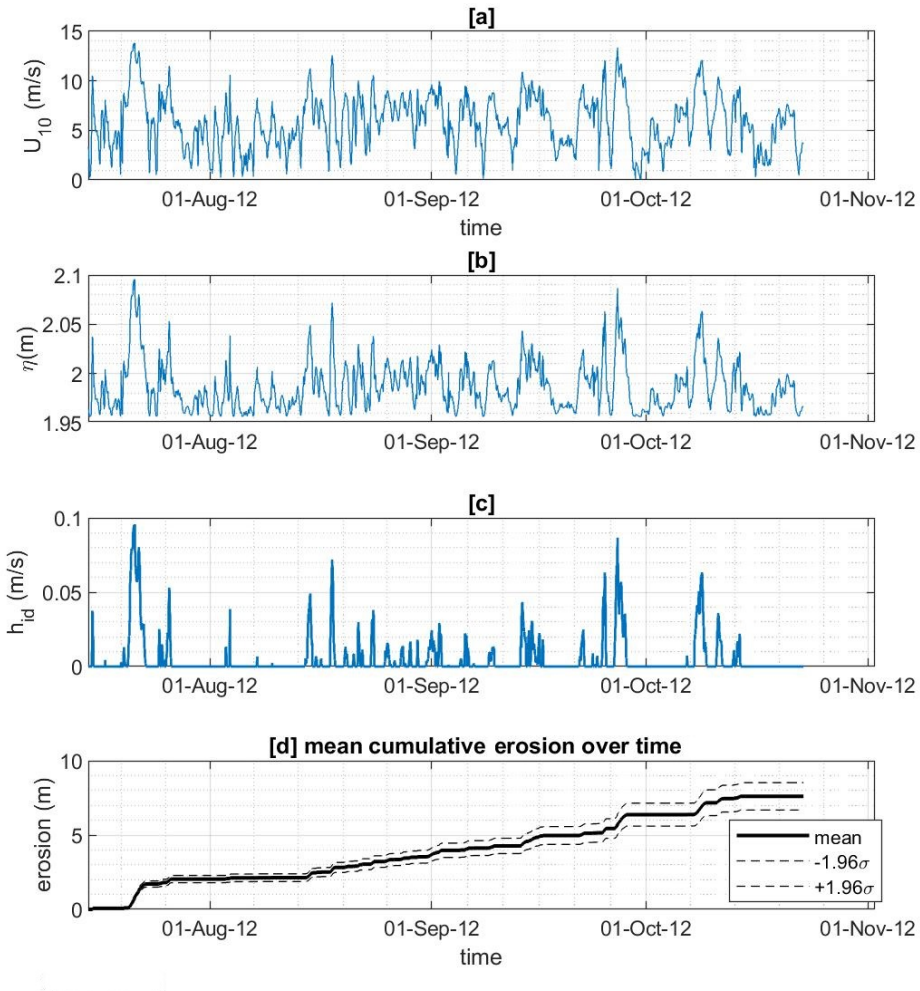


Figure 5.27: Cumulative erosion over the summer of 2013 of Case #P is shown. Subfigure (a) displays the wind speed during the summer of 2013. The wind speed is input for the storm surge module which calculates the storm surge level shown in subfigure (b), which in turn is used to find the inundation depth h_{id} in subfigure (c). Until here, the model is deterministic. The coastal erosion as time series is calculated for each case of $n = 1000$ in the Monte Carlo simulation. The distribution of the calculated erosion rate follows a normal distribution. Shown in the subfigure (d) are the mean erosion (thick black line) with $\pm 1.96\sigma$ drawn as dotted lines ($\sigma =$ standard deviation).

5.3 Data-driven temperature model of permafrost

This section demonstrates a data-driven temperature model of permafrost with one example. The model is described in detail in journal paper C.2.

The model is based on the Eq. 3.19 (section 3.5, page 54). Boreholes with thermistors are placed in the study area to measure temperature within bluffs. An abridged temperature measurement of one of the boreholes, bh2, is shown in Figure 5.28; a complete analysis (both by FFT and single harmonic) is provided in Appendix C.2.

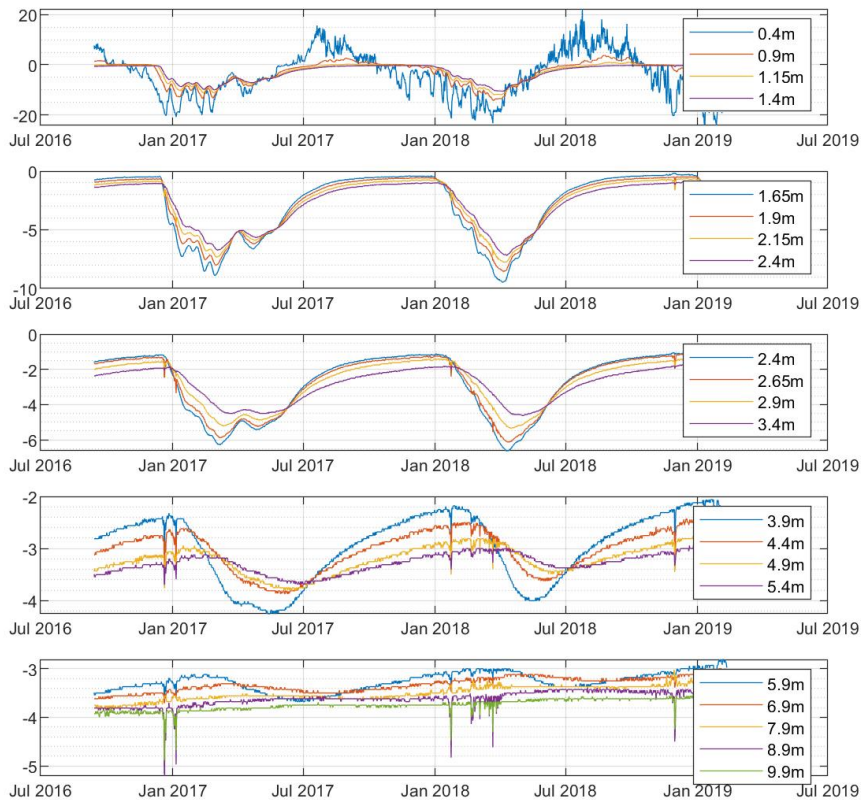


Figure 5.28: Temperature measurements of permafrost in a coastal bluff from depth 0.4 to 9.9m (bh#2, 21 nodes).

5.3.1. Pre-processing of the raw data

The filed measurements contain some values which are clearly an error in the sensor. Before proceeding, these values were identified and cleared. Unusual values can greatly affect the quality of curve fitting. A trend within the time series may be observed. Since a trend was not considered when we sought the analytical solution, the trend must be removed before the calibrations.

5.3.1.1. Removal of outliers

Any observation over three times the median absolute deviations (MAD) away from the median is considered a measurement error and termed as an outlier. The outliers are replaced with the value generated by the piece-wise cubic spline interpolation.

5.3.1.2. Removal of trend

The observations from the field typically have an upward or downward trend of the mean temperature. A first-order de-trend model is used to remove the trend from the observation.

$$Y_{p,q} = O_{p,q} - T_{q,1} \times O_{p,q} \quad (5.8)$$

where the p is the number of nodes along depth, q is the number of nodes in time-series, $O_{p,q}$ is the matrix of the training data set and $T_{q,1}$ is the matrix of the de-trending parameters and $Y_{p,q}$ is the refined observations. When the calibrated solutions are used to make predictions, the trend values are required to be included. The estimated trend values using the parameters $T_{q,1}$ are added back using the relation $T_{q,1} \times O'_{p,q}$; where $O'_{p,q}$ is the predicted observation matrix.

5.3.2. Training and testing dataset

The continuous temperature measurement of bh2 is divided into training and testing datasets (shown in Table 5.5).

Table 5.5: The temperature measurements are of 882 days. The time series is divided into training and testing datasets. Measurements of 705 days are used to determine the parameters (Islam et al. 2021).

time-series	Training data-set			Testing data-set		
	from	to	total days	from	to	total days
bh2	13-09-16	18-09-18	705	18-09-18	10-02-19	178

5.3.3. Fast Fourier Transformation of training dataset

An FFT analysis on the time series of the temperature measurements at bh2 is shown in Figure 5.29. FFT decomposes the measurements into a combination of harmonic functions. The figure shows that the highest amplitude of such harmonic function is found at lower frequencies. Along the depth, the amplitude of the harmonic reduces exponentially.

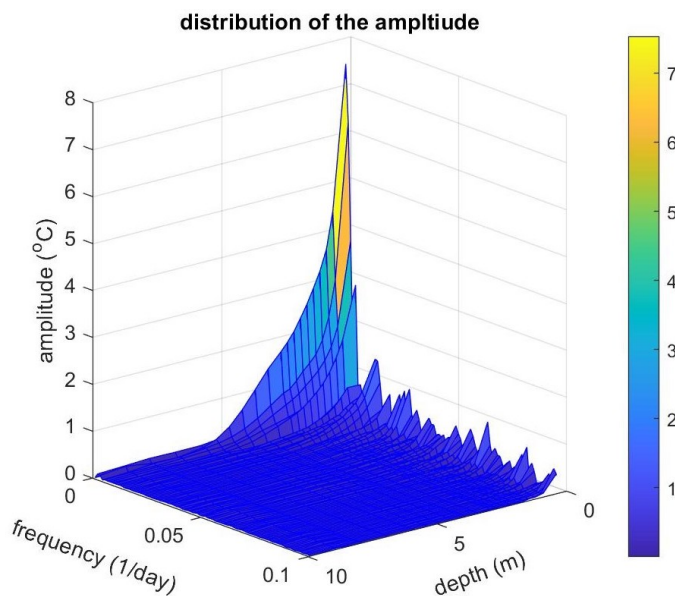


Figure 5.29: A fast Fourier transformation (FFT) decomposes the measurement of the temperature of bh2 (Islam et al. 2021). The highest amplitude is found at the lower frequencies. The amplitudes of the harmonic functions decrease exponentially along the depth.

5.3.4. Regression to estimate the parameters and reverse FFT

A separate regression is performed for each of the harmonic functions obtained from the FFT to determine the parameters. Table 5.6 shows the result of the top three harmonics (based on amplitude).

Table 5.6: An exponential curve ($a \cdot e^{-bz}$) is fitted to the amplitude distributions along the depth (where z is the depths). Only the top three harmonic functions are shown in the table.

time-series	parameter	rank of the peaks (n)		
		n=1	n=2	n=3
bh2	a	6.514121	3.667414	1.746538
	b	0.79755	1.32577	1.46048
	R^2	0.990179	0.98182	0.994857

The amplitude reduction is different for each component, but analysis shows phase lags are the same for all components; only along the depth does phase lag increase linearly. As a result, we only need one regression to determine the phase lag along the depth. The result of the regression of the phase lag is shown in Table 5.7. The lag is found to be around 25 days per unit (m) of depth.

Table 5.7: Phaselags of the signal determined by CPSD analysis, fitted to linear equation $a - mz$.

Time series	a	m	lags(days/m)	R^2
bh2	-0.0310	0.0399	25.0403	0.980723

5.3.5. Simulation Vs measurements

As shown in the previous section, the parameters estimated from the regression are now used to simulate temperature from the same time period of the testing dataset. The predicted values are compared with the measured value. The result of bh2 is shown in Figure 5.30.

To present the accuracy of the prediction, along the two axes, observed and predicted temperatures are placed. A 45°line is drawn. Every dot is a prediction of the model; an accurate prediction will put the dot on the line. The RMSE and SEE errors are also shown; both errors are reduced along the depth.

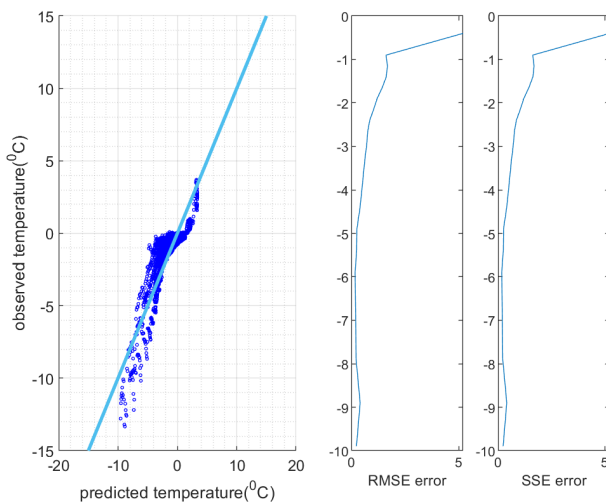


Figure 5.30: Comparing the observation and prediction. Along the x-axis prediction and along the y-axis, the observed values are placed. An accurate prediction will put the point on the blue line of the figure (Islam et al. 2021).

5.3.6. Discussion

The following conclusions are drawn for the model:

1. The result demonstrates that when the temperature at the surface (boundary condition) is expressed as single harmonic (detailed in Appendix C.2), the model performs worse than the combination of harmonics (FFT component).
2. The RMSE error is higher near the surface and sharply decreases along the depth. This limits the reliability of the model to predict temperature near the surface during summer.
3. The model over-estimate the temperature around $-10^{\circ}C$, these are the observations near the surface during winter.
4. The phase lag is measured to be around 22 to 28 days/m along the depth. This means the highest temperature of the permafrost at 3m depth occurs almost 75 days later.

CHAPTER 6

Conclusions and recommendation for the future works

6.1 Conclusion

This study focuses on developing a comprehensive model that can simulate thermodenudation and thermoabrasion simultaneously. As a complement to the combined model, a data-driven temperature model of permafrost and a probabilistic application of thermoabrasion are also developed.

The salient findings of the thesis on the challenges of the numerical modelling of the Arctic coastal erosion problem are summarised as follows:

1. A combined model of thermodenudation and thermoabrasion is developed, calibrated and validated for unlithified Arctic coasts. The nearshore morphology is included in the model, which is one of the novelties of the study.
2. Thermoabrasion is a complex mechanism that depends on the unique combination of various parameters such as storm surge, sea water temperature, and elevation of the beach. The collapse always coincides with the storm but not all storms lead to a collapse. No correlation between the intensity of the storm (in terms of wind speed) and collapse is found. The probability of collapse increases along with the duration of the storm though.
3. The inclusion of wave and wave-related mechanical forcing is an important driver of erosion. A sensitivity analysis demonstrates that erosion is reduced by almost 97% when waves are excluded from the simulation.

4. Simulation of the combined model shows that thermodenudation is not limited by the thawing depth; rather it depends on the slope stability and hydrodynamic forcing that can remove the loose sediments from the base of the bluffs.
5. The elevation of the beach indirectly controls the erosion mechanism, especially prominent for thermoabrasion. The sediments exerted from the collapse bluffs thwart the niche development; thus, a time lag is observed between two consecutive collapses.
6. The probabilistic model using Monte Carlo simulation assuming a normal and log-normal distribution of the input parameters demonstrates the crest retreat follows a normal distribution.
7. The data-driven temperature model of permafrost demonstrates that it is possible to estimate permafrost temperature when only measurement at the surface is available, given that some parameters are calibrated using previous full-scale measurements.

6.2 Future development

6.2.1. Process-based model of thermodenudation and thermoabrasion

1. Only the slumping of the thawed permafrost under the gravitational force is modelled. Various other mass move modes, such as retrogressive thaw slumping, are not considered.
2. The model excluded the accumulation and melting of snow. Another related effect of snow melting, water flow inside the bluff is not modelled. A snow submodule that tracks the thickness of the snow and its effect on the thermal processes will improve the accuracy of the model.
3. Threshold value control is used to include the presence of sea ice. However, the model currently acts in a binary mode where sea ice is ignored when the ice concentration is less than 20%. The damping of the waves because of the floating ice will also improve the model's fidelity.
4. A depth averaged critical slope (m_{cr}) is used to model slumping. One depth-averaged value is calibrated for each zone in the study area. A matrix of m_{cr} values at different depths and geological conditions will increase the model's accuracy.
5. In the thermoabrasion mechanism, the collapse of the bluff is predetermined. Two modes, shear failure and momentum failure are considered, but the failure planes

are already defined. To improve the accuracy of the coastal profile after the bluff collapses, a finite element model at the bluff face may be used. It will better predict the irregular bluff slope.

6.2.2. Probabilistic approach for data-poor environment

1. The probabilistic model excluded the morphological changes of the seabed, which limits its application to be used for long-term prediction. The inclusion of a simulation of nearshore morphology will put a computational demand that will limit the iterations within the Monte Carlo simulation. An empirical model of nearshore morphology will increase the fidelity of the model without causing a significant increase in the computation.
2. The probabilistic model is 1D which limits the inclusion of longshore sediment transport. It will be a significant improvement to include sediment transport due to waves and currents, both in longshore and cross-shore directions.

6.2.3. Data driven temperature model of permafrost

1. The model bypasses the effect of the energy requirement of permafrost phase changes. The inclusion of the phase changes in the regression model will certainly improve the fidelity of the model; however, many of the associated parameters need to be measured in situ such as horizontal water flow and convective heat transfer inside porous media.
2. A continuous field measurement of a few years with a good time resolution, such as 3 hours or less, will allow capturing the daily temperature variations. The model currently uses a 12-hour timestep which can not capture the daily temperature changes.

Bibliography

- Andersland, O. B., Ladanyi, B., et al. (2003). *Frozen ground engineering*. John Wiley & Sons.
- Are, F. (1988). Thermal abrasion of sea coasts (part i).
- Are, F., Reimnitz, E., Grigoriev, M., Hubberten, H.-W., and Rachold, V. (2008). The influence of cryogenic processes on the erosional arctic shoreface. *Journal of Coastal Research*, 24(1):110–121.
- Are F, E. (1988). Thermal abrasion of sea coast. *Polar Geogr. and Geol*, 12:1–157.
- Baranskaya, A., Novikova, A., Shabanova, N., Belova, N., Maznev, S., Ogorodov, S., and Jones, B. M. (2021). The role of thermal denudation in erosion of ice-rich permafrost coasts in an enclosed bay (gulf of kruzenstern, western yamal, russia). *Frontiers in Earth Science*, 8:659.
- Barnhart, K. R., Anderson, R. S., Overeem, I., Wobus, C., Clow, G. D., and Urban, F. E. (2014a). Modeling erosion of ice-rich permafrost bluffs along the alaskan beaufort sea coast. *Journal of Geophysical Research: Earth Surface*, 119(5):1155–1179.
- Barnhart, K. R., Overeem, I., and Anderson, R. S. (2014b). The effect of changing sea ice on the physical vulnerability of arctic coasts. *The Cryosphere*, 8(5):1777–1799.
- Belova, N., Baranskaya, A., Kokin, O., Kuznetsov, D., Shilova, O., Shabanova, N., Vergun, A., and Ogorodov, S. (2016). Monitoring of the thermoabrasional and accumulative coasts near the underwater gas pipeline route across the baydaratskaya bay, kara sea. In *MANAGING RISKS TO COASTAL REGIONS AND COMMUNITIES IN A CHANGING WORLD. EMECS'11-SEACOASTS XXVI*, pages 112–122.
- Box, J. E., Colgan, W. T., Christensen, T. R., Schmidt, N. M., Lund, M., Parmentier, F.-J. W., Brown, R., Bhatt, U. S., Euskirchen, E. S., and Romanovsky, V. E. (2019). Key indicators of arctic climate change: 1971–2017. *Environmental Research Letters*, 14(4):045010.

- Brown, J., Hinkel, K. M., and Nelson, F. (2000). The circumpolar active layer monitoring (calm) program: research designs and initial results. *Polar geography*, 24(3):166–258.
- Brown, J., Jorgenson, M. T., Smith, O. P., and Lee, W. (2003). Long-term rates of coastal erosion and carbon input, elson lagoon, barrow, alaska. In *Eighth International Conference on Permafrost*, volume 21, page 25.
- Brown, J. and Solomon, S. (1999). Arctic coastal dynamics. In *Report of an international workshop. Woods Hole, USA.: Geological Survey of Canada*.
- Bull, D. L., Brown, E., Choens, R. C., Connolly, C. T., Flanary, C., Frederick, J. M., Jones, B. M., Jones, C. A., Ward Jones, M., and McClelland, J. W. (2020). Arctic coastal erosion: Modeling and experimentation. Report, Sandia National Lab.(SNL-NM), Albuquerque, NM (United States); Sandia
- Casas-Prat, M., Wang, X. L., and Swart, N. (2018). Cmp5-based global wave climate projections including the entire arctic ocean. *Ocean Modelling*, 123:66–85.
- Casas-Prat, M. and Wang, X. L. (2020). Projections of extreme ocean waves in the arctic and potential implications for coastal inundation and erosion. *Journal of Geophysical Research: Oceans*, 125(8):e2019JC015745.
- Chylek, P., Li, J., Dubey, M., Wang, M., and Lesins, G. (2011). Observed and model simulated 20th century arctic temperature variability: Canadian earth system model canesm2. *Atmospheric Chemistry and Physics Discussions*, 11(8):22893–22907.
- Cohen, J., Screen, J. A., Furtado, J. C., Barlow, M., Whittleston, D., Coumou, D., Francis, J., Dethloff, K., Entekhabi, D., and Overland, J. (2014). Recent arctic amplification and extreme mid-latitude weather. *Nature geoscience*, 7(9):627–637.
- Dean, R. G. and Dalrymple, R. A. (1991). *Water wave mechanics for engineers and scientists*, volume 2. world scientific publishing company.
- Farquharson, L. M., Mann, D., Swanson, D., Jones, B., Buzard, R., and Jordan, J. (2018). Temporal and spatial variability in coastline response to declining sea-ice in northwest alaska. *Marine Geology*, 404:71–83.
- Frederick, J., Mota, A., Tezaur, I., and Bull, D. (2021). A thermo-mechanical terrestrial model of arctic coastal erosion. *Journal of Computational and Applied Mathematics*, 397:113533.

- Frederick, J. M., Thomas, M. A., Bull, D. L., Jones, C. A., and Roberts, J. D. (2016). The arctic coastal erosion problem. *Albuquerque, NM: Sandia National Laboratories SAND2016-9762*, 122.
- Fritz, M., Vonk, J. E., and Lantuit, H. (2017). Collapsing arctic coastlines. *Nature Climate Change*, 7(1):6–7.
- Fuchs, M., Lenz, J., Jock, S., Nitze, I., Jones, B. M., Strauss, J., Günther, F., and Grosse, G. (2019). Organic carbon and nitrogen stocks along a thermokarst lake sequence in arctic alaska. *Journal of Geophysical Research: Biogeosciences*, 124(5):1230–1247.
- Gao, Z., Fan, X., and Bian, L. (2003). An analytical solution to one-dimensional thermal conduction-convection in soil. *Soil Science*, 168(2):99–107.
- Gao, Z., Lenschow, D. H., Horton, R., Zhou, M., Wang, L., and Wen, J. (2008). Comparison of two soil temperature algorithms for a bare ground site on the loess plateau in china. *Journal of Geophysical Research: Atmospheres*, 113(D18).
- Ghoreishian Amiri, S., Grimstad, G., Kadivar, M., and Nordal, S. (2016). Constitutive model for rate-independent behavior of saturated frozen soils. *Canadian Geotechnical Journal*, 53(10):1646–1657.
- Ghoreishian Amiri, S., Kadivar, M., and Grimstad, G. (2015). *A thermo-hydro-mechanical constitutive model for saturated frozen soils*, pages 1024–1031. IOS Press.
- Gibbs, A., Richmond, B., Erikson, L., and Jones, B. (2018). Long-term retreat of coastal permafrost bluffs, barter island, alaska. In *5th European Conference on permafrost; EUCOP5: Chamonix, France*, volume 1, pages 1–2.
- Gruber, S. and Haeberli, W. (2007). Permafrost in steep bedrock slopes and its temperature-related destabilization following climate change. *Journal of Geophysical Research: Earth Surface*, 112(F2).
- Guégan, E. (2015). *Erosion of permafrost affected coasts: rates, mechanisms and modeling*. Thesis, Norwegian University of Science and Technology (NTNU).
- Günther, F., Overduin, P. P., Sandakov, A., Grosse, G., and Grigoriev, M. N. (2015a). Thermo-erosion along the yedoma coast of the buor khaya peninsula, laptev sea, east siberia. In *Proceedings of the Tenth International Conference on Permafrost, Volume 1: International Contributions*, pages 137–142. The Northern Publisher, Salekhard, Russia.

- Günther, F., Overduin, P. P., Sandakov, A. V., Grosse, G., and Grigoriev, M. N. (2013). Short-and long-term thermo-erosion of ice-rich permafrost coasts in the laptev sea region. *Biogeosciences*, 10(6):4297–4318.
- Günther, F., Overduin, P. P., Yakshina, I. A., Opel, T., Baranskaya, A. V., and Grigoriev, M. N. (2015b). Observing muostakh disappear: permafrost thaw subsidence and erosion of a ground-ice-rich island in response to arctic summer warming and sea ice reduction. *The Cryosphere*, 9(1):151–178.
- Hequette, A. and Barnes, P. W. (1990). Coastal retreat and shoreface profile variations in the canadian beaufort sea. *Marine Geology*, 91(1-2):113–132.
- Holland-Bartels, L. E. and Pierce, B. S. (2011). An evaluation of the science needs to inform decisions on outer continental shelf energy development in the chukchi and beaufort seas, alaska. *US Department of the Interior, US Geological Survey*.
- Hoque, M. A. and Pollard, W. H. (2009). Arctic coastal retreat through block failure. *Canadian Geotechnical Journal*, 46(10):1103–1115.
- Hoque, M. A. and Pollard, W. H. (2016). Stability of permafrost dominated coastal cliffs in the arctic. *Polar Science*, 10(1):79–88.
- Hu, G., Zhao, L., Wu, X., Li, R., Wu, T., Xie, C., Qiao, Y., Shi, J., Li, W., and Cheng, G. (2016). New fourier-series-based analytical solution to the conduction–convection equation to calculate soil temperature, determine soil thermal properties, or estimate water flux. *International Journal of Heat and Mass Transfer*, 95:815–823.
- Hugelius, G., Strauss, J., Zubrzycki, S., Harden, J. W., Schuur, E., Ping, C.-L., Schirrmeister, L., Grosse, G., Michaelson, G. J., and Koven, C. D. (2014). Estimated stocks of circumpolar permafrost carbon with quantified uncertainty ranges and identified data gaps. *Biogeosciences*, 11(23):6573–6593.
- Irrgang, A. M., Bendixen, M., Farquharson, L. M., Baranskaya, A. V., Erikson, L. H., Gibbs, A. E., Ogorodov, S. A., Overduin, P. P., Lantuit, H., and Grigoriev, M. N. (2022). Drivers, dynamics and impacts of changing arctic coasts. *Nature Reviews Earth & Environment*, 3(1):39–54.
- Irrgang, A. M., Lantuit, H., Manson, G. K., Günther, F., Grosse, G., and Overduin, P. P. (2018). Variability in rates of coastal change along the yukon coast, 1951 to 2015. *Journal of Geophysical Research: Earth Surface*, 123(4):779–800.

- Isaev, V., Kioka, A., Koshurnikov, A., Pogorelov, A., Amangurov, R., Podchasov, O., and Sergeev, D. (2016). Field investigation and laboratory analyses; baydaratskaya bay 2016.
- Isaev, V., Koshurnikov, A., Pogorelov, A., Amangurov, R., Podchasov, O., Sergeev, D., Buldovich, S., Aleksyutina, D., Grishakina, E., and Kioka, A. (2019a). Cliff retreat of permafrost coast in south-west baydaratskaya bay, kara sea, during 2005–2016. *Permafrost and Periglacial Processes*, 30(1):35–47.
- Isaev, V., Koshurnikov, A., Pogorelov, A., Amangurov, R., Podchasov, O., Sergeev, D., Buldovich, S., Aleksyutina, D., Grishakina, E., and Kioka, A. (2019b). Cliff retreat of permafrost coast in south-west baydaratskaya bay, kara sea, during 2005–2016. *Permafrost and Periglacial Processes*, 30(1):35–47.
- Isaev, V., Pogorelov, A., Amangurov, R., Komarov, O., Gorshkov, E., Belova, N., Aleksyutina, D., and Kokin, O. (2017). Field investigation and laboratory analyses; baydaratskaya bay 2017.
- Islam, M. A. (2018). Erosion in the arctic: A thermoabrasion model to predict shoreline change after an extreme event. Master’s thesis, NTNU.
- Islam, M. A. and Lubbad, R. (2022). A process-based model for arctic coastal erosion driven by thermodenudation and thermoabrasion combined and including nearshore morphodynamics. *Journal of Marine Science and Engineering*, 10(11):1602.
- Islam, M. A., Lubbad, R., Amiri, S. A. G., Isaev, V., Shevchuk, Y., Uvarova, A. V., Afzal, M. S., and Kumar, A. (2021). Modelling the seasonal variations of soil temperatures in the arctic coasts. *Polar Science*, 30:100732.
- Jones, B., Irrgang, A., Farquharson, L., Lantuit, H., Whalen, D., Ogorodov, S., Grigoriev, M., Tweedie, C., Gibbs, A., and Strzelecki, M. (2020). Arctic report card 2020: Coastal permafrost erosion. Technical report, United States. National Oceanic and Atmospheric Administration. Office of Oceanic and Atmospheric Research.
- Jones, B. M., Farquharson, L. M., Baughman, C. A., Buzard, R. M., Arp, C. D., Grosse, G., Bull, D. L., Günther, F., Nitze, I., and Urban, F. (2018). A decade of remotely sensed observations highlight complex processes linked to coastal permafrost bluff erosion in the arctic. *Environmental Research Letters*, 13(11):115001.
- Jones, B. M., Hinkel, K. M., Arp, C. D., and Eisner, W. R. (2008). Modern erosion rates and loss of coastal features and sites, beaufort sea coastline, alaska. *Arctic*, pages 361–372.

- Kobayashi, N. (1985). Formation of thermoerosional niches into frozen bluffs due to storm surges on the beaufort sea coast. *Journal of Geophysical Research: Oceans*, 90(C6):11983–11988.
- Kobayashi, N. and Aktan, D. (1986). Thermoerosion of frozen sediment under wave action. *Journal of waterway, port, coastal, and ocean engineering*, 112(1):140–158.
- Kobayashi, N., Vidrine, J., Nairn, R., and Soloman, S. (1999). Erosion of frozen cliffs due to storm surge on beaufort sea coast. *Journal of coastal research*, pages 332–344.
- Kokin, O., Pogorelov, A., Gorshkov, E., Komarov, O., Amangurov, R., Simonsen, V., and Isaev, V. (2019). Field investigation and laboratory analyses baydaratskaya bay 2018.
- Koven, C. D., Riley, W. J., and Stern, A. (2013). Analysis of permafrost thermal dynamics and response to climate change in the cmip5 earth system models. *Journal of Climate*, 26(6):1877–1900.
- Kupilik, M., Ulmgren, M., and Brunswick, D. (2020). Bayesian parameter estimation for arctic coastal erosion under the effects of climate change. *IEEE Journal of Selected Topics in Applied Earth Observations and Remote Sensing*, 13:3595–3604.
- Lachenbruch, A. H. and Marshall, B. V. (1969). Heat flow in the arctic. *Arctic*, 22(3):300–311.
- Lantuit, H., Atkinson, D., Paul Overduin, P., Grigoriev, M., Rachold, V., Grosse, G., and Hubberten, H.-W. (2011). Coastal erosion dynamics on the permafrost-dominated bykovsky peninsula, north siberia, 1951–2006. *Polar Research*, 30(1):7341.
- Lantuit, H., Overduin, P. P., Couture, N., Wetterich, S., Aré, F., Atkinson, D., Brown, J., Cherkashov, G., Drozdov, D., Forbes, D. L., et al. (2012). The arctic coastal dynamics database: a new classification scheme and statistics on arctic permafrost coastlines. *Estuaries and Coasts*, 35(2):383–400.
- Lantuit, H. and Pollard, W. (2008). Fifty years of coastal erosion and retrogressive thaw slump activity on herschel island, southern beaufort sea, yukon territory, canada. *Geomorphology*, 95(1-2):84–102.
- Leont'yev, I. (2003). Modeling erosion of sedimentary coasts in the western russian arctic. *Coastal Engineering*, 47(4):413–429.
- Lim, M., Whalen, D., Martin, J., Mann, P., Hayes, S., Fraser, P., Berry, H., and Ouellette, D. (2020). Massive ice control on permafrost coast erosion and sensitivity. *Geophysical Research Letters*, 47(17):e2020GL087917.

- Longuet-Higgins, M. S. (1970). Longshore currents generated by obliquely incident sea waves: 1. *Journal of geophysical research*, 75(33):6778–6789.
- Manson, G., Solomon, S. M., Forbes, D. L., Atkinson, D., and Craymer, M. (2005). Spatial variability of factors influencing coastal change in the western canadian arctic. *Geo-Marine Letters*, 25(2):138–145.
- Manson, G. K. and Solomon, S. M. (2007). Past and future forcing of beaufort sea coastal change. *Atmosphere-Ocean*, 45(2):107–122.
- Martini, I. P. and Wanless, H. R. (2014). Sedimentary coastal zones from high to low latitudes: Similarities and differences. Geological Society of London.
- McRoberts, E. and Morgenstern, N. R. (1974). The stability of thawing slopes. *Canadian Geotechnical Journal*, 11(4):447–469.
- Nairn, R., Solomon, S., Kobayashi, N., and Virdrine, J. (1998). Development and testing of a thermal-mechanical numerical model for predicting arctic shore erosion processes. In *Permafrost: Proceedings of the Seventh International Conference, Yellowknife, NWT, June 23-27*, pages 789–795. Centre d’études nordiques, Université Laval, Québec, Canada.
- Nairn, R., Solomon, S., Kobayashi, N., and Virdrine, J. (1999). Development and testing of a thermal-mechanical numerical model for predicting arctic shore erosion processes. In *Permafrost: Proceedings of the Seventh International Conference, Yellowknife, NWT, June 23-27*, pages 789–795. Centre d’études nordiques, Université Laval, Québec, Canada.
- Nicolsky, D. J., Romanovsky, V. E., Panda, S. K., Marchenko, S. S., and Muskett, R. R. (2017). Applicability of the ecosystem type approach to model permafrost dynamics across the alaska north slope. *Journal of Geophysical Research: Earth Surface*, 122(1):50–75.
- Nielsen, D. M., Pieper, P., Barkhordarian, A., Overduin, P., Ilyina, T., Brovkin, V., Baehr, J., and Dobrynin, M. (2022). Increase in arctic coastal erosion and its sensitivity to warming in the twenty-first century. *Nature Climate Change*, 12(3):263–270.
- Notz, D., Haumann, F. A., Haak, H., Jungclaus, J. H., and Marotzke, J. (2013). Arctic sea-ice evolution as modeled by max planck institute for meteorology’s earth system model. *Journal of Advances in Modeling Earth Systems*, 5(2):173–194.

- Novikova, A., Belova, N., Baranskaya, A., Aleksyutina, D., Maslakov, A., Zelenin, E., Shabanova, N., and Ogorodov, S. (2018). Dynamics of permafrost coasts of baydaratskaya bay (kara sea) based on multi-temporal remote sensing data. *Remote Sensing*, 10(9):1481.
- Ogorodov, S., Aleksyutina, D., Baranskaya, A., Shabanova, N., and Shilova, O. (2020). Coastal erosion of the russian arctic: An overview. *Journal of Coastal Research*, 95(sp1):599–604.
- Ogorodov, S., Arkhipov, V., Kokin, O., Marchenko, A., Overduin, P., and Forbes, D. (2013). Ice effect on coast and seabed in baydaratskaya bay, kara sea. *Geography, Environment, Sustainability*, 6(3):21–37.
- Ogorodov, S. A., Baranskaya, A. V., Belova, N. G., Kamalov, A. M., Kuznetsov, D. E., Overduin, P. P., Shabanova, N. N., and Vergun, A. P. (2016). Coastal dynamics of the pechora and kara seas under changing climatic conditions and human disturbances. *Geography, environment, sustainability*, 9(3):53–73.
- Overeem, I., Anderson, R. S., Wobus, C. W., Clow, G. D., Urban, F. E., and Matell, N. (2011). Sea ice loss enhances wave action at the arctic coast. *Geophysical Research Letters*, 38(17).
- Pearson, S., Lubbad, R., Le, T., and Nairn, R. (2016). Thermomechanical erosion modeling of baydaratskaya bay, russia with cosmos. In *Scour and Erosion, Proceedings of the 8th International Conference on Scour and Erosion, edited by: Harris, J., Whitehouse, R., and Moxon, S., CRC Press/Balkema, EH Leiden, The Netherlands*, page 281.
- Ping, C., Michaelson, G., Guo, L., Jorgenson, M., Kanevskiy, M., Shur, Y., Dou, F., and Liang, J. (2011). Soil carbon and material flux across the eroding coastline of the beaufort sea, alaska. *J. Geophys. Res. Biogeosci.*, 116:G02004.
- Plaxis (2021). Accessed: 2021-07-25.
- Ravens, T., Peterson, S., Panchang, V., and Kaihatu, J. (2018). *Arctic coastal erosion modeling*, page 47. World Scientific Singapore.
- Ravens, T., Ulmgren, M., Wilber, M., Hailu, G., and Peng, J. (2017). Arctic-capable coastal geomorphic change modeling with application to barter island, alaska. In *OCEANS 2017-Anchorage*, pages 1–4. IEEE.
- Ravens, T. M., Jones, B. M., Zhang, J., Arp, C. D., and Schmutz, J. A. (2012). Process-based coastal erosion modeling for drew point, north slope, alaska. *Journal of Waterway, Port, Coastal, and Ocean Engineering*, 138(2):122–130.

- Roelvink, D., Reniers, A., Van Dongeren, A., Van Thiel de Vries, J., Lescinski, J., and McCall, R. (2010). Xbeach model description and manual. *Unesco-IHE Institute for Water Education, Deltares and Delft University of Technology. Report June*, 21:2010.
- Rolph, R., Overduin, P. P., Ravens, T., Lantuit, H., and Langer, M. (2021). Arcticbeach v1. 0: A physics-based parameterization of pan-arctic coastline erosion. *Geoscientific Model Development Discussions*, pages 1–26.
- Romanovsky, V. and Osterkamp, T. (1997). Thawing of the active layer on the coastal plain of the alaskan arctic. *Permafrost and Periglacial processes*, 8(1):1–22.
- Rowland, J., Jones, C., Altmann, G., Bryan, R., Crosby, B., Hinzman, L., Kane, D., Lawrence, D., Mancino, A., and Marsh, P. (2010). Arctic landscapes in transition: responses to thawing permafrost. *Eos, Transactions American Geophysical Union*, 91(26):229–230.
- Russell-Head, D. (1980). The melting of free-drifting icebergs. *Annals of glaciology*, 1:119–122.
- Saha, S., Moorthi, S., Wu, X., Wang, J., Nadiga, S., Tripp, P., Behringer, D., Hou, Y.-T., Chuang, H.-y., Iredell, M., et al. (2014). The ncep climate forecast system version 2. *Journal of climate*, 27(6):2185–2208.
- Schirrneister, L., Grosse, G., Wetterich, S., Overduin, P. P., Strauss, J., Schuur, E. A., and Hubberten, H. (2011). Fossil organic matter characteristics in permafrost deposits of the northeast siberian arctic. *Journal of Geophysical Research: Biogeosciences*, 116(G2).
- Schneider, A. K. (2017). *Assessing Stability of Coastal Bluffs Due to Combined Actions of Waves and Changing Ambient Temperatures in the Arctic*. Thesis, Department of Civil and Environmental Engineering.
- Schuur, E. A., McGuire, A. D., Schädel, C., Grosse, G., Harden, J. W., Hayes, D. J., Hugelius, G., Koven, C. D., Kuhry, P., and Lawrence, D. M. (2015). Climate change and the permafrost carbon feedback. *Nature*, 520(7546):171–179.
- Serreze, M., Barrett, A., Stroeve, J., Kindig, D., and Holland, M. (2009). The emergence of surface-based arctic amplification. *The Cryosphere*, 3(1):11–19.
- Shabanova, N., Ogorodov, S., Shabanov, P., and Baranskaya, A. (2018). Hydrometeorological forcing of western russian arctic coastal dynamics: Xx-century history and current state. *Geography, Environment, Sustainability*, 11(1):113–129.

- Sinitsyn, A. O., Guegan, E., Shabanova, N., Kokin, O., and Ogorodov, S. (2020). Fifty four years of coastal erosion and hydrometeorological parameters in the varandey region, barents sea. *Coastal Engineering*, 157:103610.
- Stallman, R. (1965). Steady one-dimensional fluid flow in a semi-infinite porous medium with sinusoidal surface temperature. *Journal of geophysical Research*, 70(12):2821–2827.
- Steele, M., Ermold, W., and Zhang, J. (2008). Arctic ocean surface warming trends over the past 100 years. *Geophysical Research Letters*, 35(2).
- Stein, R. and Macdonald, R. W. (2004). The arctic ocean organic carbon cycle: present and past. *Springer, Berlin–New York*, 336:194.
- Stopa, J. E., Ardhuin, F., and Girard-Ardhuin, F. (2016). Wave climate in the arctic 1992–2014: Seasonality and trends. *The Cryosphere*, 10(4):1605–1629.
- Stroeve, J. and Notz, D. (2018). Changing state of arctic sea ice across all seasons. *Environmental Research Letters*, 13(10):103001.
- SWAN (2021). Simulating waves nearshore (swan), delft university of technology, <https://swanmodel.sourceforge.io/>.
- Thomson, J. and Rogers, W. E. (2014). Swell and sea in the emerging arctic ocean. *Geophysical Research Letters*, 41(9):3136–3140.
- Tweedie, C. E., Escarzaga, S. M., Cody, R. P., Manley, W. F., Gaylord, A. G., Aiken, Q., Lopez, A. F., Aguirre, A., George, C., and Nelson, L. (2016). Patterns and controls of erosion along the elson lagoon coastline, barrow, alaska (2003-2016). In *AGU Fall Meeting Abstracts*, volume 2016, pages EP12B–02.
- Van Wijk, W. R. and De Vries, D. (1963). Periodic temperature variations in a homogeneous soil. *Physics of plant environment*, 1:103–143.
- Verhoef, A., van den Hurk, B. J., Jacobs, A. F., and Heusinkveld, B. G. (1996). Thermal soil properties for vineyard (efeda-i) and savanna (hapex-sahel) sites. *Agricultural and Forest Meteorology*, 78(1-2):1–18.
- Vincent, W. F., Lemay, M., and Allard, M. (2017). Arctic permafrost landscapes in transition: towards an integrated earth system approach. *Arctic Science*, 3(2):39–64.
- Vonk, J. E., Sánchez-García, L., Van Dongen, B., Alling, V., Kosmach, D., Charkin, A., Semiletov, I. P., Dudarev, O. V., Shakhova, N., and Roos, P. (2012). Activation of old carbon by erosion of coastal and subsea permafrost in arctic siberia. *Nature*, 489(7414):137–140.

- Wegner, C., Bennett, K. E., de Vernal, A., Forwick, M., Fritz, M., Heikkilä, M., Łącka, M., Lantuit, H., Laska, M., and Moskalik, M. (2015). Variability in transport of terrigenous material on the shelves and the deep arctic ocean during the holocene. *Polar Research*, 34(1):24964.
- White, F. M., Spaulding, M. L., and Gominho, L. (1980). Theoretical estimates of the various mechanisms involved in iceberg deterioration in the open ocean environment. Report, RHODE ISLAND UNIV KINGSTON.
- Wobus, C., Anderson, R., Overeem, I., Matell, N., Clow, G., and Urban, F. (2011). Thermal erosion of a permafrost coastline: improving process-based models using time-lapse photography. *Arctic, Antarctic, and Alpine Research*, 43(3):474–484.
- Young, I. R. (1999). *Wind generated ocean waves*. Elsevier.

APPENDIX A

Coastal profiles

A.1 Four zones of a coastal profile

The four zones of the Arctic coast in terms of erosion, thermal energy transfers and involvement of various physical processes are described in Figure A.1. The four zones are defined as follows:

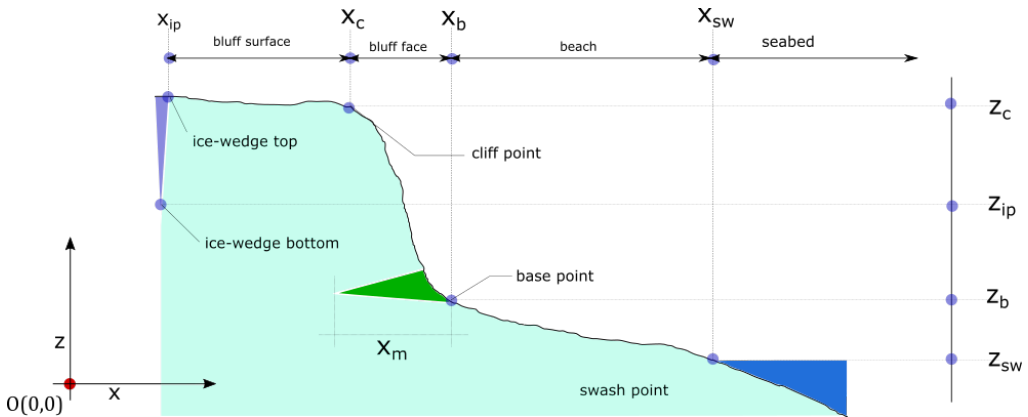


Figure A.1: The coastal profile is divided into four sections based on the thermal energy transfer mechanism.

1. bluff surface: it is the surface behind the cliff point X_c . The slope in the zone is zero or close to zero. The surface is covered with vegetation during the summer. Subsidence due to the thawing of the permafrost is the major change in the profile. Thawing depth is dependent on the convection of air and solar radiation. We assume the erosion due to surface run-off is negligible (based on field observation). The bluffs are usually filled with ice-wedge polygons. The organic-active layer at the top of the surface has negligible shear strength but can contribute to the lower erodibility to surface run-offs.

2. bluff face: It is the steepest slope of the profile, in between the base point X_b and cliff point X_c and the most active part of the profile. The thawing process contributes directly to the mass loss by slumping and cliff retreat.

3. beach: The narrow beach in front of the bluff from the base point X_b to the swash point X_s . The thawed sediments accumulate on the beach. The collapsed bluffs fall on the beach. The beach is subject to inundation during the summer storms. The return currents created during the storms sort out the accumulated sediments and transport them offshore.

4. seabed: It is defined from the swash point X_s to the offshore. The general direction of the sediment transport is offshore since there exist no restoration mechanisms at the Arctic beaches. The wave-induced particle movement is enough to transfer heat (convective heat transfer). The thawing depth is not the limiting factor, i.e., the permafrost lies quite deep. However, due to sea ice, sediment transport during the winter is negligible.

A.2 Coastal profiles

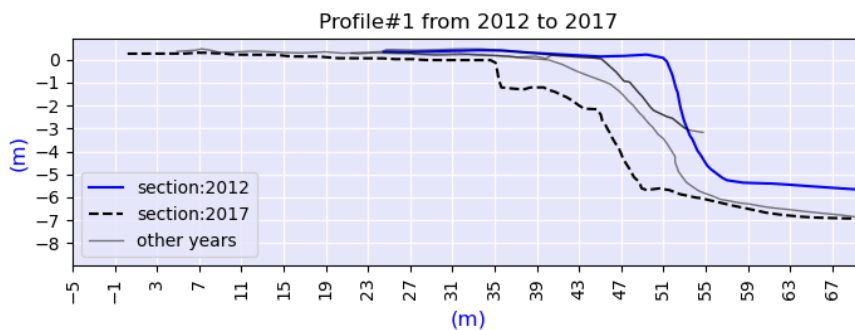


Figure A.2: Profile#1

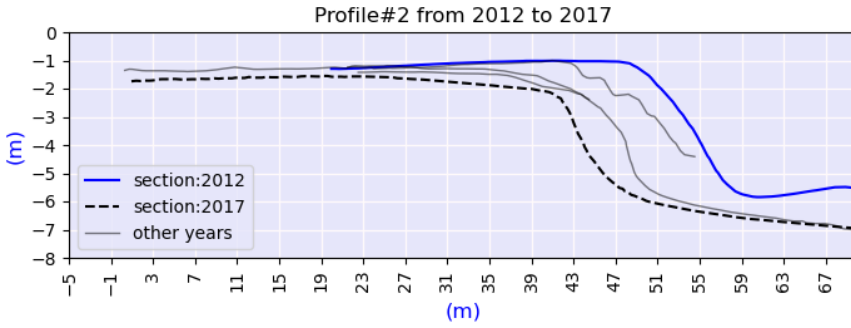


Figure A.3: Profile#2

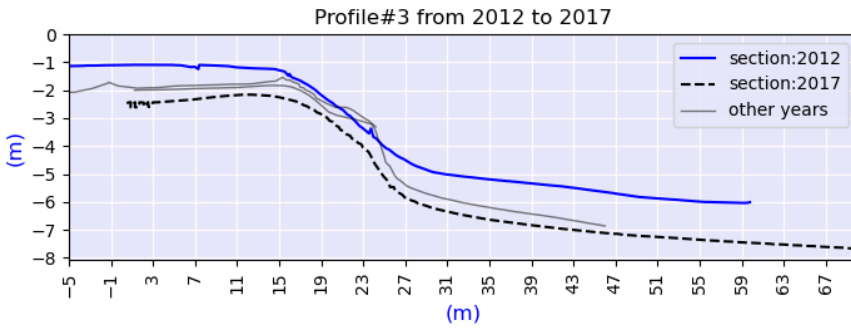


Figure A.4: Profile#3

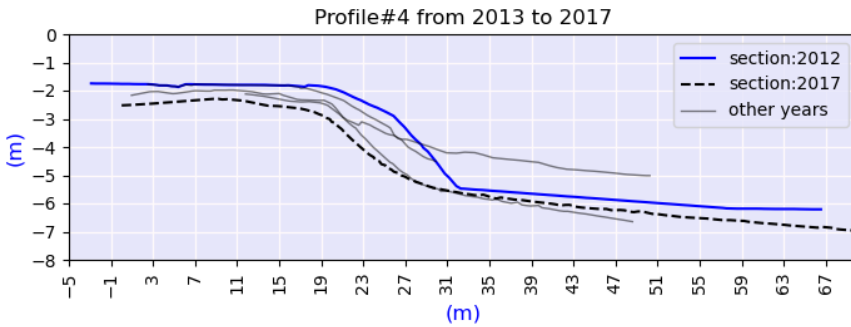


Figure A.5: Profile#4

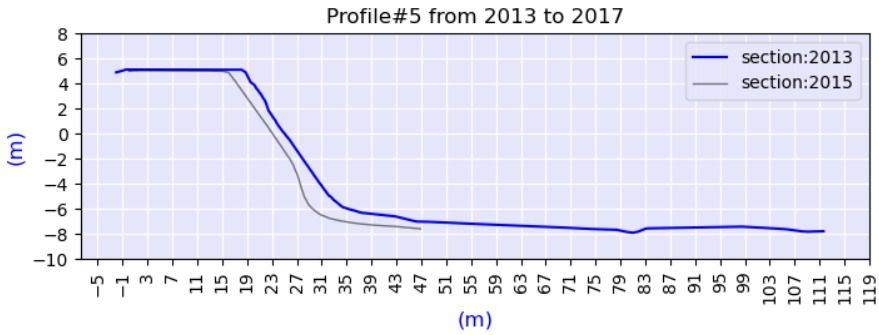


Figure A.6: Profile#5

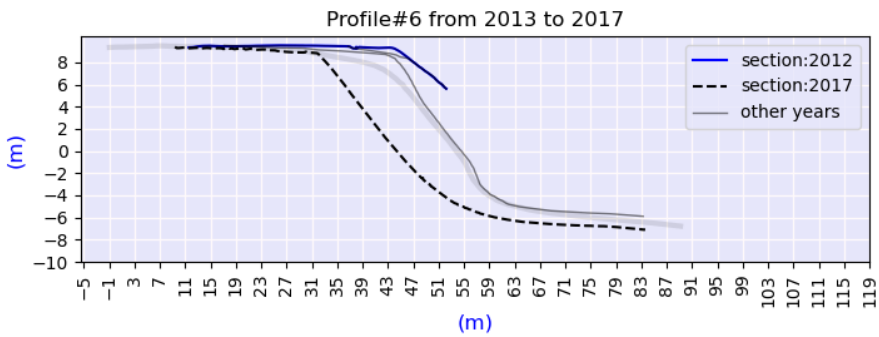


Figure A.7: Profile#6

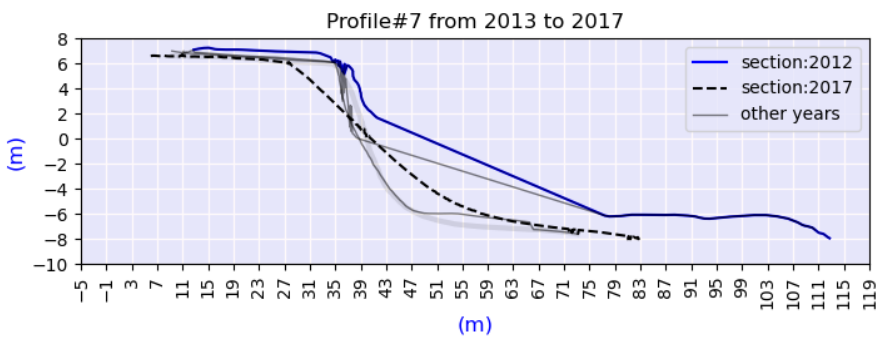


Figure A.8: Profile#7

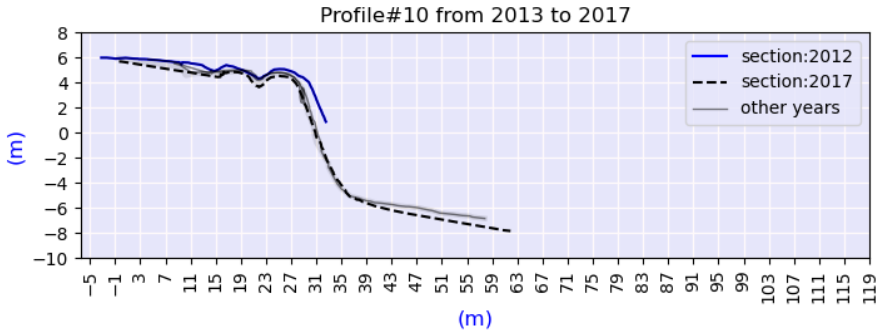


Figure A.9: Profile#8

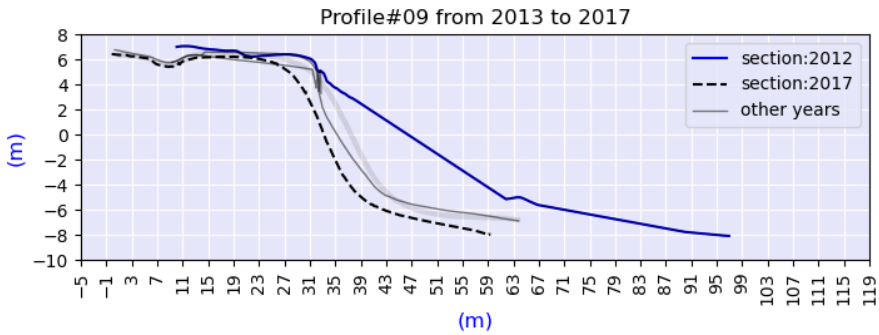


Figure A.10: Profile#9

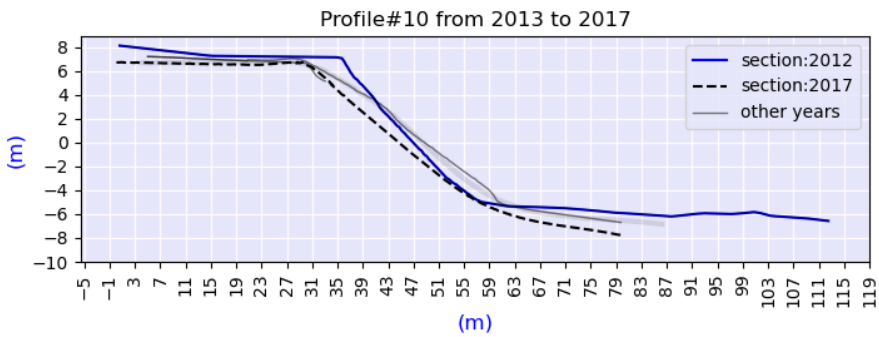


Figure A.11: Profile#10

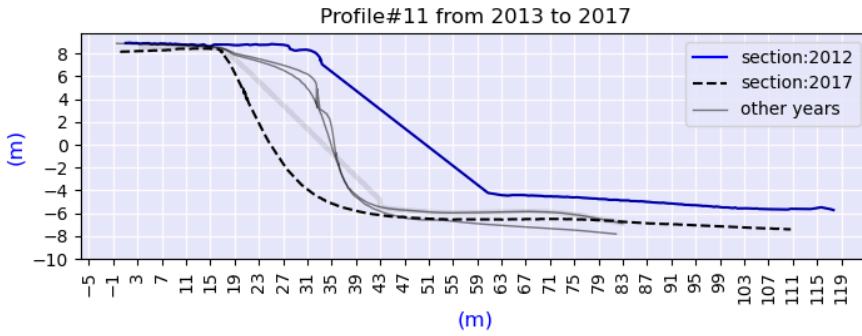


Figure A.12: Profile#11

APPENDIX B

Numerical implementations

B.1 Storm surge submodule

Storms are caused by the differences in the pressure; wind blows from the high pressure zones to the low pressure zones. The centre of the storm is typically the low-pressure zones. Wind fields are driven along the pressure gradients. When wind blows over the ocean surface, ocean surface waves are created. The stress created by the wind on the ocean surface also pushes the water towards the onshore which creates the surge. Shallow bathymetry increases the effect of surge. The surge level is also influenced by the shape of the coast, the surge level is magnified if coast is funnel shaped. The storm surge level is typically above the highest astronomical tides. The surge is created by (a) pressure differences, (b) wind stress and (c) Coriolis effect along with the wave set-up.

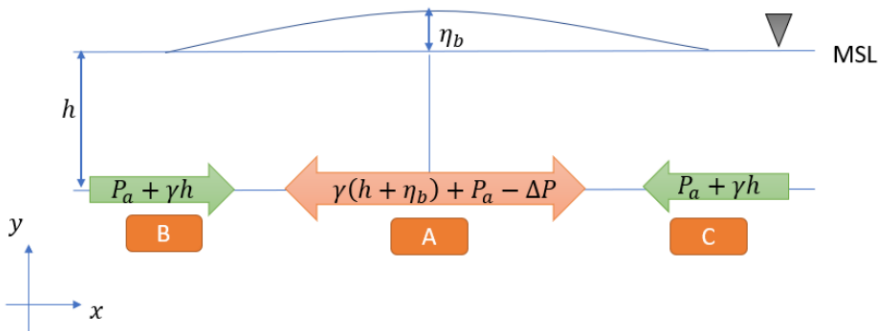


Figure B.1: The water level changes from the low pressure (point A) to the high pressure (point B).

Surge created by the pressure differences is shown in Figure B.1. The pressure at point A (centre of the storm) and point B (outside of storm) are as follows: point B: $P(h) =$

$\rho gh + P_a$ point A: $P(h + \eta_b) = \rho_w g(h + \eta_b) + P_a - \Delta P$ Where P_a is the air pressure at point A, $\Delta P = P_a - P_b$ is the pressure difference, ρ_w is the density of seawater, h is the water depth and η_b is the water level increase due to pressure differences. η_b has to be such that the pressure at these two points is equal. Equating the equation leads to the following relation:

$$\eta_b = \Delta P / \rho_w g \quad (\text{B.1})$$

As a rule of thumb, the relation $\eta_b = 1.04\delta P$ is used where ΔP is measured in millibars and η_b is measured in centimeter (Dean and Dalrymple, 2004). Observations shows the value of η_b is quite small, for a storm class 5 the surge level due to pressure drop is measured to be around 9 cm.

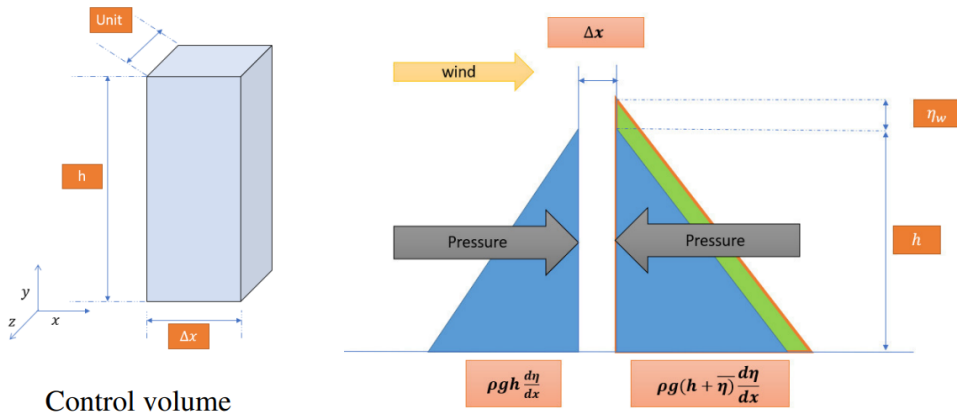


Figure B.2: surge created by the wind stress on the surface.

The empirical formula for the wind stress is $\tau_s = \rho C_f U^2$ where C_f is the friction factor of the wind-air surface and U is the wind velocity. A typical value of C_f is 1.2×10^{-6} to 3.4×10^{-6} (Dean and Dalrymple 1991). Wind stress working on the surface creates a force $\tau_s \Delta x$ acting along the wind velocity. The water column rises η_w to counter the force. The force balance equation is as follows:

$$\frac{1}{2} \rho g (h + \eta_w)^2 - \frac{1}{2} (h + \eta_w + \Delta \eta_w)^2 = (\tau_b - \tau_s) \Delta x \quad (\text{B.2})$$

The force balancing equation then leads to the relation of storm surge with wind velocity

$$\frac{dn_w}{dx} = \frac{\tau_s - \tau_b}{\rho_w g(h + \eta_w)} \quad (\text{B.3})$$

Examining the equation we can deduce that the water depth has a profound implication, the surge level is inversely depended on the water depth (h). The water level changes due to the currents can be described with the equation:

$$\frac{d\eta_c}{dx} = \frac{fv}{g} \quad (\text{B.4})$$

Where f is the Coriolis parameter which is equal to $2\phi\sin\omega$ [ω =angular velocity of earth= 7.272×10^{-5} rad/sec and ϕ is the latitude of the location] and v is the shore parallel depth averaged currents.

The depth averaged along shore velocity v can be estimated from the following equation:

$$v = \sqrt{\frac{8C_f U}{f}} \quad (\text{B.5})$$

The surge level due to pressure drop is very small. Assuming the surge due to pressure changes as zero, we end up with the following equation for a combined storm surge:

$$g(h + \eta)d\eta/dx = (h + \eta)fv + \tau_{sx}/\rho_w \quad (\text{B.6})$$

Where h is the time averaged water depth, η is the magnitude of the surge due to combination of windstress and currents, τ_{sx} is the wind stress normal to the shore and ρ_w is the density of the water.

When the slope of the bed is considered, the equation can be re-written as:

$$g(h + \eta)\left[\frac{d(h + \eta)}{dx} - \frac{dh}{dx} - \frac{fv}{g}\right] = \frac{\tau_{sx}}{\rho_w} \quad (\text{B.7})$$

When $h \gg \eta$ the solution of the equation for η becomes very small which is true for the deep water of the ocean. Based on this observation, we use the boundary condition $\eta = 0$ at the offshore zones. The equation is a steady state condition since no time derivative is found in the equation. However, the input parameters for the storm surge model are time dependent such as the wind speed, currents and water depth.

B.2 Sensitivity analysis of the process-based model

B.2.1. The Effect of Tide

Water level fluctuation due to tide (h_t) is simulated in XBeach as one of the input parameters. Figure B.3 depicts the effect of excluding tide from the model. In our study, area, the tidal range is 70 centimetres, so the effect of the tidal fluctuation on the output of the numerical model appears small. The deviation from the base case is not very high. Both the thermodenudation and thermoabrasion are reduced, and the bluff collapses are delayed as h_{id} values become smaller with lower frequency.

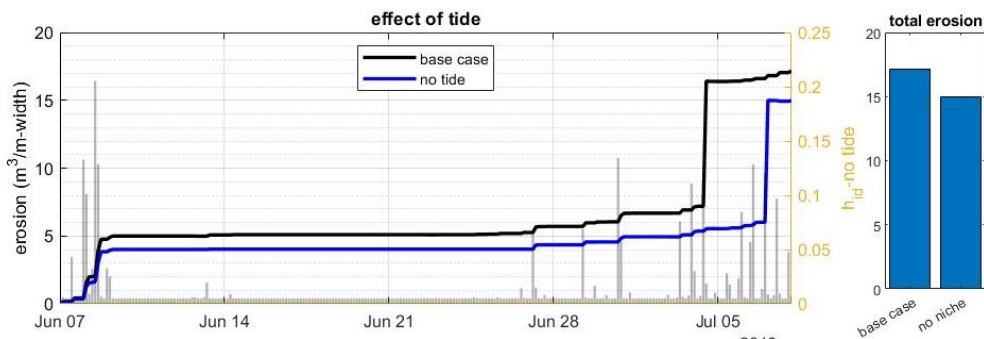


Figure B.3: The effect of tide on erosion.

B.2.2. The Effect of Water Level

The model is highly sensitive to water level (wl , defined using Equation (10)). The incremental water level changes (10 cm) are shown in Figure B.4. The frequency of the bluff collapse is related to the wl . The erosion volume shows a linear relation with the input parameter wl . The erosion volume increases about three times causing a 30 cm elevation in water levels.

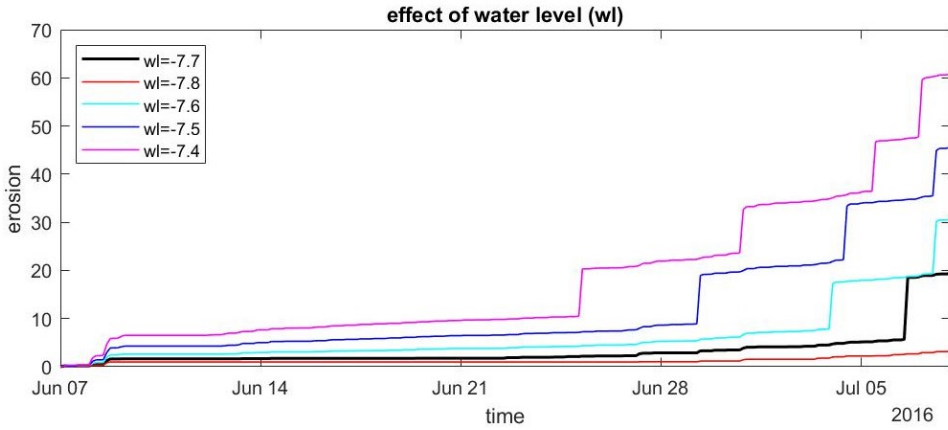


Figure B.4: The effect of water level inputs on erosion.

B.2.3. The effect of water temperature

The effect of sea water temperature is observed on the quicker growth of niche. The result is the faster and bigger bluff collapse.

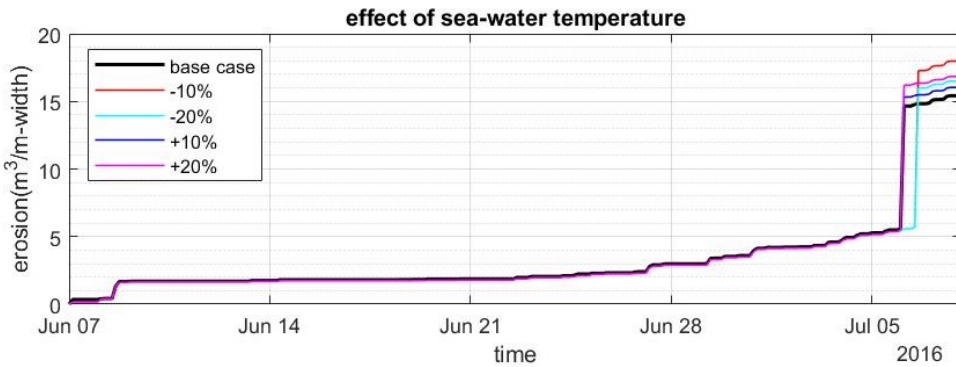


Figure B.5: The effect of water temperature on erosion.

B.2.4. The effect of air temperature

The effect of the air temperature is the increase of thermodenudation. Higher air temperature increases the initial thawing and demonstrated higher erosion rate. However, the erosion is quickly stabilised and no significant difference is observed.

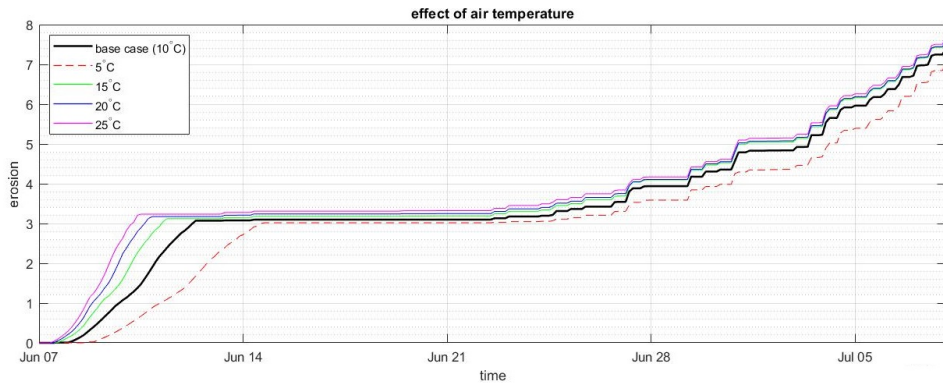


Figure B.6: The effect of air temperature on erosion.

B.2.5. The effect of convective heat transfer coefficient of water

The sensitivity analysis suggest the convective heat transfer coefficient of water has no significant effect on the erosion volume.

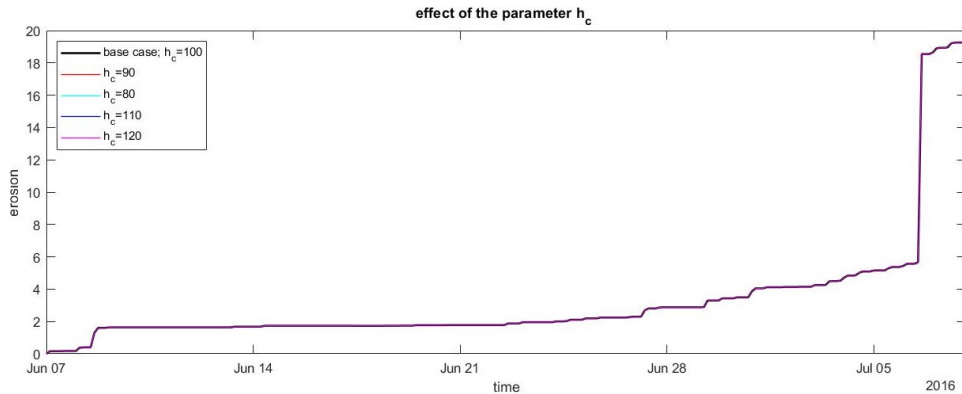


Figure B.7: The effect of convective heat transfer coefficient of water on erosion.

B.2.6. The effect of XBeach parameter 'dry slope'

The XBeach parameter 'dry slope' initiate the avalanching of the sand dune. Even though the Arctic coasts does not have a dune, we applied different values of the parameter to demonstrate that Arctic coasts does not behave like warmer climate. The effect of the parameter is not significant.

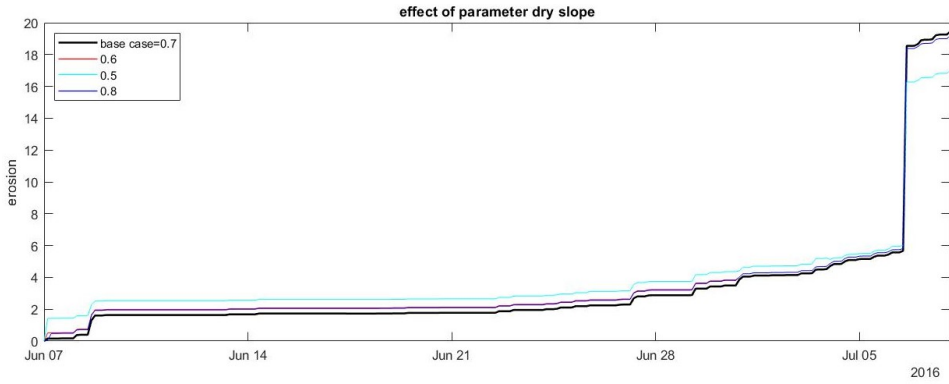


Figure B.8: The effect of convective heat transfer coefficient of water on erosion.



APPENDIX C

Journal papers

C.1 Journal Paper#1

Article

A Probabilistic Model of Coastal Bluff-Top Erosion in High Latitudes Due to Thermoabrasion: A Case Study from Baydaratskaya Bay in the Kara Sea

 Mohammad Akhsanul Islam ^{1,*}  and Raed Lubbad ¹ and Mohammad Saud Afzal ² 
¹ Department of Civil and Environmental Engineering, Norwegian University of Science and Technology, 7491 Trondheim, Norway; raed.lubbad@ntnu.no

² Department of Civil Engineering, Indian Institute of Technology Kharagpur, West Bengal 721302, India; saud@civil.iitkgp.ac.in

* Correspondence: mohammad.a.islam@ntnu.no

Received: 30 January 2020; Accepted: 28 February 2020; Published: 3 March 2020



Abstract: Arctic coastal erosion demands more attention as the global climate continues to change. Unlike those along low-latitude and mid-latitude, sediments along Arctic coastlines are often frozen, even during summer. Thermal and mechanical factors must be considered together when analysing Arctic coastal erosion. Two major erosion mechanisms in the Arctic have been identified: thermodenudation and thermoabrasion. Field observations of Arctic coastal erosion are available in Baydaratskaya Bay in the Kara Sea. The objective of this study is to develop a probabilistic model of thermoabrasion to simulate the measured coastal erosion at two sites where observations suggest thermoabrasion is dominant. The model simulates two time periods: (a) the summer of 2013 (2012–2013) and (b) the summer of 2017 (2016–2017). A probabilistic analysis is performed to quantify the uncertainties in the model results. The input parameters are assumed to follow normal and lognormal distributions with a 10% coefficient of variation. Monte Carlo simulation is applied to determine the erosion rates for the two different cases. The simulation results agree reasonably well with the field observations. In addition, a sensitivity analysis is performed, revealing a very high sensitivity of the model to sea-level changes. The model indicates that the relation between sea-level rise and thermoabrasional erosion is exponential.

Keywords: thermodenudation; thermoabrasion; probabilistic model; permafrost; storm surge; niche growth; bluff collapse

1. Introduction

Almost one-quarter of the land surface in the Northern Hemisphere is permafrost [1]. The thawing of permafrost releases carbon dioxide and methane on the order of hundreds of gigatons [2]. The American and Canadian coastlines exhibit the highest erosion rates throughout the Arctic region [3]. These annual rates are also among the greatest in the world. In Arctic Alaska, the coastal erosion rates reach as high as 15 m/year [4]. However, if annual erosion within the Arctic is considered only within the open water season window (typically spanning three months), the adjusted erosion rates can be eight times greater than those in the Gulf of Mexico [5]. The alarmingly high rate of present-day erosion is expected to increase due to climate warming [6]. The global climate is confronted with a noticeable shrinkage of the sea-ice cover, and the rate of Arctic land warming is 3.5 times greater than the average 21st century warming rates predicted in global climate models [7].

Accelerated erosion rates have been reported throughout the coastal regions of the Arctic corresponding to the broader spatial extent of open water, the longer open water period and the

increased thawing rate of coastal permafrost [8]. Arctic coastal communities are highly affected by rapid coastline retreat, and valuable resources are at risk. Erosion causes large-scale land loss and potential risks to coastal infrastructure, including the oil and gas industry. These conditions are forcing planners to counter the uncertainties and possibilities that arise from rapid erosion [9]. The coastline of the Kara Sea is the longest among all the water bodies within the Arctic Ocean [10] and composes more than one-quarter of the total length of Arctic coastline [11]. Isaev et al. [12] reported erosion rates as high as 29.1 m/year along the coast of the Kara Sea. The mean annual erosion rate along this coast is estimated to be in the range from 0.2 m to 2.0 m per year [13]. Jones et al. [6] reported that the mean annual erosion rate in Alaska along the north-facing coastline between Drew Point and Cape Halkett was 13.6 m/year during 2002 to 2007 and 17.1 m/year during 2007 to 2009.

The mechanisms of Arctic coastal erosion are different from those in warmer regions of low-latitude and mid-latitude [14]. Unlike the coastal erosion occurring on the beaches of low-latitude and mid-latitude coasts, the retreat of coastlines at high latitudes comprises both mechanical and thermal processes. The sediments within bluffs in the Arctic are often permanently frozen. The thawing of permafrost is typically the critical step in the overall sequence of processes leading to coastal erosion. Thermodenudation is the continuous degradation of a frozen coast during the summer by thawing and slump failures. Upon being exposed to warm weather, a portion of a frozen bluff will start to thaw under the impacts of warm air, energy from solar radiation and the melting of snow [15]. When a frozen bluff starts to melt, the mechanical strength of the soil is reduced. At some point, the stability of the slope cannot be maintained, and slope slipping occurs [16]. It was observed that thermodenudation could contribute up to 0.4 m of coastal retreat per year in the Kara Sea, where bluffs are mostly silt and silty clay [17]. On the other hand, thermoabrasion is an episodic yet infrequent phenomenon of Arctic coastal erosion. Bluff failure occurs when a niche destabilises the overhanging portion of the bluff. The mechanical abrasion of the base of the bluffs by the incoming warmer seawater distinguishes thermoabrasion from thermodenudation as water can reach the base of the bluff only during the storms. The three most important environmental parameters responsible for thermoabrasion are the size and position of the ice-wedge polygon and the niche growth rate [18]. Bluff failure can be explained from both geotechnical and hydrodynamic perspectives. From a geotechnical point of view, the authors of [19] proposed that the weight of the overhanging bluff must not exceed the strength of the bluff. Hoque and Pollard [20] proposed a similar model in which bluff collapse can occur along different planes, determined by the mechanical properties of the permafrost and the position of the ice wedge. Kobayashi [21] developed an analytical solution for niche growth during a storm based on the conservation of mass, sediments and salinity. Vidrine [22] developed an integrated solution to the conservation of thermal energy, which was subsequently adopted by Nairn et al. [23] in the software COSMOS 2D. Ravens et al. [24] modelled the erosion occurring at Drew Point, Alaska based on thermoabrasion; they simulated thermoabrasion as a combination of four consequential processes based on simplified physics, and they adopted the [21] model for niche growth. Ravens et al. [24] found that the erosion rate was most sensitive to the elevation of the beach in front of the coastal bluff. Barnhart et al. [4] further improved the model in [24] by using a smaller time-step, relatively more realistic erosion of collapsed bluffs and the application of other niche growth models. Barnhart et al. [4] and Hoque et al. [18] regarded the collapse of the bluff as essentially overturning around the base of the bluff, which was confirmed by field observations. Hoque et al. [18] modelled thermoabrasion as a combination of the tensile strength of frozen soil, the niche depth inside the bluff and the ice-wedge location and depth. However, they did not consider failure along predetermined planes; rather, they postulated that the combination of various environmental parameters determines the failure planes inside the bluff. Isaev et al. [12] estimated the rate of retreat of coastal bluffs based on the relation among the wave energy flux, ground temperature and resistivity of frozen ice-rich material on the premise that the resistivity of frozen materials is significantly higher than that of unfrozen materials. They further observed that wind-driven wave activity during the open water season influences the magnitude of retreat, whereas

recent temperature increases contributed relatively little to coastal retreat during the period of 2005 to 2016 along the coastline of the Kara Sea.

In this paper, we develop a numerical model to simulate coastal erosion due to thermoabrasion. The model is based on recent observations and adopts some of the existing modules cited in the literature. Using the Monte Carlo simulation technique, we run the model thousands of times to perform a probabilistic analysis of coastal erosion at two sites of Baydaratskaya Bay in the Kara Sea. The statistical distributions of the inputs for the model are assumed to be normal and lognormal with a 10% coefficient of variation. The parameters of these distributions are estimated from measurements and data available in the literature. The statistical parameters of the distributions of the output (mean and standard deviation) are presented in this paper and compared with available full-scale measurements. We not only validate the model against in situ data, but also investigate the sensitivity of the model to its input parameters. In the following sections, we introduce the study site and the field data. Thereafter, we describe the governing equations of the numerical model, the numerical scheme and the input parameters for the Monte Carlo simulation. Subsequently, we present the model results and discuss the validity of the model against available data and the sensitivity of the model to changes in the input parameters, and we suggest improvements for further work. Finally, we draw the most important conclusions of this study.

2. Field Measurements of Arctic Coastal Erosion in the Kara Sea, Russia

Field measurements of Arctic coastal erosion are available for the coast of Baydaratskaya Bay situated in the Kara Sea (68.853096° N; 66.891730° E), as shown in Figure 1. The field campaign was started in 2012 with support from the Centre for Research-based Innovation (CRI): Sustainable Arctic Marine and Coastal Technology (SAMCoT). The area has been investigated by Lomonosov Moscow State University (MSU) every year since 2012. The measurements are taken at the end of each summer to record the final shoreline position of the year. Soil temperatures are measured throughout the year using thermistor strings (GeoPrecision, Ettlingen, Germany) placed within boreholes drilled in 2012 and 2013. Once summer ends, the shore is covered with snow, and the sea freezes, where sea-ice will also be covered with snow. The sea along the shoreline has a depth of around 10 m which enables large storm surges in the summer (one of the prerequisites for the thermoabrasion process). The region is sporadically populated with very limited infrastructure. The study site is located at a distance of 3.6 km in the northwest (NW) direction from the cofferdam of the Bovankenkobo-Uhta gas pipeline [25].

2.1. Geomorphology and Cryology of the Study Area

The Baydaratskaya Bay, situated between the Yugra Peninsula and the Yamal Peninsula, is approximately 350 km long and 250 km wide at its mouth. The study area lies in the northern geocryological zone and features practically continuous permafrost. Three major geomorphological features are distinguishable within the study area: beaches, laida and bluffs. The beaches are sandy and not wider than 50 m. Bluffs with elevations in the range of 4 to 6 m (sandy clay deposits) are termed zone S1, and those with elevations of 12–17 m are termed zone S2 (see Figure 2). The native term “laida” describes a treeless part of the tundra terrain with peat substratum, permafrost close to the surface and covered with low shrubs, mosses and liverworts. The spatial extent of the laida zone is around 500 m along the coast and has been stable in recent years, and is thus excluded from this study. Field measurements have been conducted each year beginning in 2012 with Trimble differential global positioning system (DGPS) equipment in two places: (a) low bluff zones (S1) and (b) high bluff zones (S2) (see Figure 2a). The elevation measurements extend typically a distance of 2 m to 3 m into the open water and the shoreline is noted in the measurements. The exact position of the shoreline at mean sea level is determined via the standard procedure of linear regression of the Lidar data. In total 11 cross-sections were profiled each year. In some of these cross-sections,

thermoabrasion was the dominant erosion mechanism. The bluff retreated over a range of 10 to 60 m (average value of 30 m) during the 7 years of observations [25].

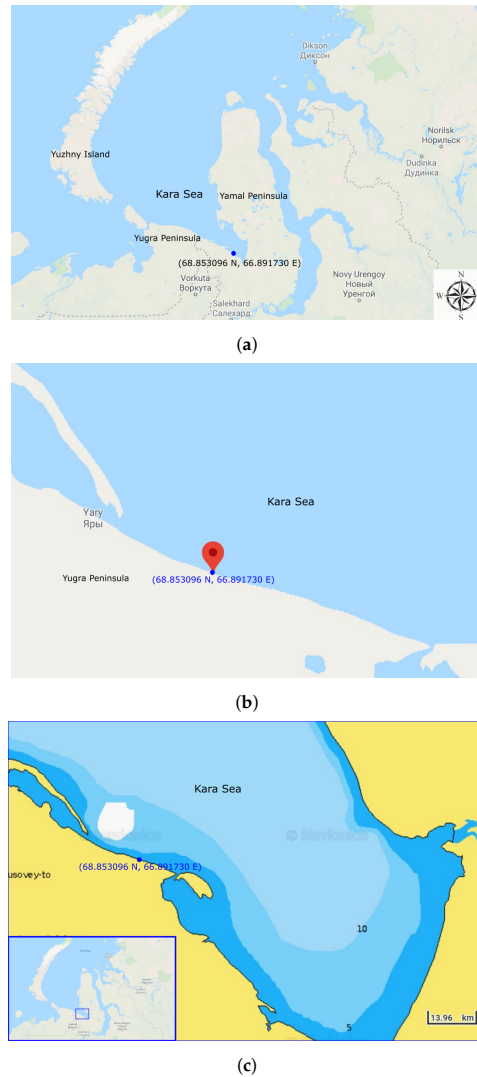


Figure 1. The study location is situated along the coast of the Kara Sea and in between the Yugra Peninsula and the Yamal Peninsula. The sea is shallow and funnel-shaped, which makes it susceptible to large storm surges (image source: a and b: Google Earth and c: [navionics.com](https://www.navionics.com)). (a) The study location is along the Kara sea (68.853096° N, 66.891730° E). (b) The beach is located near the 69° N latitude; straight but the orientation is around 45° with horizontal line. (c) Bathymetry of the study area. Near the shore, the depth is 10 m.

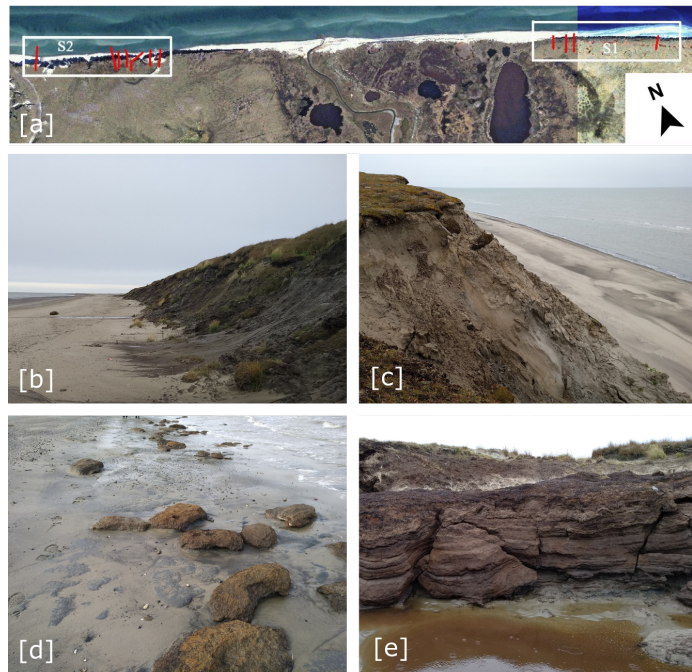


Figure 2. (a) Beach profile lines in zone S1 and zone S2 (thick red lines) from the surface of the bluff to the swash zone of the beach. (b) Bluff in zone S1 and (c) bluff in zone S2. Zone S1 has an uneven bluff surface, a relatively gentle bluff slope and a wide and smooth beach (subfigure (b)), whereas zone S2 comprises a steeper bluff slope and a narrower beach (subfigure (c)). (d) Remnant of an earlier collapsed bluff. Sizes of the collapsed bluff are not big enough to disrupt storm surge and to prohibit the growth of niche at the base of bluffs. However, the active layer with dead vegetation still resists degradation, whereas the rest of the collapsed bluff eroded. (e) Niches in the bluff face. The uneven shape of the niche indicates various levels of storm surges. (image source: (panel (a): [25] and panels (b–e): authors, summer, 2019)

Zone S2 is composed of dusty marine sands with a 5 mm thick peat layer and a 10 cm thick ice layer. The land surface in zone S1 is rough and complicated by extensive lake basins in different stages of development. In contrast, the land surface of zone S2 has fewer thermokarst lakes and is covered by a network of ice-wedge polygons [25]. The changes in a typical beach profile in recent years are shown in Figure 3.

2.2. Physical Parameters and Environmental Forcing

The beaches in the study area are 15 m to 50 m wide and are smooth with slightly sloped (0.0015 to 0.0025) sand surfaces lacking vegetation. The bases of the bluffs on the beaches are 1.8 m to 2.3 m above mean sea level. The tidal range of the study area is 0.7 m [26]. Waves reach the base of the bluffs when the storm surges levels are in the range of 1.5 to 2 m. The entire research area is covered by moss and moss-lichen tundra in combination with other types of Arctic tundra [25].

The bay is typically ice-free until the end of September due to thermohaline stratification from warmer and saltier water coming through the Kara Strait [26]. The bay has a salinity range of 20–25 ppt [27]. The tidal currents do not exceed 0.3 m/s [26]. The bay has a depth of less than 10 m near the shore. The currents near the area of interest lie in the range of 0.18 to 0.25 m/s with marginally

higher velocities during flooding events [28]. Storm surges in the region can reach 2 m [29], and the root-mean-square wave height (H_{RMS}) is found to range from 1.3 m to 1.8 m with a peak period of approximately 6 s. The historical rate of recession of the site varies from 0.5 to 1.5 m/year.

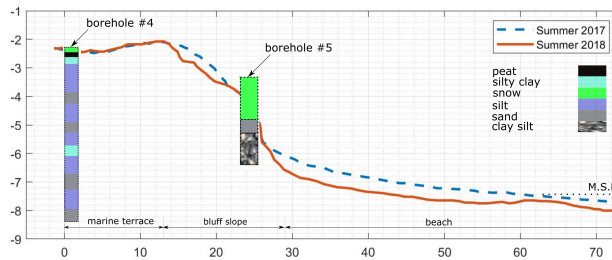


Figure 3. Typical cross section at zone S1 depicting the positions of the boreholes. The boreholes are equipped with thermistor strings to measure the temperature every ten minutes at various levels [25].

3. Conceptual Model of Thermoabrasion

A typical coast with simplified features is considered for the development of the conceptual model (shown in Figure 4). The coast consists of a high, frozen bluff with a narrow beach in front of it. In the calm conditions, the wave run-up does not touch the base of the bluffs. Therefore, only thermodenudation of the bluff is possible: thermoabrasion is possible only when there is water at the base of the bluff. As the base of the bluff is one to few metres above the mean sea level, only during the storm when the surge is significant (1.5–2 m) water reaches the base of the bluffs. Thus, thermoabrasion is episodic and only occurs at the extreme events.

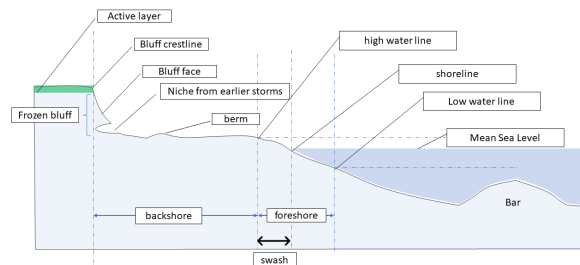


Figure 4. Schematic of a typical Arctic coast. A frozen bluff stands at the end of the beach. Storm surges can flood the beach and reach the base of the bluffs where a niche forms.

In calm conditions, waves are assumed to break on the beach in front of the frozen bluff and wave hydrodynamics triggers the morphological changes of the beach, which are unrelated to thermoabrasion. During the storm, the beach is submerged and waves with higher energy breaks on the beach due to depth limitation before reaching the base of the bluff. The effect of the waves, return current and erodibility of the soil allows a niche growth at the base of the bluff. As long as there is water at the base of the bluffs, the niche grows inwards. At a critical niche depth, the hanging bluff loses its stability and collapses.

The depth and shape of the niche and growth rate of the niche are influenced by the wave during the storm. The information of the wave is estimated from the water depth since the waves are depth limited on the beach in a similar way the waves are depth limited at surf zone. The depth of the water indirectly determines the wave condition at the base of the bluffs, and thus the extent of a niche inside the bluff can be directly related to the storm surge level (empirical and analytical solution of niche

growth is discussed in Section 3.2). The fine sediments cannot sustain the wave actions, and therefore they are transported offshore by return currents. Only relatively coarse sand remains on the beach. The beach is above mean sea level, so water cannot reach the base of the bluff except during the storm. Thawed sediments on the lower part of the beach are removed during high tides.

3.1. Storm Surge Module

A one-dimensional simplified storm surge model is adopted to calculate the increase in the water level (η) (see Figure 5) from the mean seawater level (M.S.L.). The water level rises during a storm due to barometric pressure gradients in the low-pressure storm, the stress coming from wind flows, the Coriolis force induced by earth rotation, and the shape of the bay and the wave set-up. The 1D model described here can not capture the shape of the bay. We also exclude the effect of pressure gradient as the surge level due to the pressure drop is small (less than 10 cm). The generation and propagation of waves during the storm and their effect on the beach profile are omitted from the model since we only focus on the niche at the base of the bluff. The waves are depth-limited on the beach during storms [21], and they break on the narrow beach before reaching the base of the bluff. It is computationally less demanding to estimate only the surge and the inundation depth (h_{id}) at the base of the bluff and assume the wave conditions rather than to simulate the evolution of waves from offshore.

The cross-shore steady-state solution of the equation of motion of Dean and Dalrymple [30] (given in Equation (1)) for a straight and long coast is used as the basis of the storm-surge module:

$$g \cdot (h + \eta) \cdot \left[\frac{d(h + \eta)}{dx} - \frac{dh}{dx} - \frac{f \cdot v}{g} \right] = \frac{\tau_{sx}}{\rho_w} \quad (1)$$

where h = beach water depth, η = increased water level due to storm, g = gravitational acceleration, x = offshore-directed position coordinate, f = Coriolis parameter equal to $2\Omega \sin\phi$ (Ω = angular rate of rotation of the Earth = $7.272 \times (10)^{-5}$ rad/s), ϕ = latitude of the considered site, v = magnitude of the depth-averaged currents parallel to the shore, dh/dx = slope of the seabed, ρ_w = water density (variation due to temperature ignored) and τ_{sx} = shore-normal shear stress on the surface of the water from the wind, calculated as $\tau_{sx} = \rho_w C_D U_{10}^2$, where $C_D \approx 2 \times 10^{-6}$ is a drag coefficient and U_{10} is the shore normal wind speed at 10 m elevation. Wave-induced set-up and pressure induced surges are not included in this equation.

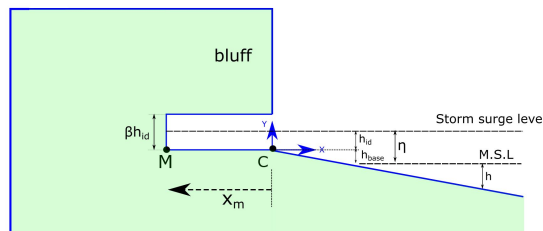


Figure 5. Definition of geometrical parameters to estimate the growth of the niche (as per the work in [21]). Point C in the figure is the origin of coordinates (0,0), x_m = the depth of niche, h_{id} = the inundation depth at the base (assumed constant during the time-step of the global model and calculated as $h_{id} = (\eta - h_{base})$, M is the niche melting front advancing inward, and βh_{id} is the opening of the niche.

3.2. Niche Growth Module

When the water level reaches the base of the bluff during a storm surge, a niche forms. The niche grows into the bluff; ice present within the bluff starts to melt and some sediments may be extruded. A strong return current generated by the storm washes away these sediments. The analytical solution

of niche growth at the base of the bluffs during a storm surge is developed in [21] (given in Equation (2)). Three conservation equations of mass, salinity, and sediments are used to establish the rate of niche growth. To reach the solution, few assumptions are made: (i) waves are depth-limited close to the base of the bluff that means waves break before reaching the base of the bluffs; (ii) the water depth is constant during the growth of the niche; and (iii) the diffusivity constants for the momentum, salinity, and sediment concentration are the same as those in the surf zone given by Longuet-Higgins [31] as $\epsilon = Ah(gh)^{0.5}$ (where the empirical parameter $A = 0.4$ and h is the water depth at surf-zone).

The opening of the niche is assumed to be βh_{id} (see Figure 5); Kobayashi [21] suggests the typical value of β to be 2. In the model of Kobayashi, the wave conditions near the base of the bluff is estimated from the water depth (h_{id}). Although the assumption of constant water depth at the base of the bluff is required to derive Equation (2), our thermoabrasion module is capable of handling variable water depth by treating it as constant only within each time-step of 600 s. This makes Equation (2) to be applicable within the time step and allows the calculation of the niche depth and height relative to the current water depth.

The major input parameters of niche growth modules are given in Table 1.

Table 1. Input parameters for the niche growth model.

Parameter	Symbol	Estimated Value	Remarks
Physical properties			
Inundation depth	h_{id}	-	to be calculated
Salinity of the seawater inside the niche	S	0.03 ppt	no salt in the ice inside the bluff
Salinity of the ice inside the bluff	S_i	0	assumption
Suspended sediment (initial)	C	0	assumption
Porosity of the frozen sediments	n	0.4	assumption
Density of ice	ρ_i	916 kg/m ³	
Density of sediments	ρ_s	2650 kg/m ³	measurement
Density of water	ρ_w	1010 kg/m ³	
Specific heat of suspended sediment	C_s	0.8374 kJ/kg-K	[4]
Specific heat of seawater	C_w	4.187 kJ/kg-K	
Specific heat of ice	C_i	2.108 kJ/kg-K	
Latent heat of ice	L_i	334 kJ/kg	
Initial conditions			
Sediment concentration	C_a	0 kg/m ³	[21]
Salinity concentration	S_a	30 ppt	measurements
Temperature	T_a	3 °C	measurements (averaged)
Empirical constant of Josberger	m	0.06 °C per ppt	[21]
Salinity of the melting point	S_m	-	to be calculated
Momentum diffusivity at the melting point	η_a	-	to be calculated
Opening of niche (empirical)	β	2	[21]
Empirical parameter of the diffusivity index	A	0.4	[31]

Kobayashi et al. [21] reached an analytical solution with these above mentioned input parameters, expressed as follows,

$$x_m = 2 * \zeta_m * (\epsilon t)^{0.5} \quad (2)$$

where x_m = the niche depth (see Figure 5), t = duration of contact of the water at the base of bluff, ζ_m = an empirical parameter related to temperature and ϵ is the diffusivity index, which is determined by the empirical formula of Longuet-Higgins [31] as $\epsilon = Ah(gh)^{0.5}$. Kobayashi [21] determines if the suspended sediment concentration before the storm is zero and salinity of the seawater is 30 ppt, the value of ζ_m can be approximated to $\zeta_m = 0.0094T_d$, where T_d is the difference in temperature between the incoming water temperature and ice melting temperature inside niche (0 °C). Equation (2) represents two driving forces of the thermoabrasion. The parameter ζ_m represents the thermal component and ϵ represents the inundation depth and mechanical abrasion by the storm surge.

3.3. Bluff Collapse Module

The bluff collapse module is adopted from Barnhart et al. [4] to simulate bluff failure. The model considers the relatively low tensile strength at the ice-wedge boundary. This bluff collapse module is sensitive to the position of the ice-wedge boundary. Therefore, the distribution of ice-wedge polygons at the site is an important parameter for the module. The niche depth at which the bluff collapses is termed the critical niche depth (x_p). As shown in Figure 6, bluff collapse is determined by the balance of moments around the base of the bluff (point M):

- the resisting moments, i.e., the self-weight, $T_r = \rho_b g \int_0^{y_{top}} \int_{x_{edge}}^{x_p} (x_p - x) dx dy$
- the moment from the force acting at the vertical failure line, $T_f = \int_0^{y_{base}} \tau_i (x_{edge} - x_p) dy$
- the moment from the force acting at the horizontal failure line, $T_b = \int_{x_{edge}}^{x_p} \tau_b (x_p - x) dx$
- the moment from the weight of the overhanging bluff, $T_d = \rho_b g \int_{y_{base}}^{y_{top}} \int_0^{x_p} (x_p - x) dx dy$

where x_p = niche depth at which the stability is lost, x_{edge} = position of the ice-wedge polygon from the base of the bluff, y_{base} = y coordinate of the top of the niche growth melting point, y_{top} = y coordinate of the top of the bluff, ρ_b = density of the bluff, g = gravitational acceleration, τ_b = the tensile strength of the frozen bluff and τ_i = tensile strength of ice.

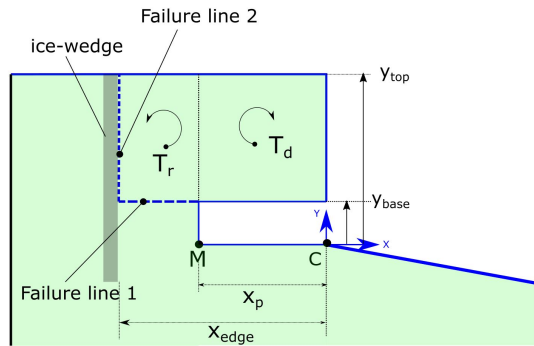


Figure 6. Stability of an overhanging bluff over a niche. Two failure lines are marked 1 (horizontal) and 2 (vertical). The forces acting along the horizontal failure line creates moment T_b at the base of the bluff and forces acting along the vertical failure line creates moment T_f . The moment from the overhanging portion (T_d) is the counterbalancing moment for destabilisation and the rest of the block volume is providing the resisting moment T_r . The balance is lost when $T_d > T_r + T_b + T_w$.

The governing equation for the stability is given in Equation (3):

$$\rho_b g \int_{y_{base}}^{y_{top}} \int_0^{x_p} (x_p - x) dx dy = \rho_b g \int_0^{y_{top}} \int_{x_{edge}}^{x_p} (x_p - x) dx dy + \int_{x_{edge}}^{x_p} \tau_b (x_p - x) dx + \int_0^{y_{base}} \tau_i (x_{edge} - x_p) dy \quad (3)$$

After the failure of the bluff, the collapsed block is disregarded from the model and the bluff is exposed immediately to the water.

3.4. Numerical Scheme

For the numerical parameterization of the governing equations, an explicit Euler scheme is used. The numerical model has a time step of 10 min (600 s) for the three modules. The grid size is 1 m for the storm surge module and bluff collapse module, but a higher spatial resolution (10 cm) is used for the niche growth module since this module is more sensitive. The algorithm for the interaction

between the three modules is explained in Figure 7. The major input parameters for the storm surge module other than the global physical parameters are the bathymetry and shore normal wind speed measured at 10 m elevation. The storm surge module calculates the surge level (η) for the particular time step using Equation (1). Then, inundation depth (h_{id}) is calculated, and if only the value of h_{id} is greater than zero (the condition: water reached the base of the bluff is satisfied), it is passed on to the niche growth module as an input parameter. The niche growth module calculates the depth of the niche (x_m) and passes it to the bluff collapse module. The bluff collapse module checks the stability of the bluff for that time step. If the bluff is stable, no erosion is recorded and the global model moves to the next time step. Table 2 summarises the major input and output parameters of the three modules.

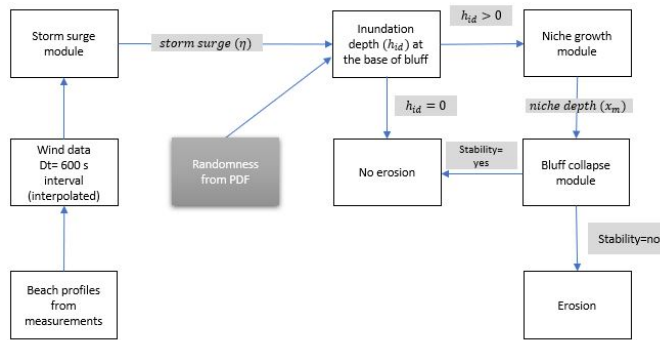


Figure 7. Algorithm of the model with three numerical modules and Monte Carlo simulation.

Table 2. Major input and output parameters of the three modules.

Module	Input	Output	Remarks
Storm surge module	Bathymetry, wind speed and sea-water density	For every time step	1D line model, quasi-static equation
Niche growth module	Storm surge level (η), inundation depth (h_{id}) as defined in Figure 5, temperature of seawater, and diffusivity index Equation (2)	For every time step	1D, not an empirical formula, based on conservation of mass, energy and salinity
Bluff collapse module	Tensile strength of bluff and ice, bluff height and ice content in bluff	Stability	2D model, highly dependent on the geometry of frozen bluffs

The wind data are obtained from the hindcast model of the NCEP Climate Forecast System Reanalysis (CFSR) provided by the National Oceanic and Atmospheric Administration (NOAA) and downloaded through the Danish Hydraulic Institute (DHI) website.

3.5. Probabilistic Model of Arctic Coastal Erosion

To account for the uncertainties in the input parameters, a probabilistic analysis based on Monte Carlo simulation is carried out. The algorithm of the probabilistic approach is shown in Figure 7. Two assumptions are made: (1) the environmental parameters are independent, i.e., the correlation is set to null, and (2) the coefficient of variation (CoV) is set to be 10%, whereas most of the distributions of the input parameters are considered to follow a normal distribution (details of the distributions and related statistical parameters are shown in Table 3). One-thousand runs are performed for the Monte Carlo simulation using the algorithm depicted in Figure 8.

The parameters of the probabilistic distributions used for the major parameters are given in Table 3.

Table 3. Distributions of the input parameters for the numerical model. Here, $N[x,y]$ = normal distribution with a mean of x and a standard deviation of y , $D[z]$ = deterministic value of z and $\text{Log N}[x,y]$ = lognormal distribution with a mean of x and a variance of y .

Parameter	Symbol	Distribution
Bluff height	$y_{top} - y_0$	$N[5.2,0.52]$ for case #1 $N[14,1.4]$ for case #2
Inundation depth	h_{id}	deterministic [calculated]
Ice-wedge size	x_{edge}	$N[14,1.4]$
Salinity of seawater	S_a	$N[30,3]$
Porosity of frozen sediments	n	$D[0.4]$
Density of ice	ρ_i	916 kg/m^3
Density of sediments	ρ_s	$D[2650 \text{ kg/m}^3]$
Seawater temperature	T_a	$N[\text{monthly mean, 10\% cov}]$
Friction factor	c_f	$D[1 \times 10^{-6}]$
Longshore current	v	$N[1,0.1]$
Beta (Kobayashi formula)	β	$N[2,0.2]$
Tensile strength (ice)	T_i	$\text{Log N}[1 \times 10^4 \text{ Pa, } V = 100]$
Tensile strength (bluff)	T_b	$\text{Log N}[2 \times 10^4 \text{ Pa, } V = 200]$

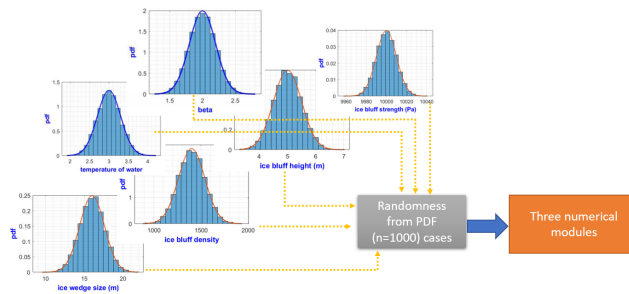


Figure 8. Generation of cases for the Monte Carlo simulation.

4. Results and Discussion

Field measurements are available for eleven profiles at the Baydaratskaya Bay. Isaev et al. [25] reported that both the thermodenudation and thermoabrasion mechanisms are active in the study area. The model can not be applied to all the profiles because some profiles were measured while covered with snow (mostly in the year 2014 and 2013). The profiles are analysed based on the three geometric criteria:

- horizontal crest retreat (cr),
- average slope of bluff face (s) and
- height of the bluff (bh)

In Figure 9, these parameters are defined as

- the average slope of the bluff face (s) after the retreat, $s = (y_1 - y_2)/(x_1 - x_2)$
- the average slope of the bluff face (s) before the retreat, $s = (y_{1'} - y_{2'})/(x_{1'} - x_{2'})$
- the bluff heights (bh) are defined as, $bh = y_1 - y_2$ and $bh' = y_{1'} - y_{2}'$
- the horizontal crest retreat (cr) is defined as, $cr = x_{1'} - x_1$

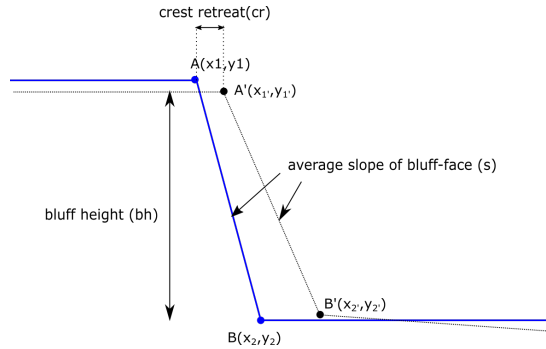


Figure 9. Definition of the horizontal crest retreat (cr), the average slope of the bluff-face (s) and the height of the bluff (bh). The bluff retreated from $A'B'$ line to now AB line. The crest retreated from point $A'(x_1', y_1')$ to $A(x_1, y_1)$ whereas the base retreated from $B'(x_2', y_2')$ to $B(x_1, y_1)$.

Crest retreat (cr), bluff height (bh) and slope of the bluff-face (s) of the 11 profiles are summarised in Table 4. As the profiles are not continuously measured during the open water season, it is not possible to accurately attribute the annual erosion rate to thermodenudation and thermoabrasion. Field observations suggest thermoabrasion is the dominating erosion mechanism where the slope of the bluff-face is steep (enables bluff collapse) and the crest retreat is high (episodic, infrequent and high erosion). Out of all the profiles, the following 16 cases shown in Figure 10 are retained when we apply the filter: $s > 0.1$ and $cr > 0.1$ m. The top right corner of the figure indicates a high annual crest retreat and steep bluff-face slope: two indicators of thermoabrasion.

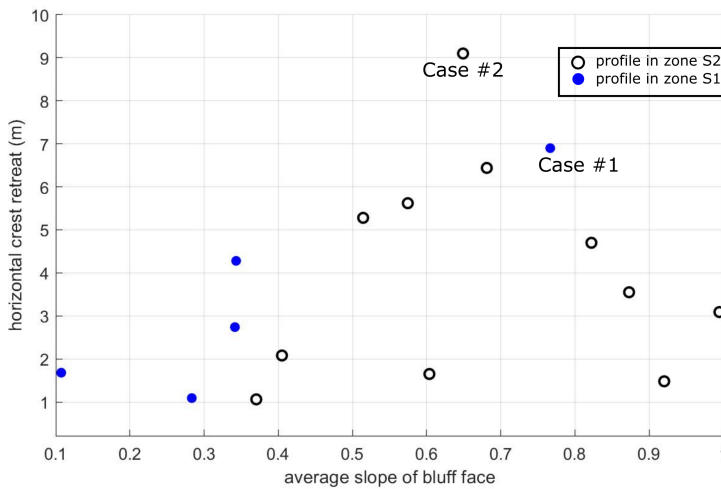


Figure 10. Thermoabrasion is the dominating erosion mechanism for the cases in the top-right zone (steeper slope and higher erosion rate). Two cases are chosen from zone S1 and zone S2 such that the crest retreat is very high compared to the other profiles and the average slope of the bluff-face is steeper.

Table 4. Crest retreat (*cr*), bluff height (*bh*) and slope of the bluff-face (*s*) of the 11 profiles during 2012 to the 2017. “n.a” in the table indicates data not available.

Profile Number	Parameter	2017	2016	2015	2014	2013	2012
1	s	0.38	0.34	0.28	n.a	n.a	0.77
	cr	n.a	4.28	1.09	2.05	1.01	6.90
	bh	5.63	6.21	6.78	−0.12	−0.12	5.47
2	s	0.41	0.25	n.a	0.04	0.03	−0.02
	cr	n.a	−5.49	n.a	n.a	8.39	5.89
	bh	4.04	4.97	n.a	−1.28	−1.12	1.09
3	s	0.23	0.34	0.26	0.11	0.09	n.a
	cr	n.a	2.74	−2.06	1.68	−0.16	n.a
	bh	4.37	3.74	3.86	3.35	−1.41	0.10
4	s	0.19	n.a	0.72	0.12	0.12	−0.09
	cr	n.a	n.a	n.a	−1.53	−5.82	7.74
	bh	3.11	n.a	3.43	−2.37	−1.67	1.82
5	s	0.84	0.92	1.13	n.a	n.a	n.a
	cr	n.a	−0.69	n.a	0.23	n.a	n.a
	bh	13.73	13.94	12.89	15.25	n.a	n.a
6	s	0.56	0.65	0.60	n.a	n.a	n.a
	cr	n.a	9.10	1.65	2.02	−0.54	n.a
	bh	14.84	13.77	13.92	8.82	9.32	n.a
7	s	0.31	0.57	0.99	n.a	n.a	n.a
	cr	n.a	5.62	3.09	−0.33	0.98	n.a
	bh	13.47	12.92	11.27	5.61	5.76	n.a
8	s	0.89	0.96	0.92	n.a	n.a	n.a
	cr	n.a	−0.54	1.48	−1.75	0.27	n.a
	bh	9.86	9.61	9.43	4.81	4.90	n.a
9	s	0.88	0.87	0.02	n.a	n.a	n.a
	cr	n.a	3.55	1.21	−1.88	n.a	n.a
	bh	10.77	10.91	0.19	6.04	n.a	n.a
10	s	0.36	0.31	0.37	n.a	0.51	n.a
	cr	n.a	−0.36	1.06	0.17	5.28	n.a
	bh	13.68	13.49	12.52	6.76	12.37	n.a
11	s	0.48	n.a	0.68	0.82	0.40	n.a
	cr	n.a	2.35	6.44	4.70	2.08	n.a
	bh	14.80	7.96	14.25	12.47	12.88	n.a

Two profiles are selected for numerical modelling, namely, Case #1 (zone S1) and Case #2 (zone S2) (shown in Figures 11 and 12, respectively), where observation suggest that thermoabrasion is the dominating erosion mechanism and thus suitable for our current model.

Cases #1 and #2 originate from different time periods and exhibit different geological characteristics (average bluff heights of 5.2 m vs. 14 m, respectively), making the assumption of mutual exclusivity reasonably valid. Case #1 is chosen from the low-lying bluffs with an average height of 5 m. The profile was measured at the ends of the summer seasons of 2012 and 2013. As the sea and the coasts are covered during the rest of the year, bluff erosion can be possible only during the summer. Therefore, for Case #1, the erosion measured along the profile occurred in the summer of 2013. Similarly, for Case #2, the measurements were completed at the ends of the summer seasons of 2016 and 2017, indicating that the erosion measured in Case #2 occurred during the summer of 2017. The niche is more prominent at the location of Case #2 than at that of Case #1 [25]. The wind roses of the two time periods indicate the storm’s directions are almost perpendicular to the coast which satisfies the limitation of the 1D model condition.

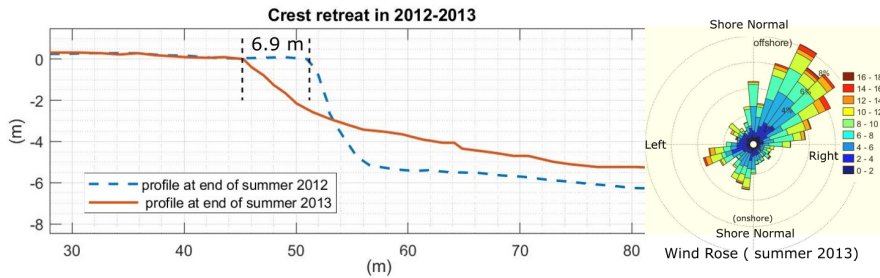


Figure 11. Case #1: The profile is situated in zone S1. Crest retreat of 6.9 m is recorded at the end of the summer of 2013. The wind rose diagram derived from the wind speed data of summer 2013 is shown at the right panel. The diagram is adjusted 49.28° so that shore-normal (offshore) direction is in the top. The wind rose diagram indicates that the dominating wind direction is inclined about 30° towards the shoreline.

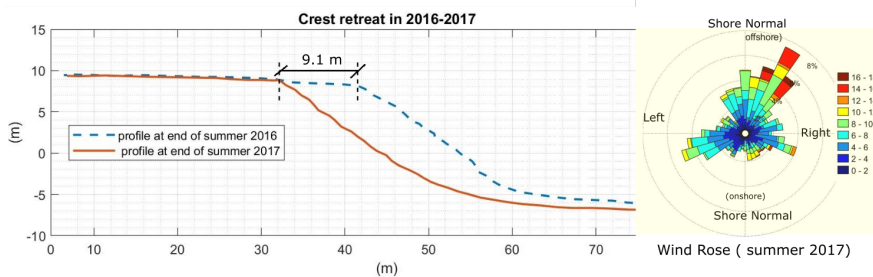


Figure 12. Case #2: The profile is situated in zone S2. Crest retreat of 9.1 m is recorded from the end of the summer of 2017. The wind rose diagram of summer 2017 (adjusted to the shore-normal (offshore) position) indicates, dominating wind direction is the same as that of summer 2013. However, the wind speed is considerably higher for Case #2.

4.1. Determination of Crest Retreat in the Two Cases

The three numerical modules mentioned in Sections 3.1–3.3 are coupled together to simulate crest retreat due to thermoabrasion. Degradation of the collapsed bluff is not explicitly modelled as mentioned earlier in Section 3.3, as the field observations suggest the size of the collapsed blocks on the beach are not significantly large enough to halt the incoming seawater during the storm and to prohibit the development of niche at the base behind it [25]. The probabilistic model calculates erosion due to storm surges for one thousand cases; each iteration is different from the others. The output of the numerical model is composed of one-thousand erosion rates per year, which are normally distributed.

Case #1: Crest Retreat during Summer of 2013

Crest retreat of 6.9 m was measured during the period of 2012–2013 at the mouth of the Sabryavpenzya River, which is termed Case #1, as shown in Figure 11. The model calculates the crest retreat one-thousand times for the Monte Carlo simulation. The value of the crest retreat is considered a random variable following a normal distribution. The mean crest retreat with a 95% confidence limit is calculated to be 6.67 m with a standard deviation of 0.39 m whereas 6.9 m was

recorded in the field measurements. Figure 11 shows the measured bed profile for Case #1, whereas subfigure *d* in Figure 13 shows the cumulative mean erosion during the summer of 2013.

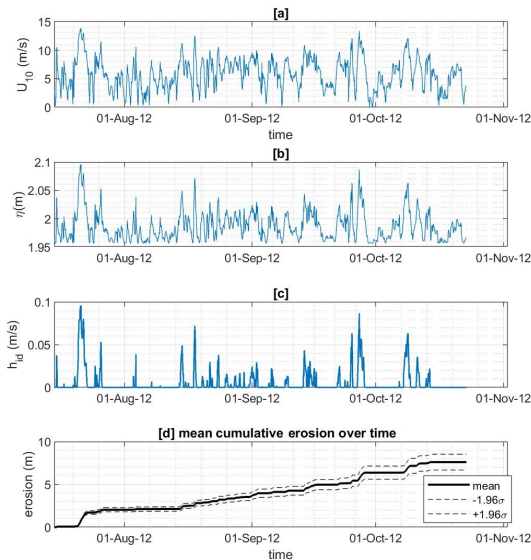


Figure 13. Cumulative erosion over the summer of 2013 in Case #1. Subfigure (a) displays the wind speed during the summer of 2013. The wind speed data are the major input for the storm surge module which calculates the storm surge level shown in subfigure (b), which in turn is used to find the inundation depth h_{id} in subfigure (c). Finally, the coastal erosion overtime is calculated for each case of $n = 1000$ in the Monte Carlo simulation. The distribution of the calculated erosion rate follows a normal distribution. Shown in the subfigure (d) are the mean erosion (thick black line) with $\pm 1.96 \sigma$ drawn as dotted lines ($\sigma =$ standard deviation).

Case #2: Crest Retreat during the Summer of 2017

The crest retreat to the left of the mouth of the Sabryavpenzya River was measured to be 9.1 m during the period of 2016–2017 [12]. This part of the coast has higher frozen bluffs (14 m) than the bluffs in Case #1, and the slope of the bluff face is almost vertical. Similar to Case #1, one-thousand samples of input parameters are generated for the Monte Carlo simulation, and the erosion is calculated as a random variable which follows a normal distribution. A mean erosion of 8.31 m is calculated with a standard deviation of 0.49 m. Figure 14 shows the mean cumulative erosion time series.

The numerical model determined the erosion rates for the two different cases (as detailed in Table 5). The assumption of mutual exclusivity is validated from the erosion patterns of the two cases. Case #1 shows many small storms in 2013 that almost continuously caused erosion throughout the summer season, whereas the profile of Case #2 shows only a few early storms in 2017 that caused abrupt but short-term erosion; few events occurred throughout the rest of the summer season. It is also observed that the numerical model underestimates the erosion by 3.4% for Case #1 and 8.8% for Case #2. The numerical model considers only thermoabrasion, which is a simplification of reality since other erosion mechanisms certainly exist. This may be the reason why the numerical

model underestimates the erosion relative to the field measurements. However, the model performance serves as proof of concept, and the behaviour is found to agree with the expected real-world physics.

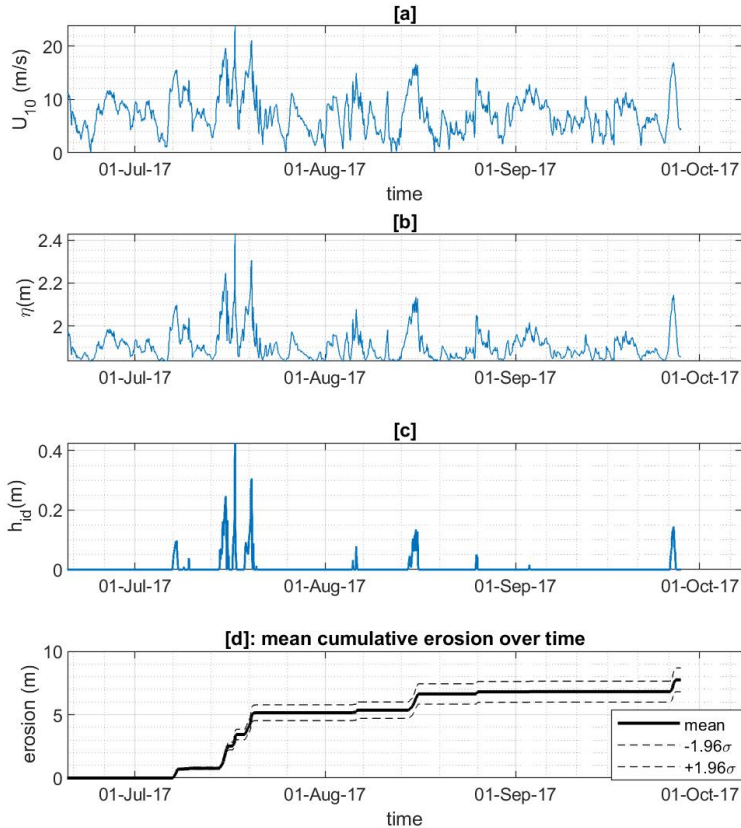


Figure 14. Cumulative erosion over the summer of 2017 in Case #2. The wind speed data are shown in subfigure (a). Using the storm surge module, the surge levels are calculated (subfigure (b)). With the inundation depth, h_{id} calculated in subfigure (c), the erosion is calculated accordingly (shown in subfigure (d)). The crest retreat is calculated for $n = 1000$ cases in the Monte Carlo simulation. The outcome of the global model is one thousand calculated crest retreat values which follow a normal distribution. The mean erosion is drawn as a thick black line with $\pm 1.96 \sigma$ drawn as dotted lines to show how the uncertainty of the prediction increases over time.

Table 5. Summary of erosion in the two cases.

Case	Measured Results		Field Measurements	Deviation (%)
	Mean	Standard Dev.		
Case #1	6.6694 m	0.3903	6.9 m	3.4%
Case #2	8.3050 m	0.4868	9.1 m	8.8%

4.2. Sensitivity Analysis

The numerical model developed in this study considers only thermoabrasional erosion, and thus cannot be applied universally. As this model works in a data-poor environment, a proper understanding of the responses of the numerical model must be achieved. A sensitivity analysis was performed on the probability of bluff failure (shown in Figure 15). It is found that the probability of bluff failure ranges from null to negligible during the first three hours of the storm. Afterwards, the probability of failure exhibits a linear relation with the duration of the storm and niche growth.

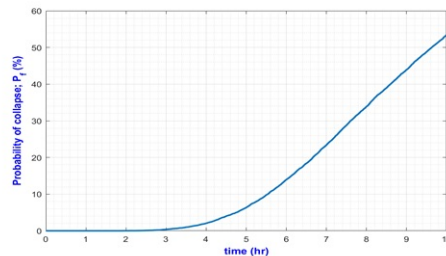


Figure 15. Probability of bluff collapse during a storm.

The sensitivity analysis results of the other variable environmental conditions are shown in Table 6.

The model is sensitive to the critical niche depth (x_p); a shorter critical niche depth increases the rate of erosion. The critical niche depth is dependent on the ice-wedge polygon size (x_{edge}). A sensitivity analysis of the Barnhart [4] model indicates that the relation between x_p and x_{edge} is linear; a larger polygon size increases the critical niche depth and thus decreases the probability of bluff failure.

Table 6. Sensitivity of the erosion rate to variations in model parameters compared to the base case of 2012–2013.

Change in Parameter	Erosion Rate (m/year)	Change Compared to Measured Values (%)
Reduction of 5 m in the critical niche depth	14.24	113.5 %
Decrease of 0.1 m in sea level	0.647	−90.3 %
Increase of 0.1 m in sea level	49.11	636 %
Increase of 10% in wind speed	20.42	0.206 %
Increase of 10% in seawater temperature	7.09	6.3 %

5. Conclusions

A theoretical model is developed based on field observations of the physical processes involved in coastal erosion due to thermoabrasion. The governing equations of the theoretical model are based on fundamental physics, e.g., the conservation of mass, energy, salinity and sediments. The governing equations are discretised in time and space. A probabilistic analysis is performed to counter the uncertainties resulting from the data-poor environment. The model is a simplification of real-world physics. It can be only be applied for a short duration since most of the wave hydrodynamics is not included in the model. Out of all the morphological changes due to thermoabrasion, only the crest retreat is simulated. The resulting numerical model can calculate short-term shoreline erosion due to thermoabrasion during storms.

The numerical model is applied to two cases involving different geological features in two different years. The salient outcomes of the numerical model are as follows.

- Thermoabrasion is episodic and discontinuous, not continuous like other Arctic erosion processes.

- There is a small time-lag between the inundation depth h_{id} and niche growth rate. This time lag can be attributed to the initial resistance of the bluff face to the growth of a niche.
- Coastal erosion is dependent on the intensity of extreme events. Even though Case #1 faced more storms during 2013, the erosion in Case #2 during 2017 is higher than that in Case #1 in 2013 as the intensity and duration of extreme events were significantly higher in 2017.

A sensitivity analysis is carried out to determine the impacts of changes in the environmental parameters. The key findings of the analysis are as follows.

- The growth of the niche mainly depends on the inundation depth at the base of the bluff, the temperature of incoming waves and the wave height (which is depth-limited).
- The thermoabrasion process is highly sensitive to changes in sea level; therefore, the coasts where thermoabrasion is the dominant erosion process are at higher risk under sea-level rise.
- The sediment concentration and salinity of seawater have very little effect on thermoabrasion when compared to the other input parameters.
- The sensitivity analysis also reveals that the height of the bluff is a secondary factor for thermoabrasion. Field observations also validated this.

The model developed in this study assumes simplified physics, and thus has a very low computational demand at the price of sacrificing information about wave hydrodynamics and morphological changes. This low demand for computational resources allows the model to run one thousand times for the Monte Carlo simulations. A high number of cases is important for a probabilistic model, such as a Monte Carlo simulation. Even though the model is preliminary and simplified, only a 10-min time-step is used, which is a rather dense resolution when compared with similar kinds of models. For example, the authors of [24] used a time-step of 12 h for their model and the comprehensive model in [4] uses time step of 60 min.

The model described herein is a 1D model that considers sediment transport only in the cross-shore direction, similar to many Arctic erosion models. Moreover, we only considered the longshore current; the model does not calculate the longshore sediment transport or nearshore hydrodynamics, such as wave breaking, shoal formation and current-wave interactions. From the field observations, it is clear that similar to the low-latitude and mid-latitude coasts, longshore sediment transport in the Arctic coast is responsible for long-term changes in the shoreline even though the open water season is only three months. The current model considers only the effects of storms, so longshore sediment transport is excluded since the morphological footprint of longshore sediment transport takes a considerable amount of time to be visible. For a long-term prediction of shoreline changes, various additional parameters, including longshore sediment transport, wave evolution, and changes in bathymetry, must be incorporated into the model.

The current model focuses on the two driving forces of thermoabrasional erosion during a storm: (a) the thermal driving force originating from warm sea water and (b) the mechanical driving force of storm surge. Field observations indicate that thermoabrasional erosion is prominent in ice-rich bluffs consist of clay sediments. Clay sediments extruded from the degraded collapsed block are not deposited near swash zones; rather, they are most likely carried off to the deep sea by the strong return currents generated by storm surges. As such, clay sediments do not contribute to beach development. Based on this observation, cross-shore fine sediment transport is excluded from the current model. However, both the cross-shore transport of clay sediments and the longshore transport of sandy sediments are important for long-term predictions of shoreline positions. The global model can be applied to other coasts where thermoabrasion is the dominating erosional mechanisms. The model can be used for other coasts in the Arctic region without modification as no empirical formula is used. Even though in theory the model can be used for long-term prediction of the coastal erosion, we can not suggest it as other environmental parameters which are omitted in the model become important in longer duration model run.

The success of the proposed model, which predicts erosion with probabilistic statistics, serves as a proof of concept. For low-quality metocean information available on the Arctic coasts, the potential

to predict shoreline changes and the probability of bluff failure may be valuable for planning and protection endeavours.

Author Contributions: Conceptualisation, M.A.I., R.L. and M.S.A.; formal analysis, M.A.I. and M.S.A.; methodology, M.A.I.; validation, M.A.I., R.L. and M.S.A.; software, M.A.I.; resources, M.A.I., R.L. and M.S.A.; data collection, M.A.I. and R.L.; writing—original draft preparation, M.A.I. and M.S.A.; writing—review and editing, M.A.I., R.L. and M.S.A.; investigation, M.A.I. and M.S.A.; supervision, R.L. and M.S.A.; project administration, R.L. and M.S.A. All authors have read and agreed to the published version of the manuscript.

Funding: This research was funded by the EU H2020-funded Nunataryuk project, where it is filed as part of deliverable 6.4, and by the NCPOR//PACER Outreach Programme (POP) Initiative on “Predictive Tools for Arctic Coastal Hydrodynamics and Sediment Transport”.

Acknowledgments: The report is written as part of the EU H2020-funded Nunataryuk project, where it is filed as part of deliverable 6.4, and by the NCPOR//PACER Outreach Programme (POP) Initiative on “Predictive Tools for Arctic Coastal Hydrodynamics and Sediment Transport”. This research is also supported by Sustainable Arctic Marine and Coastal Technology (SAMCoT), Norwegian University of Science and Technology (NTNU), Lomonosov Moscow State University (MSU) and Sponsored Research and Industrial Consultancy (SRIC), Indian Institute of Technology Kharagpur.

Conflicts of Interest: The authors declare no conflicts of interest.

References

- Zhang, T.; Barry, R.G.; Knowles, K.; Heginbottom, J.; Brown, J. Statistics and characteristics of permafrost and ground-ice distribution in the northern hemisphere. *Polar Geogr.* **1999**, *23*, 132–154. [\[CrossRef\]](#)
- Anisimov, O.; Reneva, S. Permafrost and changing climate: The Russian perspective. *Ambio* **2006**, *35*, 169–75, doi:10.1579/0044-7447(2006)35[169:PACCTR]2.0.CO;2. [\[CrossRef\]](#)
- Frederick, J.M.; Thomas, M.A.; Bull, D.L.; Jones, C.A.; Roberts, J.D. *The Arctic Coastal Erosion Problem*; Technical Report SAND2016-9762; Sandia National Laboratories: Albuquerque, NM, USA, 2016.
- Barnhart, K.R.; Anderson, R.S.; Overeem, I.; Wobus, C.; Clow, G.D.; Urban, F.E. Modeling erosion of ice-rich permafrost bluffs along the Alaskan Beaufort Sea coast. *J. Geophys. Res. Earth Surf.* **2014**, *119*, 1155–1179. [\[CrossRef\]](#)
- Reimnitz, E.; Graves, S.M.; Barnes, P.W. *Beaufort Sea Coastal Erosion, Sediment Flux, Shoreline Evolution, and the Erosional Shelf Profile*; U.S. Geological Survey: Reston, VA, USA, 1988.
- Jones, B.M.; Arp, C.D.; Jorgensen, M.T.; Hinkel, K.M.; Schmutz, J.A.; Flint, P.L. Increase in the rate and uniformity of coastline erosion in Arctic Alaska. *Geophys. Res. Lett.* **2009**, *36*. [\[CrossRef\]](#)
- Lawrence, D.M.; Slater, A.G.; Tomas, R.A.; Holland, M.M.; Deser, C. Accelerated Arctic land warming and permafrost degradation during rapid sea ice loss. *Geophys. Res. Lett.* **2008**, *35*. [\[CrossRef\]](#)
- Ravens, T.; Peterson, S.; Panchang, V.; Kaihatu, J. Arctic coastal erosion modeling. In *Advances in Coastal Hydraulics*; World Scientific: Singapore, 2018; p. 47.
- Prowse, T.D.; Furgal, C.; Chouinard, R.; Melling, H.; Milburn, D.; Smith, S.L. Implications of climate change for economic development in northern Canada: Energy, resource, and transportation sectors. *Ambio* **2009**, *38*, 272–281. [\[CrossRef\]](#) [\[PubMed\]](#)
- Soluri, E.; Woodson, V. World vector shoreline. *Int. Hydrogr. Rev.* **1990**, *67*, 27–35.
- Lantuit, H.; Overduin, P.P.; Couture, N.; Wetterich, S.; Aré, F.; Atkinson, D.; Brown, J.; Cherkashov, G.; Drozdov, D.; Forbes, D.L.; et al. The Arctic coastal dynamics database: a new classification scheme and statistics on Arctic permafrost coastlines. *Estuar. Coasts* **2012**, *35*, 383–400. [\[CrossRef\]](#)
- Isaev, V.; Koshurnikov, A.; Pogorelov, A.; Amangurov, R.; Podchasov, O.; Sergeev, D.; Buldovich, S.; Aleksyutina, D.; Grishakina, E.; Kioka, A. Cliff retreat of permafrost coast in south-west Baydaratskaya Bay, Kara Sea, during 2005–2016. *Permafrost. Periglac. Proc.* **2019**, *30*, 35–47. [\[CrossRef\]](#)
- Baranskaya, A.; Belova, N.; Kokin, O.; Shabanova, N.; Aleksyutina, D.; Ogorodov, S. Coastal dynamics of the Barents and Kara Seas in changing environment. In Proceedings of the 13th International MEDCOAST Congress on Coastal and Marine Sciences, Engineering, Management & Conservation, Mellieha, Malta, 31 October–4 November 2017; Volume 1, pp. 281–292.
- Afzal, M.S.; Lubbad, R. Development of predictive tool for coastal erosion in Arctic—A review. In *Proceedings of the Fourth International Conference in Ocean Engineering (ICOE2018)*; Murali, K., Sriram, V., Samad, A., Saha, N., Eds.; Springer: Singapore, 2019; pp. 59–69.

15. Guégan, E. *Erosion of Permafrost Affected Coasts: Rates, Mechanisms and Modelling*; NTNU: Trondheim, Norway, 2015.
16. Pearson, S.; Lubbad, R.; Le, T.; Nairn, R. Thermomechanical erosion modelling of Baydaratskaya Bay, Russia with COSMOS. In *Scour and Erosion, Proceedings of the 8th International Conference on Scour and Erosion (Oxford, UK, 12–15 September 2016)*; CRC Press: Boca Raton, FL, USA, 2016; p. 281.
17. Vasiliev, A.; Kanevskiy, M.; Cherkashov, G.; Vanshtein, B. Coastal dynamics at the Barents and Kara Sea key sites. *Geo Mar. Lett.* **2005**, *25*, 110–120. [[CrossRef](#)]
18. Hoque, M.A.; Pollard, W.H. Stability of permafrost dominated coastal cliffs in the Arctic. *Polar Sci.* **2016**, *10*, 79–88. [[CrossRef](#)]
19. Harper, J.R. The Physical Processes Affecting the Stability of Tundra Cliff Coasts. 1978. Available online: digitalcommons.lsu.edu (accessed on 30 January 2020).
20. Hoque, M.A.; Pollard, W.H. Arctic coastal retreat through block failure. *Can. Geotech. J.* **2009**, *46*, 1103–1115. [[CrossRef](#)]
21. Kobayashi, N. Formation of thermoerosional niches into frozen bluffs due to storm surges on the Beaufort Sea coast. *J. Geophys. Res. Oceans* **1985**, *90*, 11983–11988. [[CrossRef](#)]
22. Kobayashi, N.; Vidrine, J.C. *Combined Thermal-Mechanical Erosion Processes Model*; Center for Applied Coastal Research, University of Delaware: Newark, DE, USA, 1995.
23. Nairn, R.; Solomon, S.; Kobayashi, N.; Vidrine, J. Development and testing of a thermal-mechanical numerical model for predicting Arctic shore erosion processes. In *Permafrost, Proceedings of the Seventh International Conference, Yellowknife, NWT, Canada, 23–27 June 1998*; Centre d'études nordiques, Université Laval: Laval, QC, Canada, 1998; pp. 789–795.
24. Ravens, T.M.; Jones, B.M.; Zhang, J.; Arp, C.D.; Schmutz, J.A. Process-based coastal erosion modeling for drew point, North Slope, Alaska. *J. Waterw. Port Coast. Ocean Eng.* **2011**, *138*, 122–130. [[CrossRef](#)]
25. Isaev, V.; Kokin, O.; Pogorelov, A.; Gorshkov, E.; Komarov, O.; Amangurov, R.; Simonsen, V. *Field Investigation and Laboratory Analyses Baydaratskaya Bay 2018*; Norwegian University of Science and Technology: Trondheim, Norway, 2019. doi:10.13140/RG.2.2.26964.24968. [[CrossRef](#)]
26. Harms, I.; Karcher, M. Modeling the seasonal variability of hydrography and circulation in the Kara Sea. *J. Geophys. Res. Oceans* **1999**, *104*, 13431–13448. [[CrossRef](#)]
27. Stein, R.; Fahl, K.; Fiitterer, D.; Galimov, E.; Stepanets, O. River run-off influence on the water mass formation in the Kara Sea. In *Siberian Rer Run-Off in the Kara Sea: Characterisation, Quantification, Variability and Environmental Significance*; Elsevier: Amsterdam, The Netherlands, 2003; Volume 6, p. 9.
28. Odisharia, G.; Tsvetsinsky, A.; Mikhailov, N.; Dubikov, G. Specialized information system on environment of Yamal Peninsula and Baydaratskaya Bay. In *Proceedings of the 7th International Offshore and Polar Engineering Conference, Honolulu, HI, USA, 25–30 May 1997*.
29. Leont'yev, I. Coastal profile modeling along the Russian Arctic coast. *Coast. Eng.* **2004**, *51*, 779–794. [[CrossRef](#)]
30. Dean, R.G.; Dalrymple, R.A. *Coastal Processes with Engineering Applications*; Cambridge University Press: Cambridge, UK, 2004.
31. Longuet-Higgins, M.S. Longshore currents generated by obliquely incident sea waves: 1. *J. Geophys. Res.* **1970**, *75*, 6778–6789. [[CrossRef](#)]



© 2020 by the authors. Licensee MDPI, Basel, Switzerland. This article is an open access article distributed under the terms and conditions of the Creative Commons Attribution (CC BY) license (<http://creativecommons.org/licenses/by/4.0/>).

C.2 Journal Paper#2



Contents lists available at ScienceDirect

Polar Science

journal homepage: www.elsevier.com/locate/polar

Modelling the seasonal variations of soil temperatures in the Arctic coasts

Mohammad Akhsanul Islam^{a,*}, Raed Lubbad^a, Seyed Ali Ghoreishian Amiri^a, Vladislav Isaev^b, Yaroslav Shevchuk^b, Alexandra Vladimirovna Uvarova^c, Mohammad Saud Afzal^d, Avinash Kumar^e

^a Civil and Environmental Engineering Department, Norwegian University of Science and Engineering (NTNU), Norway

^b Department of Geocryology, Lomonosov Moscow State University (MSU), Russia

^c Vernadsky Institute of Geochemistry and Analytical Chemistry of RAS, Russia

^d Department of Civil Engineering, Indian Institute of Technology, Kharagpur, India

^e National Center for Polar and Ocean Research (NCPOR), Goa, India

ARTICLE INFO

Keywords:

Soil temperature
Arctic coastal erosion
Thermodenudation
Permafrost thawing

ABSTRACT

The soil temperature within the Arctic coasts within the continuous permafrost is not widely measured; the temporal and spatial resolutions of the measured temperature observations are relatively high. In this study, we examined the methods to interpolate, hindcast and forecast temperature measurements within the active layer and shallow permafrost when the temperature measurements at the surface or near the surface are available. The temperature variations along the year are periodic, and hence attempts are made to express the seasonal variations with a combination of periodic function (Fourier components); which are used as boundary conditions to reach the analytical solutions. The temperature measurements from surface to about 10 metre of depths at the Baydaratskaya Bay, Kara Sea are available. We adopted a data-driven model based on simplified analytical closed-form solution derived from the boundary conditions. The parameters of the solution are calibrated from the field measurements and validated with field observations. The model then can be used to hindcast and forecast temperature at any points within the soil.

1. Introduction

The erosion of the Arctic coasts reflects the complex interaction between climate, coastal morphology and geology in which the unique environmental conditions related to permafrost are subject to thermal and mechanical instability (Are, 1988). Field observations identified various erosion mechanisms such as a bluff failure by niche erosion (thermoabrasion), bluff face thaw (thermodenudation), retrogressive slumping processes in the Arctic coasts, either separately or in combinations (Vijay et al., 2018). The models by Naim et al. (1998), Kobayashi et al. (1999), Leont'yev (2003, 2004), Hoque and Pollard (2009), Ravens et al. (2012) and Barnhart et al. (2014) describe the Arctic coastal erosion as an effect of the hydrodynamic and thermal driving forces on standardised one-dimensional (1D) or two-dimensional (2D) coastal profiles to simulate coastal erosion because of the thermoabrasion process. Thermal energy transfer based on air–water–soil temperature profiles, thawing of permafrost and the degradation of the mechanical strength of the soil are ignored in most of the existing conceptual models (Lantuit and Pollard, 2008). Comprehensive models of coastal erosion, including the effects of the thermodenudation process, have not yet been developed (Vijay et al., 2018). Meanwhile,

observations from the various Arctic coasts suggest that the ongoing and foreseen thermokarst activities lead to considerable erosion by thermodenudation. For example, we expect the thawing of permafrost to increase unprecedentedly in connection with the effects of climate warming (Lewkowicz, 1991). Temperature increase within permafrost will lead to an increased rate of thawing of soil ice and may speed up Arctic coastal erosion (Bernstein et al., 2008).

The permafrost is linked with the surrounding atmosphere by an active layer, vegetation and snow covers which may vary enormously with time and location (Romanovsky and Osterkamp, 1997). The active layer thickness (or the depth of the seasonal thawing) is usually estimated from satellite images, from in-situ measurements or using some semi-analytical formula. The semi-analytical formulas are based on a functional relationship between thawing depth, air temperatures and the soil's thermal properties (Lantuit and Pollard, 2008). The Stefan-type equations ($x = m \cdot \sqrt{T_{index}}$ where T_{index} is the thawing index, m is related to thermal properties of soil, and x is the thawing depth) are widely used to predict the depth of permafrost thawing or to estimate the thermodenudation rate (Romanovsky and Osterkamp, 1997). Similar simplified analytical solutions or empirical relations between the

* Corresponding author.

E-mail address: mohammad.a.islam@ntnu.no (M.A. Islam).

<https://doi.org/10.1016/j.polar.2021.100732>

Received 9 November 2020; Received in revised form 26 July 2021; Accepted 27 July 2021

Available online 11 August 2021

1873-9652/© 2021 The Authors.

Published by Elsevier B.V. This is an open access article under the CC BY-NC-ND license

(<http://creativecommons.org/licenses/by-nc-nd/4.0/>).

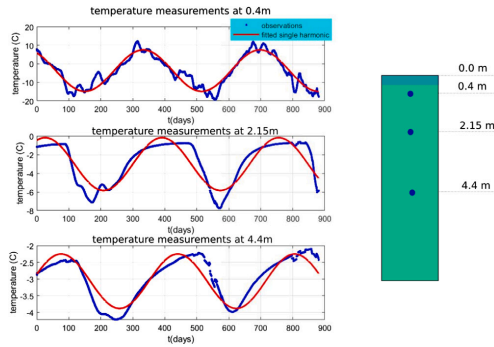


Fig. 1. The time-series of temperatures at a depth of 0.4 m, 2.15 m and 4.4 m are shown. The blue dots are observations at 12 h intervals. The total length of the observations is about 880 days. A sine-wave function is fitted (marked by the red line) using the least square error method. The soil at the depth of 4.4 m never reaches the unfrozen phase, i.e. temperature always remains below zero. (For interpretation of the references to colour in this figure legend, the reader is referred to the web version of this article.)

thawing depth and temperature measurements are also applied (Guégan, 2015; Romanovsky and Osterkamp, 1997). Limitations of all the above formulas are: (a) unable to model temporal and spatial variation of the soil temperatures, (b) the models are forced to use spatial- and temporal-averaged values of temperature and (c) restricted to assume constant thawing/freezing temperatures regardless of the variations in the soil properties (e.g. effect of the salinity, organic matter on the freezing temperature cannot be assessed) (Guégan, 2015). Only continuous and high resolution (both temporal and spatial) soil temperature profiles can solve the aforementioned limitations. Unlike other environmental parameters, we rarely measure the soil temperature on a regular basis (Holmes et al., 2008).

In this study, we adopt analytical closed-form solution to describe the temporal variation of the soil temperatures at various depths (we focus on the active layer and the shallow permafrost from 0.5 m to 10 m). We base the solution on the classical 1D heat convection-diffusion equation to describe the heat transfer in the soil with boundary conditions assuming temporal temperature variation at the air-soil interface to be periodic. The temperature variation at the soil surface expressed as a harmonic function is a suitable boundary condition to depict the seasonal variations. The combinations of the multiple harmonic functions can capture variations with higher accuracy and prediction errors are smaller. We proceed by calibrating and validating the solution against various consecutive years (from 2014 to 2018) of continuous full-scale data of soil temperatures (from 0 metre to 9.9 m depths) at five different locations representing different geological and meteorological conditions at Baydaratskaya Bay, Kara sea, Russia. For the calibration, we use the first 80% of the data and apply machine learning algorithms to estimate parameters like temperature wave-amplitude reduction rate, temperature wave-phase lag, soil thermal diffusivity and liquid water flux density. The remaining observations are used for the validation of calibrated solutions. The calibrated and validated solutions for the Arctic coasts presented in this paper may be used to (1) hindcast, and forecast soil temperatures at various depths of the soil on the basis of temperature measurement at or near the surface, (2) estimate the thawing depth and thawing rates during the summer and refreezing during the winter; taken into account the variation of the freezing/thawing temperatures with the soil properties, and (3) improve the understanding of the thermodenudation initiation process and hence improve the capabilities of Arctic coastal erosion models.

2. Seasonal variation of temperature in the Arctic coasts

In this section, we use full-scale observations to establish an understanding of the problem. A comprehensive description of the full-scale data is provided in Section 3.3. Here, we present one temperature profile (see Fig. 1) only as a sample of the measurements.

Fig. 1 shows temperature measurements at three different depths, i.e., at 0.4 m, 2.15 m, and 4.4 m. The three temperature measurements are about 880 days, which means each time series consists of at least two summers and two winters. Each of the three chosen observations represents a certain layer of the soil in the Arctic. Typically, the active layer on which some vegetation can be seen is 0.5 m to 1 metre deep. The layer below the active organic layer is the transitional active layer. It is low on organic material; but subject to annual freezing and unfreezing, i.e. during summer, the soil is free of ice. The layer at 4.4 m is permafrost. The temperature at the permafrost layer never rises more than zero degrees, i.e. during summer, the layer stays frozen.

A sine-wave is fitted on each of the observations (red line). Attempts are made to represent the seasonal temperature variations with a single harmonic function. One of the earliest model is the sine-wave model, where the periodical temperature changes are described using a single harmonic function (a sine function with time period of 365 days). Van Wijk and De Vries (1963) and Andersland et al. (2003), proposed the following equation to express the temperature variation at any depth in the soil:

$$T_g(z, t) = T_m(z) + T_a(z) \cdot \sin(2\pi f t + \phi(z)) \quad (1)$$

where T_m is the mean temperature, T_a is the amplitude of the harmonic sine wave, f is the frequency of the wave, f interchangeable with ω ($= 2\pi f$)-the angular frequency, ϕ is the phase of the wave. As shown in the Fig. 1, the amplitude, T_a and the phase, ϕ are different at two depths but the frequency, f remains the same. When Eq. (1) is applied to Arctic coasts temperature measurements (as shown in Fig. 1) where temperature variations also follow a periodical cycle, some deviations are noticed. The errors of fitting a sine-waves are prominent close to the peaks, which are again greater at a depth of 2.15 m when compared with 0.4 m and 4.4 m of depth. According to our understanding, the significant cause of such deviations is due to the requirement of latent heat of phase-change. The effect of phase change on the deviations are (1) delay in reaching the peak and (2) sometimes slightly lower amplitude at the peaks.

To model the above observations, one can in principle solve the heat balance equation in porous medium as shown in Eq. (2) with boundary and initial conditions (Plaxis, 2021).

$$\frac{\partial}{\partial t} (nS\rho_w e_w + n(1-S)\rho_v e_v + (1-n)\rho_s e_s) = -\nabla \cdot (\underline{J}_w + \underline{J}_v) + Q_T \quad (2)$$

where e_w , e_v and e_s are the internal energy in the water, vapour and solid phases, Q_T is the heat source term, \underline{J}_w and \underline{J}_v are the advective internal energy flux in water, vapour and soil (porous medium), n is porosity of the soil, ρ_w , ρ_v and ρ_s are the density of the water, vapour and soil.

It is possible to solve Eq. (2) numerically, but one has to pay special attention to the phase change and enforce the right conditions at the moving boundary. We use the software Plaxis to solve Eq. (2). Plaxis is a commercial finite element software developed to model geotechnical problems. The software features 2D deformation and stability analysis. It also includes a module that offers to simulate geothermal effects, heat flow within the soil, temperature distributions and phase change. The software can simulate temperature-dependent water properties which enables it to simulate permafrost in the Arctic coasts (Plaxis, 2021).

As a boundary condition, the temperature measurements at 0.4 m and 4.4 m are used and analyses are performed to simulate the temperature profile at 2.15 m. The numerical model is based on the porous medium's heat balance equation, including the major thermal processes such as conduction, convection by water and mass balance with phase

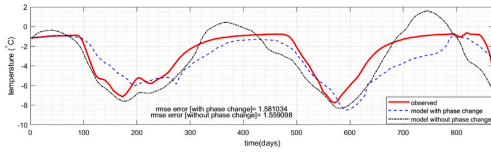


Fig. 2. The numerical modelling using Plaxis. The observations at the 0.4 m and 4.4 m are used as a boundary condition. The model estimates the temperature at the 2.15 m depth. The estimated observations are then compared with the available observation.

changes, non-isothermal deformation, soil freezing, and unfreezing. Two different approaches are used, (1) considering the latent heat of phase change with measured parameters and (2) considering the depth-averaged equivalent thermal conductivity but ignoring the phase change. It is observed that the model, when not considering the heat loss and gain during a phase change, has almost the same level of error when compared with a model that considers the latent heats (Fig. 2). When a whole cycle is considered, the energy required to melt the ice within the soil's pores at the active layers returns during the freezing phase if yearly averaged water content remains constant. At a yearly averaged value, the net effect of the heat flow changes due to latent heat of ice melting is cancelled out by the release of heat during the freezing. The figure also shows that neglecting the phase change can still be a good approximation if equivalent (calibrated) soil parameters are used. From this observation, we come to one of our main hypotheses in this study, i.e., the temperature variation in the permafrost can be modelled using a data-driven approach by solving 1D one-phase heat balance equation with calibrated soil parameters, i.e. solution to Eq. (2).

Based on this observation, a data-driven model is developed using the simplified conduction-convection equation and the analytical solution. The solution of the equation is used to train the numerical model to find out the patterns and correlations between the time series of the temperatures at various depths. The analytical solution is the guiding principle for the algorithm to seek out the correlation and establish a localised custom relation between some basic parameters to predict the temperature at various depths. In the next sections, we describe the analytical solution used which is the basis of the pattern-seeking of the machine learning algorithm.

2.1. Simplified thermal model

A typical Arctic coastal profile is shown in Fig. 3. A cliff stands at the end of a narrow beach. During the winter, the beach, bluff face and the cliff are covered with snow while the sea is covered with ice. Coastal erosion due to thermodenudation occurs during the summer after the snow is melted away. The direction of the heat transfer is downward during the summer when the air temperature is warmer than the soil temperature. The direction changes during winter as the air temperature near the surface becomes colder than the permafrost temperature. Our domain of interest is the Arctic coastal cliff and the narrow beach where thermodenudation occurs. In this study, we want to find a reliable method to estimate the temperature profiles inside the cliff and the beach, estimating the temperature on a large scale. This will allow an accurate estimate of the permafrost thawing depth and improve modelling of Arctic coastal erosion due to thermodenudation.

2.1.1. Conduction-convection heat equation

To estimate the temporal variations of the soil temperature at any depth, we idealise the problem as a one-dimensional (1D) heat transfer problem. Let us assume that points A and B are two points at different depths inside the cliff shown in Fig. 3. The distance between these two points and the coordinate system used is shown in Fig. 3. The axes x and y are assumed to be along the cross-shore and alongshore direction, respectively, the positive z -axis points to the downward direction.

2.2. Governing equation to establish a data-driven model

The 1D heat convection-diffusion equation can be used to describe the heat transfer in the soil between point A and point B. Based on the conservation of the energy, the Fourier thermal conduction and convection equation for the 1D case is expressed as: (Stallman, 1965; Gao et al., 2003, 2008),

$$\frac{\partial T(z, t)}{\partial t} = \frac{\partial^2 k(z)T(z, t)}{\partial z^2} + \frac{\partial W(z)T(z, t)}{\partial z} \quad (3)$$

where k is the thermal diffusivity (unit = m^2s^{-1}) and $k = \lambda/C_g$ where λ is the thermal conductivity (unit = $\text{Wm}^{-1}\text{C}^{-1}$) and C_g is the volumetric heat capacity of the soil (unit = $\text{Jm}^{-3}\text{C}^{-1}$), W is the liquid water flux density. $W = \partial k/\partial C_w/C_g w \eta z$, $\partial k/\partial z$ is the gradient of the soil thermal diffusivity in z direction, C_w is the heat capacity of the water ($\text{J}^\circ\text{C}^{-1}\text{m}^{-3}$), w is the liquid water velocity (m/s), η is the volumetric water content of the soil (unit-less).

Eq. (3) is used as the governing equation of the problem; the equation is valid for every point regardless of the temperature profiles. However, the equation does not count for the heat sink or source at the melting phase due to the phase change of water. As we have seen in Section 2, the effect of the phase change is the deformation of the sine wave and lag of the peak positive temperature.

2.2.1. Boundary conditions

The form of the fundamental solution of the Eq. (3) depends on the boundary conditions. For $z = \infty$ or at sufficient deep soil, the solution of the equation reaches a steady state, i.e. the effect of the surface-boundary conditions cannot be seen anymore. A time series of the temperature measurements can be applied as a boundary condition at point A. One of the properties of the heat equation is that it retains the initial shape of the boundary condition (detail example is provided in Appendix C). The time series at point A can be expressed as a known form of the function to reach the analytical solution. We considered the temperature measurements at point A ($z = z_1$) as a function of time but a combination of harmonic functions with different amplitudes and time periods. Application of the boundary condition can lead to the respective solutions of Eq. (3); presented in the next section.

2.2.2. Analytical solution: a combination of harmonic functions as boundary condition

Applying Eq. (4) as a surface boundary condition to Eq. (3) (as temperature profile at point A at a depth z), a solution to soil temperature T_z can be expressed as shown in Eq. (5) (see Verhoef et al., 1996; Hu et al., 2016):

$$T(z = 0, t) = T_m(z) + \sum_{n=1}^N T_{a_{0n}} \sin(2\pi f_n t - \phi_{0n}), n = 0, 1, 2, \dots, N \quad (4)$$

The effect of the phase changes is captured by the Fourier decomposition which a single sine wave model fails to do. The effect of change in the shape and the lag of the peak are accounted for when the time series is decomposed. Theoretically, the Fourier decomposition can be decomposed to $N/2+1$ number of components where N is the number of observations. The analytical solution is presented as (see Verhoef et al., 1996; Hu et al., 2016):

$$T_z(z, t) = T_m(z) + \sum_{n=1}^N T_{a_{0n}} e^{[-\frac{W-\alpha}{2k}]z} \sin\left[2\pi f_n t - \phi_{0n} - z \frac{\beta_n}{2k}\right] \quad (5)$$

where T_m is independent of the frequency, $T_{a_{0n}}$ is the amplitude of each harmonic function, ϕ_{0n} is the phase of each harmonic function at the surface. W and k are independent of the harmonic functions but dependent on depth (for simplicity, W and k are made depth-averaged), and α and β are different for each harmonic function. We can rewrite part of the Eq. (5) as follows:

$$T_{a_{0n}}(z, t) = T_{a_0} \cdot e^{-z \sum_{n=1}^N RRFS_n} \quad (6)$$

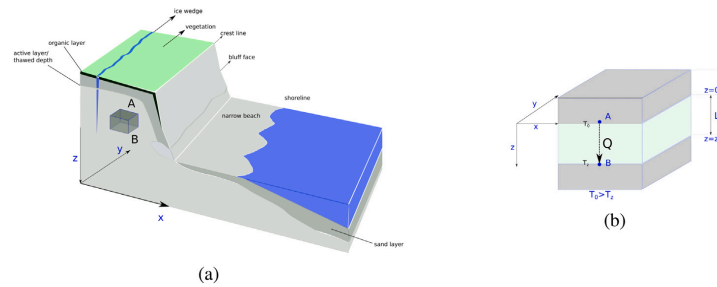


Fig. 3. (a) A typical Arctic beach at the inception of the summer is shown. The coast consists of a cliff at the end of the profile and ice-wedge polygons are visible on the cliffs. The active layer is beginning to thaw. Higher organic contents distinguish it from the rest and are situated just under the soil surface. The beach in front of the cliff is narrow, which has an elevation such that during the high tides, water does not reach the base of the bluff. (b) The heat flux between two points (A and B) inside the soil is shown. The z-axis is assumed positive towards the downwards directions, i.e. the heat flow during the summer is assumed positive. The temperature at point B (T_B) is smaller than that of point A (T_A).

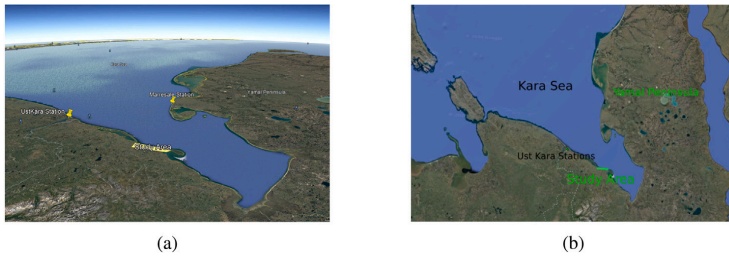


Fig. 4. The study area is on an Arctic coast on the left side of the gulf of the Kara sea. The area starts from South (Latitude:68.867459N, Longitude:66.741529E) to East South (Latitude:68.842112N, Longitude 66.984593E) along the coast. The coast is straight, and the shore-normal line creates a 72° angle with the North. Source: google earth.

$$\phi_n(z) = \phi_{0n} - z \cdot PL_{FS_n} \quad (7)$$

where $RR_{FS_n} = \frac{-W_n - a_n}{2k}$ and $PL_{FS_n} = \frac{\beta_n}{2k}$ for $n = 0, 1, 2, 3, \dots$. The solutions are independent of the frequencies; the frequencies do not change over depth (Van Wijk and De Vries, 1963). Field observations can help to calibrate the parameters of the solution. In this paper, we use the soil temperature observations of five different locations as boundary conditions to calibrate the parameters of the Eq. (5). We used the temperatures from 0 to 9.9 m depths to calibrate the parameters: amplitude reduction rate, RR and phase lag, PL .

3. Field measurements

The soil temperature has been measured at the coast of Baydaratskaya Bay in the Kara Sea. The field investigations are completed each year, started from 2012 under the leadership of the Lomonosov Moscow State University (MSU) with support from the Centre for Research-based Innovation (CRI): Sustainable Arctic Marine and Coastal Technology (SAMCoT).

3.1. Geo-morphological description of the study area

The study area is a coast named Baydaratskaya Bay, a shallow gulf at the western side of the Kara Sea (Fig. 4). The region is inside the Arctic circle, sparsely populated and with minimal access. Although many alluvial patches, lacustrine and deposits of boggy materials are found on the coast, mostly the Pleistocene marine and Glacial sediments created the area between the Yamal Peninsula and Yugra Peninsula. We believe the area was altered by the Pleistocene ice sheets, unlike the eastern Russian coasts. Massive ice beds are present in the study

area. Visible Ice wedges polygons are found along the cliffs standing at the end of the beaches and contribute to the large collapses of blocks by thermoabration (Ogorodov et al., 2020). The depression formed by the massive ice glaciers during the Pleistocene era developed the shallow gulf, and during the Holocene period, seawater submerged the area. The permafrost underneath the active layer is mostly continuous and reaches 30–70 m thickness. The gasoline pipe of Bovanenkovo-Uhta that transports gas to Europe passes the study area by 0.1 km in the SE direction (Isaev et al., 2019). The total length of the study area is 8 km. The river Ngoyuyaha divides the area into two almost equal parts. The Baydaratskaya bay is not the only depression along the coast of the Kara Sea; there exist many similar depressions. Some active faults bound the basin at the west side. The north part of the bay is formed during the Pleistocene and Holocene. The clay and bottom mud found in the deeper part of the bay are well-sorted, fine sands along Ural shoreface and silty sand along Yamal coast.

3.1.1. Zonal division based on cliff height: S#1 and S#2

The study area is divided into two distinct zones, marked S#1 and S#2, as shown in Fig. 5[a]. The low marine terrace with bluff heights around 4–6 m is termed zone S#1. Zone S#2 has bluff heights of 10–17 m. The S#1 and S#2 sites are about 3.5 km in the N-W direction from the cofferdam of the Bovanenkovo-Uhta gas pipeline. The study area is spread from North West (68.867459N, 66.741529E) to East South (68.842112N, 66.984593E). The zone S#1 is a low marine terrace with a length of about 4 km, starts directly from the gas pipeline (the most south-eastern point). The low terrace surface (up to 6 m) is smoothly sloping. The top surface of the cliffs is grassy with minor swamped hollows; some shallow thermokarst lakes are present, ice-wedge polygons are visible on the soil surface, we find many erosion trenches

Table 1

List of boreholes at the study area are shown. The boreholes are placed in the cliffs, both at the high and low marine terraces.

zone	Borehole ID	Depth	Coordinates	Drilled on	Remarks
S#1	bh2	9.9 m	N 68.853004 E 66.899996	Sep 2016	On the slope
S#1	bh3	9.9 m	N 68.852599 E 66.899767	Sep 2016	30 m inside the crest
S#1	bh4	6.2 m	N 68.853797 E 66.889794	Jun 2013	Inside the cliffs, discarded due to technical errors
S#1	bh5	9.9 m	N 68.858327 E 66.838207	Sep 2014	5 m above the water level
S#2	bh6	5 m [3.31 m]	N 68.857162 E 66.843057	Jun 2014	15 m above the water level

Table 2

Thermal properties of the sediments on the cliffs. The top organic active layer has very low thermal conductivity and act as a blanket hindering the thawing process. Other than the top organic layer, thermal properties vary little along the depth.

Location	Depth m	Soil type	Temperature during test °C	thermal conductivity (λ) W/(mK)
Excavation-1 N68.85305 E66.88763	0-0.15	Peat, middle stage of decomposition, dark brown	1.3	0.386
	0-0.20	Layering of sand light-grey, frozen and dark grey light loam, cryoturbation	1.94	0.732
	0.42-0.75	Sand, grey, fine grained, with layers of ferruginous matter	1.0	1.42
Excavation-2 N68.85361 E66.89361	0.40-0.60	Loam, dark grey, soft plasticity with deep decomposed organics	1.5	1.48
	0.60-0.9	Sand fine grain, light-grey with vertical band of ferruginous matter	1.15	1.16
	0.9-1.3	Sand fine grain, light-grey with vertical band of ferruginous matter	0.47	1.39
Excavation-3 N68.85277 E68.87778	0-0.30	Loam dark-grey, soft plasticity with ferruginous matter	3	1.64
	0.30-0.53	Sand light brownish grey, middle grain size, with ferruginous matter layers and inclusions of fine gravel matter	1.4	1.58
	0.61-1.64	sand, light-grey, middle grain size, with horizontal layers of dark sand and vertical bands of ferruginous matter	1.13	1.04

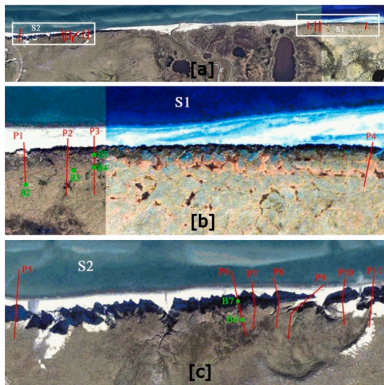


Fig. 5. The study area is divided into two zones: S#1 and S#2 identified by the bluff height differences. The longshore sediment transport exists from zone S#2 to S#1. A low lying laida separates the zones; the laida is excluded from the erosion studies. Temperature measurements at various depths are available for both the S#1 and S#2 zone.

Source: Isaev et al., 2016.

along the coastline. The bluff-heights of the S#1, from the northwest, gradually lowers and transforms into a laida of 1.5–2 m height with the Ngouyauva river valley. A laida is a low lying land in the Arctic coasts flooded during the high tides, an Arctic counterpart of the marshland found in the warmer climate. The laida shoreline is almost 1.2 km long. The laida consists of depressions with frost-thaw lakes. Some of them

are drained because of the retreat of the coastline. Lake occupancy on some of the high laida areas exceeds 50%. The lower sections of the laida are followed by the S#2 zone, a more elevated terrace of 10–17 m. This S#2 zone is 4.65 km along the coastline. Deep trenches more frequently cut the surface of the S#2 with dry thermokarst lake basins (hasyreys) and younger thermokarst lakes, polygonal-shaped frost clefts and weathering spots on the sandy soil. The cliffs mostly consist of fine sediments. Unlike the sandy dune systems of the warmer climate beaches, there is no active restoration mechanism to restore the cliffs. The soil profiles of the cliffs are depicted in Fig. 6.

3.2. Soil temperature measurements

Various boreholes are constructed in the study area to measure the temperatures (list of the boreholes provided in Table 1). Initially, two boreholes were drilled, and temperature sensors were placed during field measurements of June 2013 (bh4, 6 m deep) and June 2014 (bh6, 3.5 m deep). Bh4 borehole was dug in the low terrace (S#1), and bh6 was on the high terrace (S#2). Boreholes were dug using handheld Augers, and M_log5 W (GeoPrecision GmbH) thermistors were placed inside them. A plastic pipe protects the boreholes to avoid internal collapse. The sensors of the thermistors are typically kept 0.3 m to 0.5 m apart. But near the surface, sensors are placed at 0 m and 0.1 m to capture the surface temperature. The time interval to record the data was set to be 12 h.

3.2.1. In situ thermal conductivity measurements

Lab tests of in-situ and post-work were performed to find the mechanical and thermal properties of the permafrost/cliff during the field investigation (the summary of the thermal properties are in Table 2). The experiment was performed on the cliff faces; due to the limitation of the equipment, the investigation was completed only till 1.64 m. Thermal conductivity was measured to be quite low on top of the organic active layer.

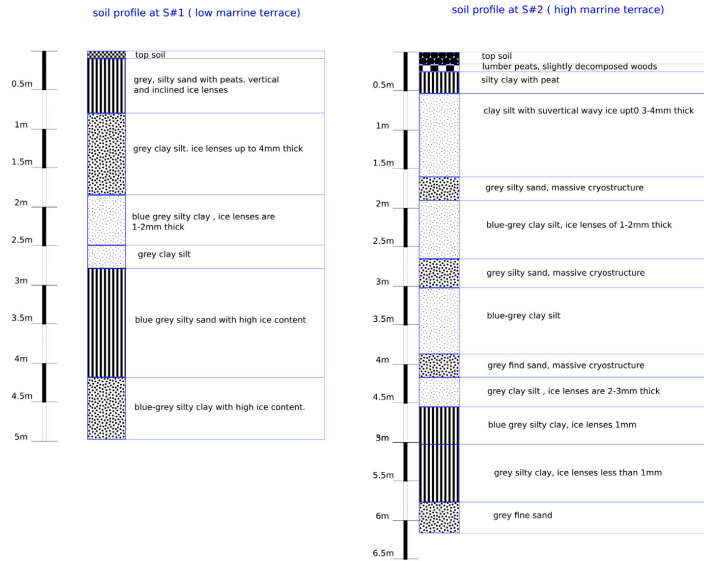


Fig. 6. Soil profiles at the two sites, S#1 and S#2. The cliffs comprise mostly fine materials. Permafrost is continuous after the depth of around 1.5 m. The active organic layer is thin, more or less 0.3 m and quite poor with nutrition for the vegetation (Field observation was made in Summer, 2014). Thermal conductivity of the soil is measured; presented in Table 2.

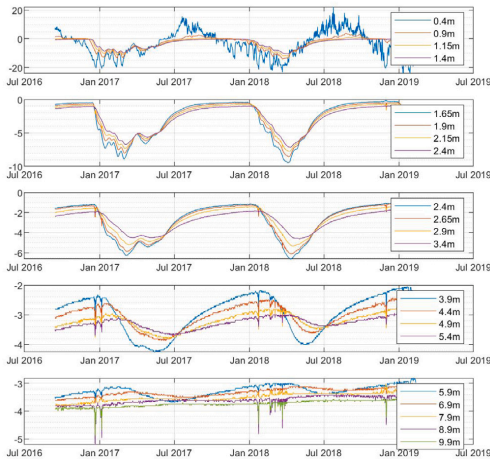


Fig. 7. Time series data of bh2: temperature measurements along with the 20 nodes from depths of 0.4 m to 9.9 m. Each sub-figure contains the data of the five depths. Some measurement anomalies are noticeable at the lower depths. However, compared to the mean values of the temperatures, the anomalies are not significant. Matlab functions 'smooth' and 'filloutliers' were used to remove the anomalies wherever required.

3.3. Field observations

We choose five sets of time series data for analysis where measurements are continuous and consistent. These observations are made throughout the year on the cliff and the beach of the Baydaratskaya.

Table 3

Summary of the temperature observations. Five time series are used for the analysis comprising temperature measurements from the zones S#1 and S#2.

Time series	Borehole ID	From	To	Total days	nodes	Depth
bh2	bh2	13-09-16	10-02-19	881	20	9.9 m
bh3	bh3	13-09-16	22-12-17	466	19	9.9 m
bh5-1	bh5	09-06-14	11-09-16	826	20	9.9 m
bh5-2	bh5	12-11-16	09-09-18	667	5	1.65 m
bh6-1	bh6	09-06-14	13-07-15	400	11	3.31 m

The earliest date of the measurements is 9 June 2014. The maximum length of the time series is 881 days (2.41 years; continuous), two periodical temperature variations are captured with the time series. The sensors measure the temperature at 12 h intervals. We lost some sensors to erosion. Moreover, temperature measurements at the deeper part of some boreholes were not appropriately captured because of some unknown sensor errors. As a result, data from all the nodes cannot be considered. The summary of the observations as time series is given in Table 3. Observations from both the high and low cliff areas (S#1 and S#2) are available. The data are re-sampled for the daily averages since the time resolution of the data is 12 h, not small enough to capture the daily temperature variation of the site. The maximum depth of the sensor was 9.9 m in both S#1 and S#2 zones. However, some anomalies are observed within the measurement due to reasons of (1) interference by local people, some strings were lost, (2) reallocation of borehole due to erosion and (3) measurement errors. To avoid the unexplained and unwanted behaviours of the measured data, parts of some time series are omitted. However, the unprocessed measurements are added in the Appendix A for references. Fig. 7 shows the time series of bh2; the rest of the time series are provided in the Appendix A.

4. Calibration of the parameters from field observation

In this study, we split the time series into two groups: training and testing data, adopting the machine learning approach. The training data

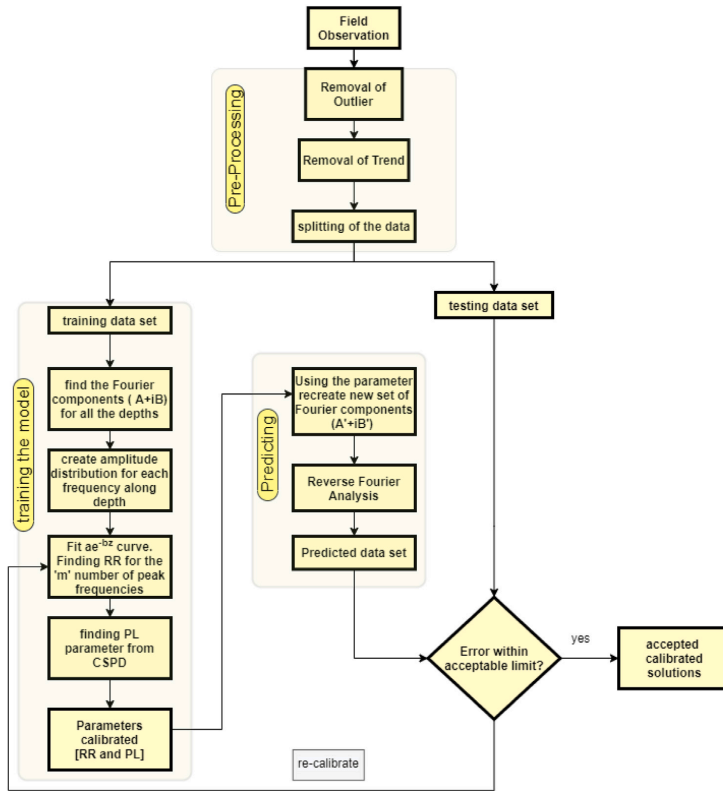


Fig. 8. The workflow of the model.

set is used to calibrate the parameters of the solutions as mentioned in Table 4, i.e. the solution is fitted to the training data set to determine the parameters (*RR* and *PL*). Thereafter, the calibrated solutions are used to numerically reproduce the remaining data, i.e. the testing data set. The calibration accuracy is determined by comparing the numerical prediction with the measurements, and the decision is made whether to accept the calibration or to re-calibrate the parameters. If the error is within the limit, the calibrated equation can be used as the governing equations to hindcast or forecast soil temperatures for the specific local area. The workflow of the methodology is shown in Fig. 8.

4.1. Pre-processing of the raw data

The field measurements contain some values which are clearly an error in the sensor. Before proceeding, these values were identified and cleared. Unusual values can greatly affect the quality of curve fitting. A trend within the time series may be observed. Since a trend is not considered when we sought the analytical solution, the trend must be removed before the calibrations.

4.1.1. Removal of outliers

Any observation over three times the median absolute deviations (MAD) away from the median is considered a measurement error and termed as an outlier. The outliers are replaced with the value generated by the piecewise cubic spline interpolation.

4.1.2. Removal of trend

The observations from the field typically have an upward or downward trend of the mean temperature. A first-order 'detrend model' is used to remove the trend from the observation.

$$Y_{p,q} = O_{p,q} - T_{q,1} \times O_{p,q} \quad (8)$$

where the p is the number of nodes along depth, q is the number of nodes in time-series, $O_{p,q}$ is the matrix of the training data set and $T_{q,1}$ is the matrix of the de-trending parameters and $Y_{p,q}$ is the refined observations. When the calibrated solutions are used to make predictions, the trend values are required to be included. The estimated trend values using the parameters $T_{q,1}$ are added back using the relation $T_{q,1} \times O'_{p,q}$; where $O'_{p,q}$ is the predicted observation matrix.

4.2. Quantification of the error

The accuracy of the curve fittings are measured using the following error formulas:

4.2.1. Standard error of estimates (SSE)

The SSE (Eq. (9)) measured the mean deviation between the fitted value and measured value.

$$SEE = \sqrt{\frac{\sum_{t=1}^N [o(t) - \hat{o}(t)]^2}{N - 2}} \quad (9)$$

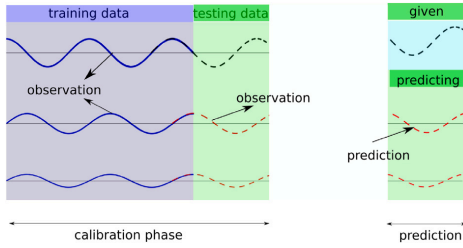


Fig. 9. 80% of the points in the time-series are used as training data (see Table 4 for details). The parameters are calibrated using the training data set. Then one observation at or near the surface is used to predict the temperatures within the soil in the testing data-set domain. Thus we obtain a predicted data set. The predicted data-set is compared with the testing data set to decide if the calibration is acceptable. If not, we re-calibrate.

where, N is the number of the samples, $\delta(t)$ is the observed N values, $\alpha(t)$ is the value estimated by the model (either sine curve fitting or by Fourier analysis).

4.2.2. Coefficient of determination (R^2)

The value of R^2 indicates the part of the variance in the dependent variable, which we can estimate from the independent variables. However, the value of R^2 does not indicate whether appropriate regression was used.

$$R^2 = 1 - \frac{\sum (o_i(t) - P_i(t))^2}{\sum (o_i(t) - \bar{o})^2} \quad (10)$$

where o_i is the i th observation, P is the prediction of the statistical model and \bar{o} is the average of the observation.

4.2.3. Root Mean Square Error (RMSE)

Root-mean-square error (RMSE) measures the differences between the fitted curve/line values and the values observed. The following equation was used to calculate RMSE.

$$RMSE = \sqrt{\frac{\sum_{i=1}^r (\delta_i - a_i)^2}{N}} \quad (11)$$

5. Result and discussion

5.1. Preparation of training and testing data

The field observations mentioned in Table 3 are used to both calibrate and validate the solution. The observations are divided into two groups: training and testing data-sets, as shown in the Fig. 9 and detailed in Table 4. The purpose of the testing data-set is to compare the output after calibration. For this study, we used 80% of the time-length of the observations as training data-set and the remaining 20% for testing data-set. The maximum days of the testing data-set is 178 days for bh2, and the minimum is 80 days for bh6, which we believe is enough to compare and estimate the errors. We could even use a higher percentage of the data-set to train the model since our problem poses no probability of a common error in machine learning: over-training. The training data-sets are used to calibrate the parameters of the Eq. (5). Then only one observation at the topmost node for the time series is used to predict the temperatures at various depths, thus obtaining the predicted data-set. An error estimate is made comparing the observation in the testing data-set with the predicted data-set.

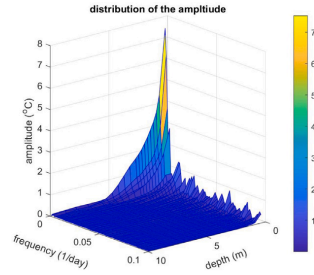


Fig. 10. The FFT analysis on the bh2 time series. The amplitude distributions over the frequencies and depth are shown. The highest amplitudes are found at the lower frequencies; also, the amplitudes reduce exponentially along with the depth. The phase of the Fourier components are randomly distributed and no relation between frequencies and depth can be found.

5.2. Calibration using training data-set

For every time series, there are 5 to 20 measurements at the nodes at different depths (detailed in Table 3). We retrieve the time series of the measurements at a 12-hour interval. Since the daily temperature variations cannot be captured when measured at 12-hour intervals, we convert the measurements to daily averages assuming that the average of the two 12-hour interval measurements represents the daily average temperature. The calibration starts with the Fast Fourier Transformation (FFT) analysis of the training data set. The output of FFT analysis on the bh2 time series is shown in Fig. 10 as an example. The amplitude distribution shows that peak amplitude ($n = 1$) are always at the lower frequencies. The amplitude reduces exponentially along with the depth. The smaller amplitudes are found at the higher frequencies representing the smaller daily variations of the temperature. A summary of the amplitude and frequency distributions for all the time series are shown in the Fig. 11. We notice that the peak frequencies of each series do not change along with the depth; it remains almost constant. However, the peak frequencies are not related to 365 days; rather, the time period ranges from 373 to 442 days. When a single sine-wave was fitted, the time period was always found to be 365 days. But when the time series is decomposed with FFT, the peak time periods are always found to be greater than 365 days. An amplitude and frequency distribution along the depth is drawn (Fig. 12). The related parameters are described in Tables 5 and 6. The amplitudes ($T_{a_n} : n = 1, 2, 3, \dots$) decays exponentially over the depth. An exponential curve $a \cdot e^{-bz}$ with two parameters a and b fits the amplitudes distributions over the depth (see the distribution of the peak frequency in Fig. 12). The results for the top three peak amplitudes are summarised in Table 6. We notice that for $n = 1$, the highest peaks, the curve fittings have better R^2 values, however, not all the curve fitting has a high R^2 value, a value of 0.623 is also observed.

5.2.1. Phase-lags estimated from Cross Power Spectrum Density (CPSD) analysis

Cross Power Spectral Density (CPSD) was used to determine the true phase-lags between the signals at different depths. For a time series, CPSD between the top layer and that time series provides the cross power spectral density (CPSD) of the two signals, using Welch's averaged, modified periodogram method (Welch, 1967) of spectral estimation. The phase difference is estimated as multiples of the π , which is converted to days as the maximum phase lag 2π is equivalent to 365 days; shown in Fig. 13. As the analytical solution suggests, the phase lag increases over depth. A linear equation: $a + m \cdot z$ is fitted for each time series. The estimated values of the parameters are given in Table 6. The R^2 values suggest the relationship is well described by a linear equation.

Table 4

The observations are divided into two groups: training and testing. 80% of the data resides in the training data-set while the rest is put on the testing data-set.

Time series	Training data-set			Testing data-set		
	from	to	total days	from	to	total days
bh2	13-09-16	18-09-18	705	18-09-18	10-02-19	178
bh3	13-09-16	21-09-17	373	21-09-17	22-12-17	94
bh51	09-06-14	18-05-16	710	18-05-16	11-09-16	116
bh52	12-11-16	29-04-18	534	29-04-18	09-09-18	133
bh61	09-06-14	24-04-15	320	24-04-15	13-07-15	80

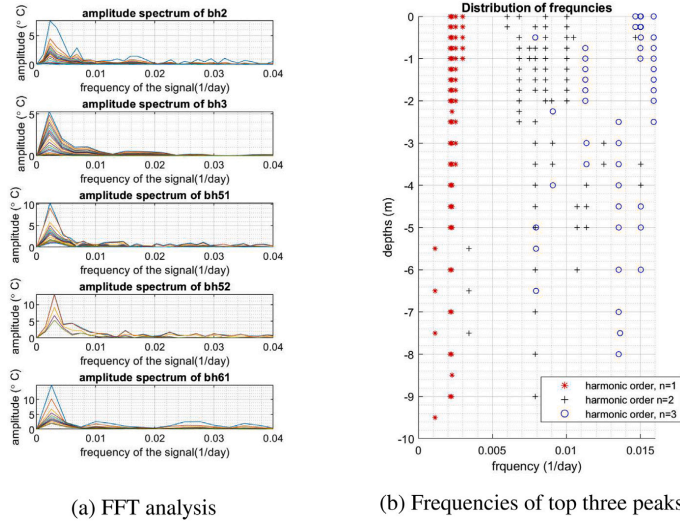


Fig. 11. (a) Fast Fourier Transformation (FFT) performed on time series reveals the low frequencies are the dominating signal. (b) Frequency distributions of the peak harmonic function (where $n = 1$ means the highest peak). The analysis shows the depth has no apparent effect on the frequencies. For the highest harmonic function, ranked $n = 1$, the frequencies are almost similar for all the time series till 5 m depth, after that some minor variations are noticeable. As for the next ranked frequencies, the range gets bigger. The spreading looks random for the $n = 3$.

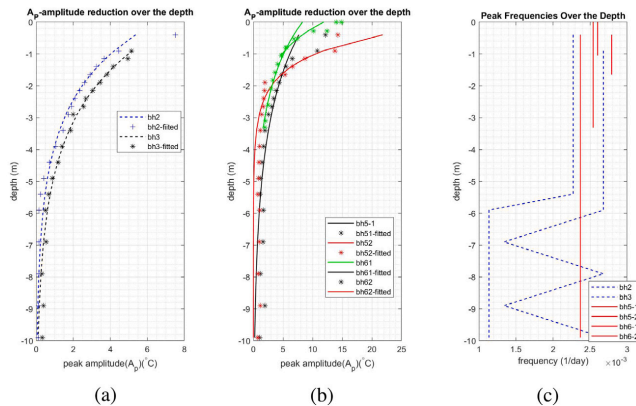


Fig. 12. The peak amplitude A_p for the $n = 1$, the peak frequency over the depth are depicted. The amplitude reduction is exponential; however, the frequency reduction is not observed till 5 m. The peak amplitudes at depth over 5 m are quite small (less than 1°C).

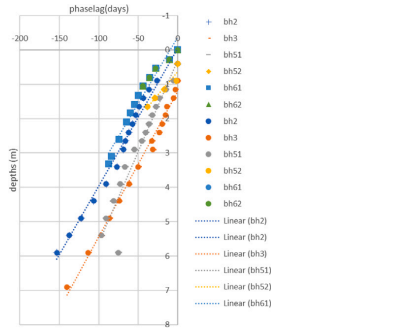


Fig. 13. The phase-lag over the depth shows a linear relation. The parameters of the curve fittings are mentioned in Table 6.

Table 5

An exponential curve ($a \cdot e^{-bz}$) is fitted to the amplitude distributions along the depth (where z is the depths). Only the top three harmonic functions are shown in the table.

Time series	Parameter	Rank of the peaks (n)		
		n = 1	n = 2	n = 3
bh2	a	6.514121	3.667414	1.746538
	b	0.79755	1.32577	1.46048
	R ²	0.990179	0.98182	0.994857
bh3	a	7.645913	1.381951	1.203991
	b	0.81458	0.623	0.91589
	R ²	0.992195	0.72056	0.581092
bh51	a	8.886689	3.962007	1.80939
	b	0.60695	0.91638	0.95682
	R ²	0.859604	0.679586	0.856837
bh52	a	27.27702	7.32094	1.574875
	b	1.64306	2.22973	0.1253
	R ²	0.877128	0.877806	0.95058
bh61	a	8.281672	1.419823	1.589165
	b	0.50868	0.74842	1.25615
	R ²	0.973705	0.942894	0.991782

Table 6

Phaselags of the signal determined by CPSD analysis, fitted to linear equation $a - mz$.

Time series	a	m	lags(days/m)	R ²
bh2	-0.0310	0.0399	25.0403	0.980723
bh3	1.2221	0.0420	23.7847	0.991341
bh51	0.3061	0.0530	18.8733	0.923127
bh52	0.1039	0.0447	22.3904	0.836632
bh61	-0.1459	0.0350	28.5465	0.959164

5.2.2. Discussion on the calibration of the parameters

The following observations are made:

- For a particular frequency, the amplitude decreases exponentially over the depth (see Figs. 10 and 12). The dominant amplitudes reside at the lower frequencies. For most cases, the first few peaks are significantly higher than the rest (see Fig. 11a). As expected, the longer the original signal, the stronger the peaks at the higher frequency (noticeable for bh5-1), indicating the model will be prone to errors if the higher frequencies are ignored.
- The frequency of the peak amplitude remains constant along the depths (see Fig. 11a). However, the peak frequencies are not the same for all boreholes. The observation suggests that the time period or seasonal variability has certain intervals and does not change within a short time.

- It is also observed that the highest amplitudes are found in the first peaks (see Fig. 11a). In other words, the peak with the highest time period also has the highest amplitude.

5.3. Validation of calibrated parameters and the solution using testing data-set

After calibrated using the training data sets, the parameters are used to predict the remaining 20% of the testing data set. In this section, we discuss the predictions and assess the errors. The Fourier components are determined from the training data set. The amplitude distributions are found from the Fourier components over the depth for each frequency. An exponential curve is fitted to relate the amplitude reduction over the depth for each frequency. Once the parameters are estimated, a prediction of the testing data set can be made. One example of the prediction is shown in Fig. 14. Along the x-axis, predicted temperatures and along the y-axis observed temperature are drawn. For a perfect prediction, the dots will be placed along the blue line which is drawn at a 45°. Any deviation from the line indicates an error in the estimation. Only the bh2 time series is shown in the Fig. 14. The rest of the time series can be found in Appendix E. The errors of the estimations are drawn along the depth in the sub-figures.

The following observations are made:

- The models has quite a high error at the top layers. The high RMSE errors indicate the predictions model breaks down at the organic active layer.
- When single sine-waves were fitted along with the time series, it was found that sine-wave deviates from the observations at the summer peak temperatures; the observations were lagged and smaller in amplitude. In contrast to the single sine-waves, when a combination of the harmonic wave functions is used, the errors are more prominent at the lower peaks. i.e. during winter. In other words, the summer temperatures are underestimated, whereas the winter temperatures are overestimated.

6. Conclusion

Soil temperature measurements are available at the Arctic coasts in the Kara Sea, Russia. The beach consists of continuous permafrost. The study area has two distinct zones, S#1 with low 5 m high cliffs and S#2 with 12–15 m high cliffs. Boreholes are constructed and thermal strings are placed inside them to measure the temperature until the depth of 9.9 m. The seasonal temperature variations are observed to be periodic. The time series of the temperature measurements are modelled with the boundary conditions as a combination of the harmonic waves. In this study, we calibrated the parameters of the solutions and validated the analytical solutions.

The salient outcome of the analysis can be summarised as follows:

- The seasonal variation of the temperature in the soil can be represented by the sine wave or combination of sine waves. The amplitude of such sine waves decreases exponentially. After 5 m of depth, the seasonal variations are small (less than one degree Celsius); we can neglect the variation.
- At the core of the pattern-seeking algorithm of the data-driven model is the analytical solution of the conduction–convection heat transfer equation. For the analysis, we calibrated the parameters only considering the depth-averaged values. But we notice that the errors created with such assumption are within the acceptable limit. The solution can be used to model a large area of the coast.
- The local variations of the solution’s parameters are captured within one single parameter, RR in Eq. (6) for each frequency, i.e. for each observation at a certain location, the value of RR is different. The smaller frequencies capture the effect of the heat sink or sources, such as latent heat of phase changes.

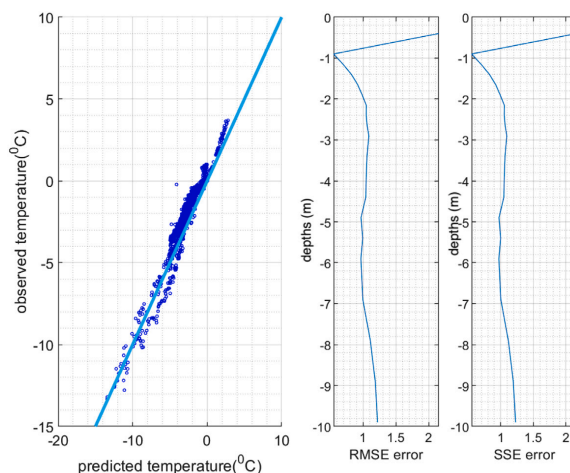


Fig. 14. Observed and predicted values are shown in the figures. A 45° line (thick blue) is drawn on the sub-figure to the left. The rest of the time series are shown in Appendix E. (For interpretation of the references to colour in this figure legend, the reader is referred to the web version of this article.)

- The phase-lag between the time series near the surface and the deeper part in the soil is considerable. The low thermal conductivity at the organic-active layer is one of the significant factors for the phenomenon. The summer high temperature of the soil at a depth of 5 m is almost 100 days behind that of surface temperature (see Fig. 13). The analytical model suggests the phase-lag should have a linear relation with depth. The observations from the field confirm the linear relation. The phase lag is estimated to be around 20 to 25 days per metre of depth.
- Zone S#2 has higher *RR* values and a lower water table, indicating very low to negligible heat transfer via convection. The error of the solutions is quite high in the shallow layers where surface run-off and precipitation during the summer is significant.
- The deviations from the observed values are most prominent at the positive temperatures, i.e. during summer. The solutions fail to capture the peak temperatures of the summer accurately.

The model did not consider the temperature profiles near the end of the cliffs, where the effect of the exposed bluff face on the temperature profile can be captured. Unlike the soil inside the cliffs, the crest and bluff-face are exposed to air on two planes. The temperature profiles will require corrections when the heat flows in two dimensions (2D). The precipitation and surface runoff from the flow of water of the thawing lakes were not considered. A separate model may be required to model the vegetation cover on the surfaces. The vegetation not only works as a blanket for the thermal energy transfer also works as cementing material against soil erosion.

Funding

This research was funded by the EU H2020-funded Nunataryuk project, where it is filed as part of deliverable 6.4.

CRedit authorship contribution statement

Mohammad Akhsanul Islam: Conceptualization, Methodology, Software, Formal analysis, Visualization, Writing:Original Draft, Writing - Review & Editing. **Raed Lubbad:** Conceptualization, Formal analysis, Investigation, Writing - Review & Editing, Supervision, Project administration, Funding acquisition. **Seyed Ali Ghoreishian Amiri:**

Formal analysis, Investigation, Software. **Vladislav Isaev:** Data curation, Investigation, Resources, Validation, Writing - Review & Editing, Supervision, Project administration. **Yaroslav Shevchuk:** Data curation, Investigation. **Alexandra Vladimirovna Uvarova:** Data curation, Investigation. **Mohammad Saud Afzal:** Validation, Writing - Review & Editing, Supervision, Funding acquisition. **Avinash Kumar:** Validation, Writing - Review & Editing, Supervision, Funding acquisition.

Acknowledgements

The report is written as part of the EU H2020-funded Nunataryuk project, where it is filed as part of deliverable 6.4, and by the NC-POR//PACER Outreach Programme (POP) Initiative on “Predictive Tools for Arctic Coastal Hydrodynamics and Sediment Transport”. This research is also supported by Sustainable Arctic Marine and Coastal Technology (SAMCoT), Norway, Norwegian University of Science and Technology (NTNU), Lomonosov Moscow State University (MSU), Russia and Sponsored Research and Industrial Consultancy (SRIC), Indian Institute of Technology Kharagpur.

Appendix A. Supplementary data

Supplementary material related to this article can be found online at <https://doi.org/10.1016/j.polar.2021.100732>.

References

- Andersland, O.B., Ladanyi, B., et al., 2003. *Frozen Ground Engineering*. John Wiley & Sons.
- Are, F., 1988. *Thermal abrasion of sea coasts (part i)*. Taylor & Francis.
- Barnhart, K.R., Anderson, R.S., Overeem, I., Wobus, C., Clow, G.D., Urban, F.E., 2014. Modeling erosion of ice-rich permafrost bluffs along the alaskan beaufort sea coast. *J. Geophys. Res. Earth Surf.* 119 (5), 1155–1179.
- Bernstein, L., Bosch, P., Canziani, O., Chen, Z., Christ, R., Riahi, K., 2008. IPCC, 2007: climate change 2007: synthesis report. IPCC.
- Gao, Z., Fan, X., Bian, L., 2003. An analytical solution to one-dimensional thermal conduction-convection in soil. *Soil Sci.* 168 (2), 99–107.
- Gao, Z., Lenschow, D.H., Horton, R., Zhou, M., Wang, L., Wen, J., 2008. Comparison of two soil temperature algorithms for a bare ground site on the loess plateau in China. *J. Geophys. Res.: Atmos.* 113 (D18).
- Guégan, E., 2015. Erosion of permafrost affected coasts: rates, mechanisms and modelling. NTNU.

- Holmes, T., Owe, M., De Jeu, R., Kooi, H., 2008. Estimating the soil temperature profile from a single depth observation: A simple empirical heatflow solution. *Water Resour. Res.* 44 (2).
- Hoque, M.A., Pollard, W.H., 2009. Arctic coastal retreat through block failure. *Can. Geotech. J.* 46 (10), 1103–1115.
- Hu, G., Zhao, L., Wu, X., Li, R., Wu, T., Xie, C., Qiao, Y., Shi, J., Li, W., Cheng, G., 2016. New fourier-series-based analytical solution to the conduction–convection equation to calculate soil temperature, determine soil thermal properties, or estimate water flux. *Int. J. Heat Mass Transfer* 95, 815–823.
- Isaev, V., Kioka, A., Koshurnikov, A., Pogorelov, a., Amangurov, R., podchasov, o., Sergeev, D., 2016. Field investigation and laboratory analyses: baydaratskaya bay 2016. <http://dx.doi.org/10.13140/RG.2.2.13836.00645>.
- Isaev, V., Koshurnikov, A., Pogorelov, A., Amangurov, R., Podchasov, O., Sergeev, D., Buldovich, S., Aleksyutina, D., Grishakina, E., Kioka, A., 2019. Cliff retreat of permafrost coast in south-west baydaratskaya bay, kara sea, during 2005–2016. *Permaf. and Periglac. Process.* 30 (1), 35–47.
- Kobayashi, N., Vidrine, J., Nairn, R., Solomon, S., 1999. Erosion of frozen cliffs due to storm surge on beaufort Sea Coast. *J. Coast. Res.* 332–344.
- Lantuit, H., Pollard, W., 2008. Fifty years of coastal erosion and retrogressive thaw slump activity on herschel island, southern beaufort sea, yukon territory, Canada. *Geomorphology* 95 (1–2), 84–102.
- Leont'yev, I., 2003. Modeling erosion of sedimentary coasts in the western Russian arctic. *Coast. Eng.* 47 (4), 413–429.
- Leont'yev, I., 2004. Coastal profile modeling along the Russian arctic coast. *Coast. Eng.* 51 (8–9), 779–794.
- Lewkowicz, A., 1991. Climatic change and the permafrost landscape, In: *Arctic Environment: Past, Present and Future*, In: Woo, MK and Gregor, DJ(Ed.), *Proceedings of a Symposium*, pp. 14–15.
- Nairn, R., Solomon, S., Kobayashi, N., Vidrine, J., 1998. Development and testing of a thermal-mechanical numerical model for predicting arctic shore erosion processes. In: *Permafrost: Proceedings of the Seventh International Conference, Yellowknife, NWT, June 23-27*. Centre d'études nordiques, Université Laval, Québec, Canada, pp. 789–795.
- Ogorodov, S., Aleksyutina, D., Baranskaya, A., Shabanova, N., Shilova, O., 2020. Coastal erosion of the Russian arctic: An overview. *J. Coast. Res.* 95 (sp1), 599–604.
- Plaxis, 2021. *Manuals:plaxis*. https://communities.bentley.com/cfs-file/_key/communityserver-wikis-components-files/00-00-00-05-58/PLAXIS2DCE_2D00_V21.00_2D00_04_2D00_Scientific.pdf. (Accessed 25 July 2021).
- Ravens, T.M., Jones, B.M., Zhang, J., Arp, C.D., Schmutz, J.A., 2012. Process-based coastal erosion modeling for drew point, north slope, alaska. *J. Waterw. Port Coast. Ocean Eng.* 138 (2), 122–130.
- Romanovsky, V., Osterkamp, T., 1997. Thawing of the active layer on the coastal plain of the alaskan arctic. *Permaf. Periglac. Process* 8 (1), 1–22.
- Stallman, R., 1965. Steady one-dimensional fluid flow in a semi-infinite porous medium with sinusoidal surface temperature. *J. Geophys. Res.* 70 (12), 2821–2827.
- Van Wijk, W.R., De Vries, D., 1963. Periodic temperature variations in a homogeneous soil. *Phys. Plant Environ.* 1, 103–143.
- Verhoef, A., van den Hurk, B.J., Jacobs, A.F., Heusinkveld, B.G., 1996. Thermal soil properties for vineyard (EFEDA-i) and savanna (HAPEX-sahel) sites. *Agricult. Forest Meteorol.* 78 (1–2), 1–18.
- Vijay, P., et al., 2018. *Advances in Coastal Hydraulics*. World Scientific.
- Welch, P., 1967. The use of fast fourier transform for the estimation of power spectra: a method based on time averaging over short, modified periodograms. *IEEE Trans. Audio Electroacoust.* 15 (2), 70–73.

C.3 Journal Paper#3

Article

A Process-Based Model for Arctic Coastal Erosion Driven by Thermodenudation and Thermoabrasion Combined and including Nearshore Morphodynamics

 Mohammad Akhsanul Islam *  and Raed Lubbad

Department of Civil and Environmental Engineering, Norwegian University of Science and Technology, 7491 Trondheim, Norway

* mohammad.a.islam@ntnu.no

Abstract: Various models have recently been developed to describe Arctic coastal erosion. Current process-based models simulate multiple physical processes and combine them interactively to resemble the unique mechanism of Arctic coastal erosion. One limitation of such models is the difficulty of including hydrodynamic forces. The available coastal erosion models developed for warmer climates cannot be applied to Arctic coastal erosion, where permafrost is a significant environmental parameter. This paper explains a methodology that allows us to use the models designed for warmer climates to simulate Arctic coastal erosion. The open-source software XBeach is employed to simulate the waves, sediment transport and morphological changes. We developed different submodules for the processes unique to Arctic coasts, such as thawing–freezing, slumping, wave-cut niche, bluff failure, etc. The submodules are coupled with XBeach to enable concurrent simulation of the two mechanisms of Arctic coastal erosion, namely thermodenudation and thermoabrasion. Some of the model’s input parameters are calibrated using field measurements from the Arctic coast of Kara Sea, Russia. The model is then validated by another set of mutually exclusive field measurements under different morphological conditions from the study area. The sensitivity analysis of the model indicates that nearshore waves are an important driver of erosion, and the inclusion of nearshore hydrodynamics and sediment transport are essential for accurately modelling the erosion mechanism.

Keywords: thermodenudation; thermoabrasion; probabilistic model; permafrost; storm surge; niche growth; bluff collapse



Citation: Islam, M.A.; Lubbad, R. A Process-Based Model for Arctic Coastal Erosion Driven by Thermodenudation and Thermoabrasion Combined and including Nearshore Morphodynamics. *J. Mar. Sci. Eng.* **2022**, *10*, 1602. <https://doi.org/10.3390/jmse10111602>

Academic Editor: Tom Ravens and Xiao Ming

Received: 02 September 2022
 Accepted: 15 October 2022
 Published: 31 October 2022

Publisher’s Note: MDPI stays neutral with regard to jurisdictional claims in published maps and institutional affiliations.



Copyright: © 2022 by the authors. Licensee MDPI, Basel, Switzerland. This article is an open access article distributed under the terms and conditions of the Creative Commons Attribution (CC BY) license (<https://creativecommons.org/licenses/by/4.0/>).

1. Introduction

Approximately one-third of the coast worldwide consists of permafrost, for which the average retreat rate is close to 0.5 m per year [1]. The annual retreat of the coastline along Alaska in the Beaufort Sea is 1.7 m per year [2]. In recent decades, the coastal retreat rate along the Kara Sea has been measured between 1 and 1.7 m per year [3]. The annual maximum retreats along the Alaskan coast were approximately 22 m for the years 2007, 2012 and 2016 [4–6]. Many other Arctic coasts are retreating at the same level of magnitude. The most significant erosion along the coast of the Kara Sea was observed to be 19.6 m in 2010–11 [7]. Observations along the various Arctic coasts have led to the establishment of a link between increased coastal erosion and a smaller extent of sea cover [8,9], warmer air temperature [10,11] and increased permafrost temperature [12].

The environmental changes due to warming of the climate are triggering significant coastal erosion in the Arctic [13]. The number of open-sea days in the Arctic is increasing rapidly [14]. The seawater temperature anomalies reached 5 °C in the Arctic Ocean [15]. The frequency and intensity of storms during summer are also expected to increase [16]. Increased thawing of permafrost inside the coastal bluffs leads to slumping and, consequently, loss of mass along the Arctic coast. On the other hand, the sea ice extent is shrinking, which enables longer fetches to generate larger waves [14]. A longer open sea season also increases

erosion along the coast. As a result, Arctic coastal retreat has increased more than twofold in the last few decades [17–20].

Increased Arctic coastal erosion poses a significant threat to residents of coastal communities. Shoreline infrastructure is compromised, heritage sites are at risk, and the lifestyle of the indigenous people is also affected [20]. Moreover, within the next decade, the surface air temperature is expected to exceed the normal range of variability. In contrast, with regard to Arctic sea ice, the natural range of variability has already been exceeded [21]. A pan-Arctic model by Nielsen et al. [12] predicts that Arctic coastal erosion will exceed the natural variability range before the end of the century, with a 66% probability of exceeding by 2023 and over 90% probability of exceeding before 2049.

Are F [22] described two mechanisms that govern coastal bluff erosion in the Arctic: thermodenudation and thermoabrasion. In the thermodenudation process, thermal energy thaws the permafrost during the summer, leading to slumping of the thawed bluffs via gravitational forces. The slumped materials are removed from the beach by waves, tides and storm surges. Thermodenudation is a continuous process and contributes to the slow retreat of the coast. In contrast, thermoabrasion is rapid and episodic. Thermoabrasion is triggered during summer storms where surges inundate the beach, leading to the formation of a wave-cut niche at the bluff's base. The growing niche becomes deep enough to trigger bluff collapse at one point. The collapsed bluff degrades on the beach and eventually washes away under hydrodynamic forcing.

There is still a limited understanding of the governing mechanisms behind Arctic coastal erosion. A fundamental element of the Arctic coasts, the presence of permafrost, creates a different condition compared to coastal erosion in a warmer climate. Permafrost acts as a slow-erodible structure when no thermal source is present. Along with thermal drivers, the mechanical component also contributes to erosion. Coastal erosion in the Arctic is sensitive to the presence of sea ice, which dampens the waves propagating towards the coast [23].

Several models have been developed to simulate Arctic coastal erosion over the past decade. Most of these models focus on bluff failure, where the growth of the niche is the central factor of the erosion mechanism. Such process-based models simulate wave-cut niche growth at the bluff base, destabilise the overhanging portion and lead to bluff failure. The earlier work of Kobayashi [24] provides the basis for most of these models. Kobayashi [24] developed an analytical solution of the inward growth rate of the niche as a function of the temperature of the incoming seawater, the depth of water at the base of the bluff and the duration of the inundation. Additionally, niche models developed for melting of icebergs via waves and currents [25,26] have also been used with modifications; for example, a factor for energy requirement ratio of pure ice and permafrost thawing [27]. Hoque and Pollard [28] modelled bluff failure as a loss of balance (moment failure) and shear failure (mechanical strength). A process-based model to connect niche growth and bluff collapse with hydrodynamic forcing was introduced by Ravens et al. [29]. They included oceanographic boundary conditions using 12-h time steps. Ravens et al. [29] coupled four physical processes as modules: storm surge, niche growth, collapse of the overhanging bluff over the niche and degradation of the collapsed bluff. Barnhart et al. [30] expanded the model of Ravens et al. [29] and incorporated the bluff stability concept of Hoque and Pollard [31]. Barnhart et al. [30] also employed smaller time steps (3 h) to capture erosion at higher temporal resolutions. To include the effect of morphological changes such as changes in the coastal profiles of the Arctic coasts, Ravens et al. [32] used the open-source software package XBeach [33] to simulate wave propagation, sediment transport, and slumping. The latter was achieved by modifying the avalanching module in XBeach originally developed for sandy dunes. Bull et al. [27] introduced finite element analysis to understand niche-induced bluff collapse in detail. Frederick et al. [34] developed the finite element model to obtain a detailed analysis of the formation of the niche and subsequent bluff collapse without assuming any predetermined failure planes Rolph et al. [35] developed a pan-Arctic level

erosion model based on thermal energy balance on the beach, a model originally proposed by Kobayashi et al. [36].

Arctic coastal erosion is a combination of various physical processes. While detailed models of some of the processes exist, for example, the formation of a wave-cut niche during a storm [24,34], a long-term generic (not site-specific) comprehensive model has yet to be achieved [37]. The process-based numerical models developed for various sites usually simplify physics. More importantly, the interactions between processes in the models are either ignored or made one-way (the processes are consequential, following a strict order of precedence). The existing models are not generic to all Arctic coasts, specifically for beaches where erosion is a mix of thermodenudation (dominated by thermal processes) and thermoabrasion (mechanically driven).

This paper describes a comprehensive model that couples the thermodenudation and thermoabrasion processes with nearshore hydrodynamics and sediment transport. The waves and related hydrodynamic forcing, together with sediment transport and morphodynamics are simulated using XBeach. The in-house modules simulate the other dominant processes related to erosion. We adopt a modular approach for the numerical implementation where the submodules communicate at three-hour intervals. The model is calibrated and validated with field measurements from one of the Arctic coasts along the Kara Sea. The behaviour of the model and potential applications are demonstrated. The simulations show that the erosion mechanism is greatly influenced by nearshore hydrodynamics and provide justification for including a hydrodynamic model to simulate Arctic coastal erosion.

2. Model Description

This paper presents a comprehensive model to simulate thermodenudation and thermoabrasion simultaneously. The processes of thawing, slumping, niche growth, bluff collapse and collapsed-bluff degradation are coupled with the coastal erosion model XBeach. Two-way coupling is established between (1) hydrodynamic forcing and sediment transport in XBeach on the one hand and (2) mechanical and thermal erosion processes in the in-house model on the other hand.

2.1. Model Domain and Input Data

Arctic coastal erosion originates offshore with wave generation and increases in water level due to storms. Thus, the domain of our model begins offshore. Four boundaries divide the domain into three zones, i.e., offshore, nearshore and beach bluffs (Figure 1). The offshore zone of the domain is contained by boundaries BC1 and BC2. The boundary BC2 is defined where the mean sea level (l_m) and wavelength (λ) bear a ratio of less than 0.5. The storm surge and wave generation in the offshore zone are simulated using a simplified 1D storm surge module [38] and SWAN [39], respectively. The SWAN and storm surge model are coupled with XBeach at the BC2 boundary. At the BC2, water level (wl) and wave conditions (H_{m_0} , T_p , θ of JONSWAP spectrum) are specified based on SWAN and storm surge model results. The transformation of the wave, wave setup and set down, and morphological changes in the nearshore zone are simulated by XBeach. Permafrost-related processes thawing and erosion of the bluffs are simulated with in-house modules and coupled with XBeach.

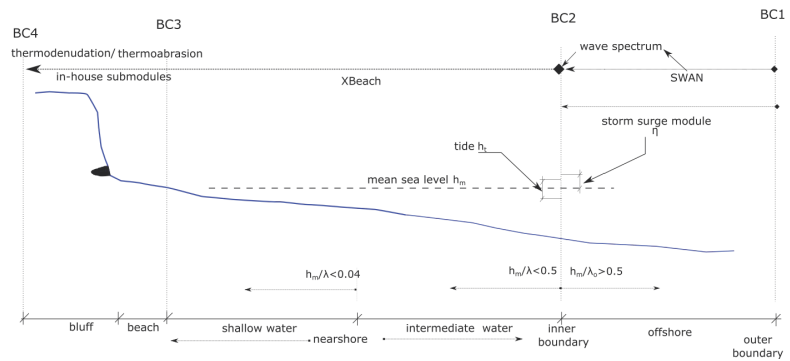


Figure 1. The spatial zones of the model are marked with four boundaries. SWAN and storm surge modules calculate the hydrodynamics boundary conditions at BC2, which acts as input for XBeach. The outputs of XBeach are used as input for the submodules of thermodenudation and thermoabrasion.

Table 1 lists the parameters used to describe thermodenudation and thermoabrasion in our model. The geometric definitions are provided in Appendix A.

Table 1. The list of main parameters used to describe the models.

Parameter	Definition	Typical Value	Units	References
thermal properties				
h_{c_a}	convective heat transfer coefficient of air	100	W/m^2-k	[36]
h_{c_w}	convective heat transfer coefficient of water	700	W/m^2-k	[36]
L_t	volumetric latent heat of permafrost	1.6×10^7	J/m^3	[36]
T_a	Temperature of air	varied	$^{\circ}C$	NOAA [40]
T_w	Temperature of water	varied	$^{\circ}C$	NOAA, [40]
T_s	Temperature of soil	varied	$^{\circ}C$	field measurements
geometry				
x_t	thawing depth	varied	m	
h_{id}	water depth at the base	varied	m	
h_m	mean sea level	varied	m	
h_t	tide compared with MSL	varied	m	
wl	water level	varied	-	calculated by Equation (11)
η	storm surge level compared with MSL	-	m	Equation (A1)
β	niche opening parameter	2	-	Kobayashi [24]
m_{cr}	critical slope of slumping	0.1–1	-	field observations
T_{HF}	distance from niche to the ice-wedge polygon	5–14	m	field observations
U_w	wind speed	-	m/s	NOAA reanalysis
time steps				
dt_x	timestep within XBeach	varied	s	XBeach Manual
dt	timestep within modules/ global timestep	10,800	s	based on 3 h sea state
dt_m	timestep between two field measurements	365	days	Field report

2.2. Thermodenudation Module

The thermodenudation module simulates thermally driven processes within the beach and bluff. The processes of permafrost thawing and slumping at the bluff face are simulated using two submodules of permafrost thaw and slumping.

2.2.1. Submodule: Permafrost Thaw

We divide the permafrost thaw along the coastal profile into four sections, as shown in Figure 2. The warmer air and seawater bring the thermal energy necessary to thaw the permafrost inside the bluffs. The sections are defined based on the nature of the convective heat transfer. The four sections are the bluff surface, bluff face, beach and seabed (definitions are in Appendix B).

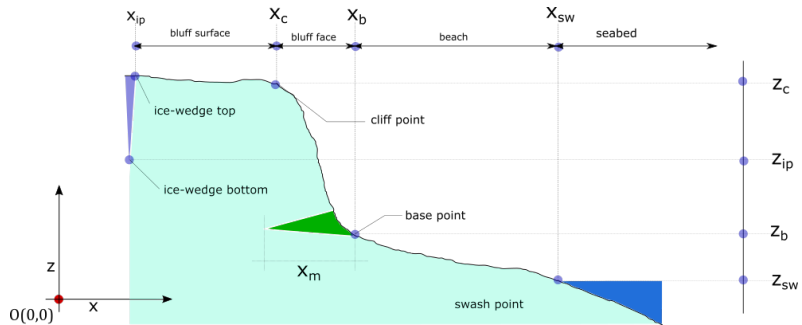


Figure 2. The coastal profile can be divided into four sections based on the thermal energy transfer mechanism. The most active portion in terms of thawing is the bluff face.

The thawing depth (x_t) is defined as the depth of permafrost thawing or freezing face from the coastal profile, normal to each point, as shown in Figure 3. The thawing depth (x_t) is time-varying; it typically has the highest value in the summer and returns to zero during the winter. Stefan’s equation can be used to determine the thawing depth (x_t) [41]:

$$x_t = \sqrt{\frac{2k_u T_0 t}{\rho_d L_s w}} \tag{1}$$

where t is the length of time (days), ρ_d is the average dry density (kg m^{-3}), L_s is the specific latent heat of fusion (J kg^{-1}), w is the water content(%), and k_u is the thermal conductivity of the unfrozen soil; a typical value of k_u can be $1.6 \text{ J m}^{-1} \text{ s}^{-1} \text{ K}^{-1}$ and T_0 are the temperatures of the bluffs. However, Equation (1) overestimates the thawing and freezing depth [41]. The equation does not consider the fluid and surface interactions, air/water velocities, turbulence and geometric orientations. Equation (1) is not suitable for our model since we want to treat the dry and wet (submerged) parts of the coastal profile separately. We adopted another approach to estimate the thawing depth by calculating the heat transfer and subsequent thawing and freezing [32]. The energy transfer from the seawater or air to the sediment is estimated from the convective heat transfer equation:

$$Q_{w/a} = h_{c_{w/a}}(T_{w/a} - T_s) \tag{2}$$

where $Q_{w/a}$ is the thermal energy transfer rate (energy per unit area per time) from water or air to the bluffs $\text{J m}^{-2} \text{ s}^{-1}$, $h_{c_{w/a}}$ is the convective heat transfer coefficient ($\text{W/m}^2 \text{ K}$); different for air and water, $T_{w/a}$ is the temperature of the water or air, and T_s is the temperature of the seabed and bluff.

Assuming the temperature of the thawed layer remains close to the melting temperature and thus $Q_{w/a}$ is responsible for the latent heat requirement of the phase change of permafrost, we can use Equation (2) together with Equation (3) to determine the thawing depth (x_t):

$$\frac{dx_t}{dt} = \frac{Q_{w/a}}{L_t} \tag{3}$$

where L_t is the volumetric latent heat of fusion, taken as $L_t = 1.6 \times 10^7 \text{ J/m}^3$ [32], dt is the time duration in seconds and x_t is the thawing depth assumed to be normal to the surface (see Figure 3).

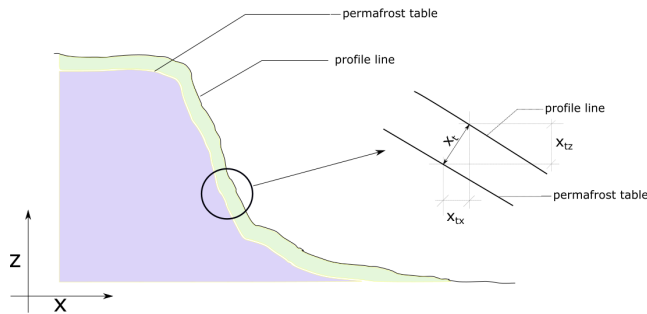


Figure 3. The thawing depth is the distance normal to the permafrost to the surface of the bluffs (x_t).

The benefits of using Equation (3) over Equation (1) in our model are (1) the convective heat transfer coefficient can be calibrated to represent the different heat fluxes at bluff-surface, bluff-face, beach and seabed and (2) the equation is also valid for freezing when the fluid temperature drops below zero, allowing the submodule to remain active for all the seasons.

2.2.2. Submodule: Slumping

The failure of the thawed sediments by gravity as a layered movement or mudflow; without active contribution from waves is considered under the thermodenudation mechanism. Several slumping failure modes such as active layer detachment, solifluction, and retrogressive thaw slump are observed in the Arctic. In this paper, a simplified 1D model of mass movement is used in which we adopt a proxy parameter called critical slope (m_{cr}). The latter defines the threshold at which the thawed material will fall under the influence of gravity (see Figure 4). In general, the combined effect of sediment size distribution, ice content, consolidation status, internal friction and cohesion will determine the value of m_{cr} . The value of m_{cr} will vary for each coastal profile and must be carefully examined and calibrated. Further, we do not consider the effect of water flow inside the bluff nor the effects of sediment creep dynamics in our simplified slumping model. Moreover, we do not impose any upper limit on mass movement in our slumping model.

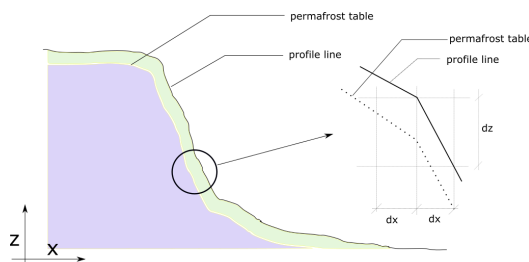


Figure 4. Slumping occurs when the thawed materials fall due to gravity. The conditions for the triggering are: (1) thawing depth (x_t) is greater than zero and (2) slope at the point (dz/dx) is greater than the critical slope (m_{cr}).

The following conditions must be fulfilled to trigger slumping.

$$\frac{dz}{dx} \geq \begin{cases} m_{cr,w} & \text{if } x_t > 0, h > 0.05m \\ m_{cr,a} & \text{if } x_t > 0, h < 0.05m \end{cases} \quad (4)$$

where dz/dx is the slope of the coastal profile at a given point, $m_{cr,a}$ and $m_{cr,w}$ are the critical slopes for dry and wet conditions, respectively, and h is the time-averaged water depth. Some parts of the beach may temporarily go underwater by wave run-ups and the time-averaged water depth (in our model three hours) will have a small positive value at some of the grid points even though the heat is exchanged from the warm air. To overcome this problem, an arbitrary small threshold value of 0.05 m is chosen. When the water depth $h \geq 0.05$ m, we consider the portion of the profile submerged. The assumptions related to slumping and numerical implementation are discussed in detail in Appendix C.2 and a standalone example of the slumping module is available in the supplementary section..

2.3. Thermoabrasion Module

During storm surges with a combined effect of waves (wave setup, wave run-up) and tide, the water reaches the base of the bluffs, and a niche starts to grow. This module simulates the niche growth, subsequent bluff collapse, and collapsed-bluff degradation as three submodules. The behaviour of the submodules is highly dependent on the boundary conditions at the base of the bluffs, especially the water level at the base of the bluffs (h_{id}) and water temperature (T_w).

2.3.1. Submodule: Niche Growth

When the water level reaches the base of the bluff (point B in Figure 5), the warm water creates a niche. The geometry depicted in Figure 5 is adapted and simplified from the Kobayashi [24] model.

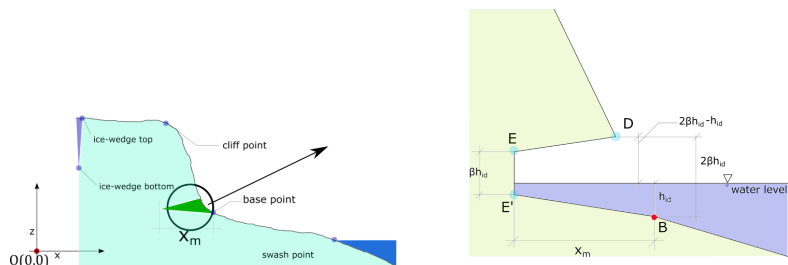


Figure 5. Niche geometry during the storm surge; simplified from Kobayashi (1985).

The water depth at the base of the bluff; point B in the figure termed h_{id} is obtained from the results of the XBeach simulation. The thawing face, line EE', is vertical and assumed to be βh_{id} , where β is the empirical parameter. The value of β is taken as 2 [29]. The niche depth, line BE' = x_m , is estimated from the equation:

$$x_m = 2\zeta_m \sqrt{\epsilon t} \quad (5)$$

where h_{id} is the time-averaged depth of water at the base of the bluff (m), g is the gravitational acceleration (m/s^2), ϵ is the surf zone diffusivity $\epsilon = Ah_{id}\sqrt{gh_{id}}$, A is an empirical constant, taken as 0.4 [42], $\zeta_m = 0.0094(T_w - T_m)$, T_w is the temperature of the seawater and T_m is the salinity adjusted melting point of the ice.

2.3.2. Submodule: Bluff Collapse

The wave-cut niche at the base of the bluff creates instability, which may lead to bluff collapse. A critical combination of the various geometric parameters, such as niche opening, niche depth, position of the ice-wedge polygon and mechanical strength parameters, such

as internal friction and cohesive strength, leads to the collapse of the bluffs. The location of the failure line and plane may vary depending on the combinations of the various parameters. Two principal modes are identified for bluff collapse: (1) shear failure and (2) overturning failure [31]. Shear failures are related to the mechanical strength of the bluffs. In Figure 6, one of the three shear failure modes is depicted (the modes are discussed in Appendix C.3). The shaded region over the niche is susceptible to collapse. The failure line, in this case, is GE, and the shaded region by the geometry GCDE is collapsed. A generalised and simplified condition of shear failure of the bluff is Equation (6) [28]:

$$c \cdot T_{ib} + W \cos \alpha \cdot \tan \phi < W \sin \alpha \tag{6}$$

where α is the angle of inclination of the failure plane, ϕ is the angle of internal friction of the bluffs, T_{ib} is the tensile failure line of the bluff (m), c is the tensile strength of the bluff (N/m), and W is the weight of the collapsed bluff (N) (weight of the GCDE portion in Figure 6a).

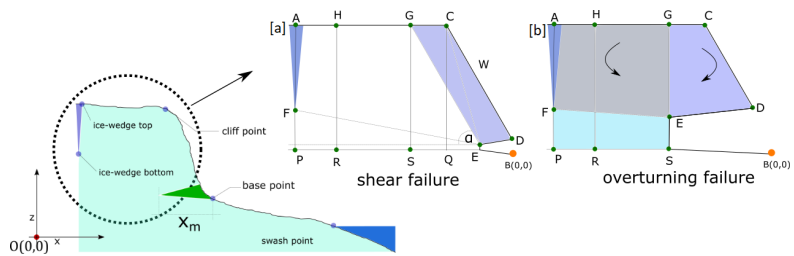


Figure 6. Two common failure modes of bluff collapse. [a] Shear failure of the bluffs, described by Equation (6) and [b] Overturning failure of the bluff, described by Equation (7).

In the overturning failure mode, the failure is initiated by the moment created by the overhanging portion of the bluff. The overturning occurs at the thawing face of the niche at point E in Figure 6b. The shaded overhanging portion (GCDE) creates the driving moment in favour of collapse, which is countered by the moment created by the remaining portion of the bluff (AHGEF). A small contribution comes from the friction along failure line EF and line AF. The failure mode is generalised by the following Equation (simplified from the models by Hoque and Pollard [28] and Barnhart et al. [30]):

$$\tau_d > \tau_r + c_p T_{HF} + c_{ice} T_{VF} \tag{7}$$

where τ_d is the moment created by the overhanging bluff at the turning point (N-m), τ_r is the opposite moment created by the rest of the bluff (N-m), c is the cohesive strength of the bluff (N/m²) (different for ice and permafrost), T_{HF} is the horizontal failure line (line FE in Figure 6), and T_{VF} is the vertical failure (line AF).

2.3.3. Submodule: Degradation of Collapsed Bluffs

The collapsed bluff remains on the beach and degrades over time. The degradation rate of the bluff can be estimated from the following Equation [29]:

$$M_i = M_{i-1} - aH^n [T_w - T_m] \tag{8}$$

where M_i is the mass of the collapsed bluff at the end of timestep i , M_{i-1} is the mass of the bluff at the end of the previous timestep $i - 1$, T_w is the seawater temperature, T_m is the salinity adjusted melting point of ice, H is the significant wave height at the 3-m water depth, and a and n are the empirical parameters. Ravens et al. [29] estimated that the values of a and n are 800 kg/m[−]°C and 1.47, respectively. In the numerical implementation of bluff degradation, we assume an immediate degradation of the collapsed bluff and

the sediments are distributed evenly on the beach. The coupled hydrodynamic module simulates the removal of sediments from the beach.

2.4. Numerical Implementation

2.4.1. Hydrodynamics of the Offshore

Wave conditions and the water level are determined at the BC2 boundary as shown in Figure 1. SWAN determines the wave generation in the domain contained by the boundaries BC1 to BC2. A one-dimensional (1D) storm surge model calculates the storm surge (η) at the BC2 boundary. Numerical implementation of the storm surge model is detailed in Appendix C.1. The storm surge model is a function of wind speed, alongshore current, pressure drop, and the Coriolis effect.

2.4.2. Hydrodynamics of the Nearshore

We choose XBeach to simulate hydrodynamics, sediment transport and morphological changes from BC2 (in Figure 1) until bluffs. The input parameters at the XBeach offshore boundary at BC2 are time series of JONSWAP spectrum for waves, tide, mean sea level, storm surge, etc. A complete list of the XBeach parameters is provided in the Appendix F. XBeach simulates the wave transformation, wave set up and set down, run up, water level, tide and morphological changes in the nearshore zone. The results of the XBeach simulation are fed into the in-house submodules of thermodenudation and thermoabrasion. The timestep for the global model is chosen to be 3 h (Figure 7). The choice of global timestep is made by following the common practice in wave modelling and is consistent with most of the available metocean databases where stationarity is usually assumed over a period of 3 h and thus the sea state within the timestep is described with a spectrum. We simulate the hydrodynamic forcing and sediment transport of nearshore with XBeach for the i -th timestep and analyse the results. We determine the bed level changes, average water depth at the base of the bluffs (l_{iq}), and the mean water depth at each grid (to determine the wet/dry condition for convective heat transfer). The output of XBeach is then fed into the submodules of slumping, thawing depth, niche growth, and bluff collapse.

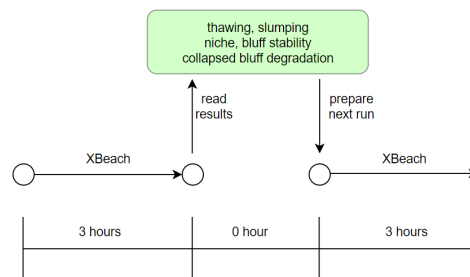


Figure 7. XBeach simulates the nearshore module. The XBeach output is analysed and used as inputs for other submodules.

2.4.3. Modelling Permafrost and Thawing Depth

The permafrost and the thawed layer above the permafrost need to be treated separately to simulate thermodenudation. The thawing submodule calculates the thawing depth at the interval of each time step. The thawed layer above the permafrost reacts to hydrodynamic forcing similar to a typical coastal profile in a tropical or subtropical climate. Within XBeach, the ‘nonerodible’ surface layer feature aims to treat the effect of hard structure on the morphological changes in the coastal profile. The ‘nonerodible’ features allow users to include a surface that is unaffected by hydrodynamic forcing, and sediment transport is not permitted even if this surface is exposed. The ‘nonerodible’ surface can be defined with ‘*ne_layer*’, and the user can place it inside the dune, beach and seabed.

The permafrost acts similarly to a nonerodible surface, only that the permafrost line is a moving boundary with respect to time. In the numerical model, we achieve it by updating the 'ne_layer' of XBeach from the thawing depth (x_t) estimated at the end of the time step.

2.4.4. Workflow of the Numerical Model

A few threshold values are pre-set in the model. First, we adopt a threshold value of 20% for ice concentration below which the effects of sea ice on waves are neglected and above which waves are assumed totally attenuated before reaching the coast. This choice of threshold value provided a good fit with the field measurement, and is also similar to the threshold values adopted by Rolph et al. [35] and Overeem et al. [14]. Further, we adopt a threshold value of 5 cm to the time-averaged water depth in the cell; below this threshold, the cell is considered dry. We should recall that the time-averaged water depth (in our model over a period of three hours) will attain a small positive value if the cell is submerged only for a small portion of the timestep. If this positive value is very small, we expect that the dominant heat exchange mechanism will be convective heat transfer from the warmer air and thus the cell is to be considered fully dry. The choice of the threshold value is optimised to assure model stability (i.e., we seek the smallest possible value without compromising the stability of the model). A value of 5 cm is considered appropriate. Finally, we adopt a threshold value of 10 cm to the time-averaged water depth at the base of the bluff (h_{id}); below this threshold, the niche module will not be activated. The choice of this value is also optimised to assure model stability similar to the above.

As discussed earlier, the morphological changes and wave transformations are simulated using XBeach. The workflow of the submodules is shown in Figure 8. At the inception of the simulation, global parameters such as the volumetric latent heat of permafrost thawing (L_t), the tensile strength of bluffs (τ), geometric parameters such as β and m_{cr} for air and water, etc., are loaded. These parameters are time-independent, i.e., remain the same for all timesteps. The input parameters, such as air temperature (T_a), water temperature (T_w), ice concentration (i_{con}), wind speed (U_w), bluff temperature (T_s), and tide (h_t) are dependent on time. The model requires the time series of these input parameters at the same time interval as the global timestep. We set the global timestep as 3 h to be consistent with the three-hour sea-state and wave spectrum.

At the beginning of the i -th timestep, we must check whether the current timestep is within the simulation duration. If the condition is satisfied, we load the input parameters from the respective time series for the i -th timestep. The numerical model checks the ice concentration (i_{con}) for the current time step. From here, it is possible to proceed following two different routes. The offshore wave generation and storm surge is calculated only if the ice concentration is less than 20%. If the ice concentration is more than 20%, then the numerical model does not run SWAN, storm surge model and XBeach. We skip to the slumping submodule. An ice concentration of more than 20% indicates no wave activity. However, thawing and slumping might still occur even without hydrodynamic forcing. The numerical model activates the slumping submodule to accommodate this condition. The slumped sediments are moved to the bluff base. Since no hydrodynamic forcing is present in this route, the deposits at the base will not be transferred, and the model allows the accumulation of slumped sediments over the time steps. The accumulated sediments may be transported later when XBeach is activated.

Another route in the workflow is triggered when the ice concentration is less than 20%. If this condition is satisfied, then SWAN and storm surge submodule are turned on. The storm surge water level (η) and wave spectrum are calculated at boundary BC2. The water level is updated at BC2 for the tide and storm surge.

The XBeach simulates sediment transport, currents, water level setup, and morphological changes. The niche submodule becomes activated when the water level at the bluff (h_{id}) reaches more than 10 cm. We also calculate the time-averaged water depth at every grid point to determine whether the coastal profile is wet or dry at the i -th time step. The dry

and wet grid points of the coastal profile are treated differently with respect to convective heat transfer and slumping (Equation (3)).

The model enters the thermodenudation module if the h_{id} is less than 10 cm (which means the sea is calm, it is a 'no storm' condition), the slumping submodule is turned on. If h_{id} is greater than 10 cm the model enters to thermoabrasion module and the niche submodule is activated. It calculates the growth of the niche (x_m). The niche geometry is fed into the bluff stability submodule to check whether a collapse is triggered. The model returns on the thawing depth submodule when no bluff failure is recorded. When the model registers a bluff failure, it estimates the collapsed bluff's size and volume, and the collapsed bluff degradation module is activated. After that, we calculate the thawing depth at each grid point for the $i + 1$ th time step. The last step of the model run at the i -th time step is registering the changes and updating the coastal profile to simulate the $i + 1$ th iteration.

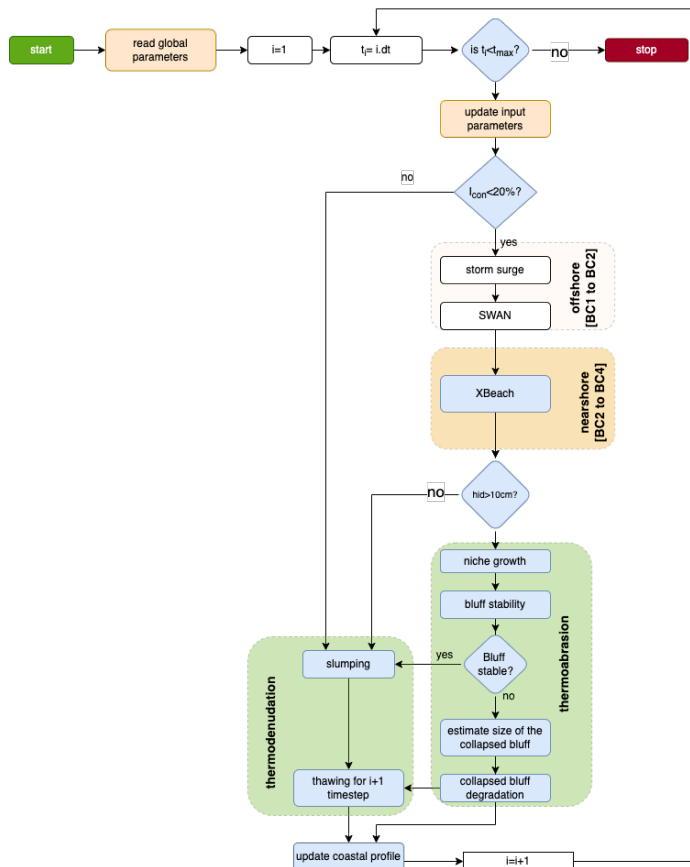


Figure 8. Numerical implementation workflow of the submodules.

The model described in this section is generic and thus applicable to most unglaciated Arctic coasts for all seasons. Both thermodenudation and thermoabrasion can be simulated simultaneously. In the upcoming sections, we demonstrate in detail the application of the numerical model. Available field observations from one of the Arctic coasts in the Kara Sea were used to first calibrate the model, and the subsequent validation was performed using another set of field observations from different years of the same coasts.

3. Field Observations

Field investigations on one of the Arctic coasts, Baydaratskya Bay in the Kara Sea, have been conducted since the summer of 2012. The study area is in the north-east region of Russia (68.853096° N; 66.891730° E). The coast is situated in the gulf between the Ural coast and the Yamal Peninsula (see Figure 9a). The region is not densely populated, there is limited infrastructure and few indigenous settlements are present. The harsh climate and lack of communication facilities hinder continuous access to the study area. Lomonosov Moscow State University (MSU), under the project Centre for Research-based Innovation (CRI): Sustainable Arctic Marine and Coastal Technology (SAMCoT), investigate the study area during summer (between June and September) when it is accessible by road. The importance of studying the area increased after the Nord Stream gas pipeline was constructed in 2011 [43]. The results obtained from the field observations, measurements, and in situ experiments form the basis of this study.

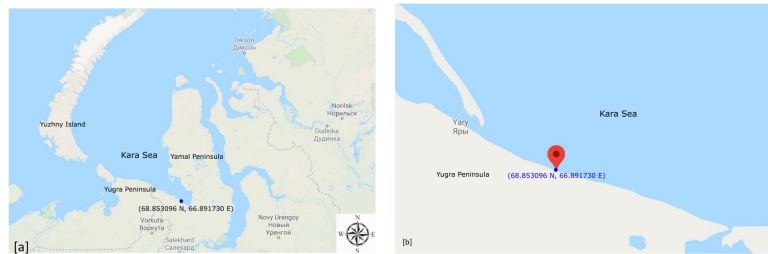


Figure 9. [a] The study area is situated in the Kara Sea between the shallow gulf of two peninsulas, Yugra and Yamal. Image source: Google Maps. [b] The Arctic beach is straight and consists of continuous permafrost; the shore-normal line creates a 73° line to the north. Image source: Google Maps.

3.1. Morphological Description

The study area can be divided into two primary observation sites, S#1 and S#2 (see Figure 10). S#1 consists of low-lying bluffs ranging between 3–5 m, whereas S#2 comprises 12–15 m of high terraces. S#1 is approximately 1.2 km long. The bluff surface is smoothly sloped. A leida (low-lying land at the coast which is flooded during summer by storm surges) with a shoreline spanning 1.4 km lies between the two sites of S#1 and S#2. The leida zone has an elevation above the tide level. Only surges created by storms in the summer can flood the leida. The surface run-off created many gullies on the surface of the area in S#1. Regarding sediment, both sites consist of silty clay, silt and silty sand. The permafrost in the study area is continuous; the annual mean temperature at a depth of 3 m is -4° Celsius [3]. The active organic layer measures approximately 0.5–0.8 m at the surface.

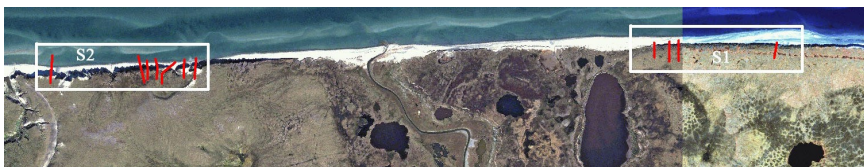


Figure 10. The study area consists of two sites, S#1 and S#2, with distinct bluff height differences. S#1 consists of low bluff heights. Coastal profiles are shown with red lines. Image source: Internal reports, SAMCoT.

3.2. Data and Methods

3.2.1. Coastal Profiles

The coastal profiles of the study area are surveyed using the Differential Global Positioning System (DGPS). Geo-referencing is completed using handheld DGPS receivers and employing some stable objects to identify the profile in the field. After that, the observations are linked to the Russian State Geodetic Coordinate System (GSK-2011). Coastal features such as bluffs and shorelines are recorded. In 2018, surveying via light detection and ranging (LiDAR) began. Figure 11 shows one profile from each site.

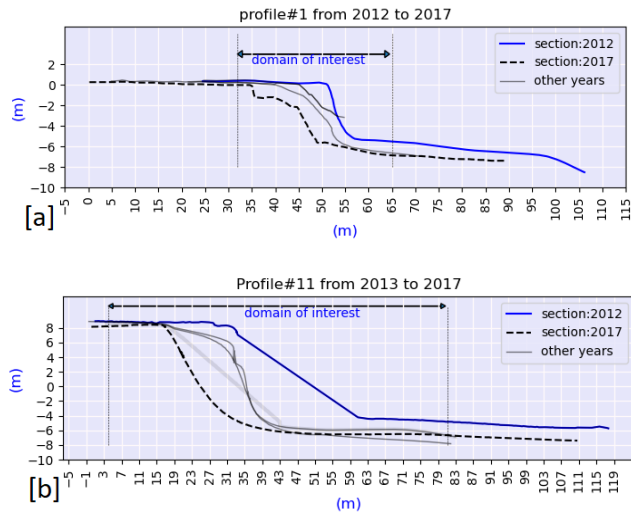


Figure 11. Measurements of two coastal profiles in S#1 and S#2 are shown. **[a]** Measurements of profile P#1 in the zone S#1. **[b]** Measurement of profile P#11 in zone S#2. The bluff height in this profile is approximately 14 m.

Profile#1 in S#1 has a bluff height of 5–6 m. The profiles were covered with snow during measurements taken in 2013, 2014 and 2015. In 2017, we distinctly noticed the collapse of the bluffs near the cliff. Profile#11 from S#2 has a similar cliff retreat magnitude. Unlike Profile#1, the slope of Profile#11 remains constant over the years.

3.2.2. Nearshore Marine Observations

The seabed slope in the study area is 0.004 to 0.01 in the nearshore [44,45]. The length of the open seawater season has been increasing in recent years. From 1979 to 2006, the open sea days increased by 34 days [46]. The salinity of the seawater ranges from 20–25 ppt [47]. The tidal range near the shore is 70 cm, and the tidal currents do not exceed 30 cm/s [48].

3.2.3. Permafrost and Soil Temperature

As part of the investigations, boreholes are constructed at the study sites. Thermistors are used to measure the temperature at 12-h intervals. The boreholes are approximately 3.5 to 9 m deep. From the measurements, we observed that at the bluff's base, the temperature does not fluctuate and remains stable between -5° to 0° Celsius.

3.3. Permafrost and Soil Properties

The dry density (ρ_d) of the sediments from the bluff is measured to be 2630 kg/m³. The particle distribution of the study area is shown in Table A1. The ice content of the bluff ranges between 15–25% [49]. During the summer, the water content of the thawed

permafrost was measured to be 29% [3]. About 60% of the sediment on the beach is within the range of 0.25–0.50 mm [3].

3.4. Erosion Pattern in the Study Area

We observed that both thermoabrasion and thermodenudation are active in the study area. During the summer, the thawing is continuous, and slumped materials accumulate on the beach. Figure 12 depicts the wave-cut niche at the base of the bluff at profile#11. The niche has not reached a critical length where the overhanging bluff is destabilised. The vertical position of the niche is higher than that at high tide. It was formed by a storm surge before the observation was made. During observation, no loose sediment was noticed at the base or inside the niche opening. The return currents must have carried away the sediments when the storm flooded the beach.



Figure 12. [a] Status of Profile#11 during the 2015 measurement. The coastal profile#11 is shown as a black line. A wave-cut niche is visible at the base of the bluffs. Image source: SAMCoT Report, 2015. [b] Permafrost inside the bluff was excavated during the field investigation in 2015. Image source: Gorshkov, SAMCoT Report 2015, [c,d] six-hour time-lapse of thermodenudation in S#1. Niche is visible at the base of the bluffs, but the bluffs are stable. Accumulation of slumped sediments at the base. Image source: Vladislav Isaev. SAMCoT Report, 2015.

The permafrost layer inside the bluffs during summer is shown in Figure 12b. The thawed layer above the permafrost is approximately 0.5 to 1 m at the bluff surface. It is clear from the figure that the thawed layer has a considerable thickness at the bluff slope. We can infer that the intensity of the slumping (mass flux) is the limiting process for thermodenudation. In other words, the thawing rate (dx_t/dt) can be higher than the reduction rate of the thawed layer (dz/dt) due to slumping.

The following summarises the observations in general:

- Thermoabrasion at the bluff face may be active, even when sea ice is present, and land-fast ice remains at the base of the bluffs. Unlike thermoabrasion, the open water season is not a prerequisite for thermodenudation.
- Thawed sediments from the bluffs fall under gravity and expose the permafrost underneath. The slumped materials are loose and accumulate on the beach.

- Wave-cut niches are developed at the base of the bluffs, while the bluffs may still be stable. Several storms may elongate the niche depth to a critical depth. Unless the niche depth reaches the critical length, the bluff remains stable.
- Thawed sediments accumulated at the base of the bluffs remain there until an extreme event creates a higher water level and return current.

4. Calibration of the Model

Some of the model input parameters, such as critical slope (m_{cr}), convective heat transfer coefficient ($h_{c_w/a}$), water level (wl), and tensile strength of permafrost (c) are usually site-specific. In this section, we attempt to calibrate these parameters against field measurements from zone S#1 and S#2 of the study area. One profile from each zone (P#1 in S#1 and P#8 in S#2) are used. These two profiles are considered mutually exclusive because the profiles are different in geometry (bluff height and bluff slope) and geological settings. We treat each profile as a separate case and expect different calibrated parameters. However, the mean sea level is kept the same for both cases.

4.1. Methodology of Calibration

The convective heat transfer coefficient of the permafrost thaw module is calibrated against measurements of the thawing depth (x_t). The thawing depth at the bluff surface is estimated from the temperature measurements at S#1. A thermistor string is installed in the borehole drilled on the bluff surface, 14.07 m from the crest of profile#3 (see Appendix E). Temperature measurements are taken at 12-h intervals along 20 nodes until reaching a depth of 2.43 m.

We do not have enough measurements to estimate uncertainties in the model input parameters, e.g., to fit a probability density function for each parameter. Hence, we used an upper- and lower-limit value for each parameter. These limits were deduced based on a theoretical evaluation or from field observations. Once the limits were identified, a trial-and-error procedure was used to calibrate some of the parameters. It should be mentioned that the available measurements were collected during testing campaigns conducted near the end of the summers of 2015 and 2016 (in mid-September, three to four weeks before winter started). The erosion measurements do not distinguish thermodenudation from thermoabrasion erosion. Therefore, we could only execute the calibration herein by running a one-year simulation (from 15.09.2015 to 14.09.2016) with different combinations of input parameters and selecting the combination that yields the minimum difference between the simulated and measured total erosion volume.

The morphological changes in the coastal profile from the shoreline to the bluffs are considered for calibration. The calibration process intends to simulate the morphological changes at the bluffs and the beaches as close as possible to the measurements. The indicators of erosion measurements, such as (a) crest retreat, (b) erosion volume, and (c) slope of the bluff face, are the targets. Out of the three erosion indicators, the primary aim is to simulate erosion by volume, i.e., the volumetric changes between the two measurements of consecutive years with minimum deviation from measurements. We measure erosion as volume changes spanning from the shoreline up to 15 m from the cliff towards the land. The erosion measurement is the volume per metre along the shore parallel line: (m^3/m —width). The following equation is used to determine the erosion volume (Figure 13):

$$E = \sum_{i=n}^N \frac{1}{2} \Delta x [(a_i + a_{i+1}) - (b_i + b_{i+1})] \quad (9)$$

where E is the erosion volume, n is the grid point at the shoreline, N is the grid point 15 m from the cliff point, Δx is the horizontal distance between two grid points, a is the measurement of the previous year and b is the measurement of the current year. A positive E value represents erosion, whereas negative values indicate accretion. We used 'net erosion' to describe the arithmetic sum of erosion and accretion.

We use root mean squared error (RMSE) to measure the performance of the calibration. The equation to calculate the RMSE values is as follows:

$$RMSE = \sqrt{\frac{\sum_{i=1}^N (o_i - \hat{s}_i)^2}{N}} \tag{10}$$

where RMSE is the root mean squared error, i is the variable, N is the number of grid points of simulation and observation, o is the observed value at the grid point and \hat{s} is the simulated value at the grid point.

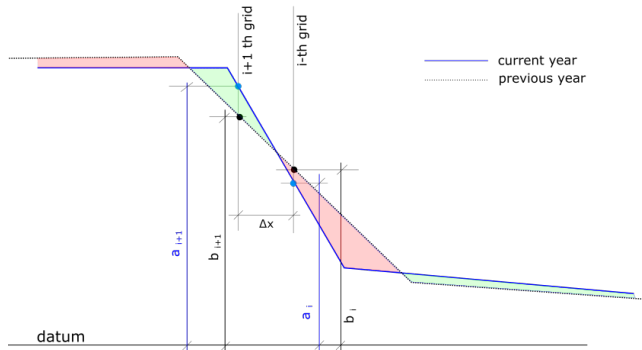


Figure 13. A schematic of erosion volume calculation where a and b are the previous and current measurements from n to N grid points. The datum can be any arbitrary level since we are measuring differences. Positive erosion volume (E) indicates erosion.

4.2. Calibration of the Convective Heat Transfer Coefficient for the Bluff Surface

A continuous time series of thawing depth for the summer of 2017 is established by interpolation of the temperature measurements from borehole#4 on profile#3 (shown in Figure A5 in Appendix E). The thawing depth (x_t) during the summer of 2017 is simulated by applying the permafrost thaw module and compared with the measurement (Figure 14a). Different h_{c_a} values are used with several iterations to seek the optimum value of h_{c_a} that ensures the lowest RMSE when compared with the thawing depth measurements (Figure 14b).

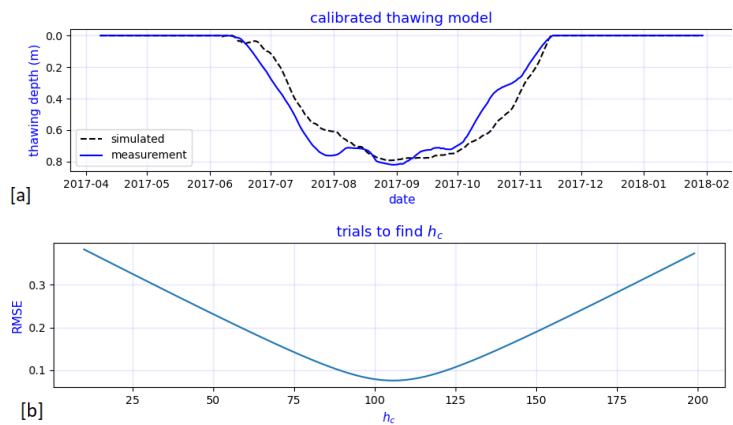


Figure 14. The thawing depth measurement and simulation by the thawing module are shown in sub-figure [a]. The convective heat transfer coefficient (h_c) is iterated to minimize the RMSE error (sub-figure [b]). The lowest RMSE error is 0.1m for h_c value of 106 for the bluff surface.

4.3. Calibration of Remaining Parameters

We choose two cases as described in Table 2 for the calibration. The case studies are termed case#1 and case#2. Both cases are from the same period. The coastal profiles of case#1 and case#2 are shown in Figure 15 and Figure 16, respectively.

Table 2. A summary of the cases for calibration.

Cases	Zone	Profile	Time		Crest Retreat (m)	Erosion (m ³ /m–width)	Accretion (m ³ /m–width)	Net Erosion (m ³ /m–width)
			From	To				
case#1	S#1	P#1	15-09-2015	14-09-2016	4.1	10.31	3.28	7.04
case#2	S#2	P#8	15-09-2015	15-09-2016	2.9	12.51	0.00	12.51

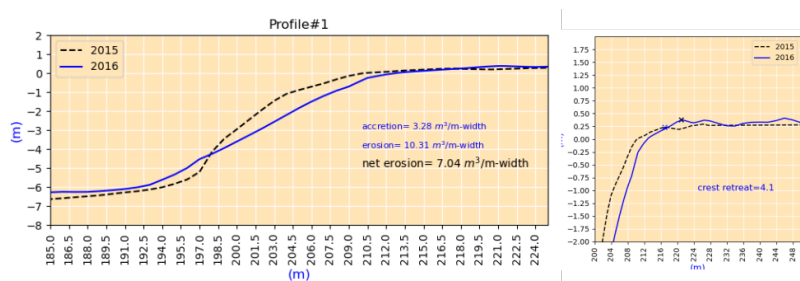


Figure 15. The coastal profiles of case #1, from 2015 to 2016.

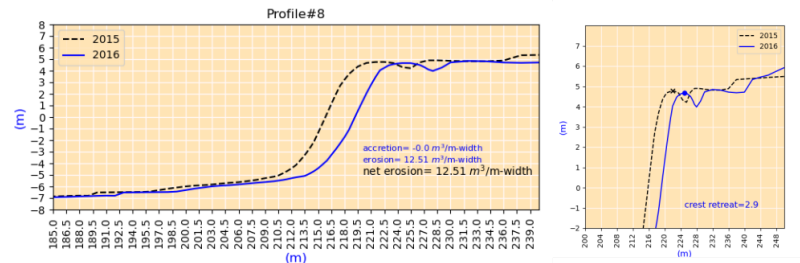


Figure 16. The coastal profiles of case #2, from 2015 to 2016.

The cases started in September 2015 and ended in September 2016. We make the following observations about the cases:

1. The bluff height for case#1 is 6 m, and for case#2 is 13 m. The bluff slope of case#1 is approximately 0.4, which is lower than the bluff slope of case#2 (0.9).
2. The cases demonstrate different erosion patterns. For case#1, we note that the profile has undergone both erosion and accretion; the value of erosion is almost three times the accretion value (Figure 15). The accretion value indicates that the sediments accumulated in the lower part of the bluffs. No accretion is measured for cases#2 (Figure 16). For case#2, all the sediment from the erosion must have been washed away offshore.
3. The crest retreat for case#1 is 4.1, which is larger than that of case#2, even though the erosion volume of case#1 is lower. Because of the higher bluff heights (13 m vs. 6 m) for a similar crest retreat, case#2 had higher erosion volume.
4. The changes in the bluff slope are negligible for case#2 but significant for case#1. For case#1, the bluff base did not retreat; instead, the crest retreated, and the bluff slope was lowered as a result.

In order to run the one-year simulation, environmental parameters to force the model are required. The air temperature, water temperature, significant wave heights (H_{m0} calculated at BC2 by SWAN), and wind speeds from September 2015 to September 2016 are shown in Figure 17. The air and sea-surface temperatures show almost no phase lag. The wind speeds are higher during the winter. Storms are defined as wind speeds greater than 10 m/s within a 36-h window. The air temperature during the summer of 2016 reached 28 °C, which presents a significant anomaly. The source of these input parameters is the NOAA reanalysis model [40].

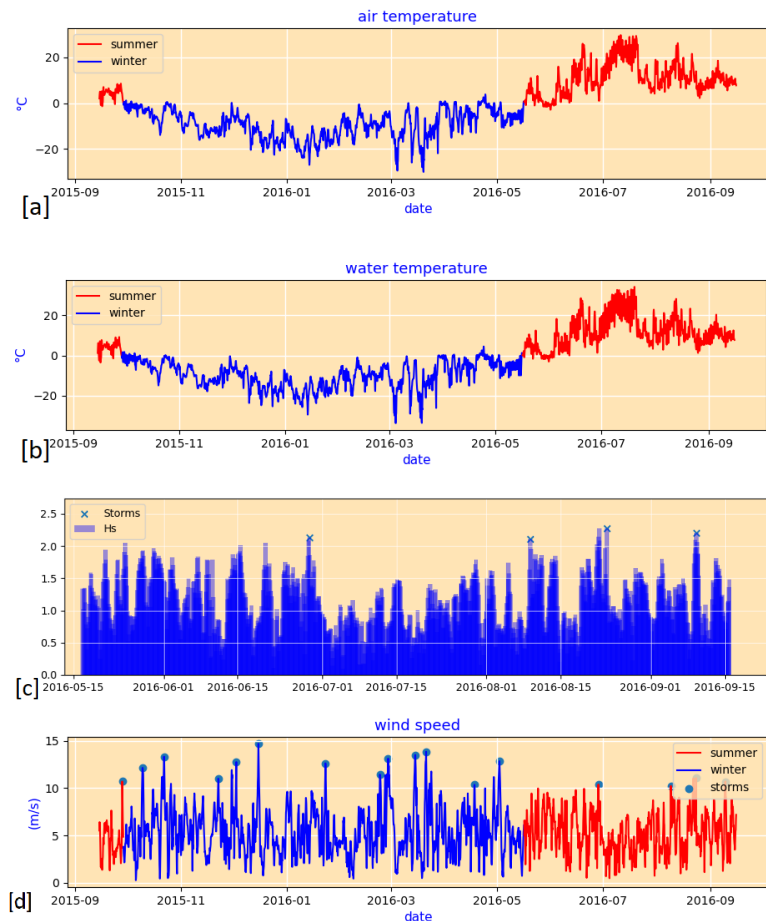


Figure 17. The environmental forcing during the calibration cases is shown. [a] The air temperature of the study area is shown; summer with a red line and winter with a blue line. Winter started on 28 September and ended on 16 May the following year. During the summer of 2016, temperature reached 28 °C. The year 2016 was the hottest in recent decades. [b] Sea-surface temperature is shown, summertime with a red line and winter with a blue line. The phase lag between air and sea-surface temperature is minimal. [c] The wave conditions at the BC2 boundary during summer, the input for the XBeach, are shown. The storms are marked with 'x'. [d] Wind speed and storms are shown. Wind speed is higher during the winter.

4.3.1. Upper and Lower Limit of the Mean Sea Level

The water level (wl) at boundary BC2 (see Figure 1) is updated at every timestep. We estimate wl at the BC2 boundary by superimposing water level changes due to tide (h_t) and storm surge (η) on the mean sea level (h_m). At the BC2 boundary, the water level (wl) is treated as the boundary condition for the XBeach, expressed by the following equation:

$$wl(t) = h_t(t) + \eta(t) + h_m \quad (11)$$

where h_m is the mean sea level, which is constant during the simulation (not a function of time), h_t denotes tidal water-level changes at three-hour intervals (interpolated from the measurement), and η is the storm surge level estimated at three-hour intervals by the storm surge submodule. For calibration, we employ the field measurements of sea level using the Russian State Geodetic Coordinate System (GSK-2011), which is also used as a datum for the numerical model. The values of h_t and η are not subject to calibration. The upper and lower limits of wl are the constraints imposed from field observations: (1) the water level does not touch the base of the bluffs during high tide on a calm day (upper limit of wl), and (2) the length of the beach from the base of bluffs to the swash zone varies from 40 to 70 m (lower limit of wl).

4.3.2. Upper and Lower Limit of the Convective Heat Transfer Coefficient

The convective heat transfer coefficient differs between the four sections (see Figure 4). In Section 4.2, we calibrated the h_{c_a} for bluff surface. The remaining three other values are calibrated using trials and errors to match the total erosion volume. As a starting point for the h_{c_w} value for water, we follow the model of Kobayashi et al. [36] as follows:

$$h_{c_w} = \frac{af_w C_w U_w}{1 + F\sqrt{0.5f_w}} \quad (12)$$

where a is the empirical parameter equal to 0.5, f_w is the wave friction factor, C_w is the volumetric heat capacity of seawater, U_w is the fluid velocity and F is the parameter depending on the turbulence and Prandtl number. Kobayashi et al. [36] estimated the value of h_c within the range of 500 to 800 W/m²-k.

For the h_{c_a} of air of bluff slope and dry portion of the beach, the initial value of iteration is determined by using the equation for the forced convection of a turbulent flow over a flat plate:

$$N_u = \frac{h_c \cdot L}{k_f} = 0.037 Re^{0.8} Pr^{1/3} \quad (13)$$

where N_u is the Nusselt number, k_f is the thermal conductivity of the fluid, L is the characteristic length, Re is the Reynolds number, and Pr is the Prandtl number. Using $Pr = 0.71$ for air, we estimate the initial value of h_{c_a} to be approximately 25 W/m²-k.

4.3.3. Upper and Lower Limit of the Critical Slope (m_{cr})

The slumping process inside the numerical model is controlled and triggered using one single parameter, the critical slope (m_{cr}), as mentioned in Equation (8). In this study, we calibrated the value of m_{cr} from the field observations. Alternatively, one can use numerical thermo-mechanical models, coupled with mechanical strength and thermal energy balance module ([50,51] or similar model) to perform slope stability of the bluffs and estimate the value of m_{cr} . The calibration is achieved by running the model with various values of m_{cr} within an acceptable range and then selecting the m_{cr} value that yields the closest estimate of total erosion volume and the profile shape. We estimated initial values for the trials from field measurements of the coastal profiles. The bluff height and bluff slope of 30 measurements are shown in Figure 18. The coastal profiles shown in the figure present observations that were free of snow at the time of measurement. These measurements were taken between 2012 and 2017 on several profiles of S#1 and S#2. The slope of the

profiles varies from 0.1 to 1.1. A distinct difference is visible between the bluff slopes of zones S#1 and S#2. The coastal profiles are measured at the end of the summer when the thermodenudation is almost complete. We infer that the slopes of the bluff faces are near-stable slopes, and thus, the critical slope should be more than these measured slopes. We also note that the profiles at S#2 have a greater bluff height and steeper slope. We used a lower limit of Figure 18 for 0.2 and 0.4 for the S#1 and S#2, respectively. The upper limit was set at 0.45 and 0.8 for S#1 and S#2. The value of Figure 18 directly affects the value of erosion volume and shape of the bluff surface.

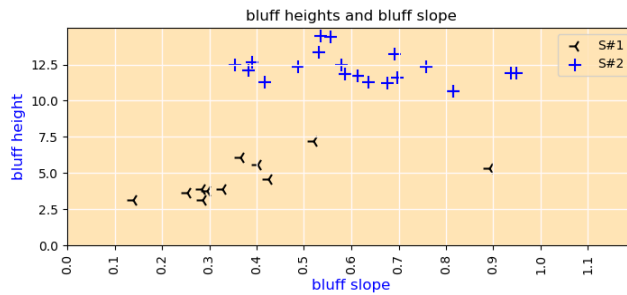


Figure 18. Relation between the bluff height and bluff slope in the study area.

4.4. Calibration Result

Application of the environmental forcing iterations is performed with the calibrated parameters to match the simulation outcome to the three targets: net erosion volume, crest retreat and bluff slope as closely as possible. A summary of the calibrated values of the parameters is shown in Table 3. In the upcoming sections, we discuss the results of the calibration.

Table 3. Summary of the calibrated parameters.

Parameter	Zone	Symbol	Calibrated Value	Unit	Remarks
convective heat transfer coefficient	S#1 & S#2	h_{c_a}	106	W/m^2-k	for bluff-surface
	S#1 & S#2	h_{c_a}	98	W/m^2-k	for bluff-slope
	S#1 & S#2	h_{c_a}	90	W/m^2-k	for beaches
convective heat transfer coefficient	S#1 & S#2	h_{c_w}	700	W/m^2-k	for sea beds
tensile strength	S#1 & S#2	τ	1×10^7	N/m	
critical slope (dry)	S#1	m_{cr}	0.34	-	
	S#2	m_{cr}	0.52	-	
critical slope (wet)	S#1	m_{cr}	0.2	-	
	S#2	m_{cr}	0.2	-	
mean sea level	S#1 & S#2	h_m	-7.6	m	

A summary of the calibration results with error measurements is shown in Table 4. The numerical model overestimates erosion volumes for both cases.

Table 4. Summary of the calibration of case#1 and case#2. (td = thermodenudation and ta = thermoabrasion).

Case	Criteria	Measured	Simulation			Error (%)	
			Volume	(%)	net		
case#1	erosion volume (m ³ /m–width)	7.04	td	2.01	24.22%	8.3	17.9%
			ta	6.29	75.78%		
	crest retreat (m)	4.1	-	-	-	3.9	4.8%
case#2	erosion volume (m ³ /m–width)	12.51	td	6.04	40.82%	14.8	18.3%
			ta	8.75	59.18%		
	crest retreat (m)	2.9	-	-	-	4	37.9%

4.4.1. Prediction of Erosion

The simulated erosion volume for case#1 and case#2 differ from the measurements by 17.9% and 18.3%, respectively (Figures 19 and 20). Thermoabrasion (ta) is the dominating mechanism, contributing 75.78% of cumulative erosion volume, whereas, for case#2, thermoabrasion (ta) is 59.18%. Four collapses are simulated for case#1, but for case#2, two collapses are triggered within the model. The h_{id} values for the case#2 are also less frequent (h_{id} values over 20 cm are shown in the secondary axis). The sediment influx by thermodenudation is nearly three times greater for case#2 compared with case#1. Since the water level (wl) is the same for both cases, we can deduce that the higher sediment influx by thermodenudation changes the nearshore morphology and influences the rate of thermoabrasion.

The two collapses in case#2 are in sync with storms. Case#1 has two additional collapses at the beginning of summer. The largest storm surge occurred during May, which did not result in any collapse. The thermal driving force of niche growth: the temperature of the water was not warm enough to rapidly grow the niche. We also notice the h_{id} values are spiked and not continuous, which is in line with our assumption that only during storm surges can water reach the base of the bluffs.

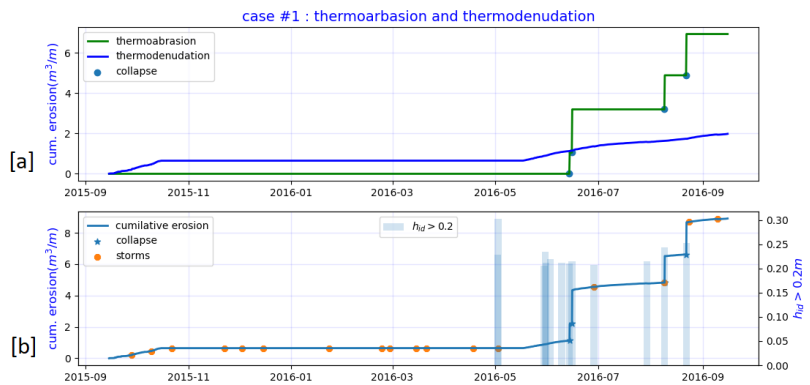


Figure 19. Results of the calibration of Case#1. sub-figure [a]:Cumulative thermoabrasion and thermodenudation are shown separately. The sudden jumps in the erosion volumes indicate a bluff collapse by thermoabrasion. sub-figure [b]:The erosion volume from the measurement was 7.04 m³/m–width, whereas the model simulated erosion of 8.3 m³/m–width. Thermodenudation contributes 2.01 out of 8.3 m³/m–width. Four collapses are simulated, and thermoabrasion contributes 75.7% of the erosion.

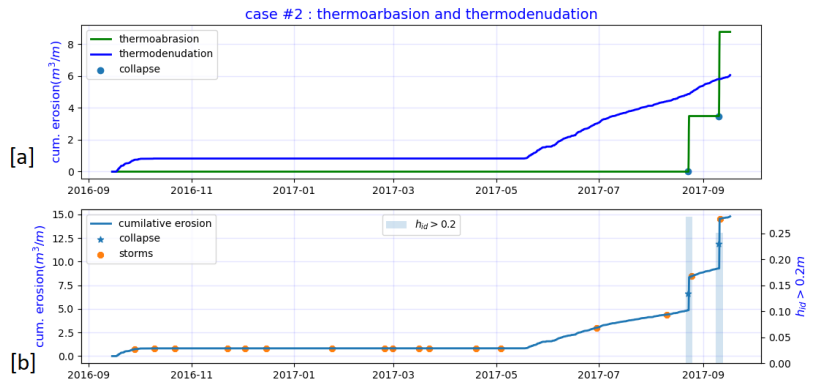


Figure 20. Results of the calibration of Case#2. sub-figure [a]:Cumulative thermoabrasion and thermodenudation are shown separately. sub-figure [b]:The erosion volume from the measurement was $12.51 \text{ m}^3/\text{m}$ –width, whereas the model simulated erosion volume was $14.8 \text{ m}^3/\text{m}$ –width. Thermodenudation contributes 6.04 out of $14.8 \text{ m}^3/\text{m}$ –width, about three-times greater than case#1. The bluff slope is steeper (0.9 vs. 0.4) and the bluff height is higher (13 m vs. 6 m). Two collapses are simulated and thermoabrasion contributes 59.18% of the erosion.

4.4.2. Prediction of Crest Retreat

The secondary aim of the simulation is to predict the crest retreat of the bluffs. The crest retreat of the Arctic coast is retrogressive, i.e., always retreating as there is no restoration mechanism such as the dune systems of the sandy beaches in warmer climates. The crest of the bluff is always moving towards the land. The annual crest retreat rate is important for predicting vulnerability and associated risks. For case #1, the crest retreat rates were 4.1 m . The model predicts crest retreats of 3.9 m (Figure 21a). For case#2, the simulation predicted a crest retreat of 4 m (Figure 21b).

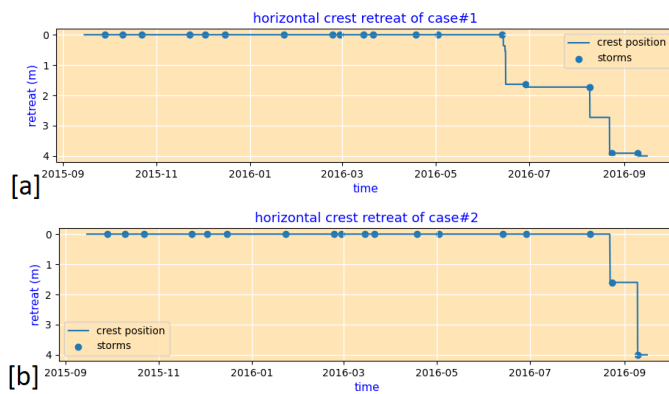


Figure 21. The crest retreat as a time series is shown. sub-figure [a]: The crest retreats coincide with the bluff collapses. The sudden drops are due to thermoabrasion, which contributed the most to the retreat. sub-figure [b]: Similar pattern is visible for Case#2.

4.4.3. Prediction of the Shape of Coastal Profile

Secondary aim of the calibration is to forecast the shape of the profile at the bluff face and the elevation of the beach. The elevation of the beach is crucial since it affects the inundation depth (h_{id}), which in turn controls the thermoabrasion. The performance of the

model for case#1 is shown in Figure 22. Before estimating the RMSE value, we ‘normalise’ the profile around the middle of the bluff slope. Hence, the RMSE values are only related to the shape of the profile, and not associated with the position of the bluff.

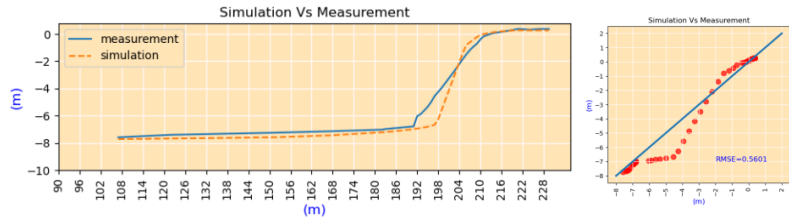


Figure 22. Case#1: Prediction of the coastal profile shape after normalising the simulation around the middle of the bluff slope. The RMSE of the prediction is 0.56 m.

For case#1, we observe that the simulation predicted a slope slightly steeper than the measurement. The predicted elevation of the beach was close to the measurements, although it overestimated the erosion by sediment transportation. The deviation is highest near the base of the bluff; errors near the beach are negligible. The model overestimates the erosion at the base of the bluffs.

For case#2, shown in Figure 23, the model simulates the slope as much as the prediction. The simulated values deviated near the cliff points and the bluff base. The prediction at the beach was close. The RMSE values are higher for case#2.

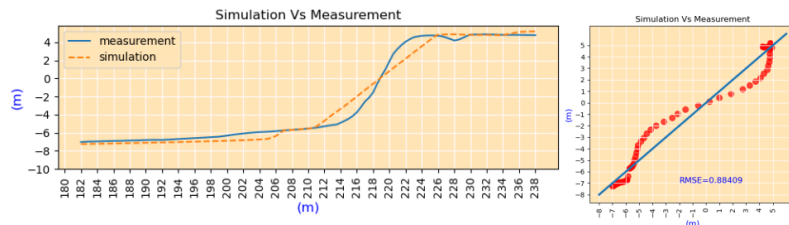


Figure 23. Case#2: Prediction of the coastal profile shape after normalising the simulation around the middle of the bluff slope. The RMSE of the prediction is 0.88 m.

5. Validation

We apply the calibrated model to another three sets of measurements to validate the model. The new cases are summarised in Table 5. Case#3 and case#4 are from profiles#1 and #8 for 2016–2017. Case#5 is from the two measurements of 2012 and 2017 on profile#1. Case#5 is selected to examine the performance of the numerical model for simulating long-term erosion. The measured erosion volume and crest retreats of all the cases are shown in Appendix G.

Table 5. A summary of the three cases for validation.

Cases	Zone	Profile	Time		Crest Retreat (m)	Erosion (m ³ /m–width)	Accretion (m ³ /m–width)	Net Erosion (m ³ /m–width)
			From	To				
case#3	S#1	P#1	15-09-2016	14-09-2017	3.2	28.73	0.00	28.73
case#4	S#2	P#8	15-09-2016	15-09-2017	3.9	11.81	0.00	11.81
case#5	S#1	P#1	13-06-2012	15-09-2017	16	71.05	0.00	71.05

5.1. Methodology of the Validation

The calibrated parameters in Table 3 are used without any changes. The time series of the input parameters: air and water temperature, wind speed, and tides are updated. The initial thawing depths for case#3 and case#4 are used from the previous simulations (the thawing depth of the last timestep for case#1 and case#2). For case#5, the initial thawing depth was taken as zero because the case starts in June, not September. From the thawing-depth patterns of cases #1 and #2, we estimate that the thawing depth in June is zero.

5.2. Validation Results

A summary of the simulation results is shown in Table 6. The results show a good agreement with the measurements.

Table 6. Summary of the validation cases.

Case	Criteria	Measured	Simulation			Error (%)	
			Volume	(%)	net		
case#3	erosion volume (m ³ /m–width)	28.73	td	10.18	39.46%	25.8	10.2%
			ta	15.62	60.54%		
	crest retreat (m)	3.2	-	-	-	3.9	4.8%
case#4	erosion volume (m ³ /m–width)	11.81	td	3.75	24.83%	15.1	27.8%
			ta	11.36	75.17%		
	crest retreat (m)	3.9	-	-	-	-	23.1%
case#5	erosion volume (m ³ /m–width)	71.05	td	23.6	29.32%	80.5	13.3%
			ta	56.9	70.68%		
	crest retreat (m)	16	-	-	-	14.8	7.5%

5.2.1. Validation of Permafrost Thawing Module

The permafrost thawing module is calibrated by seeking minimum RMSE error from the measurements of summer 2017. The module is validated using the thawing depth measurements of summer 2014 from the same borehole. The thawing depth simulation mimics the field measurements (see Figure 24). The simulation could not properly capture the duration of thawing; however, the depth is captured quite accurately. The RMSE error is 0.07 m.

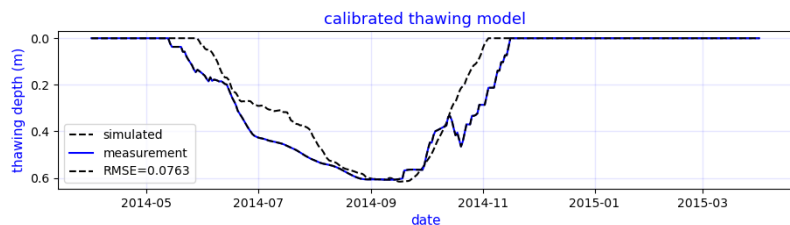


Figure 24. Validation of the thawing module is completed using measurement of the summer of 2014.

5.2.2. Validation of Case#3

A summary of the validation results is shown in Figure 25. The cumulative erosion of the profile reaches 25.8 m³/m–width, which is slightly underestimated by the simulation. The erosion is dominated by thermoabrasion, but the contribution from thermodenudation increased from the previous year, from 24.3% to 33.22% (case#1). The rate of thermodenudation was higher during the summer of 2017. However, the prediction of the beach

elevation deviated from the measurements. The shape of the bluff face was irregular, which the model failed to capture. Similar to the other cases, the deviation is higher near the base.

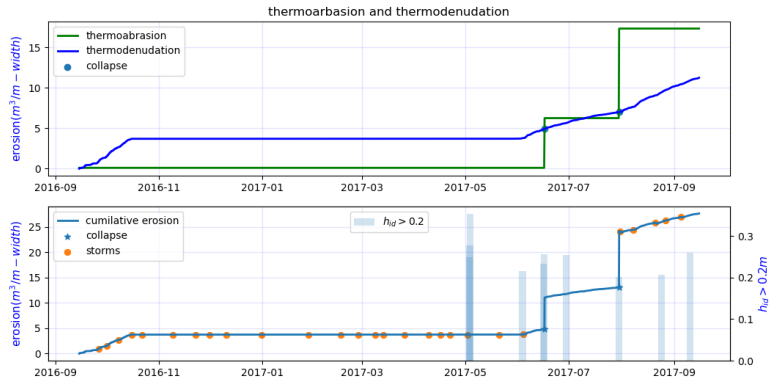


Figure 25. Validation results for case#3. Thermoabrasion is 17.23 of 25.8 m³/m–width; 66.78% of the total erosion. The collapses are fewer in number.

5.2.3. Validation of Case#4

The cumulative erosion volume simulated by the model for case#4 is shown in Figure 26; the erosion is dominated by thermoabrasion (75.17%). The model estimated an erosion volume of 15.1 m³/m–width, which is overestimated from the measurement of 11.81 m³/m–width. Compared with case#2, case#4 demonstrated different behaviour. Thermoabrasion dominated the erosion mechanism with one initial big collapse.

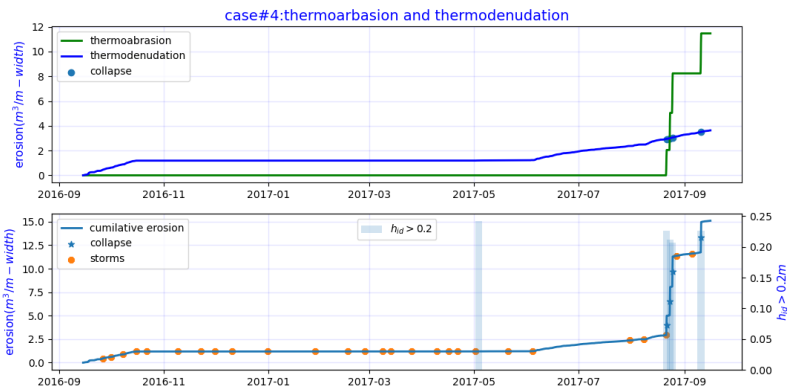


Figure 26. Validation results for case#4.

5.2.4. Case#5: Simulation of Long-Term Erosion

The application of the model for the long-term erosion simulation is demonstrated by case#5. The simulation duration of the case is five years and four months. The simulation results are shown in Figure 27.

The erosion pattern of case#5 is similar to the other cases. The erosion is dominated by thermoabrasion (70.68%). The thermodenudation rate differs each year. The h_{id} values during the simulation are shown in the secondary y-axis of Figure 27b. We observe higher h_{id} values for the earlier years; the highest h_{id} is observed during the summer of 2014. The effect of the higher h_{id} values of 2014 did not translate to many bluff collapses. The bluff

collapse by niche growth requires a positive h_{id} value, but the intensity of the erosion does not depend on the frequency and magnitude of the h_{id} values.

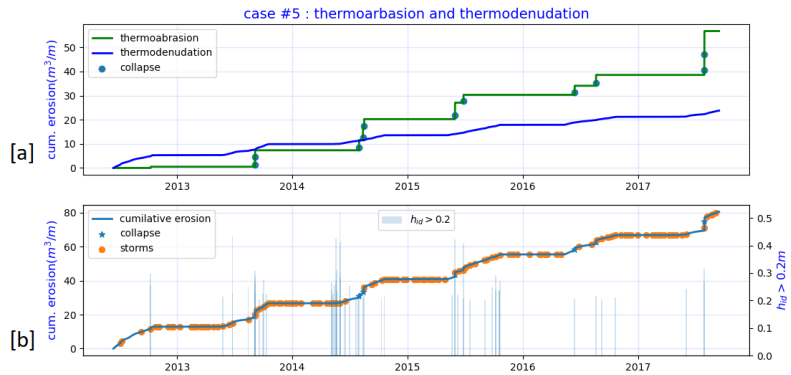


Figure 27. Validation results for case#5.sub-figure [a]: The cumulative thermoabrasion and thermodenudation is shown separately. Thermoabrasion is the dominating mechanism; similar to earlier cases. sub-figure [b]: The combined erosion volume is $80.5 \text{ m}^3 / \text{m}$ —width which is over estimation of measurement.

Deviation of the profile shape is shown in Figure 28. The deviation is higher at cliff points and bluff bases. During the five-year simulation, the beach elevation was simulated to be lower than the measurements; the deviation was nearly 0.3 m, whereas the average deviation at the grid points was 0.86 m (RMSE).

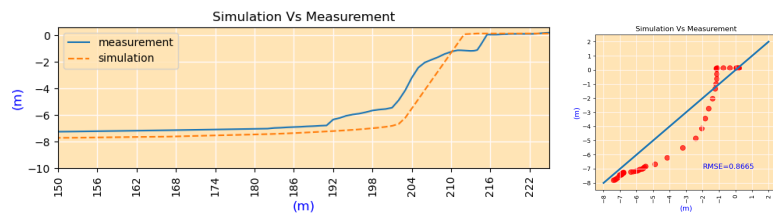


Figure 28. Shape of the profile after normalising. The RMSE value was estimated to be 0.86.

5.2.5. The Effect of Environmental Forcing on Erosion

In Figure 29, the air temperature and simulated cumulative erosion are drawn. The upwards zero crossing of the air temperature and the inception of the erosion in the summer have a small phase lag. The erosion rate correlates with air temperature; higher air temperature leads to increased erosion. At the end of the summer, the erosion stops as soon as the air temperature exhibits downwards zero crossing.

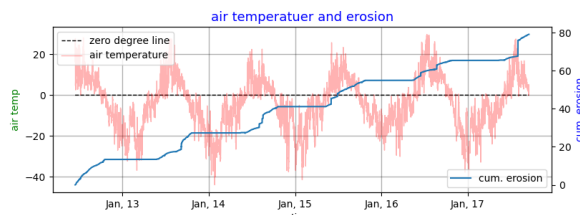


Figure 29. Air temperature and cumulative erosion (simulation).

The thawing index of air is used in many empirical equations concerning the thawing of permafrost and erosion. Figure 30 draws the measured cumulative thawing index of case#5 juxtaposed with the simulated cumulative erosion. The correlation between the two parameters is very strong even though the thawing index is only one of the environmental forcing parameters of erosion. The cause of the erosion can be partly attributed to the thawing index. We cannot establish a direct causation-relation of the thawing index of air with thermoabrasion; warm air has almost no immediate effect on erosion by thermoabrasion. From the simulation result, we notice that even though erosion is dominated by thermoabrasion, a strong correlation exists between the cumulative thawing index and cumulative erosion.

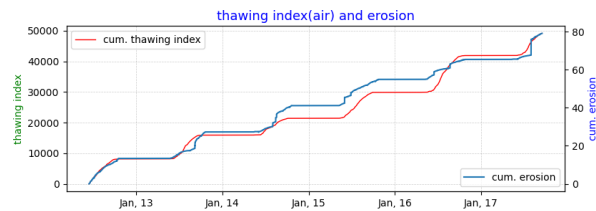


Figure 30. Cumulative thawing index and erosion (simulation).

However, the wind speed and the simulated cumulative erosion of case#5 are not correlated (Figure 31). The wind speeds are higher during the winter when there is no erosion. The bluff collapses (creating a jump on the cumulative erosion) rarely coincide with the storms of the summer. We can infer that the bluff collapse by thermoabrasion is not dominated by storms in the summer; instead, a combination of various environmental forcing results in bluff failure, justifying the inclusion of hydrodynamic and morphological submodules into the numerical model of Arctic coastal erosion.

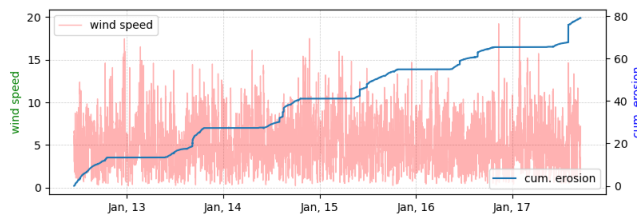


Figure 31. Wind speed and cumulative erosion (simulation).

6. Sensitivity Analysis of the Model

We cannot validate all the modules individually since the measurements are only available once a year. Only the permafrost temperature inside the bluffs is measured continuously throughout the year. The temperature measurements yield a continuous year-round measurement of thawing depth, using which we can calibrate and validate the thawing module (Section 4.2). Thermoabrasion is episodic; pre and post-bluff-collapse measurements are essential to validate. Considering the scarcity of measurements to identify and discern the individual effect of the coastal processes, a sensitivity analysis is undertaken to demonstrate the behaviour of the numerical model and its potential applicability.

6.1. Base Case

Sensitivity analysis is performed on a base case, and some conclusions are inferred. Two approaches are adopted: (a) turning off a process and comparing it with the base case and (b) amplifying or damping one environmental forcing to observe the deviation from

the base case. The base case is shown in Figure 32. The calibrated model is used to simulate the erosion of a hypothetical coastal profile over a period of 31.25 days, from 7 June 2016 to 8 July 2016. Environmental forcings are taken from NOAA reanalysis [40]. The profile has a bluff slope of 0.35, and a height of around 7 m. The base case is developed in such a way that one single mechanism does not dominate; thermoabrasion and thermodenudation are almost equal. The environmental forcing and erosion patterns are shown in Appendix H.

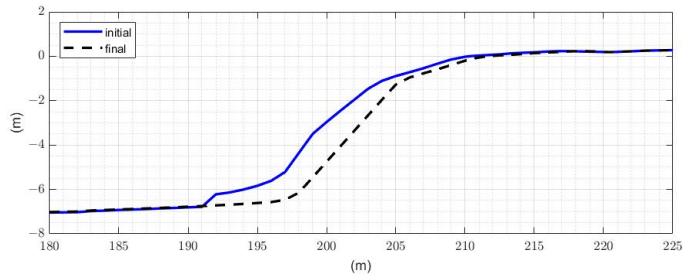


Figure 32. Profile of the base case.

6.2. The Effect of Waves

The wave is the prominent mechanical driver of both erosion mechanisms. When we turn off the wave inside the XBeach, the h_{id} values become very small to non-existent (Figure 33). No sediment transport along the cross-shore is simulated, eventually stopping thermodenudation by stabilizing the slope. The model detects almost no erosion as a result. We can infer the following:

- Thermoabrasion is controlled by both mechanical and thermal driving forces; the absence of one of the driving forces can withhold thermoabrasion.
- Mechanically driven forces do not control thermodenudation, i.e., they are not the limiting factor, but nearshore hydrodynamics can influence the rate of thermodenudation.
- Without the presence of waves, no bluff collapse occurs even when the model simulates positive values of h_{id} ; indicating the importance of the combination of thermal and mechanical drivers.

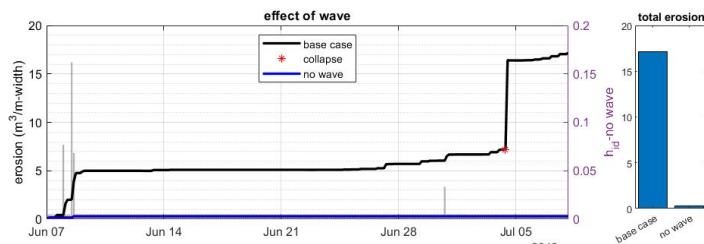


Figure 33. The effect of waves on erosion.

Figure 34 shows the effect of the amplitude of the wave heights (h_{m0}) at BC2 as an environmental forcing. A 20% increase in the significant wave height increases the cumulative erosion by more than 30% (qualitative assessment) as simulated by the model. The bluff collapses are more frequent and occur earlier in the summer when amplitudes are increased. Thermodenudation also increases as stronger waves enable a faster removal of the thawed materials from the bluff base.

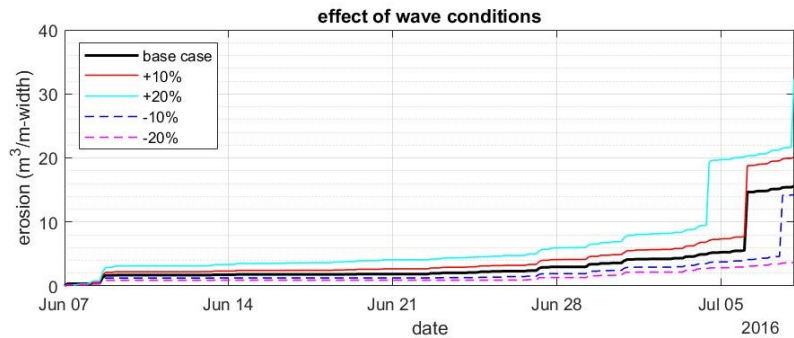


Figure 34. The effect of wave inputs on erosion.

6.3. The Effect of Niche Growth

When we turn off the niche growth module, the model essentially converts to a thermodenudation model ignoring thermoabrasion even when the other modules of thermoabrasion are active. Figure 35 describes the result where erosion is only allowed by removing the sediments from the base via waves and currents, dominating by thermodenudation. We notice an initial high erosion. The frequent h_{id} values indicate that the erosion is due to waves and currents removing the thawed material from the base of the bluffs and beaches.

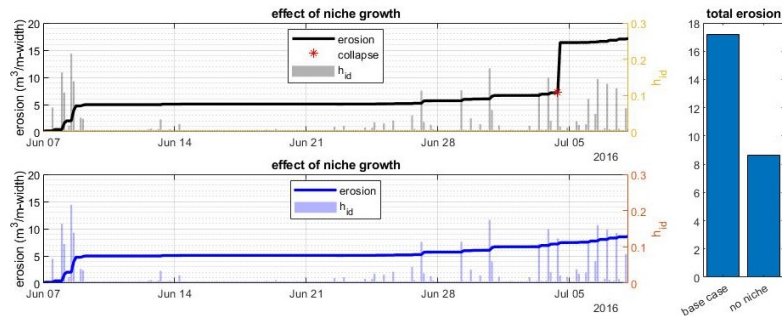


Figure 35. Effect of the niche-growing process on erosion.

6.4. The Effect of Slumping Process

The results of turning off the slumping module are shown in Figure 36. The model allows the removal of sediments from the beach, but the influx from the slumping module is turned off. The result shows that the erosion initially has smaller values than the base case. However, the erosion volume increased significantly later in summer with frequent collapses. A comparison of the h_{id} values reveals that higher and more frequent h_{id} are observed for this case, indicating the importance of the influx of sediments from the thermodenudation as an erosion-resisting mechanism in the model. The sediment influx from the slumping elevates the base and reduces the probability of thermoabrasion. Thus, two erosion mechanisms are intertwined.

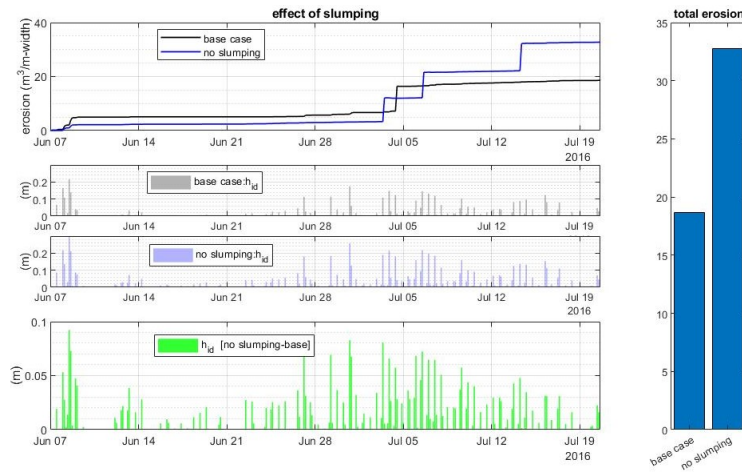


Figure 36. Effect of the slumping process on erosion.

6.5. The Effect of Tide

Water level fluctuation due to tide (h_t) is simulated in XBeach as one of the input parameters. Figure 37 depicts the effect of excluding tide from the model. In our study area, the tidal range is 70 centimetres, so the effect of the tidal fluctuation on the output of the numerical model appears small. The deviation from the base case is not very high. Both the thermodenudation and thermoabrasion are reduced, and the bluff collapses are delayed as h_{id} values become smaller with lower frequency.

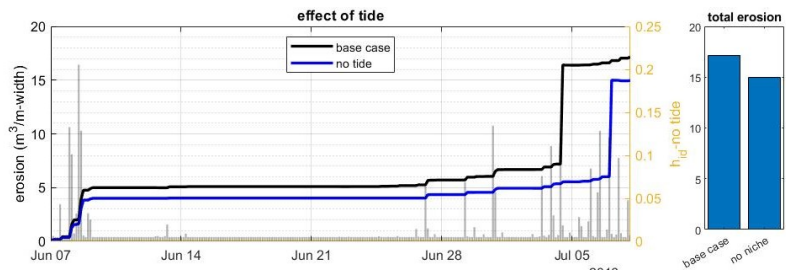


Figure 37. The effect of tide on erosion.

6.6. The Effect of Water Level

The model is highly sensitive to water level (wl , defined using Equation (10)). The incremental water level changes (10 cm) are shown in Figure 38. The frequency of the bluff collapse is related to the wl . The erosion volume shows a linear relation with the input parameter wl . The erosion volume increases about three times causing a 30 cm elevation in water levels.

The effects of water and air temperature are shown in Appendix I. The results show that the air and water temperatures are not the limiting factor for both erosion mechanisms. The air and water temperatures act as an on/off switch inside the model since niche growth and permafrost thawing are impossible without a positive temperature.

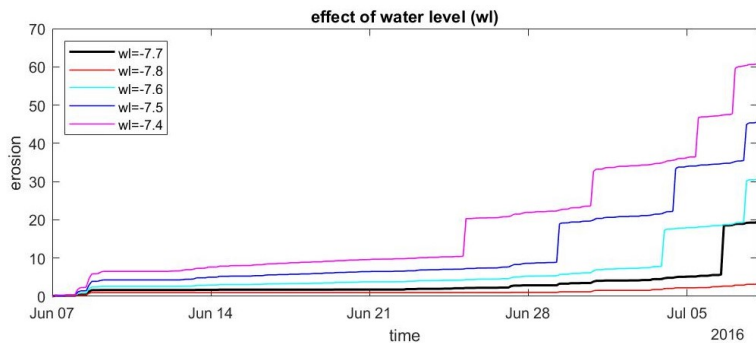


Figure 38. The effect of water level inputs on erosion.

7. Conclusions

This paper describes a comprehensive process-based model that simulates Arctic coastal erosion, including hydrodynamic forcing from the sea. The model is constructed by coupling XBeach with in-house thermal modules. The model includes the physical processes as submodules under the two major erosion mechanisms: thermodenudation and thermoabrasion. A feedback mechanism is established between the submodules so that the model can simulate thermodenudation and thermoabrasion simultaneously.

The numerical implementation of the model is described briefly, and the workflow is explained. We calibrate the model using field measurements from Baydaratskya Bay in the Kara Sea, Russia. The simulation by the calibrated model agrees reasonably with the field measurements. The analysis of the erosion patterns reveals the erosion mechanism is dependent on the nearshore hydrodynamics and morphological changes. Hence, including a proper hydrodynamic and sediment transport model to simulate Arctic coastal erosion significantly improves the fidelity.

The following conclusions can be made from the calibration process of the numerical model:

1. Erosion during the winter is negligible or absent. Barnhart et al. [30] concluded in their model that low erosion occurs at the end of summer and beginning of fall for the coast of Alaskan Beaufort Sea whereas our numerical model for Baydaratskya Bay in Kara sea simulates higher erosion at the middle and end of summer.
2. There is a slight phase lag between the commencement of summer (measured by air temperature) and the beginning of slumping. The air temperature had an upwards zero crossing at the end of May, but thawing began after June in both cases #1 and #2.
3. Smaller sudden spikes in air and water temperature at the beginning of summer do not contribute to thermodenudation. The model also does not show any immediate response to the spikes of temperature anomalies. This behaviour indicates that the limiting factor for thermal energy transfer and thawing of permafrost is the energy requirement for the latent heat of the transformation from ice to water.
4. Thermodenudation is continuous and of lower intensity, whereas thermoabrasion causes spikes in erosion volume. The limiting factors for thermodenudation and thermoabrasion are, respectively, the latent heat requirement and water depth at the base of the bluffs (h_{id}).

The model is validated by another three sets of observations, two short-term (one year) and one long-term (five years). We demonstrate that the model can simulate long-term erosion with the same level of fidelity. We infer the following concluding remarks from the results of the simulations:

1. The results of the numerical model suggest that thermoabrasion is a complex process and does not demonstrate a linear relation with the intensity of storms. In other

words, the strongest storm does not necessarily lead to a collapse. A bluff collapse by a wave-cut niche results from a combination of the nearshore beach profile, storm surge duration, water temperature, and bluff geometry. A similar observation was made by Barnhart et al. [30] for the thermoabrasion numerical model of the Alaskan Beaufort coast.

2. The two consecutive bluff collapses routinely have an interval between them, and the time lapse between the two collapses is four to six weeks. The sediments released from the collapsed bluff alter the elevation near the swash zones, reducing the probability of inundating the beach with warm water and resulting in slow niche growth. The model by Ravens et al. [29] considered a numerical elevation of the beach by about 0.28 m to calibrate the model and achieve optimised calculation. In contrast, the model proposed herein assumes the sediment from the bluffs increases the elevation of the beach and the elevation is controlled by the morphodynamic module (XBeach).
3. The parameter inundation depth, h_{id} , acts as an on-off switch for thermoabrasion; however, the numerical model does not show a clear relationship between the magnitude of h_{id} and erosion. Our model agrees with the previous observation of Ravens et al. [29] that overall crest retreat is controlled by the niche erosion process.
4. The erosion rate of thermodenudation was found to be approximately $0.4 \text{ m}^3/\text{month}$ for low bluff-height profiles in zone S#1. The erosion rate by thermodenudation for the zones with high bluff was estimated to be close to $1 \text{ m}^3/\text{month}$. The erosion rate of thermodenudation does not show a strong relationship with the thawing depth (x_t).

We conclude the following from the sensitivity analysis using a base case:

1. The hydrodynamic forcing, especially wave condition, plays a vital role in the erosion mechanism; hence the inclusion of the nearshore hydrodynamics and morphological changes is important.
2. The limiting factor for the rate of thermodenudation is found to be the critical slope (m_{cr}). In the case of thermoabrasion, the limiting factor was h_{id} .
3. Thermodenudation and thermoabrasion are intertwined; one mechanism can affect the other. For beaches where the two mechanisms are active, this feedback should be taken into consideration.

We demonstrate that coupling the physical processes as submodules to simulate Arctic coastal erosion model erosion can produce realistic coastline erosion rates. It is possible to couple the model with globally available climate reanalysis data. The simulation results are within the same order of magnitude as the field measurements. The model can be further improved by considering the following:

Future Development

1. The accumulation and melting of snow and related water flow are not exclusively modelled. Since there is no open water during the winter and coastal erosion is negligible, we did not model the effect of snow. A snow module will improve the accuracy of the model.
2. The presence of sea ice was considered in a binary mode, where we ignored sea ice when the ice concentration was less than 20%, and it was assumed to not affect the waves. The damping effect of the floating ice on the waves may also improve the model's fidelity.
3. The critical slope (m_{cr}) is taken as depth-averaged for the profiles. One depth-averaged value is estimated for each zone in the study area. A matrix of m_{cr} values at different depths and geometries will increase the model's accuracy.
4. The collapse of the bluff is predetermined. A finite element model at the bluff face may better predict the irregular bluff slope.
5. The model is applicable to the un lithified Arctic coasts since gravel is not included in the XBeach explicitly.

Supplementary Materials: The following supporting information can be downloaded at: <https://www.mdpi.com/article/10.3390/jmse10111602/s1>, File: A stand-alone module of slumping; written in Matlab.

Author Contributions: Conceptualization, M.A.I. and R.L.; methodology, M.A.I. and R.L.; software, M.A.I. and R.L.; validation, M.A.I. and R.L.; formal analysis, M.A.I.; investigation, M.A.I. and R.L.; resources, R.L.; data curation, M.A.I.; writing—original draft preparation, M.A.I. and R.L.; writing—review and editing, R.L.; visualization, M.A.I.; supervision, R.L.; project administration, R.L.; funding acquisition, R.L. All authors have read and agreed to the published version of the manuscript.

Funding: This report was written as part of the EU H2020-funded Nunataryuk project (Grant: 773421), where it is filed as part of deliverable 6.4.

Institutional Review Board Statement: Not applicable.

Informed Consent Statement: Not applicable.

Data Availability Statement: Not applicable.

Acknowledgments: The toolbox developed by the OpenEarth community (<https://openearth.community/about-oec>, accessed on: 8 October 2021) allowed better control over XBeach. The team led by Vladislav Isaev from the Department of Geocryology, Lomonosov Moscow State University (MSU), Russia obtained the field observations with support from the project Sustainable Arctic Marine and Coastal Technology (SAMCoT), Norway and Norwegian University of Science and Technology (NTNU).

Conflicts of Interest: The authors declare no conflict of interest.

Appendix A. Definitions

Below are some geometric parameters defined to explain the Arctic coasts:

1. profile line: the surface line of the beach profile not including the snow or ice sheets. During the summer, the profile line is exposed to environmental parameters.
2. permafrost table: the thawing face of the permafrost. During the winter, the line is assumed to collide with the profile line. The difference between the beach line and the permafrost table is the thawing depth.
3. base point: the point at the end of the beach where a sudden change in the slope occurs. Typically, it stands above the tidal range and in calm conditions, water level can not reach the base point.
4. cliff point: the end of the bluff-face and beginning of the bluff-surface; a sudden change in the slope.
5. ice-wedge top point: the point at the surface where the ice-wedge polygon is visible on the surface.
6. ice-wedge bottom point: not necessarily the bottom point of the ice-wedge. It is the point from which we can assume the continuity of the bluff is broken by the ice wedge.
7. swash point/line: Where the average water depth for a timestep is less than 5cm. The point(1D) or line(2D) is assumed to be constant for one timestep.
8. thawing depth: The difference between the permafrost line and profile line, calculated for the grid points on the profile line and normal to the tangent on the point at the profile line.

Appendix B. Four Zones of the Coastal Profile

The four zones of the Arctic coast in terms of erosion, thermal energy transfers and involvement of various physical processes are described in Figure 2. The four zones are defined as follows:

1. bluff surface: it is the surface behind the cliff point X_c . The slope in the zone is zero or close to zero. The surface is covered with vegetation during the summer. Subsidence due to the thawing of the permafrost is the major change in the profile. Thawing depth is dependent on the convection of air and solar radiation. We assume the erosion due

- to surface run-off is negligible (based on field observation). The bluffs are usually filled with ice-wedge polygons. The organic-active layer at the top of the surface has negligible shear strength but can contribute to the lower erodibility to surface run-offs.
2. bluff face: It is the steepest slope of the profile, in between the base point X_b and cliff point X_c and the most active part of the profile. The thawing process contributes directly to the mass loss by slumping and cliff retreat.
 3. beach: The narrow beach in front of the bluff from the base point X_b to the swash point X_s . The thawed sediments accumulate on the beach. The collapsed bluffs fall on the beach. The beach is subject to inundation during the summer storms. The return currents created during the storms sort out the accumulated sediments and transport them offshore.
 4. seabed: It is defined from the swash point X_s to the offshore. The general direction of the sediment transport is offshore since there exist no restoration mechanisms at the Arctic beaches. The wave-induced particle movement is enough to transfer heat (convective heat transfer). The thawing depth is not the limiting factor, i.e., the permafrost lies quite deep. However, due to sea ice, sediment transport during the winter is negligible.

Appendix C. Numerical Schematisation of the Submodules

Appendix C.1. Modelling Storm Surge

Storm surge is modelled by discretising Equation (A1). The setup/surge level η is assumed to be zero at the offshore boundary, where η is the water level setup from the mean sea level. The surge level, η is determined at a 3-h interval. The 3-h time-averaged wind speed is used as an input parameter. When the ice concentration near the sea, i_{com} is above 20%, the surge is set to zero, assuming damping from the ice. The following equation determines the storm surge at each grid point.

The storm surge submodule is the steady-state solution of the following Equation [38]:

$$g(h_m + \eta) \frac{\partial \eta}{\partial x} = (h_m + \eta) fV + \frac{\tau_{sx}}{\rho} + \frac{\Delta P}{\rho g} \quad (\text{A1})$$

where g is the gravitational acceleration, h_m is the mean water depth (time-averaged), $f = 2\sin\omega$ is the Coriolis frequency of Earth, ω is the latitude of the study area (in radians), ρ is the seawater density, V = depth-averaged alongshore water velocity, $\tau_{sx} = \rho C_D U_w^2$ is the stress from the wind on the surface of the water, C_D is the drag coefficient ($= 2 \times 10^{-6}$), and U_w is the wind speed at 10 m and ΔP is the pressure drop.

Equation (A1) is discretised using the forward Euler numerical scheme as follows:

$$\eta_{i-1} = \eta_i + \frac{fV_i \Delta x}{g} + \Delta x \frac{C_f U_i^2}{g(h_i + \eta_i)} \quad (\text{A2})$$

The details of the numerical model of the steady state storm surge are provided by Barnhart et al. [30] in supplementary text S1 available at: https://agupubs.onlinelibrary.wiley.com/action/downloadSupplement?doi=10.1002%2F2013JF002845&file=2013JF002845text01_March2014.pdf, accessed on 2 September 2022.

Appendix C.2. Modelling Slumping

The numerical schematisation of slumping is shown in Figure A1. The line ABCD was the original profile before slumping. Point A has a slope less than the critical slope (m_{cr}). The next grid point B has a slope greater than m_{cr} . Slumping occurred at point B, which resulted in the new line AB'C'D. The permafrost line WXYZ remained unchanged; however, the thawed layer thickness at grid points B and C changed due to slumping. The criterion to initiate slumping as described earlier:

$$S_i > m_{cr} \quad (\text{A3})$$

where S_j is the slope of the grid point j and m_{cr} is the critical slope of the grid point j .

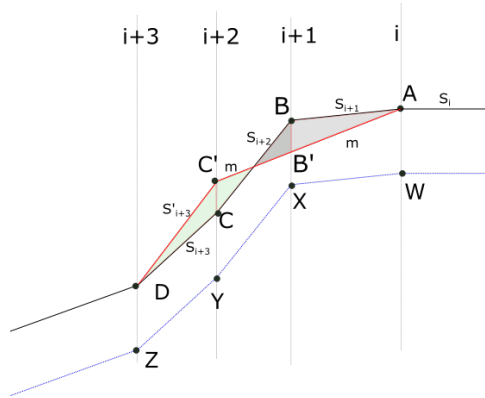


Figure A1. Numerical schematisation of slumping based on critical slope and fall by gravity only. The line ABCD is the profile line which had WXYZ permafrost line at various thawing depths of each grid point. The slope at point B is greater than m_{cr} which triggers the slumping and the new position for the point B at the same grid line is B'.

Let us assume, at the n -th timestep, the numerical submodule is checking whether slumping is triggered at each grid point. Using the critical slope criteria, the model finds point A, the i th grid point does not satisfy the criteria $S_i > m_{cr}$, then it checks the $i + 1$ th grid, the point B.

The slumping module is based on the following assumptions:

The slumping process is initiated by gravitational force only. We ignore the movement of thawed material by the water flow created as a result of permafrost thawing.

The constraints of the initiation of the slumping at the $i + 1$ th grid point (point B in the figure) are as follows:

- C1. No slumping occurs at the permafrost table, the line WXYZ, irrespective of the slope. The failure within permafrost is considered in the bluff stability submodule. This submodule only simulates until thawing depth.
- C2. The slope at the grid point before the i th cell (point A) has a lower slope than critical $S_i > m_{cr}$.
- C3. The n -th timestep has j number of iterations where j is any number iteration until Equation (A3) is no more satisfied.
- C4. For slumping at i -th grid point at j th iteration, the mass transfer is limited to two adjacent grid cells; points B and C are moved to B' and C'.
- C5. As a result of slumping, the grid point in consideration, point B, will be subsided to B', increasing the elevation of point C to C'.
- C6. The subsidence of point B is such that the area under the curve ABCD will be equal to the area AB'C'D so that the conservation of mass is maintained.
- C7. Rule C6 is overridden when the subsidence of point B' is limited by the permafrost line. Point B is not allowed to be lowered than point X. If C6 is overridden, then point C will move and still maintain mass balance. In this case, the movement of the mass will be lower.
- C8. The slumping process is always triggered in the downward direction. If for n th timestep, if two grid points have a slope more than the critical value m_{cr} , slumping will be initiated at the grid point in the higher vertical position.

There is no limit to the iterations for each time step, i.e., the module will run until all the grid points in the profile satisfy the governing equation.

If the slumping occurs, it overrides the thawing depth, x_t estimated by the thawing depth modules.

The workflow of the numerical model is shown in Figure A2. Each grid point is checked for the triggering condition, and then the profile is continuously updated until the last grid point. When all the grid points are examined, the numerical model allows for the next coupled module or next time step.

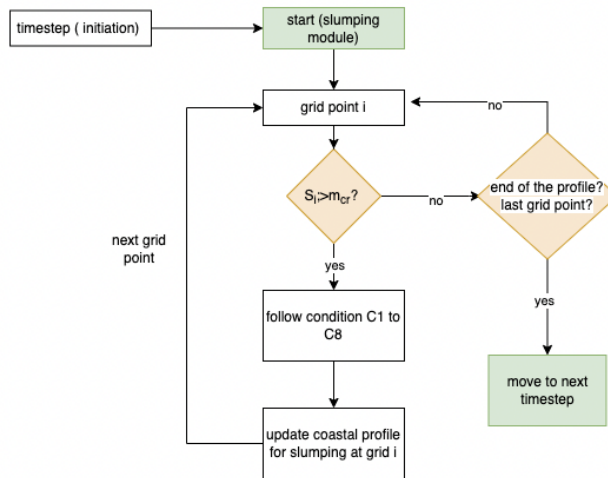


Figure A2. Workflow of the slumping module.

To demonstrate the governing rules mentioned earlier, the module is applied to a hypothetical case. The coastal profile has a 6m bluff height with a bluff slope of 0.5 (26.5°). The thawing depth is 1m at the bluff surface and beach, and 0.71 at the bluff surface.

- Figure A3a demonstrates the case when the m_{cr} is equal to the initial slope, i.e., no slumping can occur establishing the m_{cr} value acts as a triggering condition in the numerical model.
- Figure A3b demonstrate a case when we consider the $m_{cr} = 0.4$. The slumping occurred and part of the bluff surface was exposed (no thawing depth on the upper portion of the bluff surface).
- The effect of m_{cr} on the final profile is shown in Figure A3c. When we reduce the m_{cr} value to 0.3 from 0.4, keeping everything else the same, the exposed portion of the bluff surface got decreased. The slumped materials now moved further back on the beach.
- If we further decrease the m_{cr} value, the sediments are now distributed on almost 35 m along the beach (Figure A3d) and a large portion of the bluff surface is exposed.
- Figure A3e demonstrates a reduction in thawing depth on slumping. If the thawing depth is reduced to 0.5 m with a low m_{cr} value most of the bluff surface is exposed as a result.
- Figure A3f demonstrates the effect of very high thawing depth, the model behaviour is similar to active layer detachment, and a large portion of the thawed layer is moved.

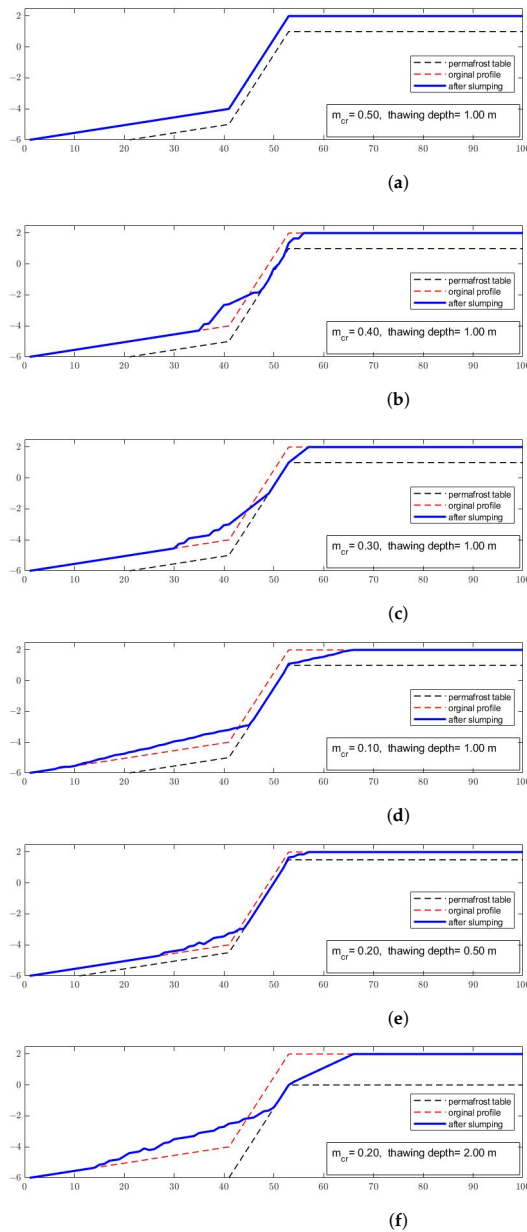


Figure A3. Application of the thawing module in some cases. (a) $m_{cr} = 0.5$, initial slope = 0.5, thawing depth = 1 m; (b) $m_{cr} = 0.4$, initial slope = 0.5, thawing depth = 1 m; (c) $m_{cr} = 0.3$, initial slope = 0.5, thawing depth = 1 m; (d) $m_{cr} = 0.1$, initial slope = 0.5, thawing depth = 1 m; (e) $m_{cr} = 0.2$, initial slope = 0.5, thawing depth = 0.5 m; (f) $m_{cr} = 0.2$, initial slope = 0.5, thawing depth = 2 m.

Appendix C.3. Modelling Bluff Stability

Four modes of failure cases are considered at each timestep. Three of them are the shear failure (mode#1 to#3) and the rest moment failure, the governing equations are described earlier. The failure modes are as follows(see Figure A4):

1. Mode#1: The failure line is CE (from the cliff point to the base point E). The bluff face got steeper as a result.
2. Mode#2: The failure line is GE. Point G is determined using the same slope of the bluff.
3. Mode#3: The failure line is FE. F is the lowest point of the ice-wedge polygon. The shear failure line is the FE.
4. Mode#4: The failure line is PE and PF. This is the moment failure mode.

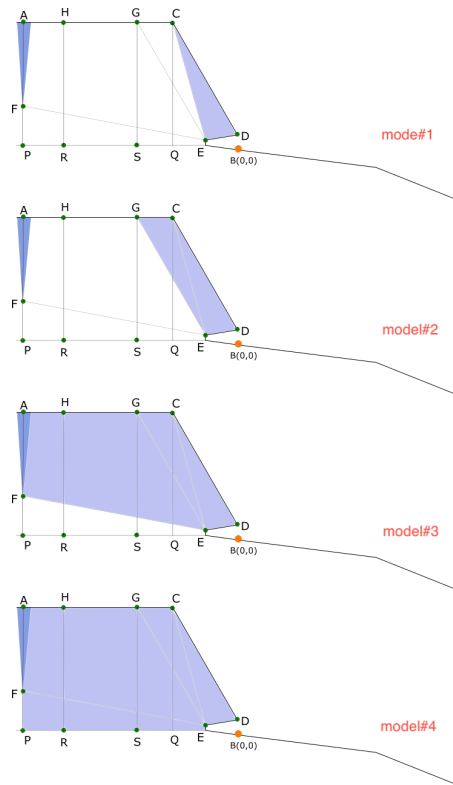


Figure A4. Stability of the overhanging bluffs.

Appendix D. Physical Properties of Permafrost

Table A1. Particle size distribution in the study area.

Particle Size (%-mm)	1.0–0.5	0.5–0.25	0.25–0.1	0.1–0.05	0.05–0.01	0.01–0.005	<0.005	<0.002	<0.001	Moisture (%)	Density (gm/cm ³)
Sample 1	0.2	1.0	59.5	24.1	7.4	0.5	0.5	1.5	5.2	29	2.63
Sample 2	0.1	0.9	58.4	26.6	5.2	1.6	0.5	1.0	5.7	29	2.64
Sample 3	0.1	0.1	64.9	23.6	3.2	0.3	0.5	1.2	6.1	29	2.64
Sample 4	0.1	0.8	62.1	24.6	3.8	0.8	0.5	1.2	6.0	29	2.63

For the detailed field report, we refer to [49], accessible at https://www.researchgate.net/publication/322103499_Field_investigation_and_laboratory_analyses_Baydaratskaya_bay_2017, accessed on 14 September 2021 .

Appendix E. Measurements of Thawing Depth

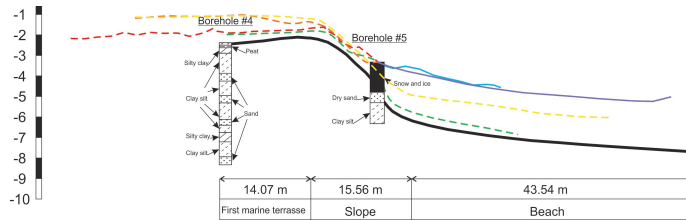


Figure A5. Position of the borehole#4 on profile#3. Image source: SAMCoT report 2015.

Nodes are positioned at 0, 5, 10, 16, 27, 35, 44, 55, 86, 100, 115, 130, 145, 164, 180, 204, 220 and 243 cm from the surface.

Trumpet curves for each month of 2014 are shown in Figure A6.

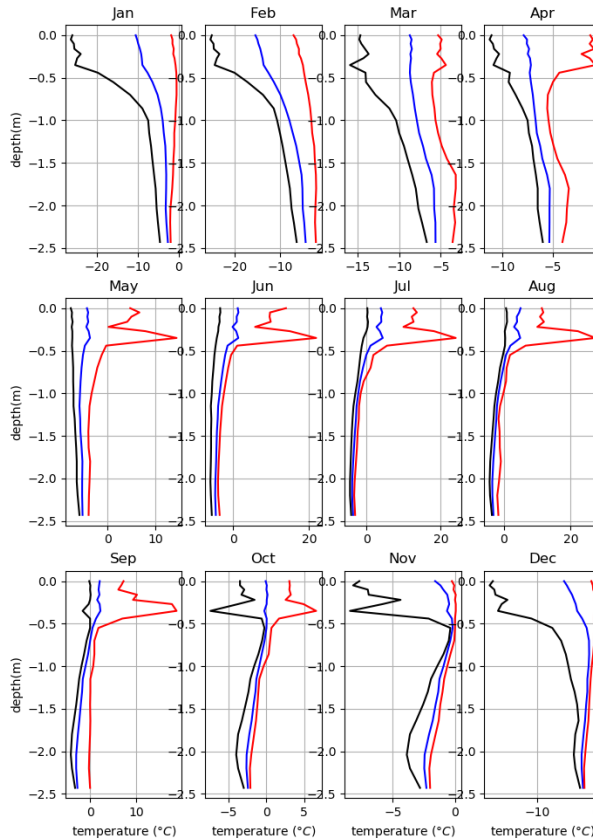


Figure A6. Trumpet curves of the temperature within bluffs for each month.

Appendix F. The Parameters of XBeach

The simulation time for every timestep is 10,900 s which is 3 h and 100 s. An additional 100 s is added to make sure the waves reach the shoreline. The simulation of morphological changes starts after 100 s. Using the 'tstart' parameters, it is controlled within XBeach.

Flow boundary condition parameters

front = abs_1d

back = abs_1d

wavemodel = stationary

tstop = 10,900

CFL = 0.900000

morfac = 1

morstart = 100

wetslp = 0.300000

dryslp = 0.700000

struct = 1

ne_layer = nebed.dep

bcfile = filelist.txt

outputformat = netcdf

tintp = 60

tintg = 60

tstart = 100

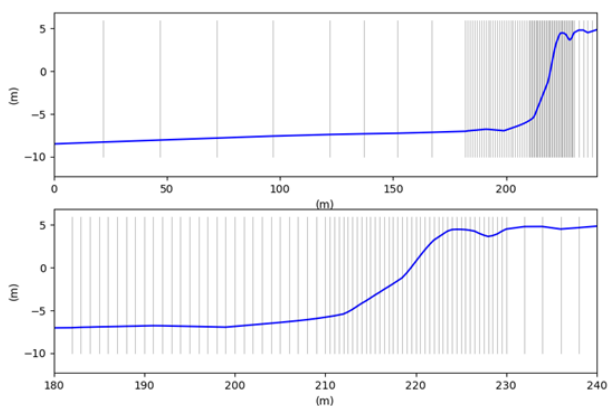


Figure A7. The variable grid spacing along x-axis.

Appendix G. Coastal Profiles for Validation Cases

Even though cases#1, #3 and #5 are on the same profile#1, the erosion pattern is different for each case. In two consecutive years, the erosion pattern drastically changed between cases #1 and #3 (Figure A8a). The bluff slope of case#3 morphed into an uneven bluff slope. The bluff slope became steeper at the lower part near the bluff base, indicating that during the summer of 2017, the hydrodynamic forcing removed a large volume of sediments from the bluff base. Case#4 on profile#8 is relatively stable, but we note the lowering of the elevation of the beach (Figure A8b). Lowering beach elevation indicates that the beach was inundated frequently during the summer of 2017, a similar conclusion we made for case#3. Case#5 is a representation of long-term erosion (Figure A8c). The erosion of the beach was significant in this case; the profile is lowered by approximately 1.5 m around the 180-m mark. However, the base of the bluffs remains almost at the same level. No positive accretion value was recorded for any of the three cases, which suggests that the accumulated sediments must have been washed away by hydrodynamic forcing.

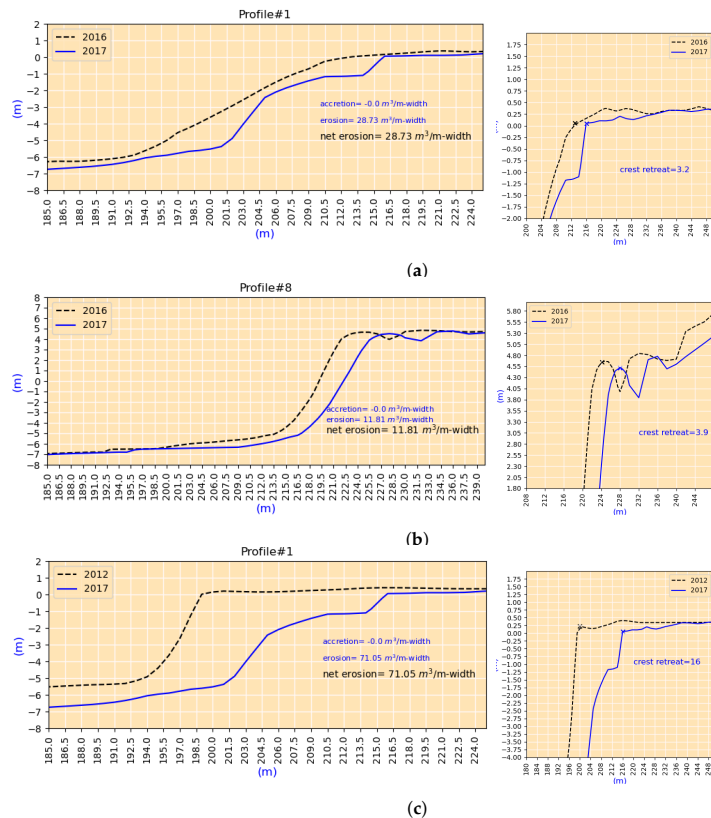


Figure A8. Coastal profiles of cases#3, #4 and #5 are shown. (a) Case#3: Measurements are of profile P#1, from 2016 to 2017. (b) Case#4: Measurement of profile P#8, from 2016 to 2017. (c) Case#5: Measurement of profile P#1, from 2012 to 2017.

Appendix H. Base Case: Environmental Forcing

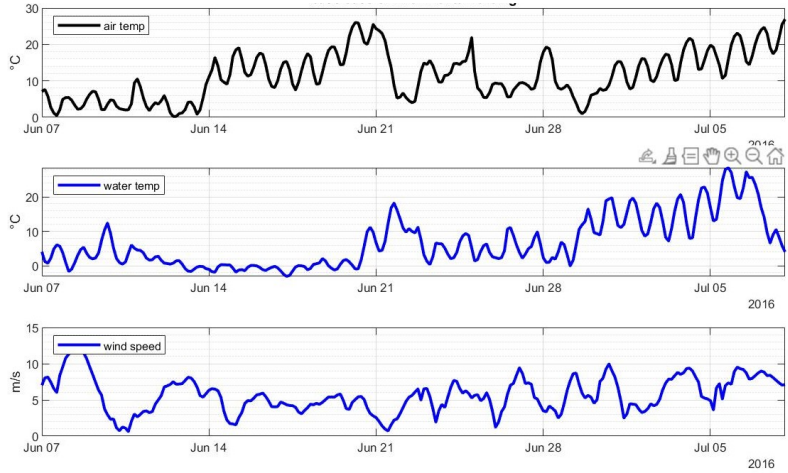


Figure A9. Environmental forcing of the base case.

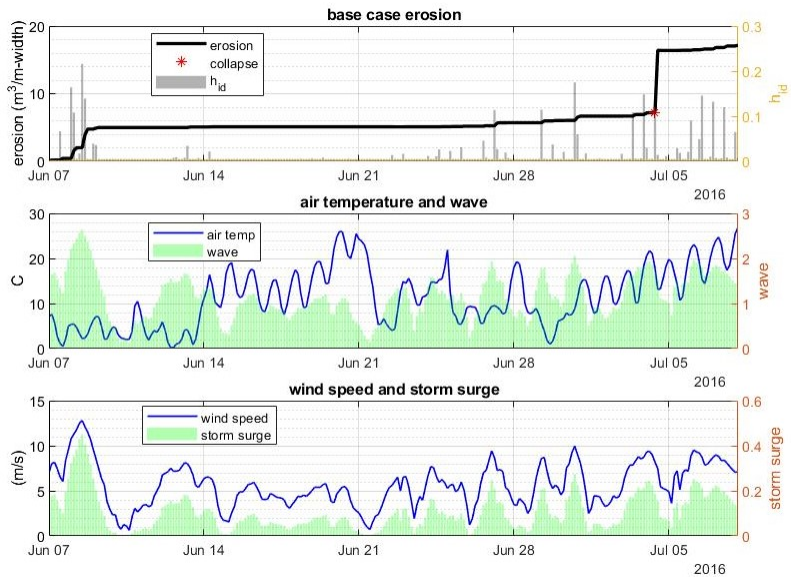


Figure A10. Erosion of the base case.

Appendix I. Effect of the Environmental Forcing

Appendix I.1. Effect of Seawater Temperature

The base case is modified to demonstrate the effect of water temperature. Instead of applying the environmental forcing as shown in Figure A9, a mean water temperature is used so that the deviation of the erosion volume over time can be identified. The mean seawater temperature of the base case was 6.65 °C . We now apply 2 to 10 °C with 2 °C increment (Figure A11). The erosion with mean 6 °C is considered the base case. For the

base case, no bluff collapse is recorded. Bluff collapse is triggered for 8 °C and 10 °C, collapse for 10 °C occurred just 12 h earlier (three timesteps). We can infer that unless the mean seawater temperature for this 32.5 days is over 6 °C, it is unlikely any bluff collapse will occur. We also notice, for the first three cases, the erosion volume is almost the same, indicating the sea-water temperature is not an important factor for the thermodenudation of the bluff surface.

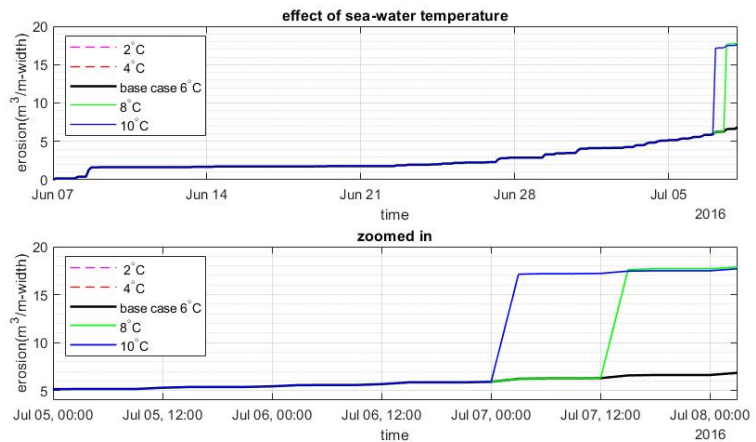


Figure A11. The effect of water temperature inputs on erosion.

Appendix I.2. The Effect of Air Temperature

Similar to the sensitivity analysis of water temperature, the base case is modified to demonstrate the effect of air temperature on erosion volume. The mean air temperature of the earlier base case is 11.45 °C. The air temperature for the modified base case is chosen as 10 °C. The new base case is chosen in such a way that thermodenudation is the dominant erosion mechanism. Keeping all other environmental forcings unchanged, only air temperature is increased and decreased. The result is shown in Figure A12. The cases indicate in our model that air temperature at the beginning of summer may be the controlling parameter for erosion, but eventually, the difference due to air temperature is not significant. However, we can not reach a conclusion from this analysis since only the thermodenudation mechanism is considered in this analysis. Thermodenudation in the study area contributes nearly 20 to 30% of the erosion volume.

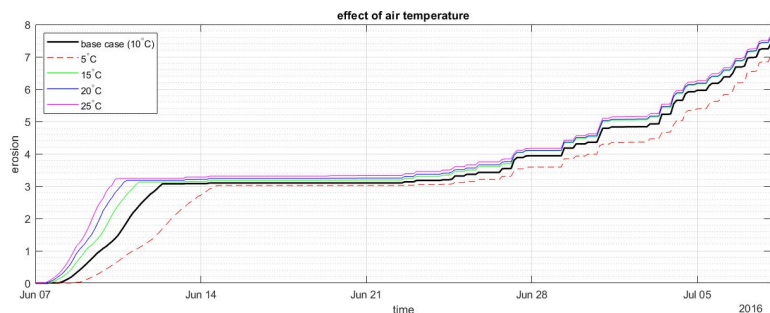


Figure A12. The effect of air temperature inputs on erosion.

References

1. Lantuit, H.; Overduin, P.P.; Couture, N.; Wetterich, S.; Aré, F.; Atkinson, D.; Brown, J.; Cherkashov, G.; Drozdov, D.; Forbes, D.L.; et al. The Arctic coastal dynamics database: a new classification scheme and statistics on Arctic permafrost coastlines. *Estuaries Coasts* **2012**, *35*, 383–400. [[CrossRef](#)]
2. Gibbs, A.E.; Richmond, B.M. *National Assessment of Shoreline Change: Historical Shoreline Change along the North Coast of Alaska, US-Canadian Border to Icy Cape*; US Department of the Interior, US Geological Survey: Washington, DC, USA, 2015.
3. Isaev, V.; Koshurnikov, A.; Pogorelov, A.; Amangurov, R.; Podchasov, O.; Sergeev, D.; Buldovich, S.; Aleksyutina, D.; Grishakina, E.; Kioka, A. Cliff retreat of permafrost coast in south-west Baydaratskaya Bay, Kara Sea, during 2005–2016. *Permafrost. Periglac. Process.* **2019**, *30*, 35–47. [[CrossRef](#)]
4. Gibbs, A.; Richmond, B.; Erikson, L.; Jones, B. Long-term retreat of coastal permafrost bluffs, Barter Island, Alaska. In Proceedings of the 5th European Conference on permafrost, EUCOP5, Chamonix, France, 23 June–1 July 2018; Volume 1, pp. 1–2.
5. Jones, B.M.; Arp, C.D.; Jorgenson, M.T.; Hinkel, K.M.; Schmutz, J.A.; Flint, P.L. Increase in the rate and uniformity of coastline erosion in Arctic Alaska. *Geophys. Res. Lett.* **2009**, *36*. [[CrossRef](#)]
6. Jones, B.; Bull, D.; Farquharson, L.; Buzard, R.; Arp, C.; Grosse, G.; Romanovsky, V. A decade of annual permafrost coastal observations indicate changes in the Arctic System. *Environ. Res. Lett.* **2018**, *13*, 1–13.
7. Ogorodov, S.; Aleksyutina, D.; Baranskaya, A.; Shabanova, N.; Shilova, O. Coastal erosion of the Russian Arctic: An overview. *J. Coast. Res.* **2020**, *95*, 599–604. [[CrossRef](#)]
8. Barnhart, K.; Overeem, I.; Anderson, R.S. The effect of changing sea ice on the physical vulnerability of Arctic coasts. *Cryosphere* **2014**, *8*, 1777–1799. [[CrossRef](#)]
9. Stroeve, J.; Notz, D. Changing state of Arctic sea ice across all seasons. *Environ. Res. Lett.* **2018**, *13*, 103001. [[CrossRef](#)]
10. Serreze, M.; Barrett, A.; Stroeve, J.; Kindig, D.; Holland, M. The emergence of surface-based Arctic amplification. *Cryosphere Discuss.* **2008**, *2*, 601–622. [[CrossRef](#)]
11. Cohen, J.; Screen, J.A.; Furtado, J.C.; Barlow, M.; Whittleston, D.; Coumou, D.; Francis, J.; Dethloff, K.; Entekhabi, D.; Overland, J.; et al. Recent Arctic amplification and extreme mid-latitude weather. *Nat. Geosci.* **2014**, *7*, 627–637. [[CrossRef](#)]
12. Nielsen, D.; Pieper, P.; Barkhordarian, A.; Overduin, P.; Ilyina, T.; Brovkin, V.; Baehr, J.; Dobrynin, M. Increase in Arctic coastal erosion and its sensitivity to warming in the twenty-first century. *Nat. Clim. Chang.* **2022**, *12*, 263–270. [[CrossRef](#)]
13. Rowland, J.; Jones, C.; Altmann, G.; Bryan, R.; Crosby, B.; Hinzman, L.; Kane, D.; Lawrence, D.; Mancino, A.; Marsh, P.; et al. Arctic landscapes in transition: responses to thawing permafrost. *Eos Trans. Am. Geophys. Union* **2010**, *91*, 229–230. [[CrossRef](#)]
14. Overeem, I.; Anderson, R.S.; Wobus, C.W.; Clow, G.D.; Urban, F.E.; Matell, N. Sea ice loss enhances wave action at the Arctic coast. *Geophys. Res. Lett.* **2011**, *38*. [[CrossRef](#)]
15. Steele, M.; Ermold, W.; Zhang, J. Arctic Ocean surface warming trends over the past 100 years. *Geophys. Res. Lett.* **2008**, *35*. [[CrossRef](#)]
16. Holland-Bartels, L.; Pierce, B. *An Evaluation of the Science Needs to Inform Decisions on Outer Continental Shelf Energy Development in the Chukchi and Beaufort Seas, Alaska*; Technical Report; US Geological Survey: Reston, VI, USA, 2011.
17. Günther, F.; Overduin, P.P.; Yakshina, I.A.; Opel, T.; Baranskaya, A.V.; Grigoriev, M.N. Observing Muostakh disappear: permafrost thaw subsidence and erosion of a ground-ice-rich island in response to arctic summer warming and sea ice reduction. *Cryosphere* **2015**, *9*, 151–178. [[CrossRef](#)]
18. Irrgang, A.M.; Lantuit, H.; Manson, G.K.; Günther, F.; Grosse, G.; Overduin, P.P. Variability in rates of coastal change along the Yukon coast, 1951 to 2015. *J. Geophys. Res. Earth Surf.* **2018**, *123*, 779–800. [[CrossRef](#)]
19. Jones, B.M.; Irrgang, A.M.; Farquharson, L.M.; Lantuit, H.; Whalen, D.; Ogorodov, S.; Grigoriev, M.; Tweedie, C.; Gibbs, A.E.; Strzelecki, M.C.; et al. Coastal Permafrost Erosion. *Arct. Rep. Card* **2020**, *15*.
20. Jones, B.M.; Hinkel, K.M.; Arp, C.D.; Eisner, W.R. Modern erosion rates and loss of coastal features and sites, Beaufort Sea coastline, Alaska. *Arctic* **2008**, *61*, 361–372. [[CrossRef](#)]
21. Landrum, L.; Holland, M.M. Extremes become routine in an emerging new Arctic. *Nat. Clim. Chang.* **2020**, *10*, 1108–1115. [[CrossRef](#)]
22. Are F, E. Thermal abrasion of sea coast. *Polar Geogr. Geol.* **1988**, *12*, 1–157. [[CrossRef](#)]
23. Squire, V.A.; Vaughan, G.L.; Bennetts, L.G. Ocean surface wave evolution in the Arctic Basin. *Geophys. Res. Lett.* **2009**, *36*. [[CrossRef](#)]
24. Kobayashi, N. Formation of thermoerosional niches into frozen bluffs due to storm surges on the Beaufort Sea coast. *J. Geophys. Res. Ocean.* **1985**, *90*, 11983–11988. [[CrossRef](#)]
25. Russell-Head, D. The melting of free-drifting icebergs. *Ann. Glaciol.* **1980**, *1*, 119–122. [[CrossRef](#)]
26. White, F.M.; Spaulding, M.L.; Gominho, L. *Theoretical Estimates of the Various Mechanisms Involved in Iceberg Deterioration in the Open Ocean Environment*; Technical Report; Rhode Island Univ. Kingston: Kingston, RI, USA, 1980.
27. Bull, D.L.; Bristol, E.M.; Brown, E.; Choens, R.C.; Connolly, C.T.; Flanary, C.; Frederick, J.M.; Jones, B.M.; Jones, C.A.; Ward Jones, M.; et al. *Arctic Coastal Erosion: Modeling and Experimentation*; Technical Report; Sandia National Lab. (SNL-NM): Albuquerque, NM, USA, 2020.
28. Hoque, M.A.; Pollard, W.H. Arctic coastal retreat through block failure. *Can. Geotech. J.* **2009**, *46*, 1103–1115. [[CrossRef](#)]
29. Ravens, T.; Jones, B.; Zhang, J.; Arp, C.D.; Schmutz, J.A. Process-based coastal erosion modeling for drew point, North Slope, Alaska. *J. Water. Port Coastal Ocean. Eng.* **2012**, *138*, 122–130. [[CrossRef](#)]